ornl

NUREG/CR-3744
Volume 2
ORNL/TM-9154/V2

OAK RIDGE
NATIONAL
LABORATORY

MARTIN MARIETTA

Heavy-Section Steel Technology Program Semiannual Progress Report for April–September 1984

C. E. Pugh

Prepared for the U.S. Nuclear Regulatory Commission
Office of Nuclear Regulatory Research
Under Interagency Agreements DOE 40-551-75 and 40-552-75

OPERATED BY
MARTIN MARIETTA ENERGY SYSTEMS, INC.
FOR THE UNITED STATES
DEPARTMENT OF ENERGY

NOTICE

Availability of Reference Materials Cited in NRC Publications

Most documents cited in NRC publications will be available from one of the following sources:

1. The NRC Public Document Room, 1717 H Street, N.W., Washington, DC 20555
2. The NRC/GPO Sales Program, U.S. Nuclear Regulatory Commission, Washington, DC 20555
3. The National Technical Information Service, Springfield, VA 22161

Although the listing that follows represents the majority of documents cited in NRC publications, it is not intended to be exhaustive.

Referenced documents available for inspection and copying for a fee from the NRC Public Document Room include NRC correspondence and internal NRC memoranda; NRC Office of Inspection and Enforcement bulletins, circulars, information notices, inspection and investigation notices; Licensee Event Reports; vendor reports and correspondence; Commission papers; and applicant and licensee documents and correspondence.

The following documents in the NUREG series are available for purchase from the NRC/GPO Sales Program: formal NRC staff and contractor reports, NRC-sponsored conference proceedings, and NRC booklets and brochures. Also available are Regulatory Guides, NRC regulations in the *Code of Federal Regulations*, and *Nuclear Regulatory Commission Issuances*.

Documents available from the National Technical Information Service include NUREG series reports and technical reports prepared by other federal agencies and reports prepared by the Atomic Energy Commission, forerunner agency to the Nuclear Regulatory Commission.

Documents available from public and special technical libraries include all open literature items, such as books, journal and periodical articles, and transactions. *Federal Register* notices, federal and state legislation, and congressional reports can usually be obtained from these libraries.

Documents such as theses, dissertations, foreign reports and translations, and non-NRC conference proceedings are available for purchase from the organization sponsoring the publication cited.

Single copies of NRC draft reports are available free, to the extent of supply, upon written request to the Division of Technical Information and Document Control, U.S. Nuclear Regulatory Commission, Washington, DC 20555.

Copies of industry codes and standards used in a substantive manner in the NRC regulatory process are maintained at the NRC Library, 7920 Norfolk Avenue, Bethesda, Maryland, and are available there for reference use by the public. Codes and standards are usually copyrighted and may be purchased from the originating organization or, if they are American National Standards, from the American National Standards Institute, 1430 Broadway, New York, NY 10018.

NUREG/CR-3744
Volume 2
ORNL/TM-9154/V2
Dist. Category RF

Engineering Technology Division

HEAVY-SECTION STEEL TECHNOLOGY PROGRAM SEMIANNUAL PROGRESS REPORT FOR APRIL–SEPTEMBER 1984

C. E. Pugh

Manuscript Completed – November 8, 1984
Date Published – December 1984

Prepared for the
U.S. Nuclear Regulatory Commission
Office of Nuclear Regulatory Research
under Interagency Agreements DOE 40-551-75 and 40-552-75

NRC FIN No. B0119

Prepared by the
OAK RIDGE NATIONAL LABORATORY
Oak Ridge, Tennessee 37831
operated by
MARTIN MARIETTA ENERGY SYSTEMS, INC.
for the
U.S. DEPARTMENT OF ENERGY
under Contract No. DE-AC05-840R21400

CONTENTS

LIST OF FIGURES

LIST OF TABLES

PREFACE

The Heavy-Section Steel Technology (HSST) Program, which is sponsored by the Nuclear Regulatory Commission, is an engineering research activity devoted to extending and developing the technology for assessing the margin of safety against fracture of the thick-walled steel pressure vessels used in light-water-cooled nuclear power reactors. The program is being carried out in close cooperation with the nuclear power industry. This report covers HSST work performed in April–September 1984. The work performed by Oak Ridge National Laboratory (ORNL) and by subcontractors is managed by the Engineering Technology Division. Major tasks at ORNL are carried out by the Engineering Technology Division and the Metals and Ceramics Division. Prior progress reports on this program are ORNL-4176, ORNL-4315, ORNL-4377, ORNL-4463, ORNL-4512, ORNL-4590, ORNL-4653, ORNL-4681, ORNL-4764, ORNL-4816, ORNL-4855, ORNL-4918, ORNL-4971, ORNL/TM-4655 (Vol. II), ORNL/TM-4729 (Vol. II), ORNL/TM-4805 (Vol. II), ORNL/TM-4914 (Vol. II), ORNL/TM-5021 (Vol. II), ORNL/TM-5170, ORNL/NUREG/TM-3, ORNL/NUREG/TM-28, ORNL/NUREG/TM-49, ORNL/NUREG/TM-64, ORNL/NUREG/TM-94, ORNL/NUREG/TM-120, ORNL/NUREG/TM-147, ORNL/NUREG/TM-166, ORNL/NUREG/TM-194, ORNL/NUREG/TM-209, ORNL/NUREG/TM-239, NUREG/CR-0476 (ORNL/NUREG/TM-275), NUREG/CR-0656 (ORNL/NUREG/TM-298), NUREG/CR-0818 (ORNL/NUREG/TM-324), NUREG/CR-0980 (ORNL/NUREG/TM-347), NUREG/CR-1197 (ORNL/NUREG/TM-370), NUREG/CR-1305 (ORNL/NUREG/TM-380), NUREG/CR-1477 (ORNL/NUREG/TM-393), NUREG/CR-1627 (ORNL/NUREG/TM-401), NUREG/CR-1806 (ORNL/NUREG/TM-419), NUREG/CR-1941 (ORNL/NUREG/TM-437), NUREG/CR-2141/Vol. 1 (ORNL/TM-7822), NUREG/CR-2141, Vol. 2 (ORNL/TM-7955), NUREG/CR-2141, Vol. 3 (ORNL/TM-8145), NUREG/CR-2141, Vol. 4 (ORNL/TM-8252), NUREG/CR-2751, Vol. 1 (ORNL/TM-8369/V1), NUREG/CR-2751, Vol. 2 (ORNL/TM-8369/V2), NUREG/CR-2751, Vol. 3 (ORNL/TM-8369/V3), NUREG/CR-2751, Vol. 4 (ORNL/TM-8369/V4), NUREG/CR-3334, Vol. 1 (ORNL/TM-8787/V1), NUREG/CR-3334, Vol. 2 (ORNL/TM-8787/V2), NUREG/CR-3334, Vol. 3 (ORNL/TM-8787/V3), and NUREG/CR-3744, Vol. 1 (ORNL/TM-9154/V1).

SUMMARY

1. PROGRAM MANAGEMENT

The total program is arranged into ten tasks: (1) program management, (2) fracture methodology and analysis, (3) material characterization and properties, (4) environmentally assisted crack-growth studies, (5) crack-arrest technology, (6) irradiation effects studies, (7) stainless steel cladding evaluations, (8) intermediate vessel tests and analyses, (9) thermal-shock technology, and (10) pressurized-thermal-shock technology. Progress reports are issued on a semiannual basis, and the chapters correspond to the ten tasks.

The work performed at Oak Ridge National Laboratory (ORNL) and under existing research and development subcontracts is included in this report. During the report period, 42 program briefings, reviews, or presentations were made, and 12 technical documents were published. Program subcontracts were extended to cover FY 1985 work.

2. FRACTURE METHODOLOGY AND ANALYSIS

Improvements were made to the ORNL fracture codes ORMGEN and ORVIRT to permit improved modeling of near crack-tip regions. The ORNL codes were distributed to eight organizations. Analyses were performed on a laboratory-sized panel specimen that shows promise for providing high K_{Ia} data in the presence of a rising K field.

Because warm prestressing (WPS) is an important beneficial factor affecting the safety of nuclear pressure vessels subjected to pressurized thermal-shock transients, an analytical description of the phenomenon, developed at the United Kingdom Central Electricity Generating Board (UK CEGB) and based on the strip-yield model, was reviewed and its physical basis clarified. This analytical method is being applied to the planning and data analysis for the pressurized thermal-shock experiments (PTSEs).

Integrated fracture-mechanics experimentation and finite-element analyses are being conducted at the Southwest Research Institute (SwRI) to develop improved predictions for crack arrest in high-upper-shelf toughness conditions. Preparations for the measurement of crack length vs time and load point displacement vs time are being made. Viscoplastic material characterization experiments were performed to enable use of the Bodner-Partom model in the finite-element fracture analyses.

The University of Maryland (UM) completed testing of three-point-bend specimens of A508 steel to determine the loss-of-cleavage temperature for this material. The investigation into the influence that constraint has on the determination of the loss-of-cleavage temperature as predicted from Charpy V-notch (CVN) specimens was also finalized by the UM.

3. MATERIAL CHARACTERIZATION AND PROPERTIES

Development of crack-arrest testing technology continued at ORNL, and tests for the American Society for Testing and Materials (ASTM) round robin were completed. Further development of the dc potential drop method was carried out. Mechanical properties characterization of the wide-plate crack-arrest material was performed along with posttest fracture examinations for PTSE-1.

4. ENVIRONMENTALLY ASSISTED CRACK-GROWTH TECHNOLOGY

Both fatigue crack-growth rate and fractography results are presented for the recently begun matrix of tests on a high-sulfur steel. Effects of frequency, R ratio, temperature, and environment are being studied, and results are consistent with existing data and show increasing growth rates with higher R ratio and temperature. Static-load cracking has been observed on two more heats of heat-affected-zone (HAZ) material, so that now cracking has been observed on all heats of HAZ that have been tested. A series of tests was completed showing electrochemical potential measurements as a function of time during two experiments. Results showed the silver/silver chloride electrode to be the most reliable in reflecting environmental changes.

5. CRACK-ARREST TECHNOLOGY

Preparations continued for conducting wide-plate crack-arrest at the National Bureau of Standards (NBS). Heavy-Section Steel Technology (HSST) plate 13A was chosen as the test material and was cut to provide material for characterization testing and wide-plate specimens. ORNL designed, machined, and shipped two specimens to the NBS. ORNL developed tentative conditions for the first test, WP-1.1, and defined benchmark statements for pretest analytical solutions. ORNL, SwRI, and the UM performed dynamic solutions using the computer codes SWIDAC and SAMCR. Mechanical properties, including fracture toughness and arrest toughness values, were determined by ORNL and Battelle Columbus Laboratories (BCL). The NBS made all preparations for performing WP-1.1, including the design of the pull-plate assemblies for the large NBS test machine, heating and cooling systems, and data acquisition system. The pretest analyses aided instrumentation placement, and WP-1.1 was successfully run in the last few days of this period.

In other areas, the UM continued to administer the ASTM E24.01.06 round robin on crack-arrest testing. BCL obtained K_{Ia} data for the WP-1.1 material at temperatures to the onset of the Charpy upper shelf, which is close to the pretest estimate of the large-specimen crack-arrest point.

In addition, BCL compilation of the Crack-Arrest Data Base was completed. It contains 478 data extending from RT_{NDT} − 114°C to RT_{NDT} + 102°C. Finally, preparations for instrumenting WP-1.1 to monitor crack speeds have been completed by BCL.

6. IRRADIATION EFFECTS STUDIES

Cooperative testing in the Fourth Irradiation Series continued, with all 1T-CS tests completed for unirradiated material and testing under way for the irradiated material. The first two capsules containing 4T-CS of high-copper weld material were irradiated under the Fifth Irradiation Series, and irradiation of the second set of capsules was initiated. The temperature profiles along the crack tip of the specimens have been very satisfactorily controlled. Metallographic studies of the three layers of stainless steel cladding used in the Seventh Irradiation Series were analyzed to expose the various microstructures present.

7. CLADDING EVALUATIONS

Work continued on preparation of a topical report on the clad-beam tests that were performed in earlier reporting periods. Further fractography work was performed.

8. INTERMEDIATE VESSEL TESTS AND ANALYSIS

Work continued on preparation of a topical report on the test ITV-8A which involved a low-upper-shelf weld. Posttest fractography and improved finite-element analyses were performed.

9. THERMAL-SHOCK TECHNOLOGY

As a part of the Integrated Pressurized-Thermal-Shock (IPTS) Program, probabilistic fracture-mechanics calculations were made for the Calvert Cliffs-1 and H. B. Robinson-2 reactor pressure vessels to obtain a best estimate of the conditional probability of vessel failure [$P(F|E)$] associated with numerous postulated transients. These studies indicated that warm prestressing could be a significant factor and that $P(F|E)$ was insensitive to the crack-arrest toughness, including the "upper-shelf" value.

The feasibility of conducting a thermal-shock experiment with a clad test cylinder and a subclad crack was investigated. The studies included two-dimensional (2-D) and three-dimensional (3-D) linear-elastic fracture-mechanics and elastic-plastic fracture-mechanics calculations for a

19-mm-deep, 6/1 semielliptical subclad crack in a clad thermal-shock experiment (TSE) test cylinder subjected to a typical TSE (liquid nitrogen) thermal transient.

10. PRESSURIZED-THERMAL-SHOCK TECHNOLOGY

Results of the first pressurized-thermal-shock test, PTSE-1, were evaluated; plans were formulated; and preparations were initiated for the next experiment, PTSE-2. The fracture surfaces of the PTSE-1 flaw were examined in detail. Information recorded by the data acquisition system was evaluated, processed, and used in posttest fracture analyses. The final results and conclusions, which will be reported in detail in a topical report now in preparation, are essentially as stated in the previous progress report. Objectives for experiment PTSE-2 were established and preparations for the test are in progress. PTSE-2 will be a study of warm prestressing and upper-shelf instability. The vessel (V-8) used in PTSE-1 will be repaired with a low-upper-shelf insert in the region to be flawed. Preliminary fracture analyses confirm the feasibility of the test.

HEAVY-SECTION STEEL TECHNOLOGY PROGRAM SEMIANNUAL PROGRESS REPORT FOR APRIL–SEPTEMBER 1984*

C. E. Pugh

ABSTRACT

The Heavy-Section Steel Technology (HSST) Program is conducted for the Nuclear Regulatory Commission. The studies are related to all areas of the technology of materials fabricated into thick-section primary-coolant containment systems of light-water-cooled nuclear power reactors. The focus is on the behavior and structural integrity of steel pressure vessels containing cracklike flaws. Starting with FY 1984, the program is organized into ten tasks: (1) program management, (2) fracture methodology and analysis, (3) material characterization and properties, (4) environmentally assisted crack-growth studies, (5) crack-arrest technology, (6) irradiation effects studies, (7) cladding evaluations, (8) intermediate vessel tests and analysis, (9) thermal-shock technology, and (10) pressurized-thermal-shock (PTS) technology. During this period, extensions were made to the ADINA-ORMGEN-ORVIRT fracture analysis codes to improve near-crack-tip modeling. Copies of these analysis codes were distributed to numerous organizations outside Oak Ridge National Laboratory (ORNL). Interpretative assessments were made of a Central Electricity Generating Board warm prestressing model. Elastodynamic analyses were performed by ORNL, Southwest Research Institute, and University of Maryland in support of the wide-plate crack-arrest tests that the National Bureau of Standards is to perform for the HSST program. Characterization studies included deformation and fracture properties tests of wide-plate material and crack-growth rate tests of low-sulfur vessel steels. Analytical assessments were made of laboratory specimens with potential for use in obtaining high crack-arrest toughness data. ORNL and two subcontractors performed K_{Ia} tests for the ASTM round robin. Irradiations were initiated for the study of K_{Ic} shifts for welds with different copper contents, and testing proceeded in the Fourth Irradiation Series. Work continued on reports covering clad-beam tests and ITV-8A that contained a low-upper-shelf weldment. Exploratory analytical fracture studies were carried out for clad cylinders undergoing thermal-shock loadings, and fracture assessments continued for the Integrated Pressurized Thermal-Shock-Program. Posttest analyses and fracture characterizations were carried out for the first pressurized thermal-shock test (PTSE-1), and preparation of the topical report on PTSE-1 progressed.

---

*This report is written in terms of metric units. Conversion from SI to English units for all SI quantitites are listed on a foldout page at the end of this report.

1. PROGRAM MANAGEMENT

C. E. Pugh

The Heavy-Section Steel Technology (HSST) Program, a major safety program sponsored by the Nuclear Regulatory Commission (NRC) at the Oak Ridge National Laboratory (ORNL), is concerned with the structural integrity of the primary systems [particularly the reactor pressure vessels (RPVs)] of light-water-cooled nuclear power reactors (LWRs). The structural integrity of these vessels is ensured by (1) designing and fabricating RPVs according to standards set by the code for nuclear pressure vessels, (2) detecting flaws of significant size that occur during fabrication and in service, and (3) developing methods of producing quantitative estimates of conditions under which fracture could occur. The program is concerned mainly with developing pertinent fracture technology, including knowledge of (1) the material used in these thick-walled vessels, (2) the flaw-growth rate, and (3) the combination of flaw size and load that would cause fracture and thus limit the life and/or the operating conditions of this type of reactor plant.

The program is coordinated with other government agencies and with the manufacturing and utility sectors of the nuclear power industry in the United States and abroad. The overall objective is a quantification of safety assessments for regulatory agencies, professional code-writing bodies, and the nuclear power industry. Several activities are conducted under subcontract by research facilities in the United States and through informal cooperative effort on an international basis. Five research and development subcontracts are currently in force, and steps have been initiated to extend each of these through FY 1985.

Effective with the beginning of FY 1984, the program tasks were slightly rearranged according to the work breakdown structure shown in Fig. 1.1. Accordingly, the chapters of this progress report correspond

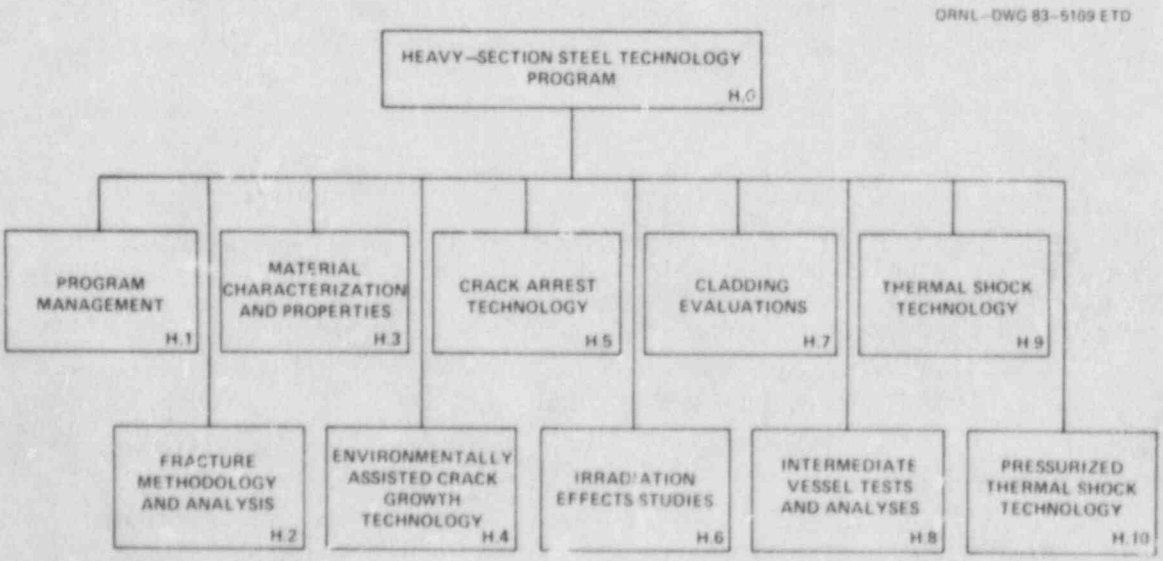

Fig. 1.1. Level-2 work breakdown structures for HSST Program.

to these ten tasks. During this period, the 5-year program plan[1] was issued as a topical report and distributed to the NRC-RF category.

Two foreign technical specialists came to ORNL on temporary assignments to the HSST program: Dr. Hermann Stamm of the Institute für Reaktorbauelemente, Kernforschungszentrum Karlsruhe, Federal Republic of Germany for 9 months; and Dr. Robert Wanner of the Swiss Federal Institute for Reactor Research for 1 year.

During this period, 43 program briefings, reviews, or presentations were made by the HSST staff at technical meetings and at program reviews for the NRC staff or visitors. There were 12 publications that include 2 technical progress reports,[2-3] 6 topical reports,[1,4-8] and 4 technical papers.[9-12]

References

1. *Heavy-Section Steel Technology Program — Five-Year Plan FY 1983–1987*, NUREG/CR-3595 (ORNL/TM-9008), Martin Marietta Energy Systems, Inc., Oak Ridge Natl. Lab., April 1984.

2. C. E. Pugh, *Heavy-Section Steel Technology Program Quart. Prog. Rep. July–September 1983*, NUREG/CR-3334, Vol. 3 (ORNL/TM-8787/V3), Union Carbide Corp. Nuclear Div., Oak Ridge Natl. Lab., March 1984.

3. C. E. Pugh, *Heavy-Section Steel Technology Program Semiannual Prog. Rep. October 1983–March 1984*, NUREG/CR-3744, Vol. 1 (ORNL/TM-9154/V1), Martin Marietta Energy Systems, Inc., Oak Ridge Natl. Lab., June 1984.

4. R. H. Bryan et al., *Quick-Look Report on the First Pressurized-Thermal-Shock Test, PTSE-1*, ORNL/PTSE-1, Union Carbide Corp. Nuclear Div., Oak Ridge Natl. Lab., March 7, 1984.

5. J. G. Merkle, *An Examination of the Size Effects and Data Scatter Observed in Small-Specimen Cleavage Fracture Toughness Testing*, NUREG/CR-3672 (ORNL/TM-9080), Martin Marietta Energy Systems, Inc., Oak Ridge Natl. Lab., April 1984.

6. H. A. Domian, *Vessel V-7 and V-8 Repair and Characterization of Insert Material*, NUREG/CR-3771 (ORNL/Sub/72-52845/1), Martin Marietta Energy Systems, Inc., Oak Ridge Natl. Lab., May 1984.

7. R. D. Cheverton and D. G. Ball, *OCA-P, A Deterministic and Probabilistic Fracture-Mechanics Code for Application to Pressure Vessels*, NUREG/CR-3618 (ORNL-5991), Martin Marietta Energy Systems, Inc., Oak Ridge Natl. Lab., June 1984.

8. W. R. Corwin, *Assessment of Radiation Effects Relating to Reactor Pressure Vessel Cladding*, NUREG/CR-3671 (ORNL-6047), Martin Marietta Energy Systems, Inc., Oak Ridge Natl. Lab., July 1984.

9. B. R. Bass et al., "Computational Methods for Fracture Mechanics Analysis of Pressurized-Thermal-Shock Experiments," *Proceedings of Third International Conference on Numerical Methods in Fracture Mechanics, March 25–30, 1984, Swansea, United Kingdom.*

10. W. R. Corwin, R. G. Berggren, and R. K. Nanstad, "Charpy Toughness and Tensile Properties of Neutron Irradiated Stainless Steel Weld Cladding," *Proceedings of the Twelfth International Symposium on the Effects of Radiation on Materials, Williamsburg, Va., June 18–20, 1984*, American Society for Testing and Materials, Philadelphia.

11. R. G. Berggren, J. R. Hawthorne, and R. K. Nanstad, "An Analysis of Charpy V-Notch Impact Toughness of Irradiated A533 Gr B Cl 1 Plate and Four Submerged-Arc Welds," *Proceedings of the Twelfth International Symposium on the Effects of Radiation on Materials, Williamsburg, Va., June 18–20, 1984*, American Society for Testing and Materials, Philadelphia.

12. B. H. Menke et al., "Effects of Neutron Irradiation on Fracture Toughness of A533 Gr B Cl 1 Plate and Four Submerged-Arc Welds," *Proceedings of the Twelfth International Symposium on the Effects of Radiation on Materials, Williamsburg, Va., June 18–20, 1984*, American Society for Testing and Materials, Philadelphia.

2. FRACTURE METHODOLOGY AND ANALYSIS

2.1 Modifications and Distribution of the ORMGEN/ORVIRT Fracture-Mechanics Analysis System

B. R. Bass R. Wanner*

During this report period, a revised version of the ORMGEN/ORVIRT[1,2] fracture-mechanics analysis system was completed. Program ORMGEN[1] automatically generates a fully three-dimensional (3-D) finite-element model of a plate or cylinder containing a user-defined straight or curved crack. Output from the ORMGEN program consists of files containing nodal point coordinates and element connectivities that completely define the 3-D finite-element model. These files are written in formats that are compatible with the ADINA[3] structural analysis finite-element program. The ORVIRT[2] program functions as a postprocessor of the conventional finite-element solution obtained from ADINA. In applications, the energy release rate is evaluated pointwise by ORVIRT from solution data written to the nodal point and element portholes of ADINA and from a virtual extension of the crack front produced by ORMGEN.

Two revisions were made to the ORMGEN mesh generating program. The first modification allows for improved modeling capability in the crack front region and for additional user control of the finite-element mesh refinement. These changes in the generated mesh are illustrated in Fig. 2.1, in which the cross section of the crack-tip region of the modified mesh is compared with that of the original mesh. Note that the transition elements of the modified mesh [shaded in Fig. 2.1(*a*)] are 20-noded isoparametric elements; by contrast, the transition elements of the original mesh [shaded in Fig. 2.1(*b*)] consist of less than 20 nodes. In addition, the user can select either two or three rings of element refinement around the crack tip to define the region in which the energy release rate is computed. Figure 2.1(*a*) depicts a region defined by three rings: Program ORVIRT has been modified to accommodate this additional flexibility in modeling the crack-tip region. These improvements should prove particularly useful for more accurate crack analysis with nonlinear material models.

Modifications were also made to the ORMGEN program to model a circumferential through-wall crack in a cylindrical pipe. These modifications were made at the request of Southwest Research Institute (SwRI). SwRI expressed interest in using the ORMGEN/ORVIRT system to analyze a long pipe containing a through-wall crack for presentation at the Committee on the Safety of Nuclear Installations (CSNI) Ductile Piping Fracture Mechanics Workshop held in San Antonio, Texas, on June 21–22, 1984. Prior to the workshop, Heavy-Section Steel Technology (HSST) analysts at Oak Ridge National Laboratory (ORNL) worked with SwRI personnel on applications of the ORMGEN/ORVIRT system to this problem.

---

*On a one-year assignment to the ORNL Heavy-Section Steel Technology Program from the Swiss Federal Institute for Reactor Research, Würenlingen, Switzerland.

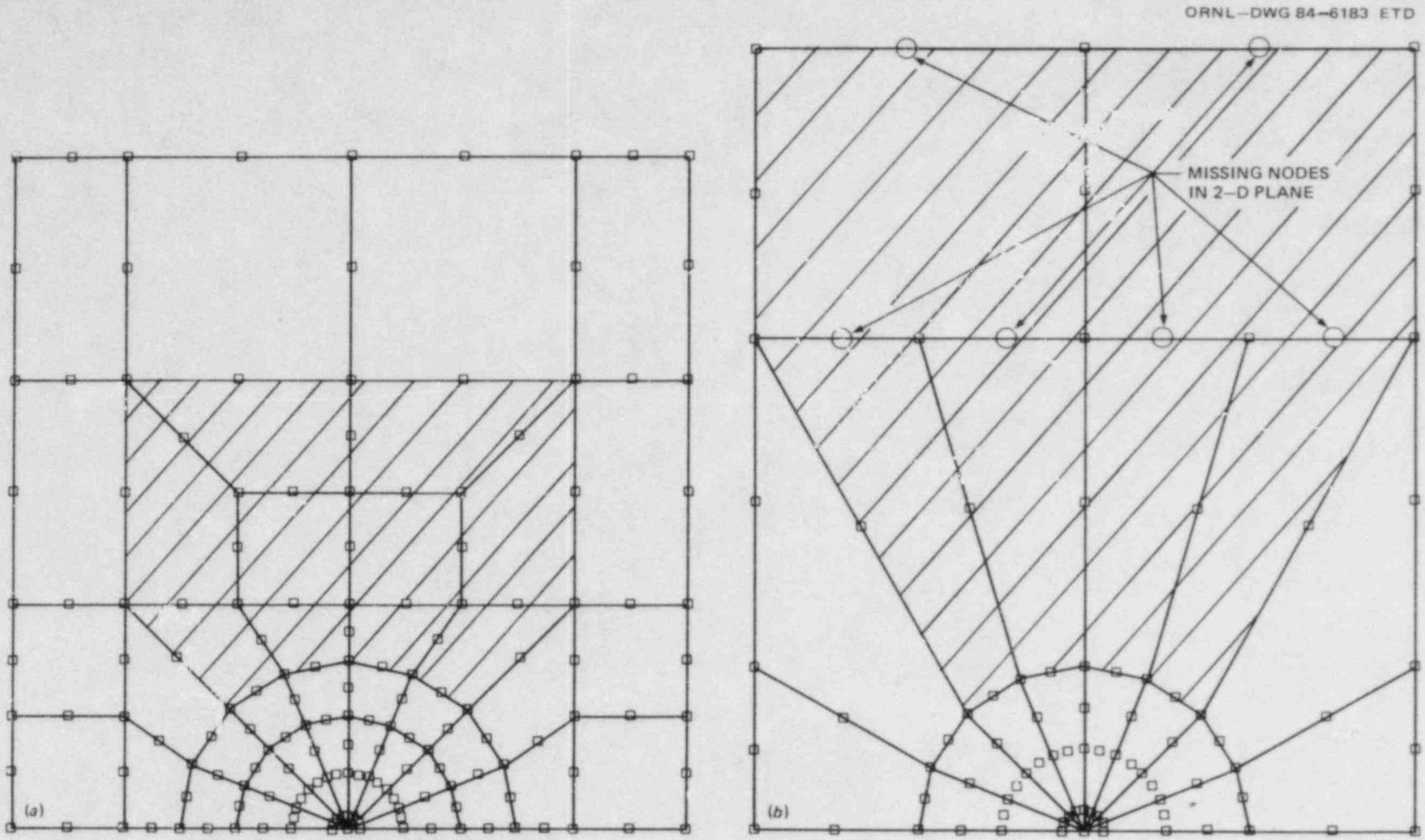

Fig. 2.1. Crack-tip region generated by program ORMGEN. (*a*) Modified ORMGEN mesh, (*b*) original ORMGEN mesh.

Development of an ADINA/ORVIRT-compatible mesh generating module for two-dimensional (2-D) finite-element models was also completed during this reporting period. Future plans call for incorporating this module into the ORMGEN program to permit generation of either 2-D or 3-D models as a user-selected option.

The ORMGEN/ORVIRT fracture analysis system was or is being distributed to the following organizations:

- Battelle Columbus Laboratories (Dr. Nu. Ghadiali)
- General Electric Research & Development (Dr. V. Kumar)
- Southwest Research Institute (Drs. M. F. Kanninen and J. Ahmad)
- Westinghouse — Bettis Atomic Power Laboratory (Dr. Ed Friedman)
- Fraunhofer — Institute für Werkstoffmechanik (Dr.-Ing. Winfried Schmitt)
- Swiss Federal Institute for Reactor Research (Dr. G. Saurer)
- Karlsruhe Research Center, Institut für Reaktorbauelemente (Dr. D. Munz)

It is anticipated that the revised version of ORMGEN/ORVIRT will be made available to these organizations following completion of code validation procedures.

During this report period, the ORMPLO graphics program was developed as a postprocessor for the ORMGEN[1] finite-element mesh generating program. The ORMPLO code, when executed on the PDP-10 system at ORNL, produces isometric plots of the 3-D finite-element mesh subdivision generated by ORMGEN. In addition, program ORMPLO produces a "roll-out" plot of the 3-D surfaces of cylindrical geometries, with optional inclusion of element and nodal point numbers. Capabilities of the ORMPLO program are illustrated in Figs. 2.2 and 2.3, which depict isometric and planar views

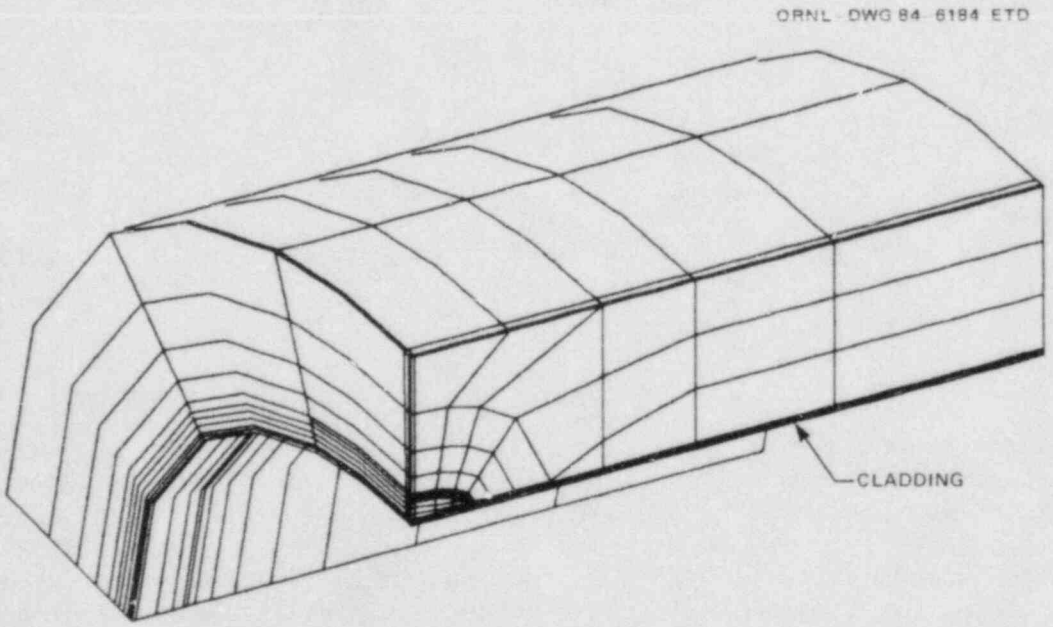

Fig. 2.2. ORMGEN-generated mesh for cylinder with elliptical surface crack. Number of elements: 579; number of nodal points: 3035.

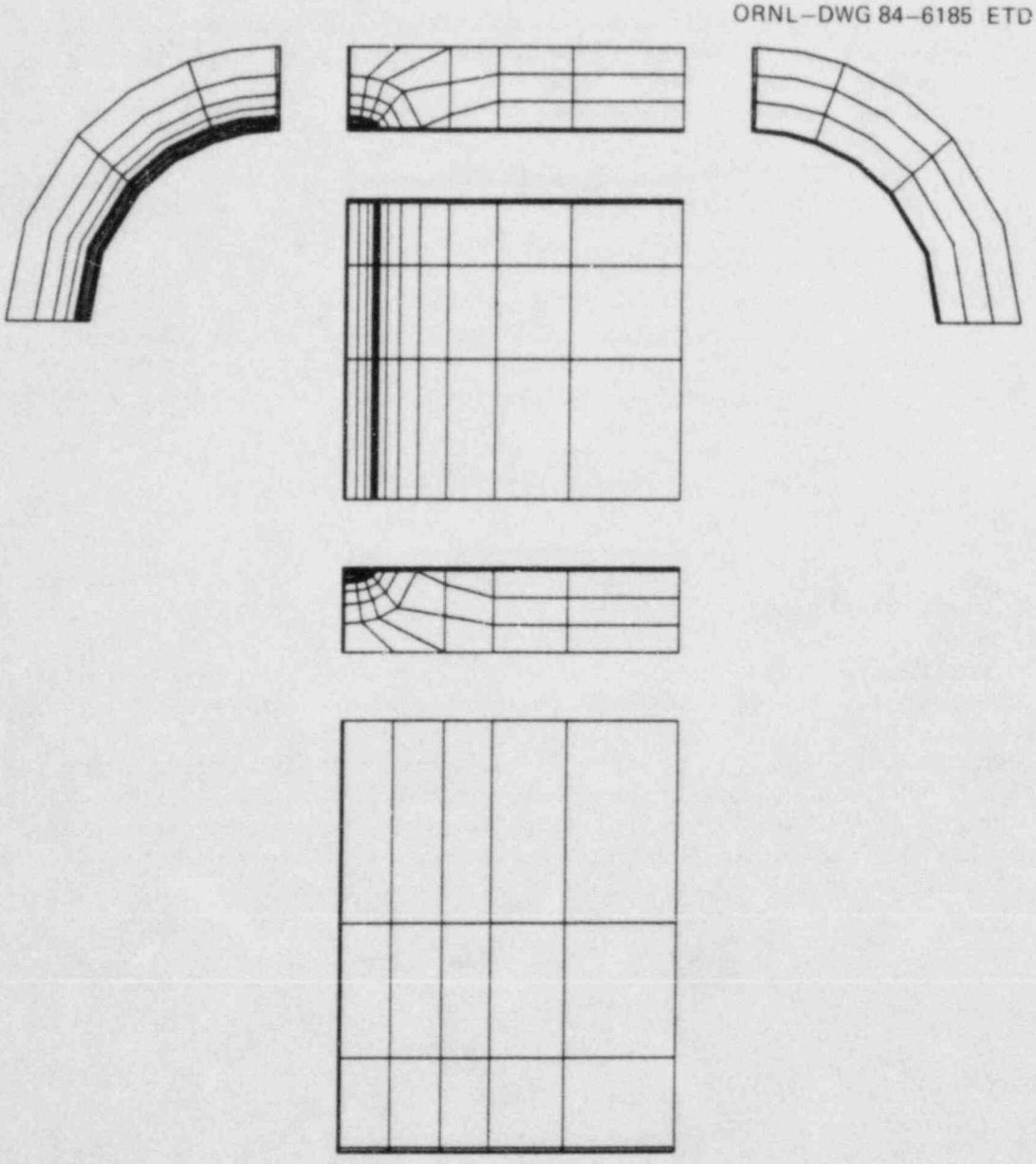

Fig. 2.3. Planar views of ORMGEN finite-element model of cylinder containing semielliptical crack.

of a 3-D finite-element model generated for a cylinder containing an axial semielliptical crack on the inner surface. The finite-element model produced by ORMGEN consists of 579 isoparametric elements and 3035 nodal points.

Future additions are planned for the ORMPLO program, including capabilities for bandwidth minimization and for generation of complete input files for the ADINA/ORVIRT fracture analysis system.[2,3]

2.2 Analysis of a Panel Crack-Arrest Specimen

H. K. Stamm*

2.2.1 Introduction

Calculations were performed to evaluate the usefulness of a relatively small panel specimen (45.7 × 76.2 × 2.54 cm) for crack-arrest experiments. The specimen is intended to be used for the measurement of K_{Ia} values at temperatures approaching the upper shelf of the material. An additional condition is that the crack arrest should take place in a rising K_I field. The evaluation assumed the capacity of available testing machines to be limited to 2447 kN.

To get crack arrest in a rising K_I field, the increase of crack-arrest toughness at the location of the propagating crack tip must be higher than the increase of K_I due to the external load. This can be achieved by applying a temperature gradient across the specimen. The crack must initiate at lower-shelf temperatures and propagate into regions at high temperature with a high K_{Ia} level. For this purpose, a panel specimen with a stub was proposed; the stub is cooled to serve as a crack starter region. By means of an eccentric load on the panel, the condition of a rising K_I field should be fulfilled. Additional forces can be applied to the stub to provide K_I levels that are high enough for crack initiation.

For the design of an appropriate specimen, calculations of stress-intensity factor (SIF) K depending on the crack length a were made for different tentative specimen geometries and load combinations using finite-element codes. Methods for SIF evaluation employing special crack-tip elements give results with high accuracy, but for calculating $K_I(a)$ curves a new mesh must be generated for each crack length considered. An easier way is to use simpler techniques with lower accuracy; that approach is still good enough for design purposes. One such technique is the crack closure method[4] outlined in the next section.

2.2.2 SIF determinations

By means of the crack closure method, it is possible to calculate the energy release rate G by two program runs. In the first, the actual loading system is applied to a structure with crack length a. A force F at the first node next to the crack tip is added in the second run. The force is applied in the direction to close the crack. From the difference between the nodal displacement components u^1 and u^2 for the first and second run, respectively (which are parallel to the applied force), the force necessary to close the crack within an element length $\ell = \Delta a$

---

*On assignment through January 1985 to the ORNL Heavy-Section Steel Technology Program from the Institut für Reaktorbauelemente Kernforschungszentrum Karlsruhe, FRG.

can be calculated:

$$F^* = \frac{F\, u^1}{u^1 - u^2} \,. \tag{2.1}$$

The energy release rate is approximately given by

$$G = \frac{F^*\, u^1}{\Delta a} \,. \tag{2.2}$$

By combining Eqs. (2.1) and (2.2), the SIF follows from the relation

$$K = \sqrt{E'\, G} = \sqrt{\frac{E'\, F(u^1)^2}{(u^1 - u^2)\, \Delta a}} \,, \tag{2.3}$$

with

$E' = E$ for plane stress,
$E' = E/(1 - \nu^2)$ for plane strain,

where E is Young's modulus and ν is Poisson's ratio. In the form described above, the method is limited to elements without midside modes in the region of the crack tip, because a linear displacement function along the element side is necessary. Figure 2.4 compares the results from this method with a handbook solution for a single-edge notched plate of width w:

$$K = \sigma_o \sqrt{\pi a} \cdot \sqrt{\left(\frac{2w}{\pi a}\right) \cdot \tan\left(\frac{\pi a}{2w}\right)} \cdot \left\{ \frac{0.752 + 2.02\, \frac{a}{w} + 0.37 \left[1 - \sin\left(\frac{\pi a}{2w}\right)\right]^3}{\cos\left(\frac{\pi a}{2w}\right)} \right\} . \tag{2.4}$$

While good agreement is shown, the method becomes more inaccurate at low and high a/w values when there are only very few elements along the crack surface and on the remaining ligament, respectively. In the following finite-element analyses, the mesh refinement in the crack plane is the same as that used to obtain the results shown in Fig. 2.4.

2.2.3 Design calculations

The first calculation for a tentative specimen geometry with a relatively small stub indicated that SIFs high enough to achieve initiation of a starter crack cannot be obtained applying a single, eccentric load to the panel. Additional forces must be applied at the stub. Taking an

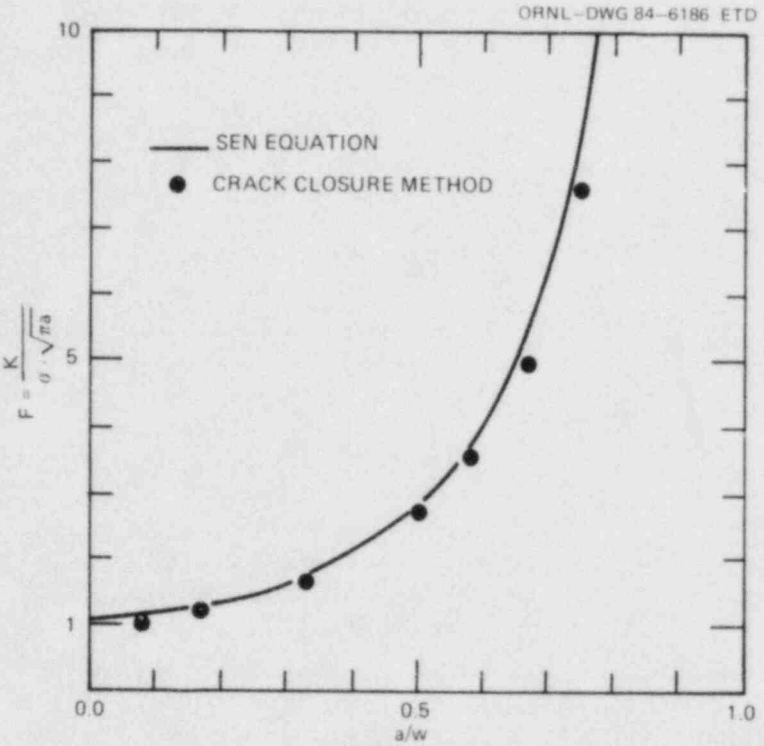

Fig. 2.4. Comparison of crack-closure method with handbook results.

upper limit of the stub forces to be $F_s \leq 89$ kN (limitation of the experimental facilities), a rather long stub is necessary to meet the conditions for crack initiation. In this case, the initial crack length can be chosen long enough and an efficient cooling of the crack-tip region is still possible. A larger distance between the load point of the stub forces and the crack tip gives rise to a higher SIF. Therefore, the second specimen considered is shown in Fig. 2.5.

The SIF for the initial crack was investigated by applying a load $F_s = 44.5$ kN at the upper surface of the stub region and a load $F_B = 2447$ kN at the upper surface of the bulk (panel) region of the specimen. The forces act as nodal point forces. Figure 2.6 illustrates the dependence of the SIF for a starter crack ($a_o = 20.3$ cm) on the point where the load is applied. The abscissa of Fig. 2.6 is the Y-coordinate of the load point of the loads F_s and F_B, respectively. Curve 1 is obtained by varying the load point of F_s only and keeping F_B fixed. The rapid decrease indicates that the force must be applied near the tip of the stub to get a high SIF. Similarly, curve 2 shows the dependence of K for a fixed F_s and a varied location of F_B. The effect of the location of F_B is not as great as the first case considered.

It becomes more important when the $K_I(a)$ curve of a propagating crack is considered. First, a discussion of the boundary conditions used in the following analyses is necessary. For the design of a crack-arrest specimen the static crack-arrest concept is adopted. The SIFs during

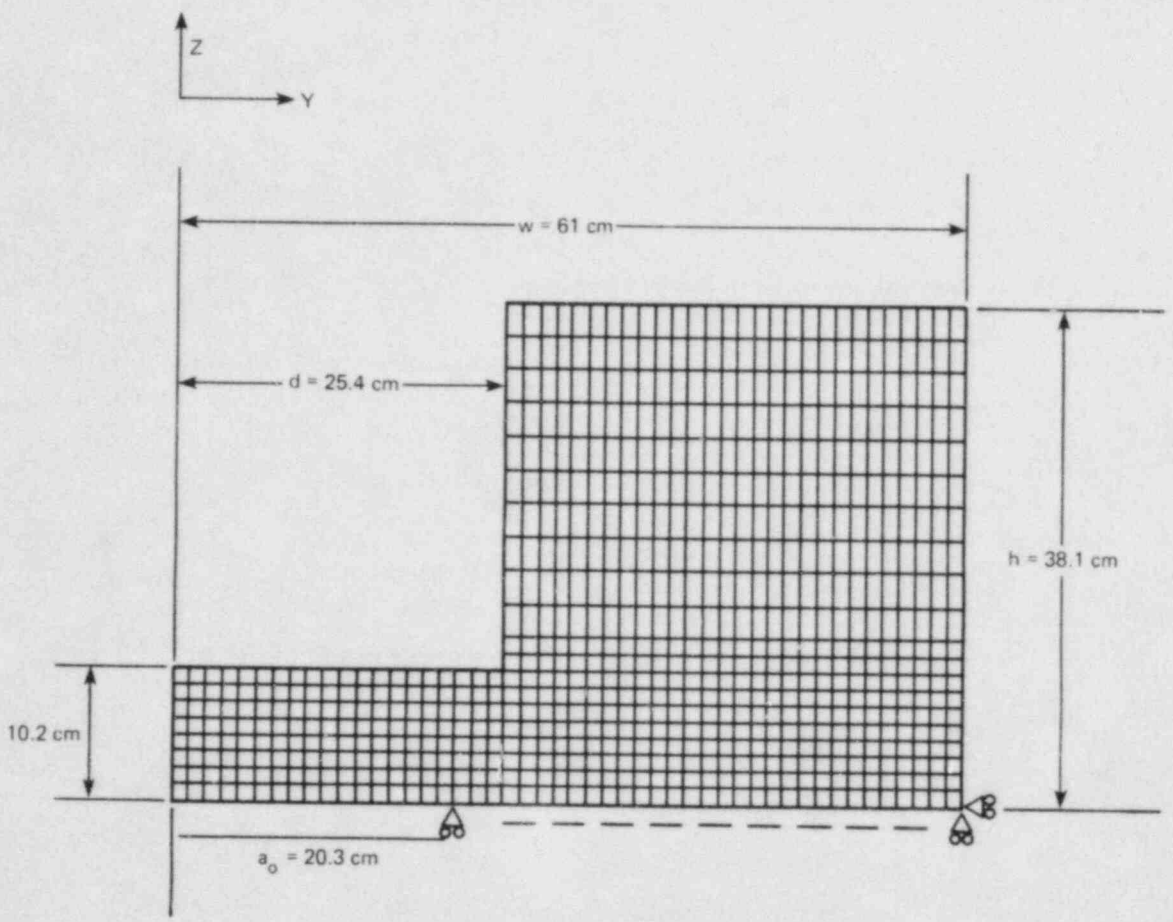

Fig. 2.5. Finite-element mesh for tentative specimen geometry and boundary conditions.

crack propagation are calculated as if the crack were stationary and are compared with a static crack-arrest toughness value K_{Ia}. The value of the statically calculated SIFs are strongly dependent on the boundary conditions assumed. Because the crack propagates very rapidly (the order of magnitude of typical flight times is several milliseconds), in the present analysis, the displacements along the upper boundaries of the stub and bulk region are assumed to be unchanged. Therefore, the displacements obtained under the combined load F_S and F_B for the initial crack length are described in those regions throughout the crack propagation. This may be a rather rough approximation for the real conditions, because the time necessary for shear waves (smallest sound velocity) to propagate from the crack tip to the upper boundary and back is about 250 μs. However, it is assumed that a rising $K_I(a)$ field obtained under fixed displacement boundary conditions is assured even if the boundary conditions are slightly different.

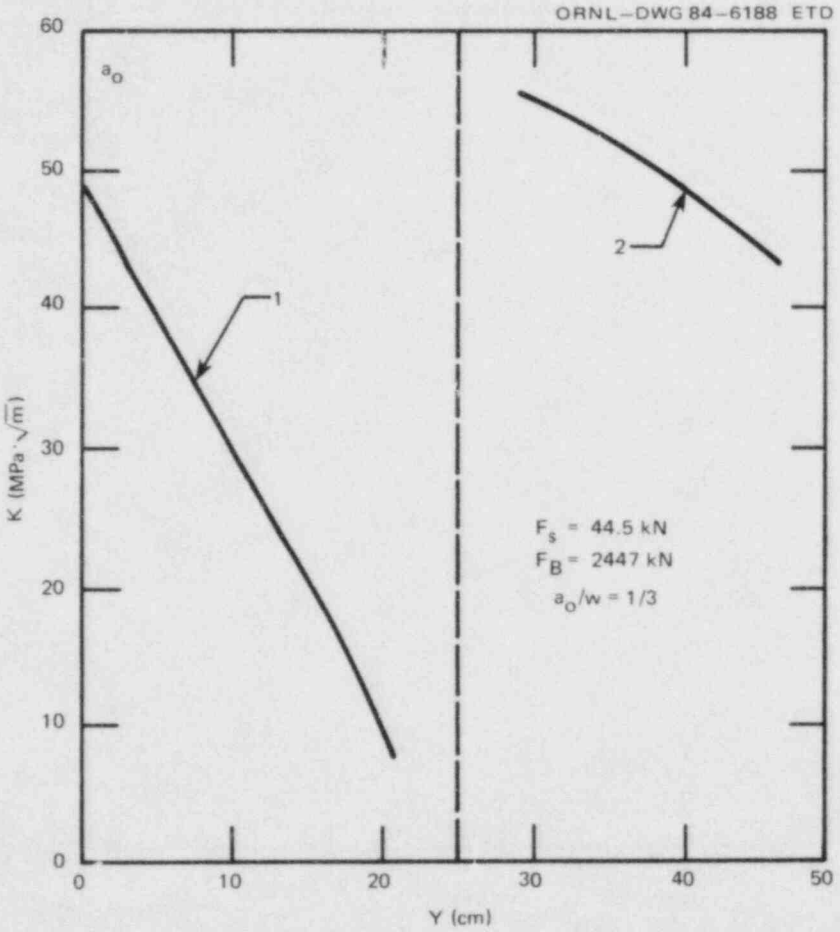

Fig. 2.6. Dependence of initial SIF on load points. Abscissa Y-coordinate of load points located at upper boundary of stub and bulk. Curve 1 load point of F_s; F_B fixed at Y = 40.6 cm. Curve 2 varying load point of F_B; F_s fixed at Y = 0.

Figure 2.7 shows $K_I(a)$ curves for three different loading systems, in which the resulting tensile forces are F_s = 44.5 kN and F_B = 2447 kN. Curve 1 is obtained by applying nodal point forces F_s and F_B at the tip of the stub (Y = 0) and on the upper-bulk boundary at Y = 30.5 cm, respectively. Crack initiation values of $K_I(a_o)$ near 65.9 MPa·$\sqrt{m}$ are reached. For crack lengths of $0.33 < a/w \leq 0.63$, the K_I field rises up to about 198 MPa·$\sqrt{m}$ and drops for higher values of a/w. The second loading system (curve 2) with a nodal point force F_s at Y = 15.2 cm and F_B at Y = 40.6 cm gives lower initiation values (see also Fig. 2.6); but, because of higher eccentricity of F_B, the range of a/w with a rising K_I field is enlarged. Curve 3 is obtained under more realistic boundary conditions, applying a homogeneous tensile stress distribution at $2.5 \text{ cm} < Y_s < 17.8 \text{ cm}$ and $33 \text{ cm} < Y_B < 48.3 \text{ cm}$ with results F_s = 44.5 kN and F_B = 2447 kN. Compared with curve 2, the initiation values

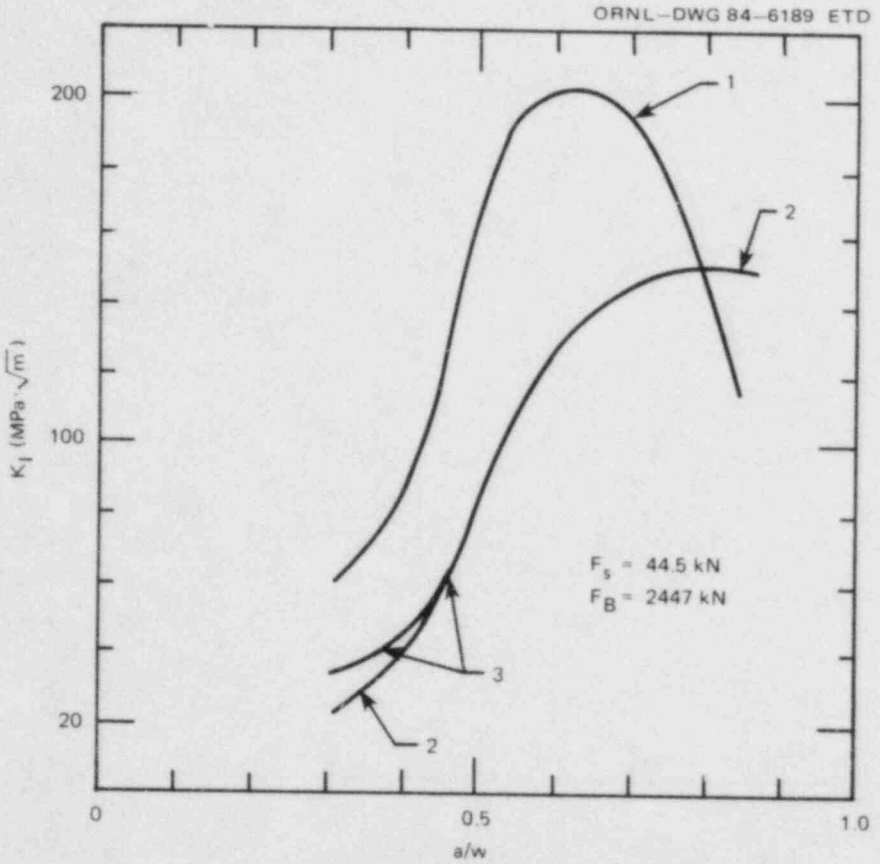

Fig. 2.7. K_I curves for various load point combinations: (1) F_s at Y = 0 cm, F_B at Y = 30.5 cm; (2) F_s at Y = 15.2 cm, F_B at Y = 40.6 cm; (3) distributed homogeneous tensile load: F_s at 2.5 cm < Y < 17.8 cm, F_B at 33.0 cm < Y < 48.3 cm.

are a little higher because the center of the applied stub forces is shifted slightly to the left. Both curves are nearly identical for deeper cracks.

Since the maximum attainable SIFs under the conditions of a wide range with rising K_I (curves 2 and 3) are still fairly low, a new specimen geometry (B) with a reduced width in the bulk region was analyzed (Fig. 2.8). Resulting loads of F_s = 66.7 kN and F_B = 2447 kN are applied at 0 cm < Y_s < 10.2 cm and 30.5 cm < Y_B < 40.6 cm as homogeneous tensile stress. The $K_I(a)$ curve is shown in Fig. 2.9. The K_I field rises to 220 MPa$\cdot\sqrt{m}$ starting with an initial value of about 60.4 MPa$\cdot\sqrt{m}$. Because of the small remaining ligament, the accuracy of the K results for long cracks (a/w > 0.8) is somewhat lower, but the goals outlined in the introduction are probably obtained.

The National Bureau of Standards (NBS) in Boulder has proposed[5] to test the crack-arrest specimen shown in Fig. 2.10. It has a shape and size similar to that discussed above, and the NBS machine can apply a

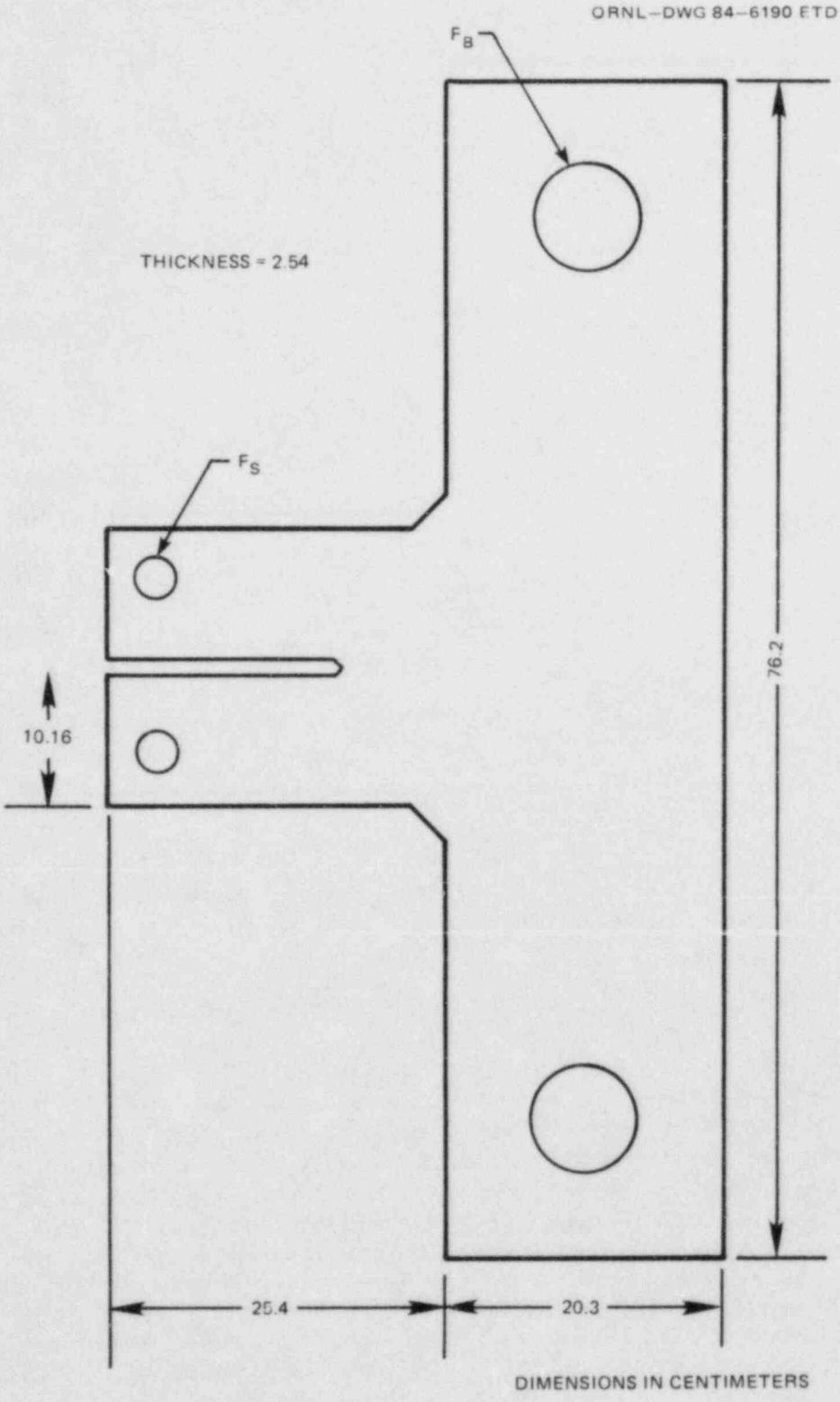

Fig. 2.8. Crack-arrest panel specimen B configuration.

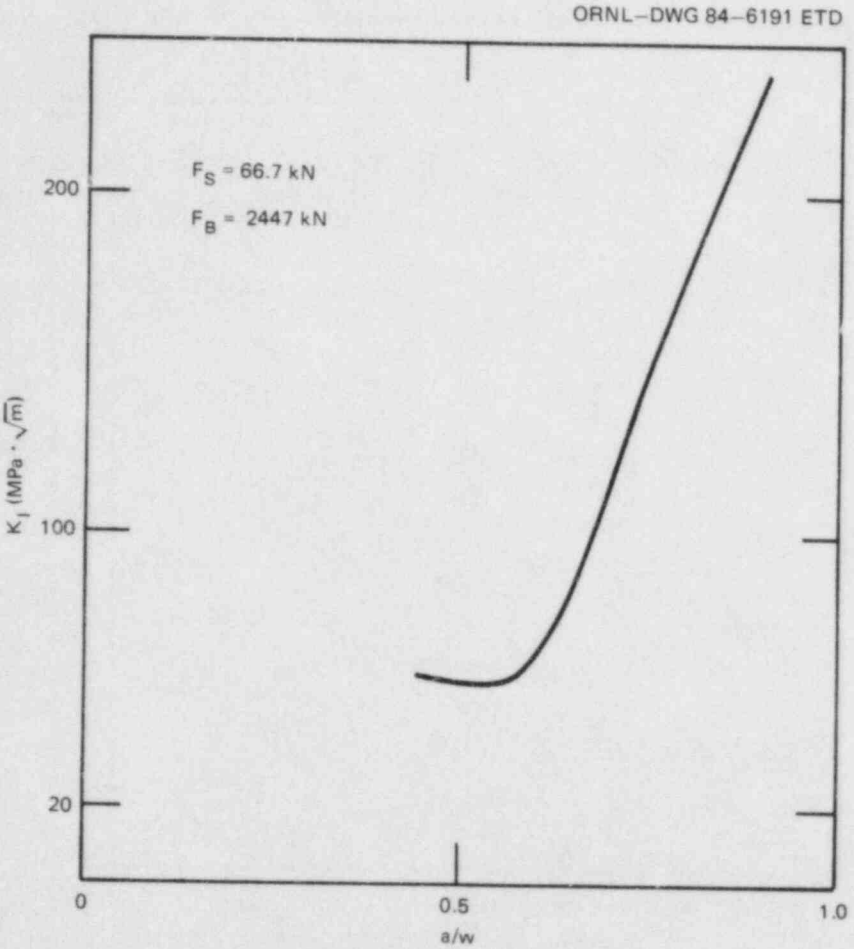

Fig. 2.9. K_I analysis for specimen B distributed tensile load; F_s at 0 cm < Y < 10.2 cm; F_B at 30.5 cm < Y < 40.6 cm.

stub force of F_s = 89 kN and a bulk force of F_B = 890 kN. The above analyses were performed for a specimen similar to that proposed by NBS and produced the $K_I(a)$ curves shown in Fig. 2.11. Prescription of the displacement on the upper boundaries of the stub and bulk region (fixed boundary) results in a decreasing $K_I(a)$ field with a low increase at higher crack lengths. For comparison, two other boundary conditions were considered — fixing the displacement at the load pins only and prescribing loads during crack extension. As expected, only the latter case shows a rising K_I field. The K values for the initial crack in the actual NBS specimen will be lower, since the stub assumed in the finite-element structure is less stiff than in reality. Nevertheless a rising K_I field with K = 220 MPa·$\sqrt{m}$ cannot be easily obtained.

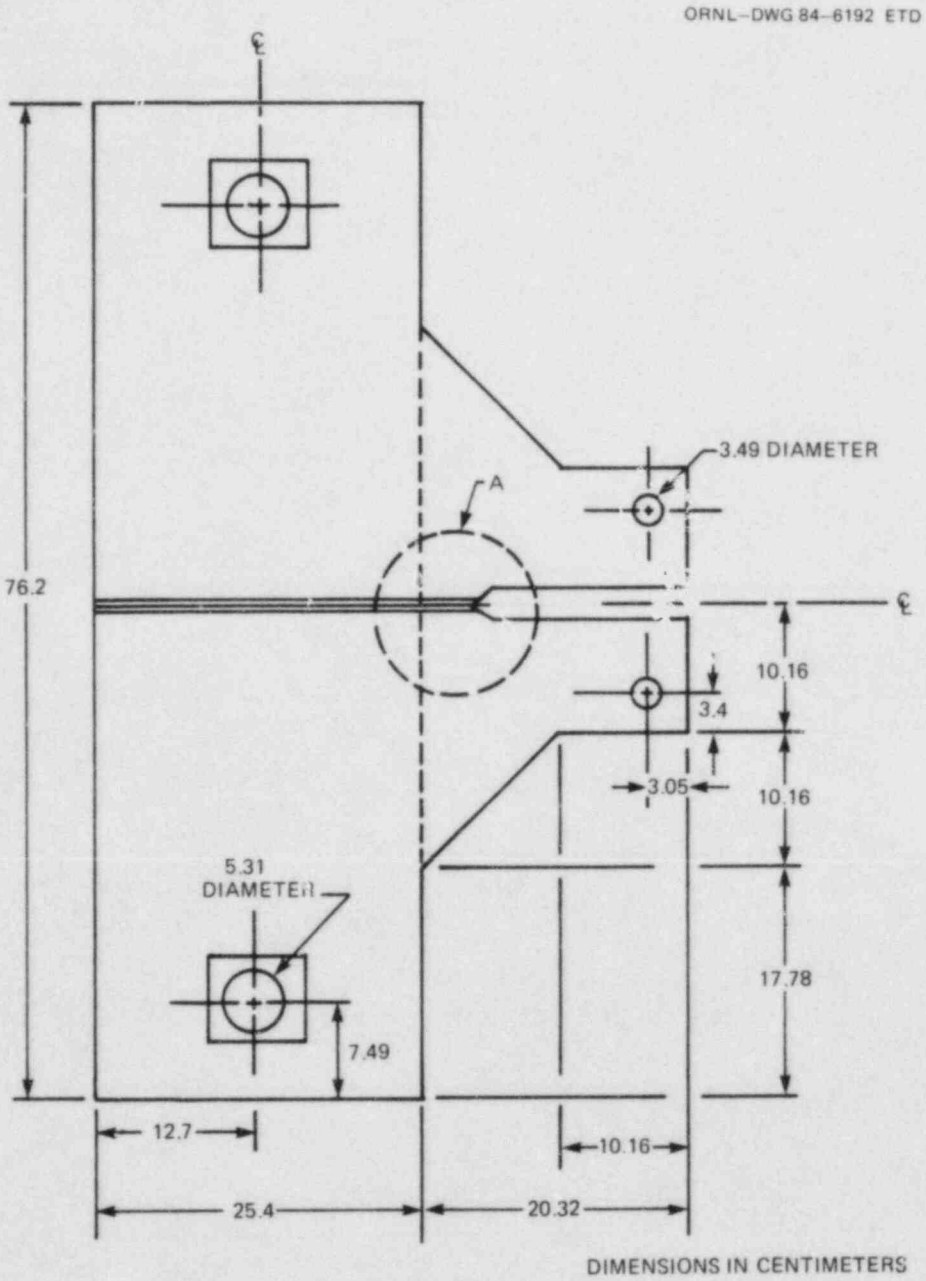

Fig. 2.10. Crack-arrest specimen suggested for testing by NBS—Boulder.

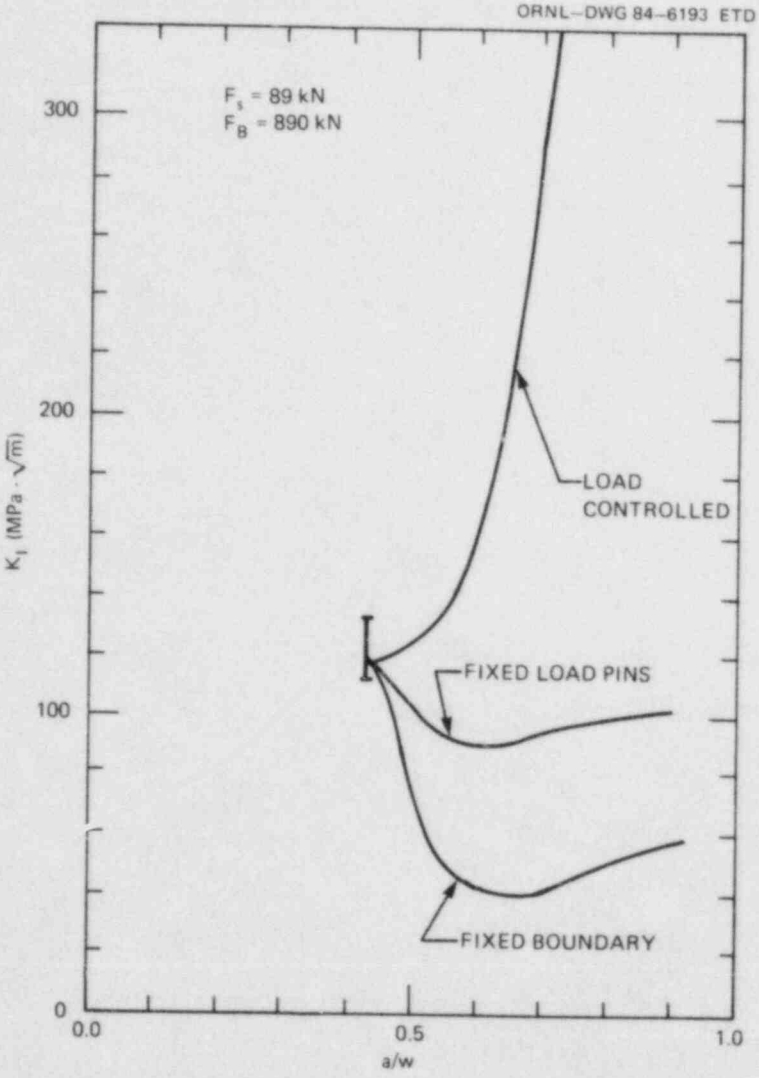

Fig. 2.11. K_I curves for a structure similar to suggested NBS specimen.

2.3 Commentary on the CEGB Strip Yield Model for Analyzing the Effects of Warm Prestressing

J. G. Merkle

2.3.1 Background

Principally as a result of efforts to develop safety criteria for nuclear pressure vessels that might be subjected to pressurized-thermal-shock (PTS) loadings, warm prestressing (WPS) has been recognized as an important physical phenomenon that under certain conditions can prevent the occurrence of cleavage fractures. WPS is a term used to describe

the experimental observations that (1) over short periods of time, fractures do not initiate when the crack-tip SIF is decreasing with time and (2) prior loading at a higher temperature (to a level above the original toughness level at a lower temperature) causes an elevated effective toughness value at the lower temperature. The first aspect of WPS, which is understandable in terms of the need for increasing plastic tensile strain to cause fracture, has been recognized for some time and, as of the Winter 1983 Addenda, is incorporated in Appendix A to Section XI of the ASME Code.[6] The second aspect of WPS, that of an effective toughness elevation caused by prior loadings at higher temperatures above the current K_{Ic} level, has been demonstrated experimentally with notched beams[7,8] and recently in the results of the first PTS experiment[9] conducted by the HSST Program (see Sect. 5.5.7). An explanation and verification of this second WPS aspect is particularly important to the proper development of PTS safety criteria for nuclear vessels because it has the potential for preventing the extension of shallow cracks that might otherwise result from repressurization occurring late in the postulated transient.

Because of the need to consider the WPS effects in vessel safety analysis in as straightforward a manner as possible, Chell et al.[10-12] developed a closed-form mathematical description of the phenomenon, based on the strip-yield model of crack-tip yielding. The calculational method was applied to the existing experimental data of Loss et al.[8] with a resulting accuracy of about ±10%. Nevertheless, the physical basis of the method was not made completely clear, and the mathematical derivations were somewhat abbreviated. Thus, there is a need for both to be examined to judge the applicability of the method to vessel safety analysis. That need was the basis for this discussion, which was aided substantially by the existence of some previous reviews on the general subject of WPS.[13-15]

2.3.2 The strip-yield plastic-zone model

To develop a mathematical description of WPS for engineering applications, two important physical aspects of the phenomenon must at least be represented. The first is crack-tip yielding, and the second is cyclic loading. If yielding is considered in an exact manner, then superposition cannot be used to describe the effects of load cycling and only numerical analyses will be practical. Furthermore, since load cycling violates the assumptions of the deformation theory of plasticity by creating nonunique relationships between stress and total strain, the J-integral is likely to become path dependent and therefore unclear. Consequently, numerical solutions will become difficult to interpret in a physical sense, and comparisons between analyses and experimental data may be rendered inconclusive by the lack of a well-defined crack extension criterion. Consequently, there is a practical motive for developing an approximate description of WPS that preserves the applicability of superposition, while still considering the effects of both yielding and cyclic loading. Such an approach was developed by Chell et al.[10-12] using the strip-yield model.

The strip-yield model (Fig. 2.12) represents the effects of yielding ahead of a crack tip by means of a mathematical extension of the crack over which yield stress closure tractions act on the opposing crack faces. The stress analysis is otherwise elastic, thus preserving the applicability of superposition for loads applied successively in time. The mathematical extension of the crack (i.e., the plastic zone) has a length that increases with load as long as loading is monotonic; thus, the elastically calculated value of K_I at the mathematical crack tip remains zero.[16] A finite opening displacement across the crack faces at the location of the physical crack tip, denoted by δ in Fig. 2.12, is termed the crack-tip opening displacement (CTOD). Calculated stretching displacements across the plastic zone in the strip-yield model, denoted by $\phi(x)$ in Fig. 2.12, vary from δ at the physical crack tip to zero at the mathematical crack tip. These displacements are usually not involved in an ordinary strip-yield analysis for a monotonically increasing load, but they are of considerable importance with regard to the WPS effects.

The basic equations of the strip-yield model were originally developed by superimposing the effects of the total remote stress and plastic-zone tractions (e.g., Ref. 16). However, it is also possible and easier to perform the analysis incrementally with the same results.[17] Referring

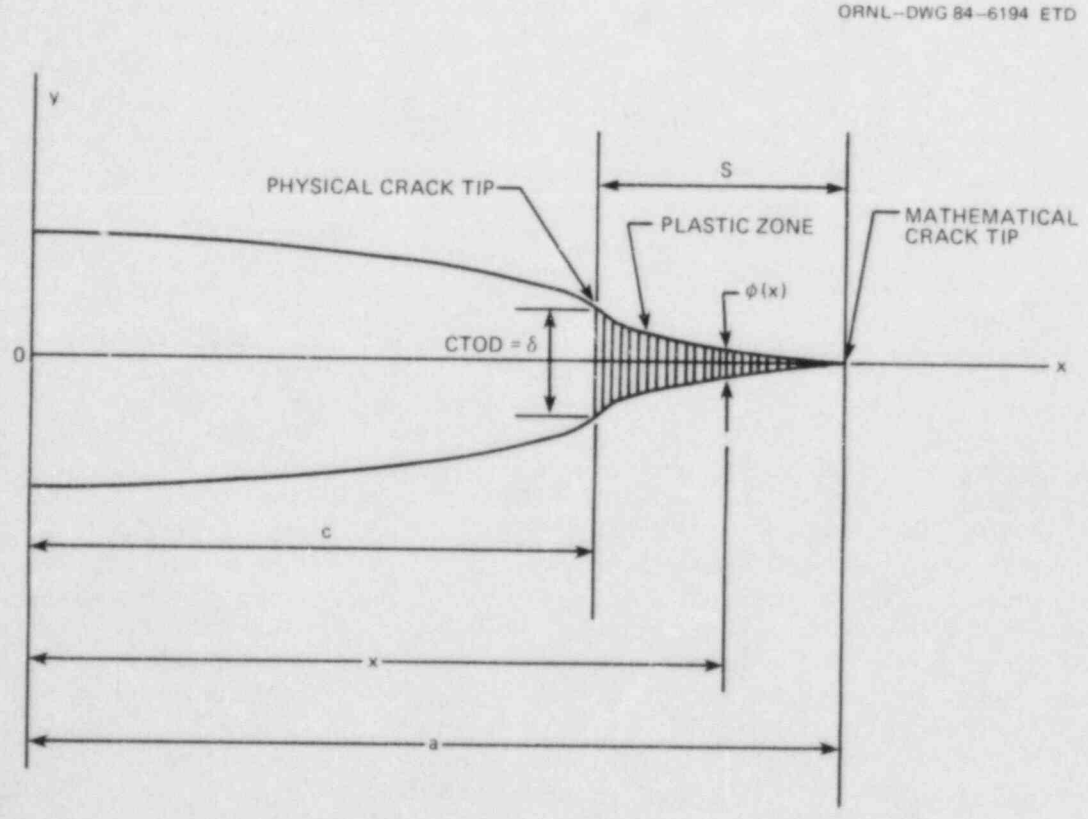

Fig. 2.12. Schematic illustration of strip-yield crack-tip plastic-zone model for monotonic tensile loading.

to Fig. 2.12 for a uniform remote stress, the plastic-zone size is given by[16,17]

$$S = c\left[\sec\left(\frac{\pi}{2}\frac{\sigma}{\bar{\sigma}}\right) - 1\right], \tag{2.5}$$

where $\bar{\sigma}$ represents the yield stress. In addition, the CTOD is given by[16,17]

$$\delta = \frac{8\bar{\sigma}c}{\pi E} \ln \sec\left(\frac{\pi}{2}\frac{\sigma}{\bar{\sigma}}\right). \tag{2.6}$$

Because Chell's analysis[12] assumes small-scale yielding, Eqs. (2.5) and (2.6) are reduced to this condition as follows. For sufficiently small values of $\sigma/\bar{\sigma}$,

$$\sec\left(\frac{\pi}{2}\frac{\sigma}{\bar{\sigma}}\right) = \left[1 - \sin^2\left(\frac{\pi}{2}\frac{\sigma}{\bar{\sigma}}\right)\right]^{-1/2} = \left[1 + \sin^2\left(\frac{\pi}{2}\frac{\sigma}{\bar{\sigma}}\right)\right]^{1/2}$$

$$= 1 + \frac{1}{2}\sin^2\left(\frac{\pi}{2}\frac{\sigma}{\bar{\sigma}}\right) = 1 + \frac{\pi^2}{8}\left(\frac{\sigma}{\bar{\sigma}}\right)^2. \tag{2.7}$$

Consequently, using Eq. (2.5),

$$S = \frac{\pi}{8}\left(\frac{\sigma^2\pi c}{\bar{\sigma}^2}\right). \tag{2.8}$$

Noting that

$$K = \sigma\sqrt{\pi c}, \tag{2.9}$$

Eq. (2.8) becomes

$$S = \frac{\pi}{8}\left(\frac{K}{\bar{\sigma}}\right)^2. \tag{2.10}$$

Also, using Eqs. (2.6) and (2.7),

$$\delta = \frac{8\bar{\sigma}c}{\pi E}\left(\frac{\pi^2}{8}\frac{\sigma^2}{\bar{\sigma}^2}\right); \tag{2.11}$$

thus,

$$\delta = \frac{K^2}{E\bar{\sigma}} . \qquad (2.12)$$

Eqs. (2.10) and (2.12) are used directly in Chell's analysis.[12]

2.3.3 Representation of cyclic loading effects

Summarizing briefly, crack-tip yielding is viewed as an incremental process by which the stress becomes equal to the current yield stress across a line of yielding that extends an incremental distance with each load increment ahead of the physical crack tip. The tangent modulus across the line of yielding is set equal to zero, so incremental displacements occur across the line of yielding as well as across the faces of the physical crack. Because the strip-yield plastic zone is only a line ahead of the real crack tip, the height of the plastic zone is zero and all displacements can be calculated elastically. The mathematical crack tip is located at the end of the line of yielding, referred to as the plastic zone. The elastically calculated SIF at the mathematical crack tip is set equal to zero, but the displacements across the faces of the mathematical crack are not zero except at its tip (Fig. 2.12). Consequently, calculated displacements exist in the plastic zone and at the physical crack tip.

With each load increment, the mathematical crack tip advances an incremental distance. The incremental displacements of the mathematical crack faces can be calculated elastically as those corresponding to the current crack length and the remotely applied incremental loading. These incremental displacements are not affected by the yield stress tractions acting along the line of yielding because these tractions do not change during the load increment. Because displacements are calculated elastically, the effects of cyclic loading on the crack-tip stress and displacement distributions can be modeled by superposition. The development of the crack-tip stress distribution will be modeled first. The displacements can then be modeled by the superposition of displacements caused by load changes.

Referring to Fig. 2.13 for the first application of load at temperature T_1, the stress and strain at a representative point in the plastic zone follow the path OAB, and a plastic zone of size S_{10} extends from the real crack tip, as shown in Fig. 2.14. The double subscripts used here, extending somewhat their use by Chell,[13] denote the final and initial load states, respectively. For unloading at a lower temperature T_2, the stress and strain follow the path BCD in Fig. 2.13. A second stress distribution is added to the first; the stress magnitude is $-(\bar{\sigma}_2 + \bar{\sigma}_1)$, and the length is S_{21}. For reloading at a still lower temperature T_3, the stress and strain follow the path DEF. A third stress distribution is added; the stress magnitude is $(\bar{\sigma}_3 + \bar{\sigma}_2)$, and the length is S_{32}.

For each load cycle or increase in yield stress, yielding must begin again at the physical crack tip and a new line of yielding must be developed. The effective yield stress governing the extension of a new line

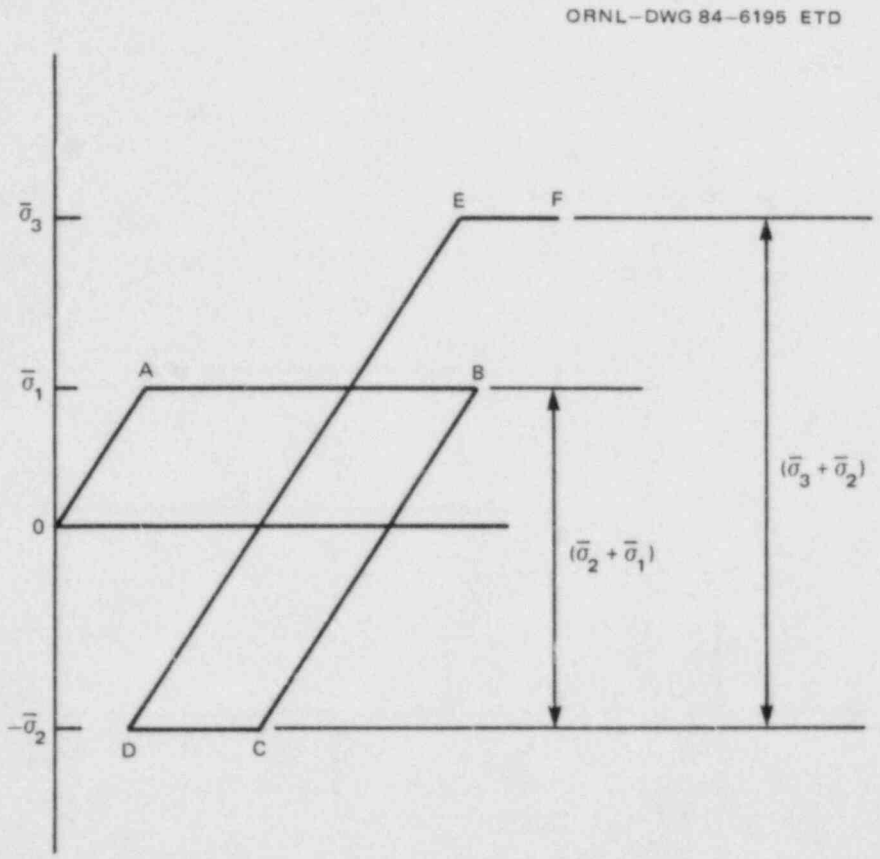

Fig. 2.13. Schematic representation of cyclic variation of stress and strain at representative point in crack-tip plastic zone as a result of concurrent changes of temperature and load cycling.

of yielding, as it progresses through the last previous zone of yielding, is the difference between the two yield stresses. The algebraic sign of each yield stress is the same as the sign of the corresponding load change. The plastic-zone size for a given load cycle is governed by the effective yield stress for that load cycle and the change in the SIF between the current and the last previous load cycle, according to Eq. (2.10). Thus, refering to Fig. 2.14,

$$S_{10} = \frac{\pi}{8}\left(\frac{K_1}{\bar{\sigma}_1}\right)^2 , \tag{2.13}$$

$$S_{21} = \frac{\pi}{8}\left(\frac{K_2 - K_1}{\bar{\sigma}_2 + \bar{\sigma}_1}\right)^2 , \tag{2.14}$$

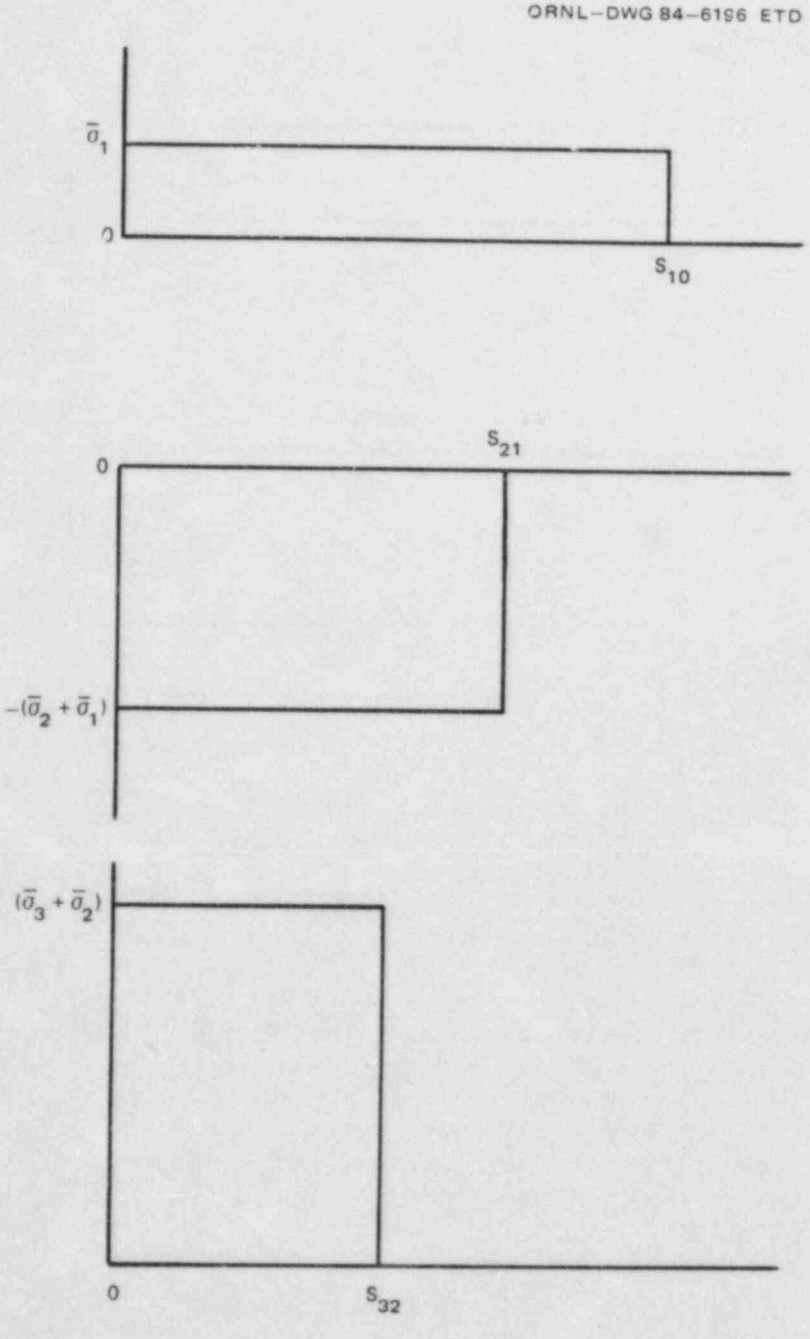

Fig. 2.14. Sequential changes in crack-tip plastic-zone stress distribution for conditions illustrated in Fig. 2.13.

and

$$S_{32} = \frac{\pi}{8}\left(\frac{K_3 - K_2}{\bar{\sigma}_3 + \bar{\sigma}_2}\right)^2 . \tag{2.15}$$

For the case of $S_{32} > S_{21}$, the magnitude of the final stress over S_{21} (Fig. 2.14) is given by

$$\bar{\sigma}_1 - (\bar{\sigma}_2 + \bar{\sigma}_1) + (\bar{\sigma}_3 + \bar{\sigma}_2) = \bar{\sigma}_1 - \bar{\sigma}_1 + \bar{\sigma}_3 = \bar{\sigma}_1 + (\bar{\sigma}_3 - \bar{\sigma}_1) , \tag{2.16}$$

thus eliminating the effect of the second load step. This equation also applies between S_{21} and the end of S_{32}. Since the superimposed stress distributions corresponding to the two terms in Eq. (2.16) are both continuous over the associated plastic-zone ranges, the corresponding displacements can be calculated by the strip-yield model.

In the previous case, the final active plastic zone does not grow at a uniform rate. For $S_{32} < S_{21}$, the size of S_{32} is given by Eq. (2.15), which implies relatively slow growth. For $S_{32} > S_{21}$, the size of S_{32} is given by

$$S_{32} = \frac{\pi}{8}\left(\frac{K_3 - K_1}{\bar{\sigma}_3 - \bar{\sigma}_1}\right)^2 , \tag{2.17}$$

which implies rapid growth.

A special case of practical interest involves constant range load cycling at a single temperature. For this case,

$$K_3 = K_1 , \tag{2.18}$$

$$K_2 = 0 , \tag{2.19}$$

and

$$\bar{\sigma}_1 = \bar{\sigma}_2 = \bar{\sigma}_3 . \tag{2.20}$$

Consequently, Eq. (2.15) gives

$$S_{32} = \frac{\pi}{8}\left(\frac{K_1}{2\bar{\sigma}_1}\right)^2 . \tag{2.21}$$

But for a further increase in K, Eq. (2.17) gives

$$S_{32} = \frac{\pi}{8}\left(\frac{\Delta K}{\sigma_0}\right)^2 . \tag{2.22}$$

For continued loading beyond the original value of K_1, the active plastic zone immediately grows from length S_{32} to length S_{10} and then continues to grow in accordance with the original monotonic relation given by Eq. (2.13).

2.3.4 Formulation of a fracture criterion

For loading, unloading, and then reloading at a lower temperature, the plastic zone during reloading will, up to some load, be contained within at least one of the previous plastic zones (Fig. 2.14). However, plastic strain will be increasing only within the currently active plastic zone. The previously developed plastic strains in the first two plastic zones remain constant. With this fact in mind, it is necessary to choose a fracture criterion; Chell et al.[10-12] use the J-integral for the path surrounding the currently active plastic zone. The choice of a specific path of integration was necessary because load cycling violates the assumptions of the deformation theory of plasticity and renders the value of J path dependent. The particular path chosen is logical because increasing plastic tensile strain is a prerequisite for tensile fracture.

The J-integral is defined by[18]

$$J = \int_\Gamma \left(W dy - \overline{T} \cdot \frac{\partial \overline{u}}{\partial x}\, ds\right) , \tag{2.23}$$

where Γ is a curve surrounding the crack tip progressing counterclockwise from the lower-flat crack face to the upper-flat crack face; W is strain energy density; the y axis is perpendicular to the notch faces and the x axis is parallel to the notch faces; $\overline{T}$ is the outward stress vector on Γ; $\overline{u}$ is the displacement vector on Γ; and ds is an element of arc length taken positive when progressing counterclockwise around Γ. Although the plastic zone is treated as part of an open crack for calculating the stretching displacements elastically, for purposes of a J-integral analysis, the same segment of the mathematical crack is assumed to be filled with a plastic material of zero initial height and zero tangent modulus.

For the strip-yield WPS model, Γ is defined as the boundary of the active plastic zone, so that

$$dy = 0 . \tag{2.24}$$

The resulting value of the J-integral, J_e, is defined by

$$J_e = -\left[\int_c^a (-\bar{\sigma}) \frac{\partial v_-}{\partial x} dx + \int_a^c \bar{\sigma} \frac{\partial v_+}{\partial x} (-dx)\right] , \tag{2.25}$$

where v_- and v_+ are the displacements of the lower and the upper boundaries of the strip-yield zone, respectively. Simplifying the signs in Eq. (2.25) gives

$$J_e = \left[\int_c^a \bar{\sigma} \frac{\partial v_-}{\partial x} dx + \int_a^c \bar{\sigma} \frac{\partial v_+}{\partial x} dx\right] . \tag{2.26}$$

Since

$$v_- = -v_+ , \tag{2.27}$$

Eq. (2.26) reduces to[18]

$$J_e = 2\bar{\sigma} \int_a^c \frac{\partial x_+}{\partial x} dx , \tag{2.28}$$

which leads to

$$J_e = \bar{\sigma} \left[2v_+(c) - 2v_+(a)\right] . \tag{2.29}$$

Since the relative displacement of the crack faces is given by

$$\phi(x) = 2v_+(x) , \tag{2.30}$$

Eq. (2.29) becomes

$$J_e = \bar{\sigma} \left[\phi(c) - \phi(a)\right] . \tag{2.31}$$

For monotonic loading, the stretching displacement at the end of the plastic zone $\phi(a)$ is zero. For cyclic loading, the value of $\phi(a)$ at the end of the currently active plastic zone is equal to the sum of the residual stretching displacements at that value of x caused by each of the previous load cycles. The value of $\phi(c)$ is obtained by adding the values for each load step. The determination of the required values of $\phi(a)$ requires an explicit equation for the variation of the stretching displacements across the plastic zone of the strip-yield model. The value of $\bar{\sigma}$ in Eq. (2.31) is the value for the final load step, because the value of

the J-integral is based on deformation theory and is therefore not history dependent.

2.3.5 Displacement analysis

The stretching displacements $\phi(x)$ across the plastic zone associated with each load change can be calculated elastically and therefore independently, using the strip-yield model. For each load change, the magnitude of the stress change in the plastic zone is used as the effective yield stress, and the tip of the currently active plastic zone is used as the mathematical crack tip. The displacement distributions resulting from loading, unloading, and reloading are illustrated schematically in Fig. 2.15. Chell[12] has used the definition

$$a = c + S \ , \tag{2.32}$$

illustrated in Fig. 2.12, where $x = 0$ is the midpoint of the crack, c is the crack half-length, and S is the plastic-zone length. Chell also uses the notation

$$\phi_{ij} = \phi_{ij} \left[x, (K_i - K_j), (\overline{\sigma}_i - \overline{\sigma}_j)\right] \ , \tag{2.33}$$

where i denotes the final state and j denotes the initial state for a load cycle. Because the strip-yield equation for ϕ_{ij} involves only $(K_i - K_j)^2$ but contains $(\overline{\sigma}_i - \overline{\sigma}_j)$ as a factor, it follows that the sign of the crack opening displacement is determined by the sign of the flow stress, and

$$\phi_{ji} = -\phi_{ij} \ . \tag{2.34}$$

In applying the strip-yield plastic-zone displacement equations to the problem of cyclic loading, it was found that even the small-scale yielding equation is too complicated to allow the development of closed-form solutions for the SIF at fracture. Consequently, Chell[12] developed a parabolic approximation for the variation of the stretching displacement with distance ahead of the physical crack tip; thus, in the strip-yield WPS model, $\phi_{ij}(x)$ is given by

$$\phi_{ij}(x) = \delta_{ij} \left(1 - \frac{\varepsilon}{S_{ij}}\right)^2 \ , \tag{2.35}$$

where

$$\varepsilon = x - c \ , \tag{2.36}$$

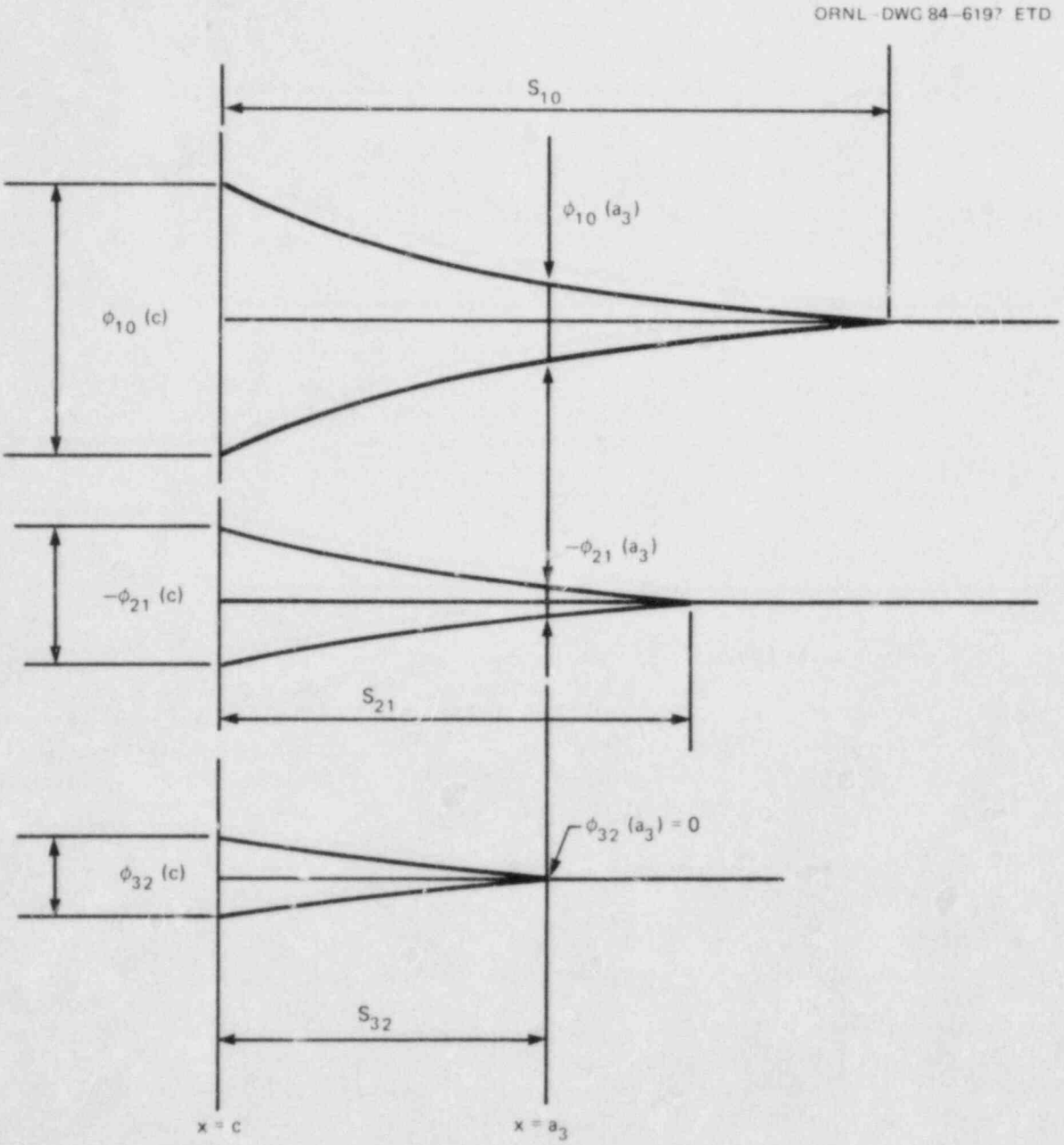

Fig. 2.15. Sequential changes in crack-tip plastic-zone stretching displacements for conditions illustrated in Fig. 2.13.

and

$$\delta_{ij} = \phi_{ij}(c) \ . \tag{2.37}$$

2.3.6 Physical significance of the fracture criterion

The physical meaning of the fracture criterion J_e requires clarification, despite the statement[10,11] that it represents the force on the currently mobile dislocations. Evidently, the term $\phi(a_3)$ must represent the effects of prior yielding near the crack tip, in terms such as crack-tip blunting or residual stress at the tip of the plastic zone. In the superposition model developed by Chell et al.,[10-12] prior plastic-zone displacements have no effect on subsequent stress distributions, but they do have an effect on J_e. It is reasonable to hypothesize that to produce crack extension, a concentration of plastic work near the crack tip is required to initiate and propagate microcracks back toward the main crack. The displacement difference between the ends of the active strip-yield plastic zone is a measure of this plastic strain gradient, and the yield stress is the multiplier that converts plastic strain to plastic work.

2.3.7 Equations for a load-cool-fracture sequence

Chell[12] identified three basic types of load sequences, depending on the relative sizes of the plastic zones developed during each load cycle. One of these, for example, is a load-cool-fracture (LCF) sequence, for which an intermediate unloading cycle does not occur, and consequently only the subscripts 1 and 3 appear in the equation for J_e. By superposition, Eq. (2.31) becomes

$$J_e = \bar{\sigma}_3 \ [\phi_{10}(c) + \phi_{31}(c) - \phi_{10}(a_3)] \ , \tag{2.38}$$

where the double subscripts on ϕ indicate the final and the initial load states, respectively. The term $\phi_{31}(a_3)$ is zero and does not appear in Eq. (2.38), because the last displacement increase at the tip of the current mathematical crack is always set equal to zero. The strip-yield model for this case is illustrated in Fig. 2.16.

Using the parabolic approximation for the variation of the stretching displacements across the plastic zone, the stretching displacement ϕ_{ij} for a specific load change is given for small-scale yielding by combining Eqs. (2.35) and (2.12) to give

$$\phi_{ij} = \frac{\Delta K_{ij}^2}{E\Delta\bar{\sigma}_{ij}} \left(1 - \frac{\varepsilon}{S_{ij}}\right)^2 \ , \tag{2.39}$$

ORNL-DWG 84-6196 ETD

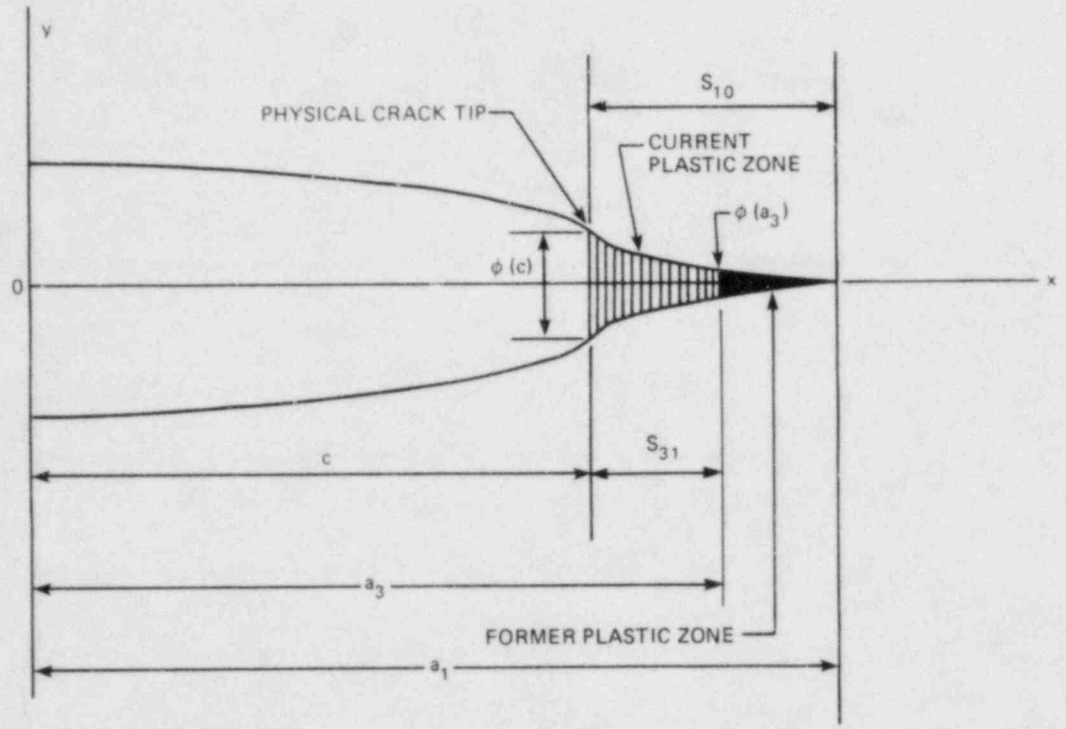

Fig. 2.16. Schematic illustration of strip-yield model for LCF sequence used for warm prestressing analysis.

where ε is the distance from the physical crack tip to the reference point and S_{ij} is the plastic-zone size for the load change under consideration. For $x = c$, $\varepsilon = 0$ and for $x = a_3$, $\varepsilon = S_{31}$. For small-scale yielding, the strip-yield plastic-zone size equation reduces to

$$S_{ij} = \frac{\pi}{8}\left(\frac{\Delta K_{ij}}{\Delta\bar{\sigma}_{ij}}\right)^2 . \tag{2.40}$$

For an LCF sequence, substituting Eqs. (2.39) and (2.40) into Eq. (2.38) and using

$$J_e = \frac{K_{Ic}^2}{E} \tag{2.41}$$

produces the quadratic equation

$$z^2 - z\left(2 + \frac{\bar{\sigma}_3 - \bar{\sigma}_1}{\bar{\sigma}_1}\right) + \left(\frac{K_{Ic}}{K_1}\right)^2 \left(\frac{\bar{\sigma}_1}{\bar{\sigma}_3}\right) = 0 \ , \tag{2.42}$$

where

$$z = \frac{S_{31}}{S_{10}} \ . \tag{2.43}$$

The solution to Eq. (2.42) is[12]

$$K_f - K_1 = \left(\frac{\bar{\sigma}_3}{\bar{\sigma}_1} - 1\right) K_1 \left\{\frac{1}{2}\left(1 + \frac{\bar{\sigma}_3}{\bar{\sigma}_1}\right)\left[1 - \sqrt{1 - \frac{4\left(\frac{K_{Ic}}{K_1}\right)^2 \left(\frac{\bar{\sigma}_1}{\bar{\sigma}_3}\right)}{\left(1 + \frac{\bar{\sigma}_3}{\bar{\sigma}_1}\right)^2}}\right]\right\}^{1/2} \ , \tag{2.44}$$

where K_f is the value of K_3 at fracture. Thus $(K_f - K_1)$ is the increase in K_I required to overcome WPS after cooling at constant load.

2.4 Investigation of Damping and of the Cleavage-Fibrous Transition in Reactor-Grade Steel*

W. L. Fourney† R. J. Sanford†
G. R. Irwin† C. W. Schwartz†
R. Chona† X-J. Zhang†

2.4.1 Cleavage-fibrous transition studies

Two techniques are being used to determine the temperature elevation necessary for loss of dominant cleavage fracturing in A508B steel. One method employs fractographic examination of the fracture surfaces of standard Charpy V-Notch (CVN) impact specimens; the other uses larger

*Work sponsored by HSST Program under Subcontract 7778 between Martin Marietta Energy Systems, Inc., and the University of Maryland.

†Department of Mechanical Engineering, University of Maryland, College Park.

(25- to 50-mm-thick) side-grooved specimens, in which the initial fibrous crack extension from a fatigue precrack is converted to rapid cleavage by using a spring plate in series with the load train of a stiff testing machine.

During this report period, a series of large-size spring-in-series fracture tests were completed using A508 steel tempered at 613°C. The specimens were loaded in 3-point bending and were side grooved to a depth equal to 12.5% of the thickness. They had a thickness of 60 mm, W = 102 mm and S/W = 4. Three tests were initially conducted; one at 80°C, one at 95°C, and a final one at 125°C. The fracture surface of the specimen at 125°C showed 2 mm of initial fibrous crack extension followed by dominant cleavage fracture. The cleavage region, however, indicated that the test temperature was close to the loss-of-cleavage temperature. Two additional specimens were, therefore, tested to bracket the loss-of-cleavage temperature more closely. The fracture surfaces from these two additional tests are presented in Fig. 2.17. These specimens were smaller in their in-plane dimensions than the original three specimens having W = 70 mm and an S/W ratio of 3. The use of these smaller in-plane dimensions would not be expected to alter the loss-of-cleavage temperature that was found to be 140 ± 5°C. This result can be compared with estimates of the loss-of-cleavage temperature of 95°C as obtained from standard CVN impact specimens and with 115°C as obtained from side-grooved CVN specimens with B = 15 mm.

It is evident from the complete test results on A508, A36, A533B, and A514 steels that the relationship between the loss-of-cleavage temperatures determined from CVN specimens and from large spring-in-series

ORNL PHOTO 5829-84

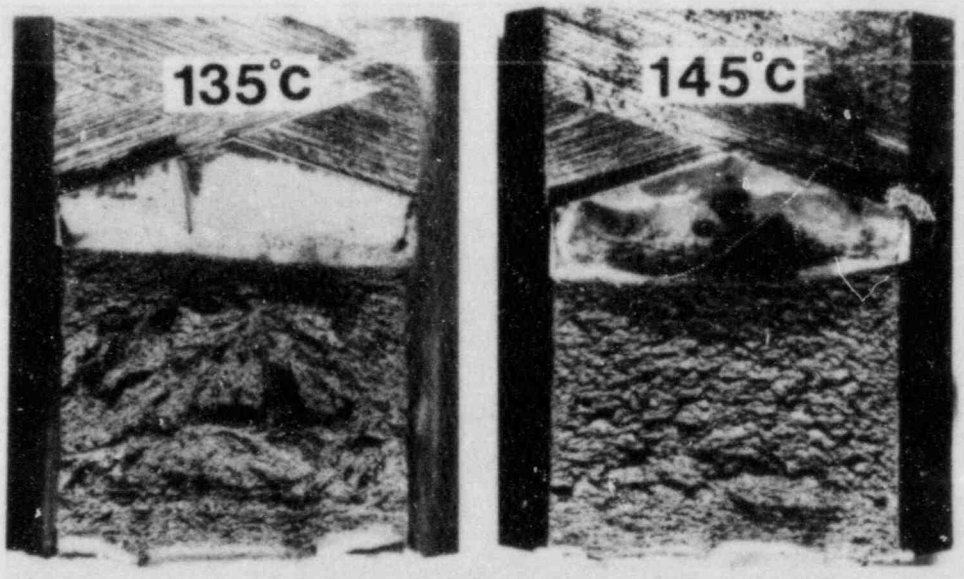

Fig. 2.17. Fracture surfaces of two specimens of A508 steel (60 mm thick) fractured with spring-in-series at indicated temperature. Rapid fibrous crack extension at 145°C did not induce cleavage.

specimens is influenced by constraint. For nuclear vessel steels, when the degree of plane strain is large, rapid cleavage may occur at temperatures as much as 45°C above the loss-of-cleavage temperature indicated by CVN specimens. Note that of the two fracture surfaces shown in Fig. 2.17, the fibrous fracture at 145°C is most nearly planar. The large irregularities of the dominant cleavage fracture at 135°C suggest a rather high-toughness mode of cleavage separation. Estimates of toughness for these tests will be reported later.

2.4.2 Fractographic examinations

Further optical studies were made of the cleavage branch crack that was bypassed by a main fracture surface as reported in Ref. 19. The fracture surface was from a Charpy specimen of A508 steel (613°C temper) tested at −40°C. The specimen was of orientation 5 as described in Ref. 20. Examinations were conducted on eight sections taken from the CVN specimen as shown in Fig. 2.18. The eight sections stepped through a thickness of 55 μm from the section presented as Fig. 2.5 in Ref. 19. Four of the eight sections are presented in Fig. 2.19 and show adjacent transverse sections through a small cleavage crack as indicated by the small black arrowhead. This locally cleaved region does not appear to have initiated from the main segments of the branch crack. From these examinations, two main results are inferred: (1) the interruption of the cleavage at each ferrite grain boundary is clearly evident and (2) the origins of cleavage are not primarily at grain boundaries and may correspond to locations of carbide clusters.

Finally, a 2-week working visit by Dr. H. P. Rossmanith from the Technical University of Vienna was used to start development of a statistical model suitable for representing principal features of the cleavage-fibrous toughness transition.

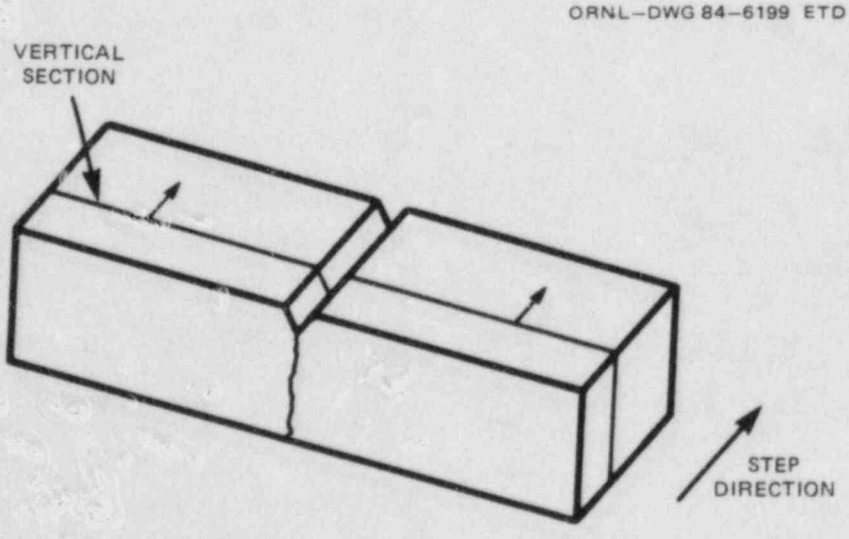

Fig. 2.18. The manner in which sections were taken from CVN specimens for further examination.

ORNL PHOTO 5830-84

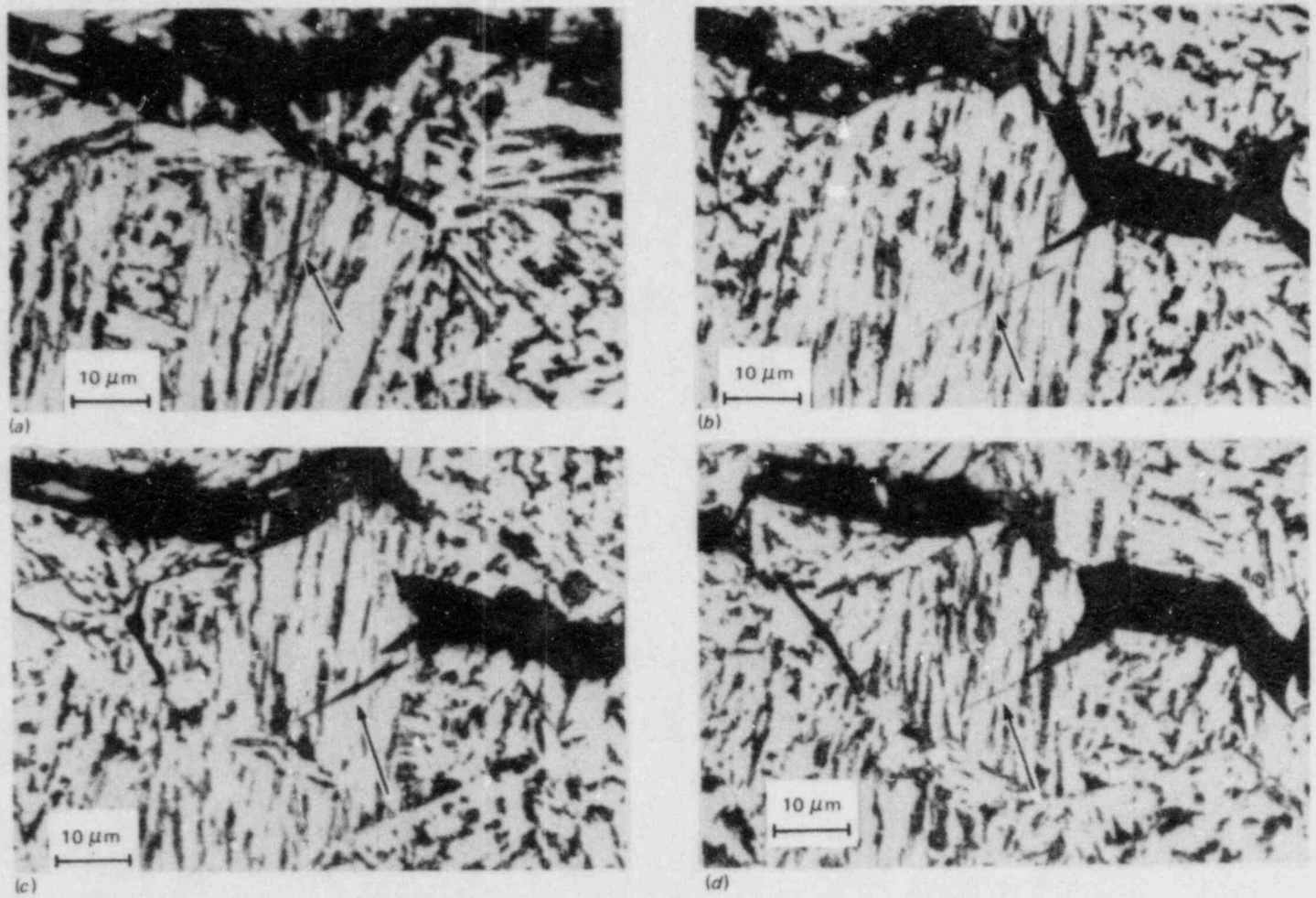

Fig. 2.19. Set of four parallel vertical section views of A508 steel CVN specimen tested at −40°C, showing nucleation of cleavage facet allowed within ferrite grain. Distances between adjacent sections are 10.0, 5.9, and 7.4 μm, respectively, for a-b, b-c, and c-d. (*a*) Vertical section G, (*b*) vertical section H, (*c*) vertical section I, (*d*) vertical section J.

2.5 Elastodynamic and Viscoplastic-Dynamic Fracture-Mechanics Analyses*

M. F. Kanninen† J. D. Achenbach‡
S. J. Hudak† J. Ahmad†
J. H. Fitzgerald† V. Papaspyropoulos†
K. Chan†

2.5.1 Objectives and approach

The principal objective of this research is to assist the HSST Program to obtain reliable material fracture toughness data for the prediction of crack arrest at high upper-shelf toughness conditions for use in postulated PTS events. This is being accomplished through research that combines finite-element analyses with (1) small-scale fracture experimentation, (2) wide-plate testing to be performed at NBS under the auspices of the HSST program, and (3) viscoplastic material characterizations. The focal point of the work is the finite-element code SWIDAC (Southwest Inelastic Dynamic Analysis Code). There are at least two reasons for utilizing this degree of complexity. First, unless the crack jump length is small, dynamic effects can significantly influence a run-arrest event in a wide-plate test. Second, crack arrest at upper-shelf conditions may involve significant strain-rate effects that will require a viscoplastic analysis capability. Thus, the research can be considered in three categories: (1) the application of existing elastodynamic analyses to the planned wide-plate tests, (2) the development of a dynamic viscoplastic analysis procedure, and (3) the development of test methods to obtain dynamic crack propagation/arrest data on high-toughness materials using small-scale laboratory specimens.

In this research, SWIDAC is being exercised in two main ways. First, it is used in the "generation-phase" to enhance the experimental effort. By using the observed crack-length history and boundary conditions as input to the analysis, values of the material crack propagation/arrest toughness parameters can be obtained directly. For linear-elastic conditions, these would be in terms of $K_{ID}(V,T)$; in viscoplastic conditions, it is likely that these analyses will extract critical values of a nonlinear fracture-mechanics parameter, for example, the crack-tip opening angle (CTOA). The second use of SWIDAC is in the "application-phase," where a specified crack propagation parameter (e.g., K_{ID}, CTOA) would be used to predict crack propagation/arrest behavior for given boundary conditions. Comparisons with experimental results obtained on wide-plate tests and in the PTSE series of vessel tests should then provide a basis for a critical assessment of the analysis procedures and of the material fracture property data base that results.

---

*Work sponsored by the HSST Program under Subcontract 37X-97306C between Martin Marietta Energy Systems, Inc., and the Southwest Research Institute.

†Engineering and Materials Sciences Division, Southwest Research Institute, San Antonio, Texas.

‡Department of Civil Engineering, Northwestern University, Evanston, Illinois.

2.5.2 Elastodynamic analyses of wide-plate tests

Elastodynamic finite-element analyses were performed on a problem previously analyzed by the University of Maryland (UM) code SAMCR to compare its predictions with those obtained using SWIDAC. The analyses modeled rapid crack propagation in a homalite single-edge notched specimen according to a prescribed $K_{ID}(V)$ relation. The specimen was loaded by a prescribed remote displacement that was held fixed during crack propagation. Crack length vs time and K vs time were computed.

The geometrical details and the finite-element mesh used in the analysis are shown in Fig. 2.20. The applied displacement δ corresponds

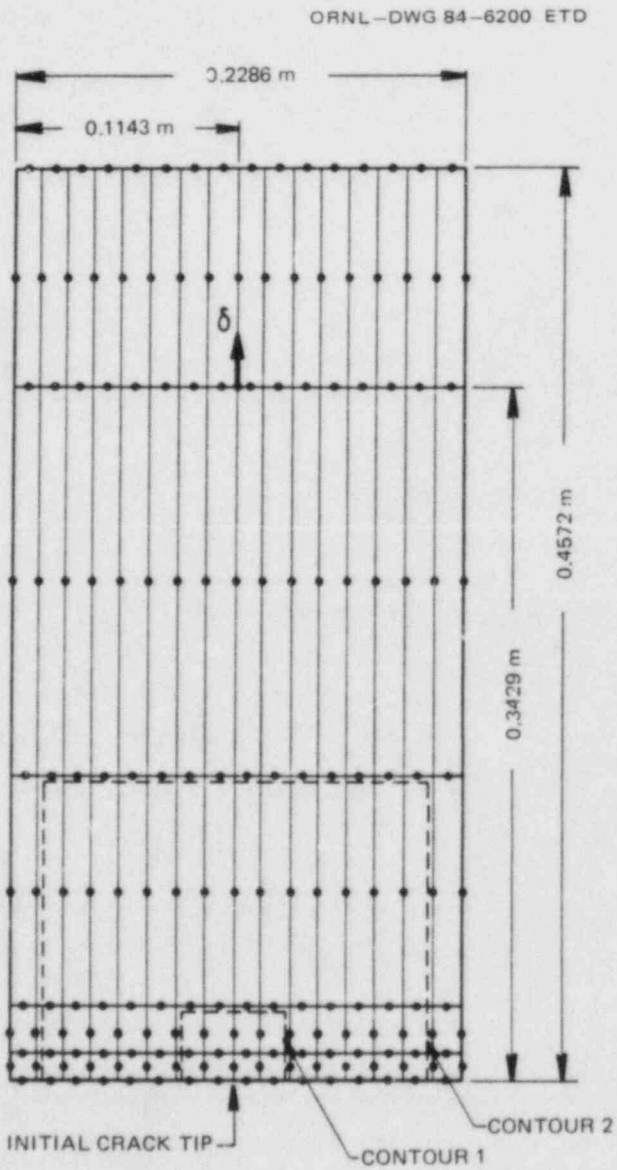

Fig. 2.20. Finite-element mesh for upper symmetrical half of single-edge notch specimen analyzed. Out-of-plane thickness of specimen was 25.4 mm.

to an initial prescribed load of 13.3 kN and crack length of 114.3 mm. This displacement was applied quasi-statically. Then, crack growth was modeled according to the prescribed $K_{ID}(\dot{a})$ shown in Fig. 2.21. The results of the analysis, along with those of UM, are shown in Figs. 2.22 and 2.23. Despite significant differences in analysis procedures used in SAMCR and SWIDAC, the agreement between the predictions of the two codes was found to be reasonably close. Further details of this analysis can be found in Ref. 21.

2.5.3 Dynamic crack propagation/arrest testing

To properly analyze the SwRI dynamic experiments, measurements of crack extension vs time, as well as the specimens' boundary conditions throughout the crack extension period, are needed. Crack extension is being monitored by using an indirect electrical potential technique and a "break-wire" technique. The former employs a commercially available gage (KRAK gage KG-C50-HT), while the latter is under development — particularly with regard to its application to side-notched specimens.

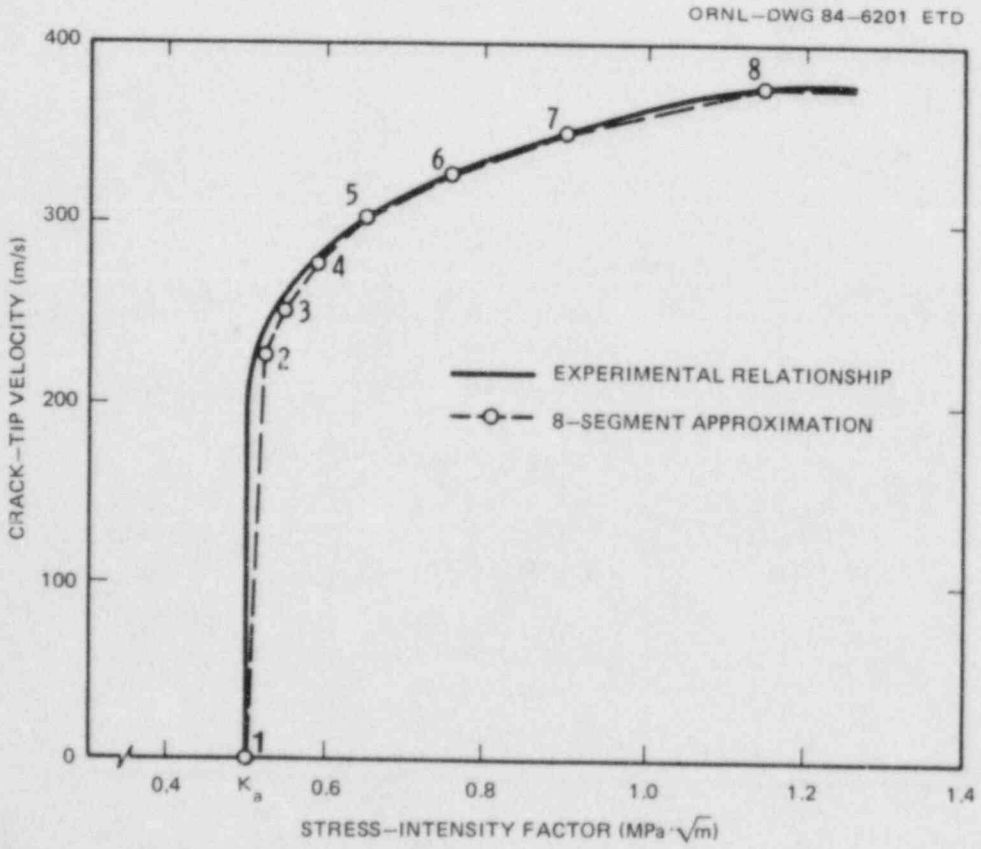

Fig. 2.21. Experimental å-K relationship and approximation used in SAMCR code.

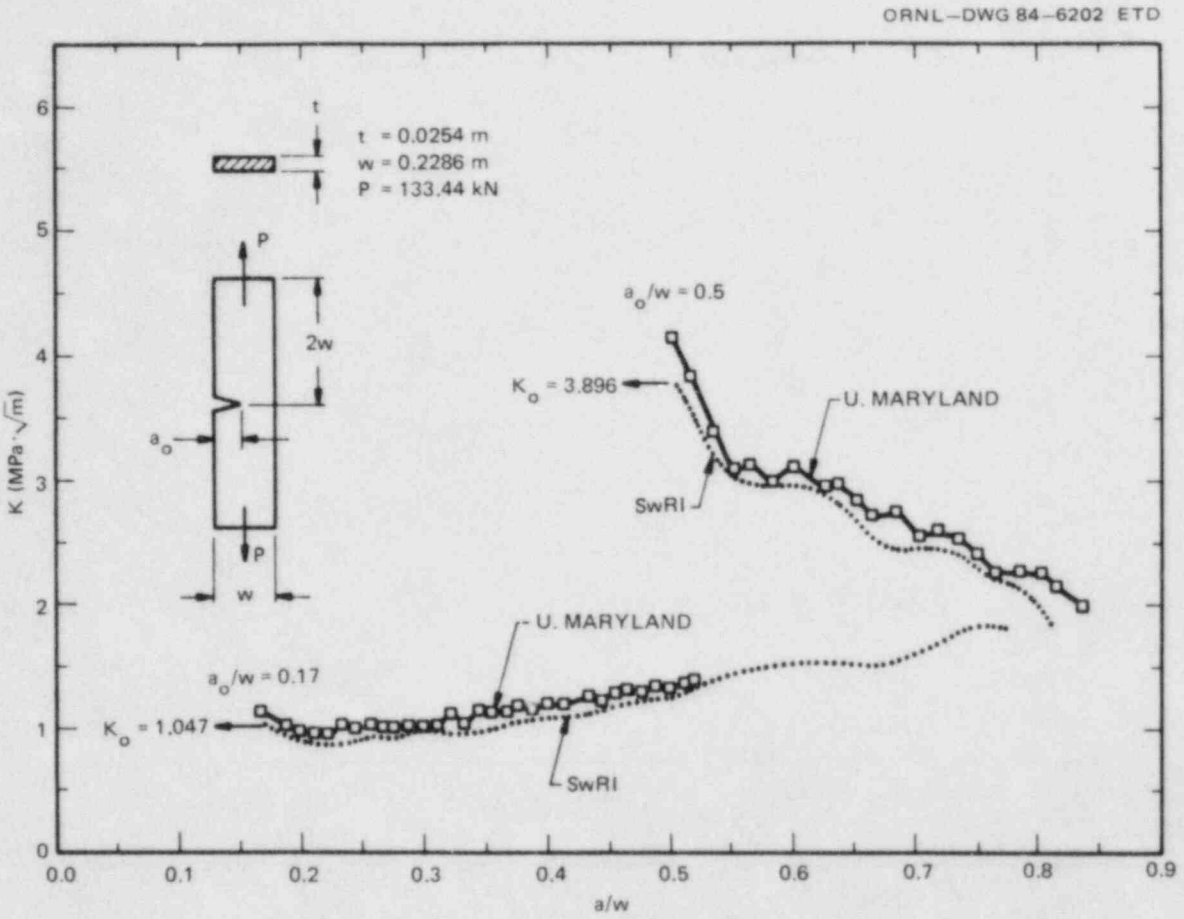

Fig. 2.22. Comparison of predicted K vs time using SWIDAC and UM codes.

Boundary conditions are being characterized in terms of load-line displacements measured using an eddy current technique.

Experiments are being conducted using wedge-loaded, compact-type specimens having an effective height-to-width (H/W) ratio of 0.6. Two specimen sizes are being used: (1) W = 100 mm and a thickness B of 25 mm and (2) W = 200 mm and B = 75 mm. Most specimens will be side-notched, thereby reducing the thickness by 25%, to promote plane strain conditions.

The eddy current technique used to monitor specimen displacement employs a noncontacting probe mounted along a keyway in one of the specimen arms. The other specimen arm then serves as the target in which eddy currents are induced. This integral attachment procedure eliminates additional fixturing whose dynamic response might confound the data interpretation.

The eddy current technique was selected because it is one of the few displacement measuring techniques with adequate frequency response to make the dynamic measurements. The transducers being used have a manufacturer-rated response of 50 kHz. Nevertheless, these transducers are

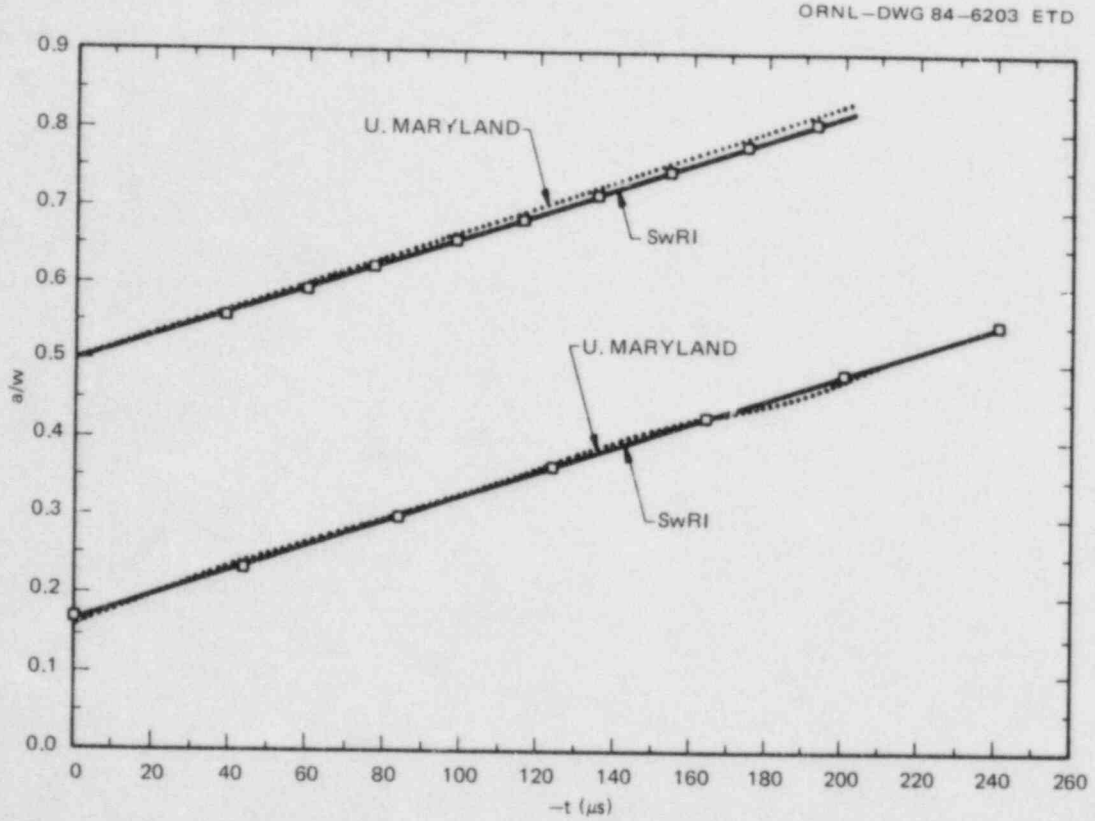

Fig. 2.23. Comparison of predicted crack length vs time using SWIDAC and UM codes.

being evaluated to assess possible frequency response problems, as well as potential inertial effects.

Although the indirect electrical potential technique using the KRAK gage has been utilized successfully for dynamic crack propagation experiments, certain problems can be anticipated with its use in the current program. Crack extension attended by large deformations and shear lips causes the foil gage to tear irregularly. Contact between the specimen and these irregularly torn edges can cause electrical shorting. This problem should be minimized by employing side notches to suppress shear lip development at the specimen surface. We anticipate that gages can be mounted within side notches if the root radius of the side notch is >3 mm.

To provide an alternative to the above crack monitoring procedure, break-wire techniques are also under development. A prototype gage has been produced using a 0.24-mm-diam Chromel-A wire having a resistance of 0.014 Ω/mm. The gage configuration is tapered with cross wires of variable length and therefore variable resistance. This configuration produces a stepwise, linear record of output voltage vs crack length as successive wires are severed during the crack propagation event. This characteristic, along with a working power of several volts, will eliminate the need for amplifiers, which are often a source of frequency response problems during dynamic testing.

Procedures are being developed to insert the above gage into the side notch using a Teflon mandrel. As an alternative, the use of conductive paints are also being explored as a means of directly producing the gage within the side-notch. Conductive paints are available in a variety of electrical resistances and can be applied to the specimen using an air brush and silkscreening technique similar to that employed in the production of electronic circuits.

Specimens are loaded using dual pins and a wedge. This system is similar to that previously used in crack-arrest testing,[22] but different from the single split-pin wedging that has evolved within ASTM for crack-arrest testing.[23,24] The current system enables crack growth gages to be mounted on both planar surfaces of the specimen and also enables access for the eddy current transducer. Uniform heating or cooling of the specimen is also easier than in the case of single split-pin loading where the specimen is in contact with a large thermal mass.

The current loading system is less stiff than the single, split-pin loading system. However, this feature is not a disadvantage in the current experiments since the specimen's boundary conditions are dynamically measured during the crack extension period. Thus, it is unnecessary to rely on a stiff loading system to approximate the condition of constant load-line displacement as is traditionally done in crack-arrest testing. In fact, the lower stiffness of the current system actually provides an advantage when testing high-toughness materials. Under these conditions, the loading system acts as a spring that stores elastic energy which becomes available as a driving force for crack growth once the crack begins to advance. This feature enhances the capacity of small specimens to test high-toughness materials.

The experimental philosophy is to first gather data at low temperature, then proceed to higher temperatures, modifying test techniques as necessary. Several small specimens (W = 100 mm) have been prepared for testing at low temperatures. The larger specimens are currently being prepared. All specimens are being machined from A533B steel provided by ORNL from the same heat of material to be used in the wide-plate tests at NBS.

An initial dynamic fracture experiment was conducted at a temperature of −50°C using a small specimen with a blunt-notch root diameter of 1 mm. However, the crack failed to initiate under these conditions. Additional specimens are being prepared with a small electrodischarge-machined (EDM) notch and with a weld-embrittled notch to facilitate crack initiation.

2.5.4 Viscoplastic material characterization

The viscoplastic properties of A533B steel were characterized by performing tensile tests on round bar specimens at strain rates ranging from 10^{-3} to 1 s^{-1} at −60, −10, 50, 100, and 175°C. Load and displacement data were recorded until final fracture. The Bodner-Partom constitutive theory was then used to model the elastic-viscoplastic behavior of A533B steel. Using the experimental tensile data and the procedure described in Ref. 25, the material constants in the Bodner-Partom model[26] were evaluated. These are tabulated in Table 2.1. In obtaining these

Table 2.1. A summary of the material constants in the Bodner-Partom model evaluated for A533B steel

Temperature (°C)	n	Z_0, Z_2 (MPa)	M_1 (MPa^{-1})	Z_1 (MPa)	D_0 (s^{-1})
−60	2.20	1200	0.061	1550	10^6
−10	2.00	1170	0.061	1550	10^6
50	1.90	1160	0.061	1550	10^6
100	1.77	1150	0.061	1550	10^6
175	1.75	1140	0.061	1550	10^6

constants, only isotropic hardening is considered; both directional hardening and thermal recovery have been neglected. As indicated in Table 2.1, the material constants D_0, M_1, and Z_1 in the Bodner-Partom model are temperature independent; on the other hand, the parameters n and Z_0 are dependent on temperature. In the temperature range of interest, n and Z_0 have been found to be well described by:

$$n = \frac{175}{T} + 1.35 \ , \tag{2.45}$$

$$Z_0 = \frac{2.44 \times 10^4}{T} + 1084 \ , \tag{2.46}$$

where T is the absolute temperature in degrees Kelvin and Z_0 is in megapascals. Also note that the material constants were obtained on the basis of the Lagrangian (engineering) stress and strain measures.

Based on the material constants in Table 2.1, the Bodner-Partom model has been used to calculate the stress-strain curves of A533B steel at various strain rates and temperatures. Figures 2.24 and 2.25 show the good comparisons that exist between the calculated and experimental yield stresses (at plastic strains of 0.2% and 10%) as functions of temperature and strain rate, respectively.

2.5.5 Preliminary development of a viscoplastic crack propagation model

Implementation of the Bodner-Partom constitutive theory[26,27] into a finite-element code for studying dynamic viscoplastic propagation was initiated. The finite-element code chosen for this purpose was VISPLAS, a 2-D code that uses an isoparametric element formulation for 4-noded (linear) and 8-noded (quadratic) elements. The nonlinear solution procedure in VISPLAS is an algorithm from Hughes and Taylor[28] commonly known as the α-method. The algorithm has been coded so the user may select an explicit ($\alpha = 0$) or an implicit ($0 < \alpha < 1$) integration procedure. This

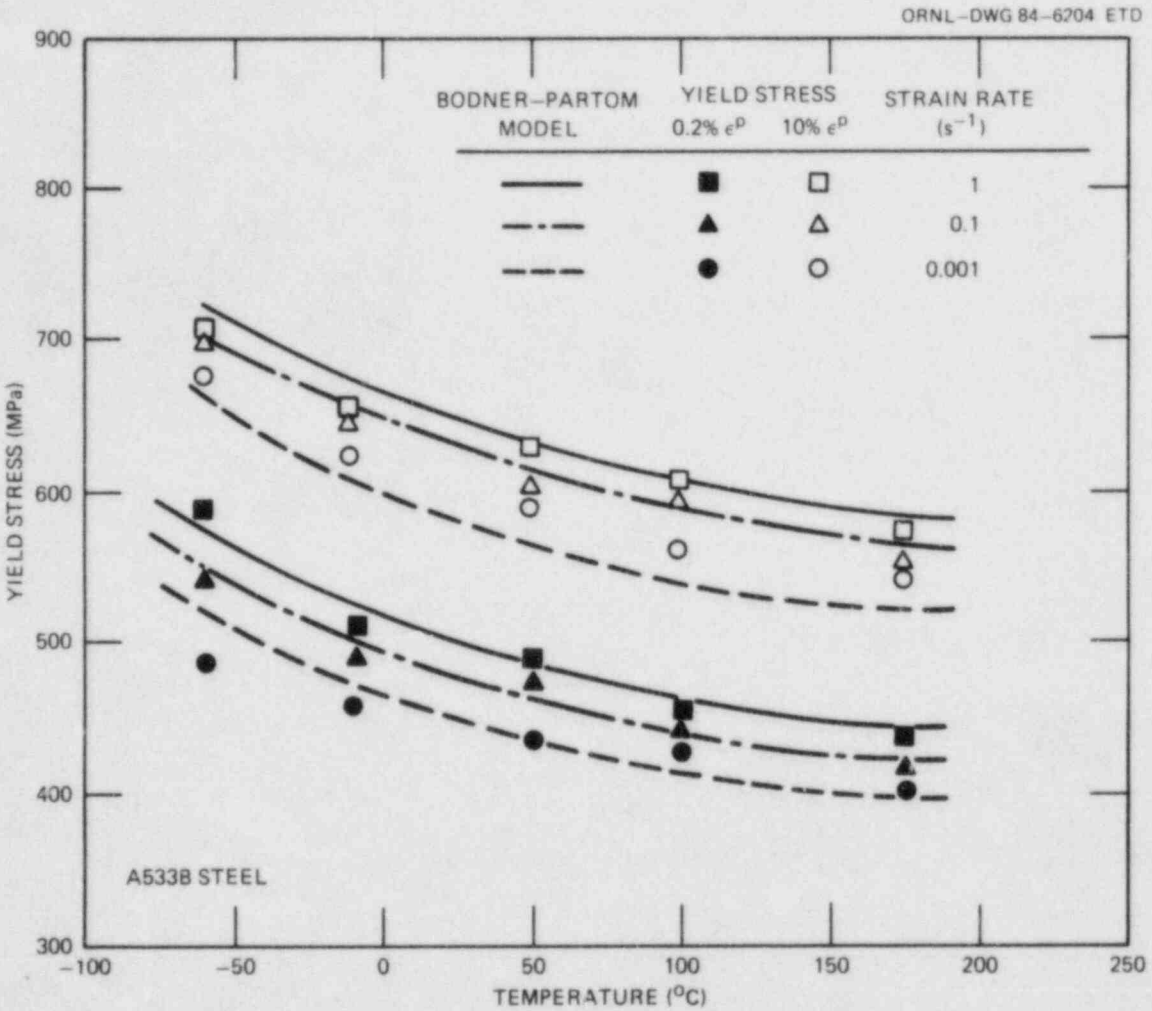

Fig. 2.24. Comparison of experimental and theoretical yield stresses as functions of temperature.

capability gives the user considerable flexibility in controlling accuracy, stability, and the computational cost of the solution. Note that the explicit method is less expensive per time step (no stiffness reformulation), but it requires smaller time steps than the implicit method to ensure stability of the solution. On the other hand, the implicit method with $0.5 < \alpha < 1$ is unconditionally stable regardless of the time-step size, but it requires reformulation of the stiffness at each step.

Evaluation of the two algorithms with the Bodner-Partom constitutive model was achieved by predicting the tensile response of René 95 at 650°C at a constant stress rate of 4000 MPa/min. Solutions using both algorithms were obtained for up to ~2% strain and for different time-step sizes. The results are summarized in Figs. 2.26–2.28. The next step in the development is to incorporate an algorithm for crack propagation modeling via a node release technique. Then, the viscoplastic analysis will be implemented in SWIDAC. This will enable viscoplastic-dynamic crack propagation analyses related to the PTS problem to be performed.

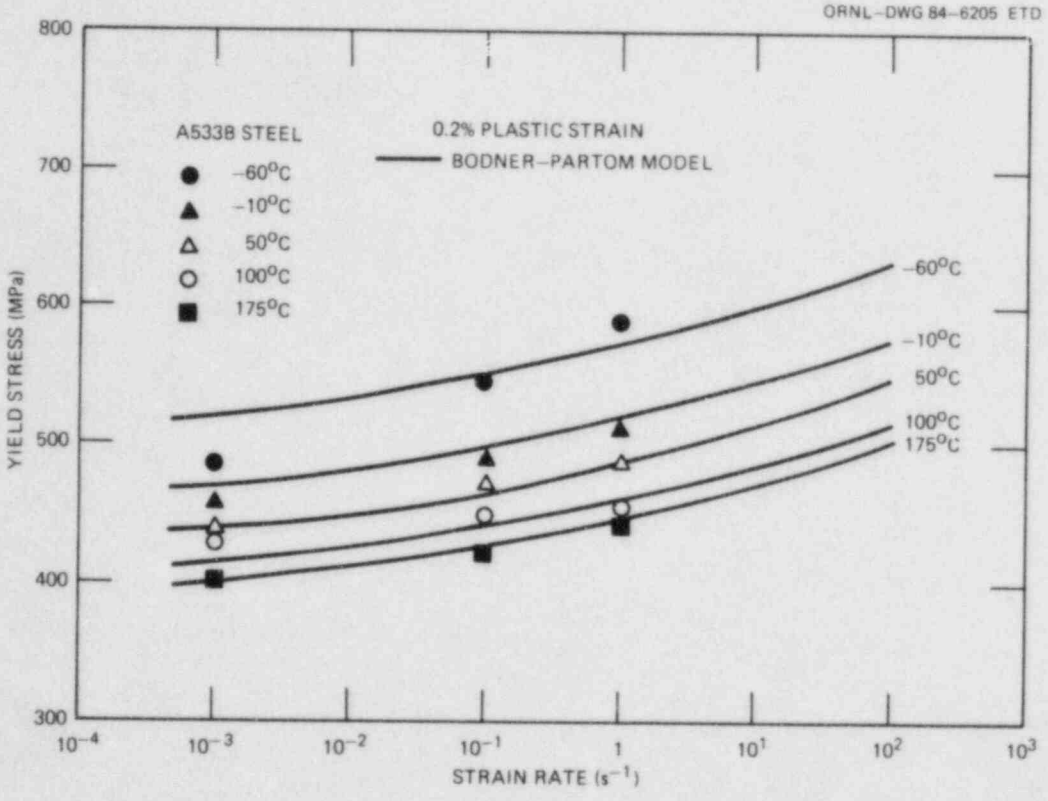

Fig. 2.25. Comparison of experimental and theoretical 0.2% ε^p yield stress as function of strain rate and temperature.

2.5.6 Asymptotic analysis of crack propagation in a viscoplastic medium

The Bodner and Partom constitutive equations[27] are for an elastic-viscoplastic work-hardening material. These equations do not require separate specification of a yield criterion, and it is not necessary to consider loading and unloading separately. Within the context of the Bodner-Partom model, both elastic and inelastic deformations are present at all stages of loading and unloading. However, the plastic deformations are very small when the material behavior should be essentially elastic.

To obtain a more realistic description of the stress and deformation state near a rapidly propagating crack tip in a Bodner-Partom material, the order of the singularities is of interest. It is assumed that the crack propagates under Mode-I conditions. To take the effects of material inertia into account, the near-tip fields are analyzed by the asymptotic method presented by Achenbach, Kanninen, and Popelar.[29] The results show that, while the near-tip plastic strain rates are bounded just as for a linearly elastic material, the total strains and the stresses display square-root singularities. This finding is of great importance for the finite-element representation of viscoplastic-dynamic crack propagation and arrest.

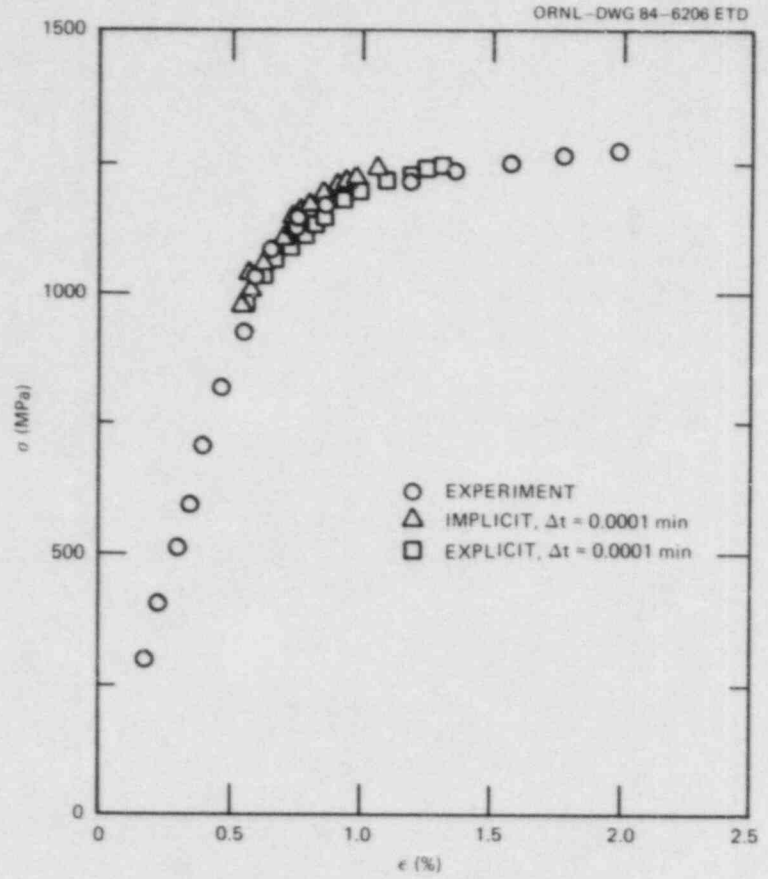

Fig. 2.26. Predicted tensile response of René 95 at 650°C under constant stress rate (4000 MPa/min) using VISPLAS with Bodner's constitutive model.

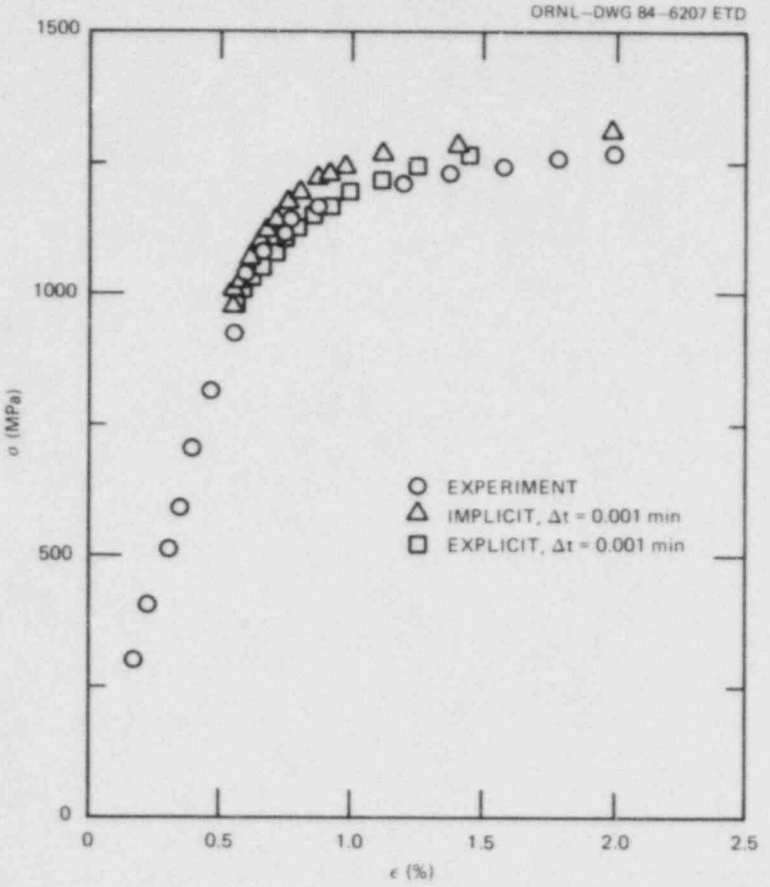

Fig. 2.27. Predicted tensile response of René 95 at 650°C under constant stress rate (4000 MPa/min) using VISPLAS with Bodner's constitutive model.

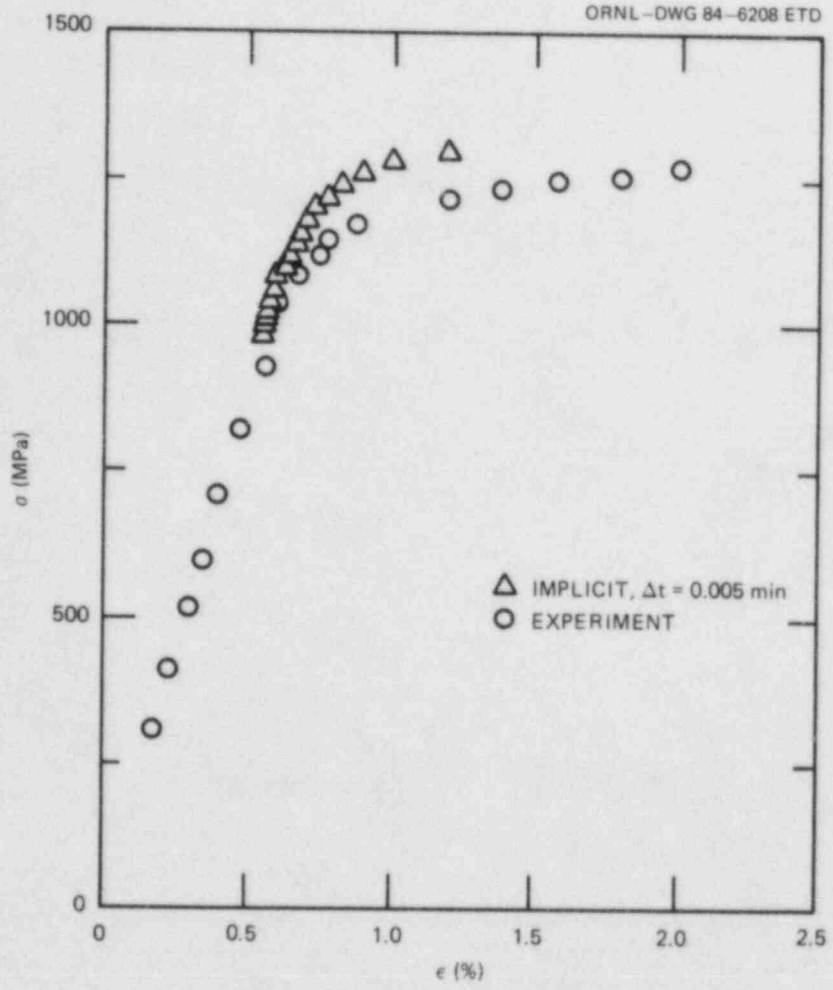

Fig. 2.28. Predicted tensile response of René 95 at 650°C under constant stress rate (4000 MPa/min) using VISPLAS with Bodner's constitutive model.

References

1. B. R. Bass and J. W. Bryson, *Applications of Energy Release Rate Techniques to Part-Through Cracks in Plates and Cylinders; Volume 1. ORMGEN-3D: A Finite Element Mesh Generator for 3-Dimensional Crack Geometries*, ORNL/TM-8527/V1, Union Carbide Corp. Nuclear Div., Oak Ridge Natl. Lab., December 1982.

2. B. R. Bass and J. W. Bryson, *Applications of Energy Release Rate Techniques to Part-Through Cracks in Plates and Cylinders; Volume 2. ORVIRT: A Finite Element Program for Energy Release Rate Calculations for 2-Dimensional and 3-Dimensional Crack Models*, ORNL/TM-8527/V2, Union Carbide Corp. Nuclear Div., Oak Ridge Natl. Lab., February 1983.

3. K. J. Bathe, *ADINA — A Finite Element Program for Automatic Dynamic Incremental Nonlinear Analysis*, Massachusetts Institute of Technology Report 82448-1 (1975, revised 1978).

4. K. Jerram, *The Use of a FEM-Stress Analysis Computer Program for the Calculation of Stress Intensity Factors*, GEGB — Berkley, Nuclear Lab., Report No. FD/B/N 1521 (1970).

5. Private communication between D. Read, National Bureau of Standards, Boulder, Colorado, and C. E. Pugh, Oak Ridge National Laboratory, Oak Ridge, Tenn., July 1984.

6. "Appendix A, Analysis of Flaw Indications," Section XI, Division 1, Rules for Inservice Inspection of Nuclear Power Plant Components, *ASME Boiler and Pressure Vessel Code*, 1983.

7. W. R. Andrews, "Effect of Loading Sequence on Notch Strength of Warm Prestressed Alloy Steel," *J. Eng. Ind.*, ASME 92, 785–91 (November 1970).

8. F. J. Loss, R. A. Gray, Jr., and J. R. Hawthorne, "Investigation of Warm Prestress for the Case of Small ΔT During a Reactor Loss-of-Coolant Accident," *J. Pressure Vessel Tech.*, ASME 101, 298–304 (November 1979).

9. R. H. Bryan et al., "Pressurized-Thermal-Shock Technology," pp. 142–73 in *HSST Program Semiannual Prog. Rep. October 1983–March 1984*, ORNL/TM-9154/V1, Martin Marietta Energy Systems, Inc., Oak Ridge Natl. Lab.

10. G. G. Chell, J. R. Haigh, and B. Vitek, *A Theory of Warm Prestressing: Experimental Validation and the Implications for Elastic-Plastic Failure Criteria*, RD/L/N63/79, Central Electricity Research Laboratories, Leatherhead, Surrey, England, August 1979.

11. G. G. Chell, *A Theory for Predicting the Failure Loads of Cracked Structures Subjected to Warm Prestressing. 1: Load Changes at Constant Temperature*, RD/L/N63/79, Central Electricity Research Laboratories, Leatherhead, Surrey, England, September 1979.

12. G. G. Chell, "Some Fracture Mechanics Applications of Warm Prestressing to Pressure Vessels," pp. 117–24 in *Proceedings 4th International Conference on Pressure Vessel Technology*, Paper C22/80, I. Mech. E., London, 1980.

13. S. Yukawa, *Evaluation of Periodic Proof Testing and Warm Prestressing Procedures for Nuclear Reactor Vessels*, HSSTP-TR-1, General Electric Company, Schenectady, New York, July 1, 1969.

14. J. J. McGowan, "Application of Warm Prestressing Effects to Fracture Mechanics Analyses of Nuclear Reactor Vessels During Severe Thermal Shock," *Nucl. Eng. Des.* 51, 431–44 (1979).

15. B. W. Pickles and A. Cowan, "A Review of Warm Prestressing Studies," *Int. J. Pres. Ves. & Piping* 14, 95–131 (1983).

16. J. N. Goodier and F. A. Field, "Plastic Energy Dissipation in Crack Propagation," pp. 103–18 in *Fracture of Solids*, ed. D. C. Drucker and J. J. Gilman, Interscience, 1962.

17. R. H. Bryan et al., *Test of 6-in.-thick Pressure Vessels; Series 3: Intermediate Test Vessel V-7A Under Sustained Loading*, ORNL/NUREG-9, Union Carbide Corp. Nuclear Div., Oak Ridge Natl. Lab., February 1978.

18. J. R. Rice, "A Path Independent Integral and the Approximate Analysis of Strain Concentration by Notches and Cracks," *J. Appl. Mech.*, ASME 35, 379–86 (June 1968).

19. W. L. Fourney et al., "Investigation of Damping and of the Cleavage-Fibrous Transition in Reactor Grade Steel," pp. 13–25 in *Heavy-Section Steel Technology Program Semiannual Prog. Rep. October 1983–March 1984*, NUREG/CR-3744/Volume 1 (ORNL/TM-9154/V1), Union Carbide Corp. Nuclear Div., Oak Ridge Natl. Lab.

20. W. L. Fourney et al., "Investigation of Damping and of the Cleavage-Fibrous Transition in Reactor Grade Steel," pp. 48–63 in *Heavy-Section Steel Technology Program Semiannual Prog. Rep. January-March 1983*, NUREG/CR-3334/Volume 1 (ORNL/TM-8787/V1), Union Carbide Corp. Nuclear Div., Oak Ridge Natl. Lab.

21. V. Papaspyropoulos, J. Ahmad, and M. F. Kanninen, *Benchmark Finite Element Analyses*, SwRI Letter Monthly Management Report (Subcontract No. 37X-97306C) to the HSST Program, April 30, 1984.

22. R. G. Hoagland et al., "A Crack Arrest Measuring Procedure of K_{Im}, K_{ID}, and K_{Ia} Properties," pp. 177–202 in *Fast Fracture and Crack Arrest*, ASTM STP 627, 1977.

23. P. B. Crosley et al., *Cooperative Test Program on Crack Arrest Toughness Measurements*, NUREG/CR-3261, Nuclear Regulatory Commission, Washington, D.C., April 1983.

24. "Proposed ASTM Test Method for Crack Arrest Fracture Toughness of Ferritic Materials," Revised: June 1984, working document of ASTM Task Group E24.01.06, 1984.

25. U. S. Lindholm, *Constitutive Modeling for Isotropic Materials*, First SwRI Annual Report, NASA contract NAS3-23925, 1984.

26. S. R. Bodner and Y. Partom, "Constitutive Equations for Elastic-Viscoplastic Strain-Hardening Materials," *J. Appl. Mech.* 42, 385–89 (1975).

27. S. R. Bodner, "Evolution Equations for Anisotropic Hardening and Damage of Elastic-Viscoplastic Materials," *Proceedings of Conference on Plasticity Today*, Udine, Italy, 1983.

28. T. Hughes and R. L. Taylor, "Unconditionally Stable Algorithms for Quasistatic Elasto/Viscoplastic Finite Element Analysis," *Comput. Struct.* 8, 169–73 (1978).

29. J. D. Achenbach, M. F. Kanninen, and C. H. Popelar, "Crack-Tip Fields for Fast Fracture of an Elastic-Plastic Material," *J. Mech. Phys. Solids* 29, 211–55 (1981).

3. MATERIAL CHARACTERIZATION AND PROPERTIES

R. K. Nanstad

3.1 Directory to Other Material Properties Reporting

Primarily for internal management and budgetary control purposes, the Heavy-Section Steel Technology (HSST) Program has made a separate task (Task H.3) of the work on material characterization and properties determinations. However, for the readers' convenience, some contributions are placed within other chapters of this report according to the larger tasks that correspond to the particular material studies. Therefore, in addition to the work reported in this chapter, please refer to Sect. 5.3 for properties studies in support of wide-plate crack-arrest tests and to Sect. 10.2 for fractographic evaluation in support of the first pressurized-thermal-shock (PTS) assessments.

3.2. ORNL Participation in ASTM Round Robin on K_{Ia} Testing

W. R. Corwin T. D. Owings

Oak Ridge National Labortory (ORNL) has completed all testing for the ASTM round robin on crack-arrest testing. The HSST Program is supporting similar testing through subcontracts at the Battelle Columbus Laboratories (BCL) and the University of Maryland (UM). The ORNL results have been transmitted to the ASTM round-robin coordinator (UM). The results will be discussed in the next progress report after the testing by the remaining laboratories is completed. The ancillary testing to be performed in conjunction with the round robin (e.g., subsize specimens inverted-pin testing) will be done at ORNL during the next reporting period. The overall status of the ASTM round-robin program is given in Sect. 5.3.3 of this report.

3.3. Direct Current-Potential Drop Studies

J. J. McGowan

Procedures are being developed for using dc-potential methods in J-integral R-curve testing. The major advantage in use of dc-potential for crack length measurement is that the R-curve test can be conducted continuously at an arbitrary strain rate. One of the most important aspects of dc-potential R-curve testing is an accurate calibration between the dc-potential values and the crack length for a chosen set of probe locations. The probe and current input locations that were selected are shown in Fig. 3.1. These locations were selected for (1) sensitivity to crack length change and (2) insensitivity to probe misplacement. Notice that active and reference probes are used. This arrangement is used to

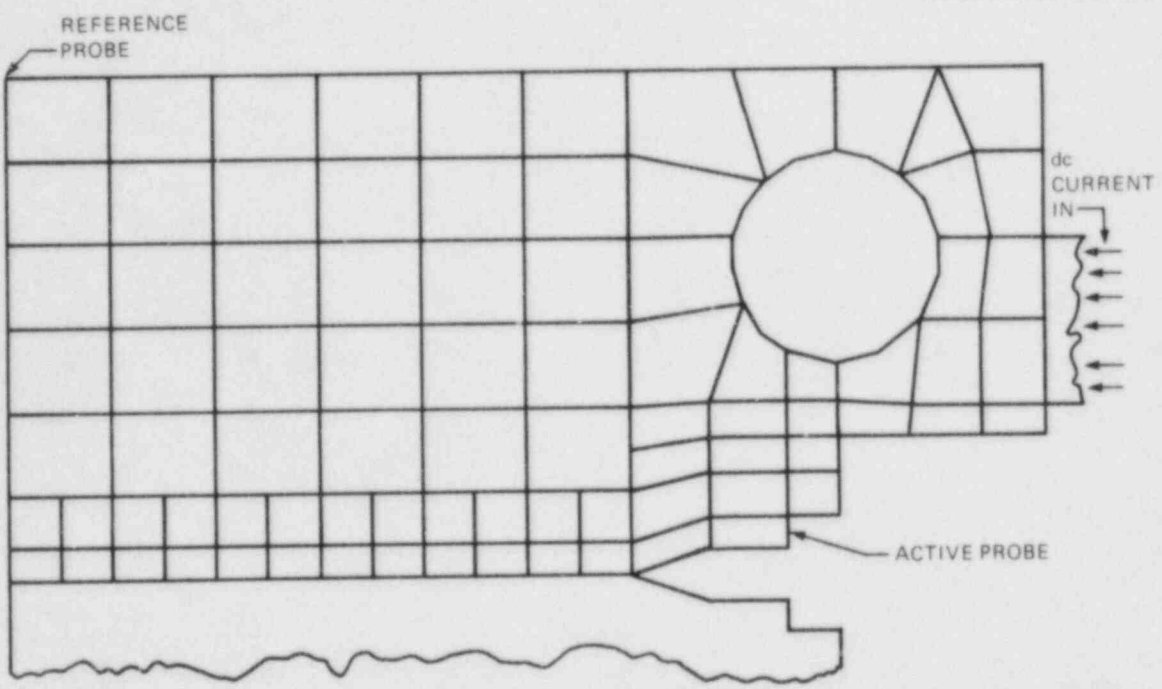

Fig. 3.1. J_{Ic} specimen geometry and probe location.

eliminate the effects of temperature-caused sensitivity changes and current changes. Three separate models were used to determine the calibration: 0.7-mm type 304L stainless steel sheet experiment, 0.03-mm aluminum sheet experiment, and 299-node finite-element analysis. Each model used the exact geometry of the J_{Ic} specimen including notches and holes. The experimental studies used a Kepko JQE-610 for current supply and an HP 3487A 5 1/2-digit voltmeter for dc-potential measurements. The analytical studies used the ADINAT computer program with 85 two-dimensional, 8-node isoparametric elements, as shown in Fig. 3.1. The results of the three studies are shown in Fig. 3.2. The agreement is quite good with a difference of a/w of 1% for $0.5 < a/w < 0.9$.

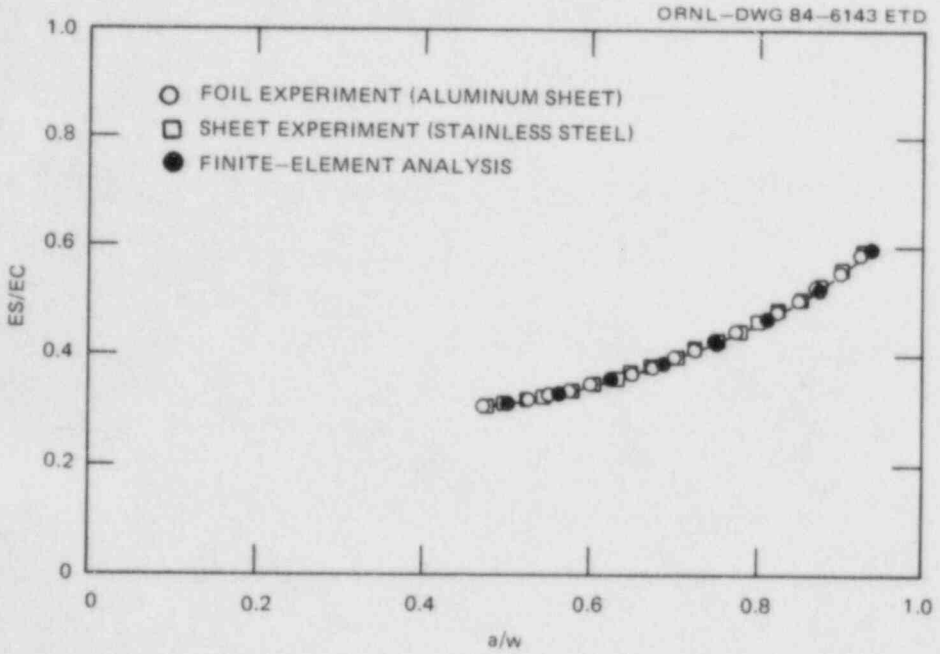

Fig. 3.2. Results of calibration models, where ES is reference potential and EC is active potential.

4. ENVIRONMENTALLY ASSISTED CRACK-GROWTH TECHNOLOGY*

W. H. Bamford† R. J. Jacko‡
I. W. Wilson‡ L. J. Ceschini‡

4.1 Introduction

The objective of this task is to characterize the crack-growth rate properties of light-water reactor (LWR) materials exposed to primary-coolant environments. The work now being conducted falls into four major areas:

1. corrosion fatigue crack-growth tests in simulated pressurized-water reactor (PWR) environment,
2. static-load K_{ISCC} tests in simulated PWR environment,
3. fractographic examination of specimen fracture surfaces, and
4. characterization of environment by measurement of electrochemical potential.

4.2 Fatigue Crack-Growth Results

The results of testing carried out earlier under this program have shown that the microstructure of the material can have an important influence on the level of crack-growth enhancement in a water environment.[1,2] That finding has been confirmed by other investigators and is now being followed up by more detailed studies. Two areas have been studied and will be reported here.

4.2.1 High-sulfur material characterization

The crack-growth behavior of high-sulfur steel is of interest because the steels are expected to exhibit the most enhancement of crack growth. A test matrix has been formulated (Table 4.1) to provide more information on a typical high-sulfur material. The heat chosen for study was a commercially produced pressure vessel steel with a sulfur content of 0.025 wt %. This was among the highest known sulfur content and is typical of the oldest materials in service in operating plants. Steels with lower-sulfur content have been produced since then to improve the fracture toughness. The matrix was designed to characterize the material behavior at different temperatures, frequencies, and R ratio values

*Work sponsored by HSST Program under Subcontract 11X-21598C between Martin Marietta Energy Systems, Inc., and Westinghouse Electric Corporation, Nuclear Technology Division.

†Westinghouse Electric Corporation, Power Systems, Nuclear Technology Division, Pittsburgh, PA 15230.

‡Westinghouse Research and Development Laboratories, Pittsburgh, PA 15235.

Table 4.1. Test matrix for study of frequency and temperature effects for high-sulfur A533B steel

Test temperature (°C)	R ratio = 0.2		R ratio = 0.7	
	Frequency (cpm)	Specimen	Frequency (cpm)	Specimen
288	1	CQ2-5	1	CQ2-6
	1[a]	CQ2-8	10	CQ2-11
	1(borated)[a]	CQ2-9		
204	1(borated)[a]	CQ2-12	1	CQ2-7
			10[a]	CQ2-10
93				

[a]Tests completed during this reporting period.

(K_{min}/K_{max}). The matrix also included a study of the effect of the boron level on crack growth. The tests completed during this period are identified in Table 4.1.

Three tests have been completed under the conditions of 288°C, one cycle per minute, and R ratio equal to 0.2. The environment has been deoxygenated water except for specimen CQ2-9, which was tested with borated water. Figure 4.1 shows that the crack-growth behavior of all three specimens was essentially the same. These results are important in a number of ways. First, specimens CQ2-8 and CQ2-5 provide a measure of the scatter to be expected in this material. This scatter results mostly from material variability, which is best characterized by the distribution of manganese sulfide inclusions. This aspect will be discussed further in Sect. 4.4, but it should be noted here that these specimens were taken from similar positions in the plate. The effect of a borated water environment on the crack growth was found to be negligible, as seen by comparing the results for specimen CQ2-9 with those for the other two.

The effect of temperature on fatigue crack growth under low R ratio conditions is shown in Fig. 4.2. There is a definite effect of temperature on the growth rate, with the higher temperature resulting in faster growth rates. Both of the tests shown in Fig. 4.2 were tested in borated water environments.

The results of the high R ratio tests are more difficult to interpret because often the crack-growth rate is stagnated at a certain point in the test, refusing to rise continuously with applied stress-intensity range ΔK, as is generally observed in low R ratio tests. This behavior has been observed in many earlier tests at high R ratio. The effect of test temperature on the high R ratio results was discussed previously,[3] and it was concluded that the growth rate is higher at a higher temperature.

The effects of frequency on the crack-growth results are shown in Figs. 4.3 and 4.4 for 204 and 288°C, respectively. In both figures,

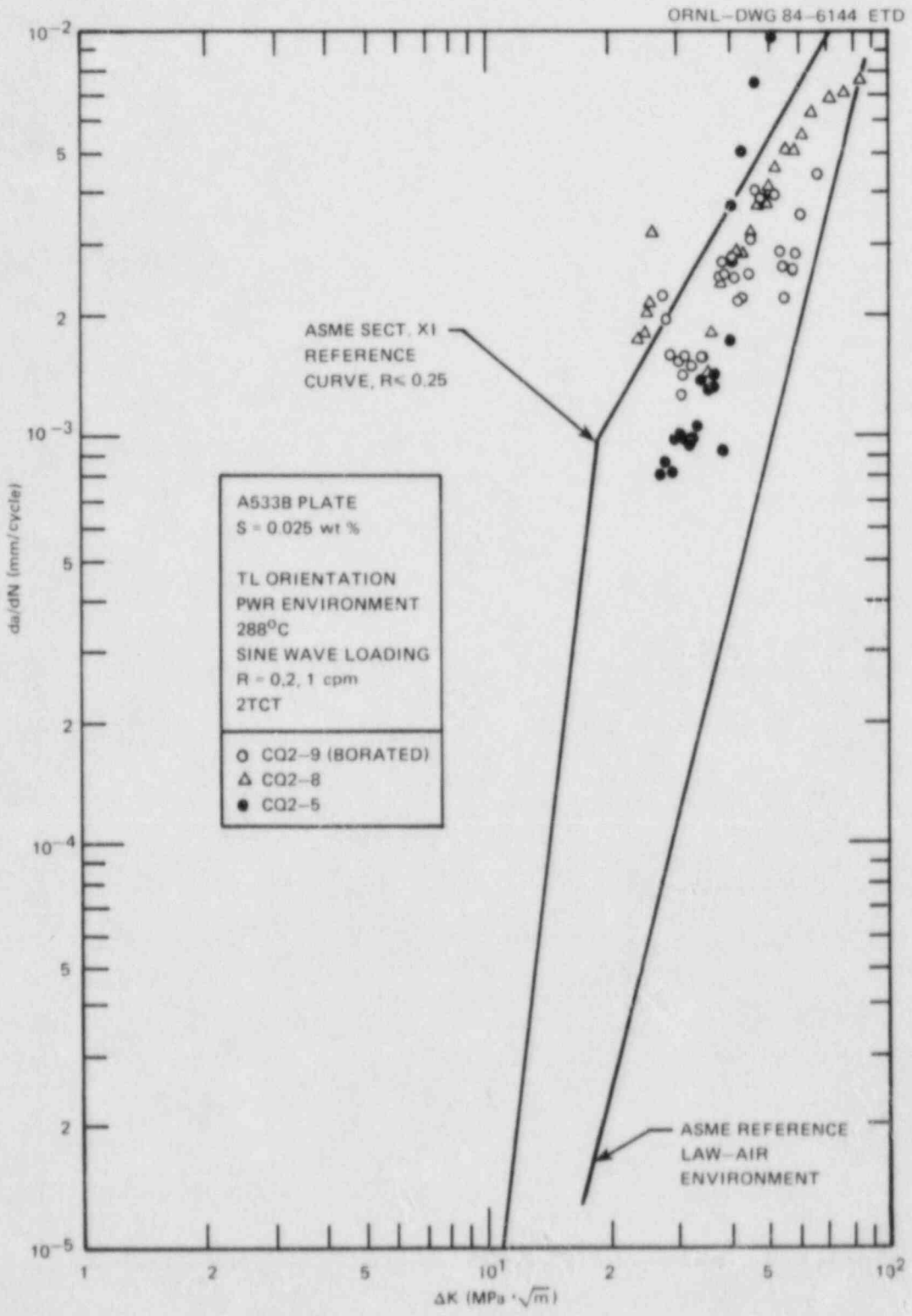

Fig. 4.1. Comparison of fatigue crack-growth rate results for high-sulfur steel tested at R = 0.2. Note similar results for borated and unborated environments.

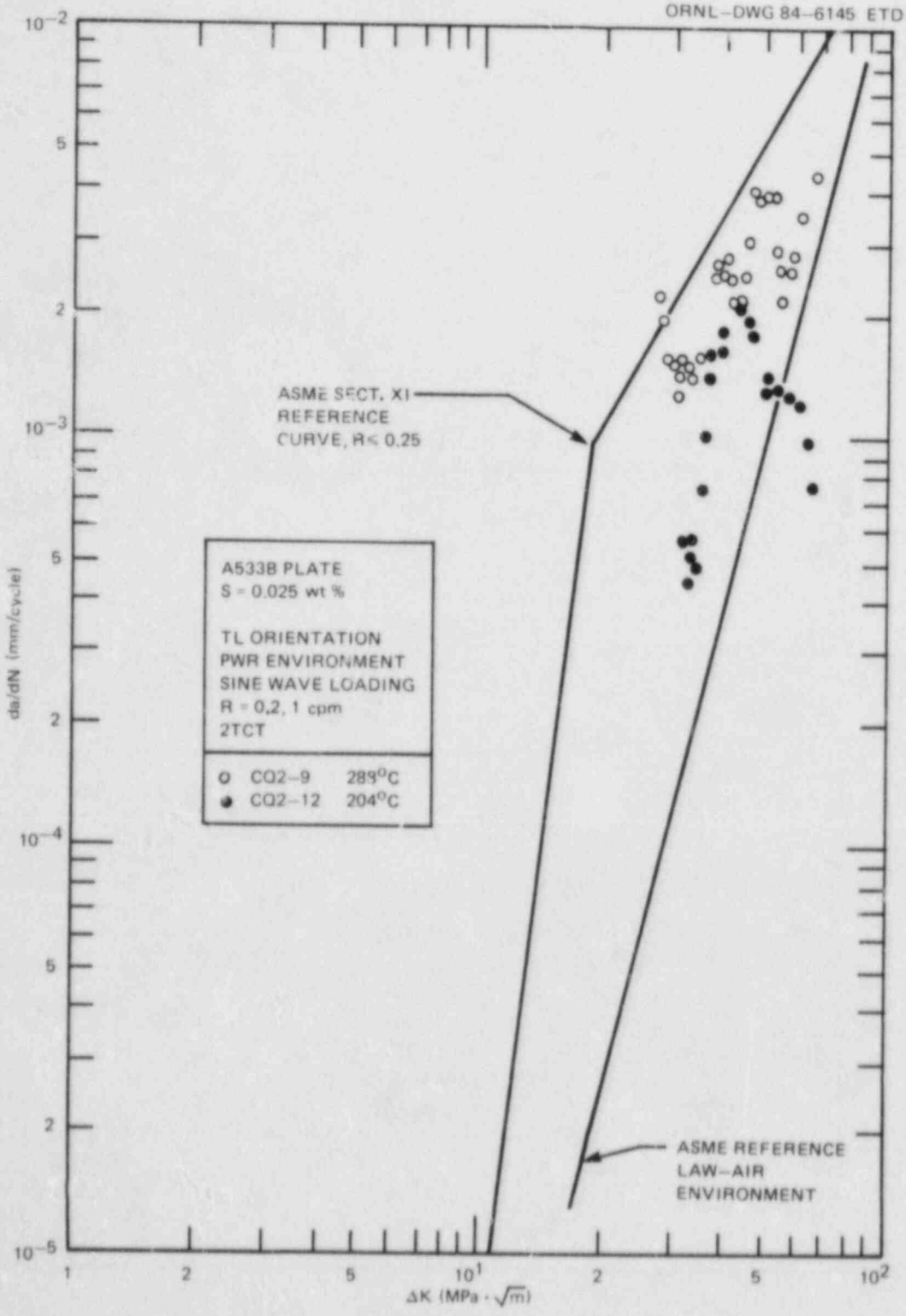

Fig. 4.2. Effect of test temperature on fatigue crack-growth rates at R = 0.2.

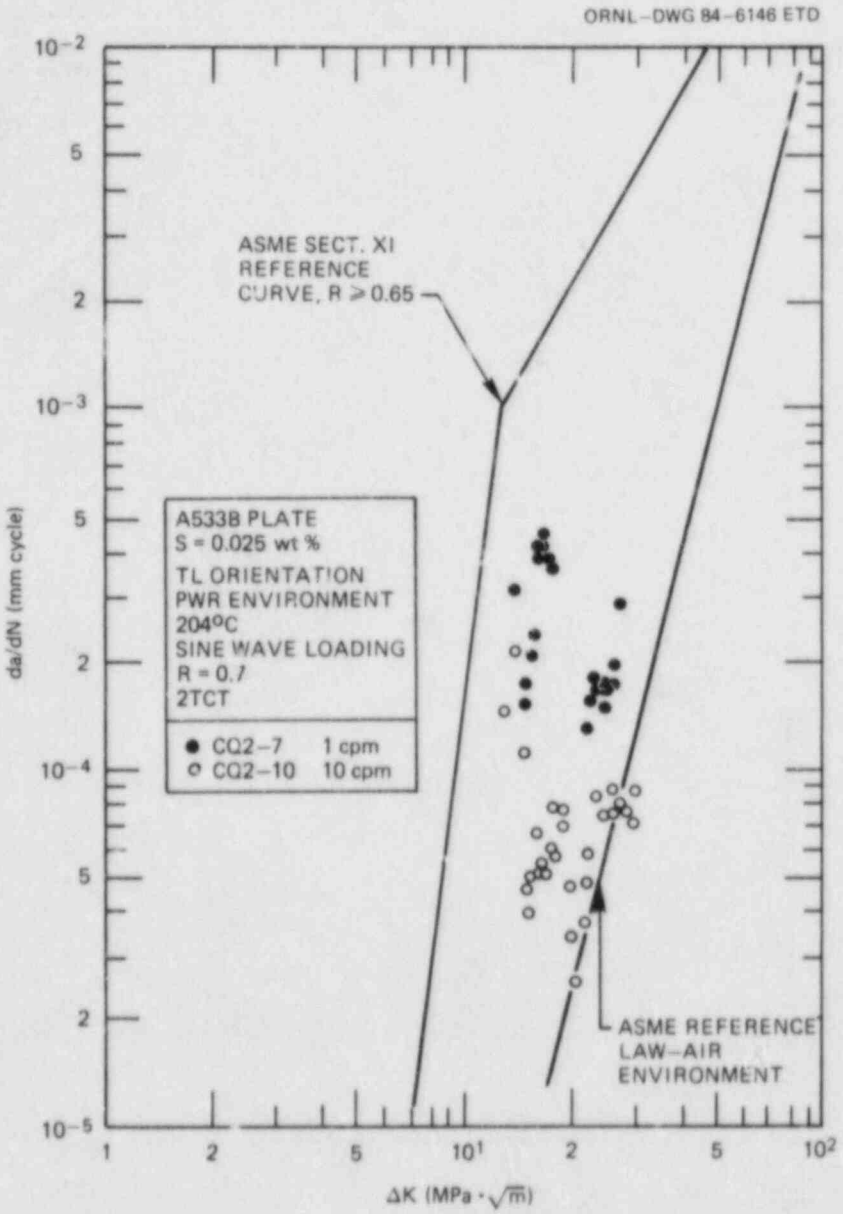

Fig. 4.3. Effect of frequency on fatigue crack-growth rates for high-sulfur heat CQ2 at R = 0.7 and 204°C in simulated PWR environment.

many accelerations and decelerations are found, but the higher crack-growth rate was found at one cycle per minute, which agrees with earlier findings.[4]

Many of these specimens were also studied fractographically. Those results are discussed in Sect. 4.4.

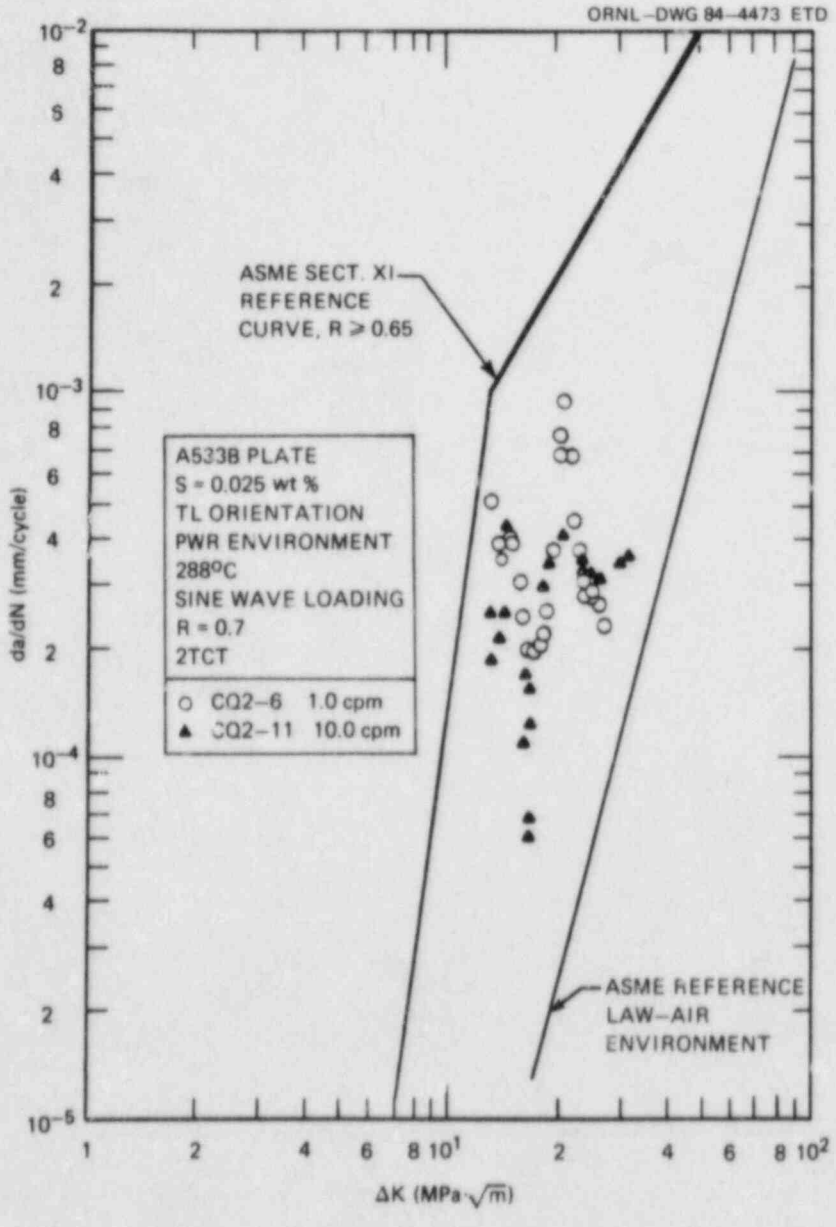

Fig. 4.4. Effect of frequency on fatigue crack-growth rates for high-sulfur heat CQ2 at R = 0.7 and 288°C in simulated PWR environment.

4.2.2 Low-sulfur material characterization

Although the level of environmental acceleration is known to be lower in low-sulfur steels, it is nonetheless important to understand the behavior of low-sulfur steels in water environments. Two heats of low-sulfur steel (content 0.004 wt %) have been characterized, and remarkably different crack-growth rate behaviors have been observed.

Figure 4.5 presents the results for these two materials at a low R ratio and includes two specimens tested by Cullen et al.[5] The results

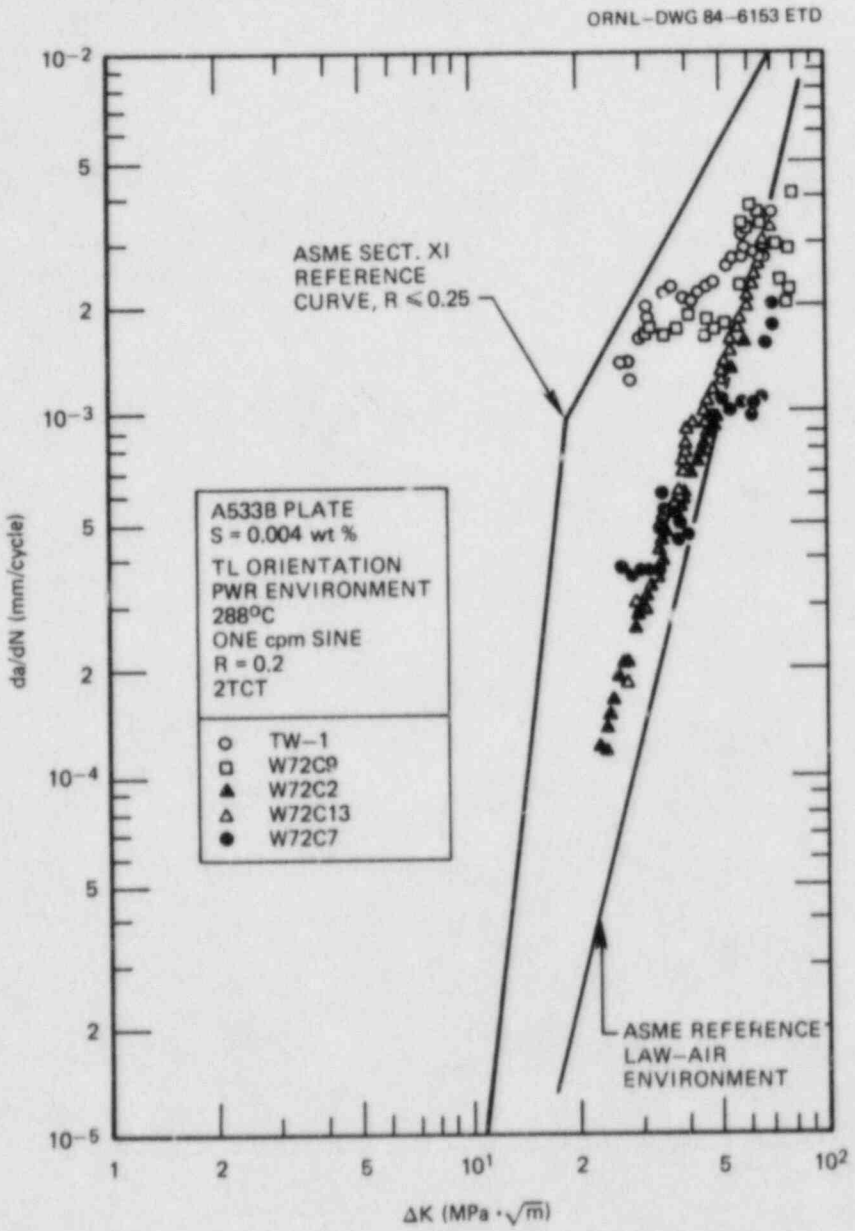

Fig. 4.5. Summary of crack-growth results for low-sulfur heat W7 compared with low-sulfur specimen TW-1 at R = 0.2. (Note: all loadings were sinusoidal except W72C2 which was ramp/reset.)

for heat "W7" show predominantly low fatigue crack-growth rates. Specimen W72C9, which showed accelerated growth, appears to be an exception rather than the rule. Extensive studies have been made to find an explanation for this behavior with no success. The "WC" specimens were taken from the same position in the plate, and the test environment chemistry was essentially identical. There was no indication in test records that would suggest that different results should be obtained. Given the

collection of results on this heat, one must conclude that the behavior of heat "WC" was not accelerated.

The other heat of low-sulfur steel TW has been characterized rather extensively in earlier testing,[1] and the results obtained at a low R ratio are consistently much more accelerated than those of heat W7, as shown in Figs. 4.5 and 4.6. The test records for heats TW1 and W72C9 were compared in detail, and no differences were obvious. Even the water chemistry results from both before and after testing compare very well for all the specimens shown in Fig. 4.5. Further study of these two heats was done fractographically. Those results are reported in Sect. 4.4.

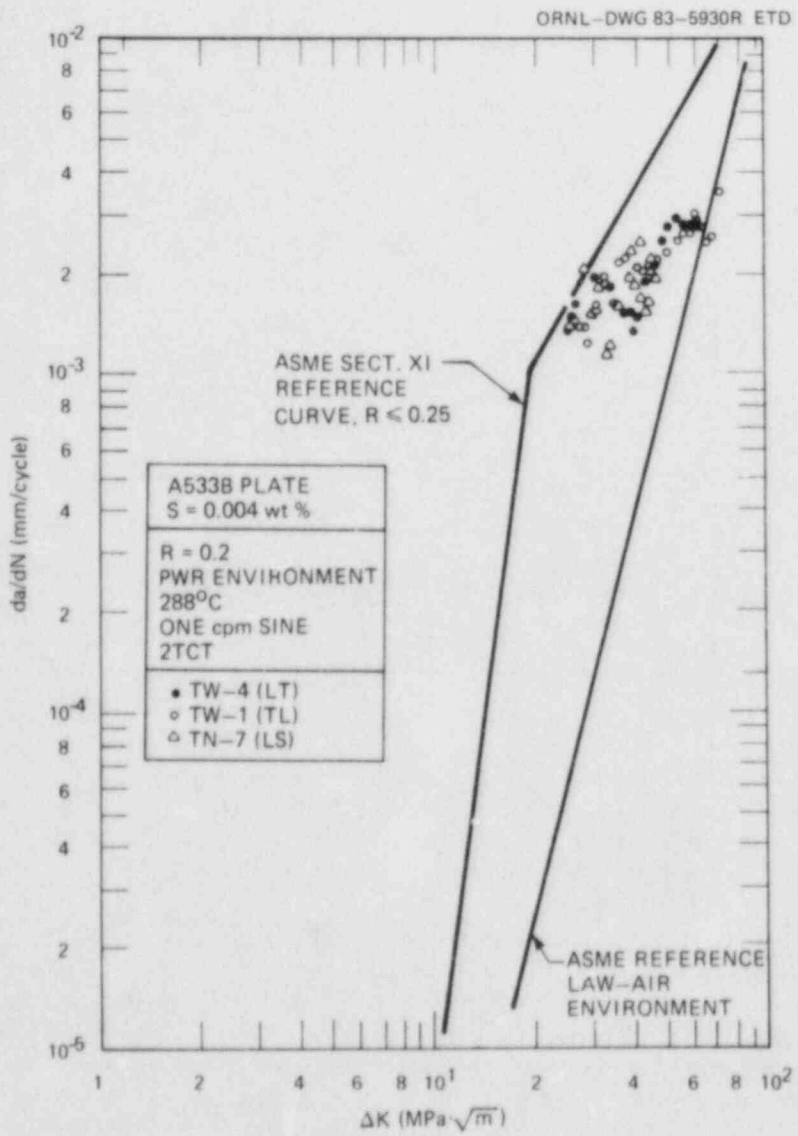

Fig. 4.6. Effects of specimen orientation on fatigue crack-growth rates for low-sulfur heat of A533B steel tested in PWR environment at R = 0.2.

4.3 Static-Load Testing

This program has included characterization of static-load crack extension behavior of pressure vessel steels and welds since 1974. The specimens are WOL type, 2.54 cm thick, and loaded to a fixed displacement by a bolt of the same material. The specimens are positioned in the bottom of two of the operating corrosion fatigue autoclaves. A recent summary of the information generated appears in Ref. 6.

Cracking under static load has been observed in all of the heat-affected-zone (HAZ) materials and in a single heat of A533B Class 1 plate. The incubation time for the HAZs has been rather short in many cases, around 2000 h, but for the plate material, the time to first cracking exceeded 37,000 h in the environment. No cracking has occurred in the welds or forging material as yet, after over 75,000 h, of which over 51,000 h have been in the environment. Table 4.2 shows the status of all specimens tested to date.

Table 4.2. Status of bolt-loaded specimens in simulated PWR environment (August 1, 1984)

Material	Specimen	Applied stress-intensity factor ($MPa\cdot\sqrt{m}$)	Total time loaded (h)	Time in environment (h)
A533 class 1 plate (HSST plate 4)	04A-114	90	74,098	48,994
	04A-116	88	74,098	48,994
A508 class 2 forging	F-13	110	75,118	51,430
	F-14	99	75,118	52,638
	F-15	88	75,118	52,638
Linde 124 weld	C-13	110	75,118	52,638
	C-14	99	75,118	52,638
Linde 124 weld HAZ	CQ-1-HAZ[a]	110	28,708 (1,816)[b]	14,394 (1,262)[b]
	CQ-2-HAZ	99	28,708	14,394
	CQ-3-HAZ	88	29,136 (3,360)[b]	12,274 (2,616)[b]
Linde 0091 weld HAZ	D-7HAZ	99	27,980	23,120
	D-8HAZ[c]	88	27,980 (7,196)[b]	10,368 (4,160)[b]
	D-9HAZ	77	27,980	23,120
Linde 124 weld HAZ	K-3HAZ	66	4,320 (4,320)[b]	4,138 (4,138)[b]
	K-4HAZ	77	4,320 (4,320)[b]	4,138 (4,138)[b]
	K-5HAZ	88	4,320 (4,320)[b]	4,138 (4,138)[b]
Linde 0091 weld HAZ	DD-3HAZ	66	5,760 (5,760)[b]	5,280 (5,280)[b]
	DD-4HAZ[a]	77	5,760 (5,760)[b]	5,280 (5,280)[b]
	DD-5HAZ	88	5,760 (5,760)[b]	5,280 (5,280)[b]

[a] Removed from testing.

[b] Hours at first observed crack extension.

[c] Extension since last report.

A total of 25 specimens have undergone testing in the environment, including specimens from A533B Class 1, A508 Class 2, and welds and HAZs made with Linde 80, Linde 124, and Linde 0091 fluxes. Fifteen specimens remain in testing. Specimen preparation and test techniques were summarized in the last progress report.[3]

Two new HAZ materials (the last two listed in Table 4.2) were added during the previous report period, and some cracking has occurred during this report period. In conjunction with these tests, fatigue crack-growth rate tests are also being performed (see Table 4.3). Figures 4.7 and 4.8 show results from two specimens of heat DD, which were tested during this report period. This heat behaves in a predictable fashion at both a high and a low R ratio, because plateaus in crack growth occur. Those plateaus have been found in other materials which have exhibited static-load cracking and could be viewed as an indicator of this sensitivity. Other materials have not shown this plateau behavior, as demonstrated by materials already discussed in this report (e.g., heats W7 and CQ2). The relation between crack-growth behavior and static-load crack growth has been discussed more extensively in Ref. 6. Note that heat DD displayed the most accelerated crack-growth rates yet observed in the high R ratio test shown in Fig. 4.8. More tests of this material and heat KH will be carried out during the next report period.

Table 4.3. Fatigue crack-growth rate testing to complement static-load tests

Test material	R = 0.2		R = 0.7	
	Frequency (cpm)	Specimen	Frequency (cpm)	Specimen
Linde 124 weld HAZ material "C"	1	C-24-HAZ-1	1	C-23-HAZ-1
Linde 124 weld HAZ material "CQ"	1	CQ-1 HAZ	1	CQ-2 HAZ
			5	CQ-3 HAZ
Linde 80 weld HAZ material "C"	1	C-3 HAZ	1	C-4 HAZ
A533B plate "04"	1	2D 3Q-6	1	02GB-2
	1	2D 3Q-5	1	2D1Q-2
Linde 0091 weld material "D"	1	D-1 HAZ	1	D-2 HAZ
			1	D-4 HAZ
			1	D-6 HAZ
Linde 124 weld material "KH"	Test results not yet available			
Linde 0091 weld material "DD"	1	DD-1 HAZ	1	DD-2 HAZ

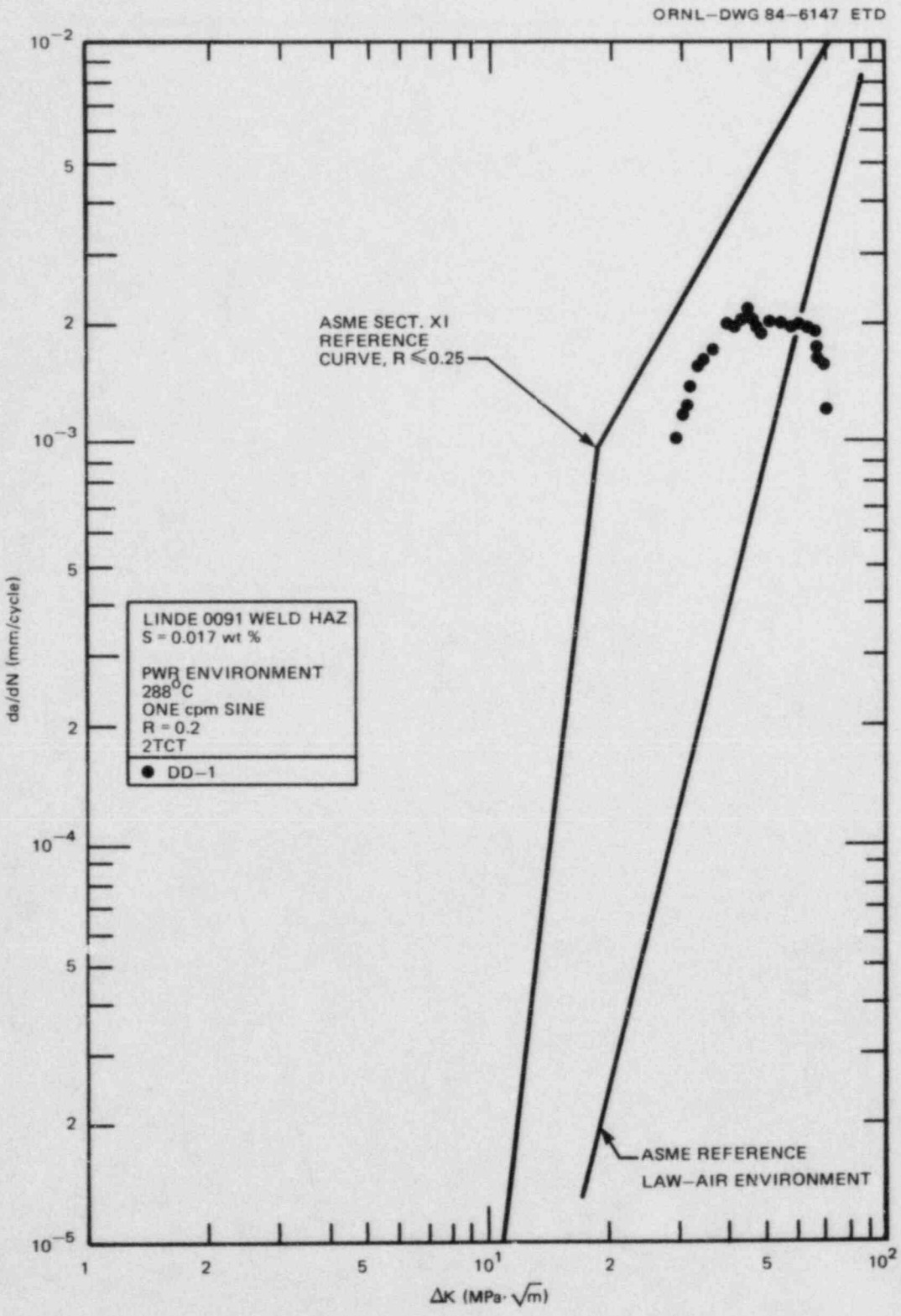

Fig. 4.7. Fatigue crack-growth behavior of specimen DD-1HAZ at R = 0.2.

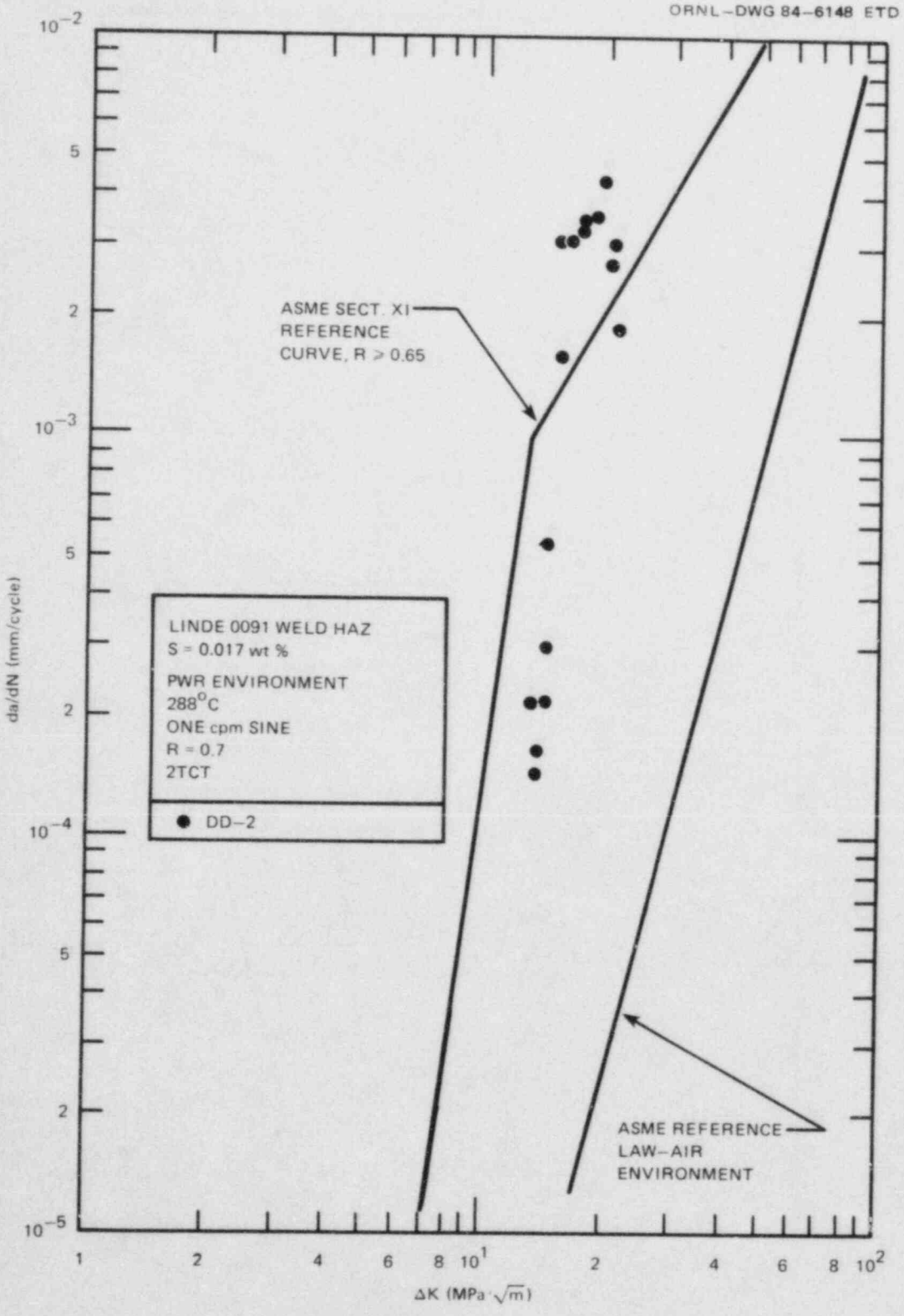

Fig. 4.8. Fatigue crack-growth behavior of specimen DD-2HAZ at R = 0.7.

4.4 Fractographic Examination of Specimen Fracture Surfaces

The scanning electron microscope (SEM) has been used to examine the fractures from the fatigue- and bolt-loaded specimens. Before examination, specimens were cleaned of corrosion product using an electrolytic technique involving scrubbing with cathodic hydrogen. The oxide removal was facilitated further by conducting the electrolytic cleaning in an ultrasonic cleaning apparatus.

During this report period, the fracture surfaces were studied. A more detailed investigation of microscopic details related to crack growth rates is to follow. Sulfur printing of the specimens is currently in progress. The specimens investigated were:

1. specimens from the study of frequency and temperature effects on high-sulfur steel (Table 4.1),
2. specimens from low-sulfur material characterization (Fig. 4.5), and
3. specimens from static-load tests (Table 4.2) and fatigue crack-growth tests to complement static-load tests (Table 4.3).

All fatigue specimens were investigated at 1.27 mm from one edge. The bolt-loaded specimens were investigated down the center.

4.4.1 High-sulfur material fractography

Specimens CQ2-9 and CQ2-12 were tested in borated water at 288 and 204°C, respectively (see Table 4.1). Both fractures were relatively smooth and exhibited ductile fatigue striations, with side cracks on most areas of the fracture (Fig. 4.9). Where the growing crack apparently intersected an inclusion [Fig. 4.9(*b*)], there was no effect on the fractography other than the local discontinuity. The test temperatures had no effect on the general fractography.

Specimens CQ2-6 and CQ2-11 were tested in water at 288°C and at 1 and 10 cycles per minute, respectively. Specimen CQ2-7 was tested at 1 cycle per minute in the same environment, but at 204°C. All three specimens exhibited a flat fracture macroscopically. Ductile striations were readily observed on specimen CQ2-6; inclusions had no effect on the fractography. Specimens CQ2-11 and CQ2-7 had a rougher texture, and no fatigue striations have yet been observed.

Specimens CQ2-7 and CQ2-12, both tested at 204°C, had a more adherent oxide that has proven more difficult to remove. This has reduced the resolution of detail on the fracture faces.

4.4.2 Low-sulfur material fractography

Specimens TW1 and W72C9 exhibited higher crack-growth rates than specimen W72C7, especially at ΔK levels approaching 20 MPa$\cdot\sqrt{m}$ (Fig. 4.5). No significant differences have been found between the fractographic details for these three specimens. All exhibit striated fatigue crack growth with side cracks and tear ridges separating the striated regions

ORNL PHOTO 5787-84

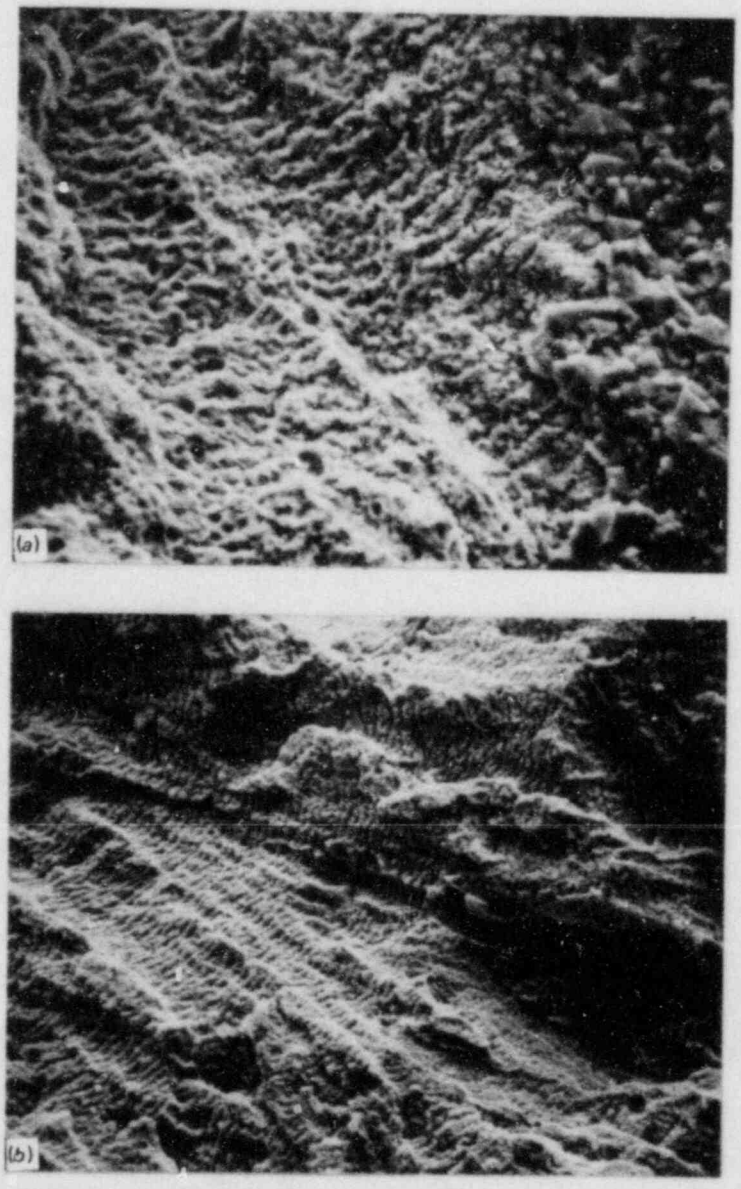

Fig. 4.9. SEM fractographs of specimen CQ2-12. (*a*) 10 mm from root of notch, 1600×; (*b*) 20 mm from root of notch, 800×.

(Fig. 4.10). The side cracking increased with increasing stress intensity. Narrow regions of ductile tearing separate the striations at the tear ridges [Fig. 4.10(*b*)].

4.4.3 Static-load and complementing fatigue specimen fractography

These specimens were from the HAZ of two weldments (Tables 4.2 and 4.3). The fatigue specimens (Table 4.3) exhibited similar fractographic details to those displayed by the base metal specimens described previously. Specimens CQ2-HAZ and DD-1HAZ, both tested at 1 cycle per minute at R = 0.2, exhibited flat fractures with ductile striations and side cracks (Fig. 4.11). No striations have been resolved on specimen DD-2HAZ tested at 1 cycle per minute at R = 0.7. Side branching is seen, [Fig. 4.12(*a*)] along with some featureless areas [Fig. 4.12(*b*)]. Some features are similar to dimples [Fig. 4.12(*c*)] but could also be corrosion pits, possibly formed after test. The fracture on this specimen started as a flat smooth surface, then moved out of plane and became rough. The reasons for this are being studied.

The bolt-loaded specimens were significantly different. Macroscopically, the cracks were rough with cracks fanning out on different planes and linking up. It has proven difficult to remove the oxide easily from specimen CQ1-HAZ, and any fine detail is not visible below the magnetite crystals. The cracking is relatively featureless at the start [Fig. 4.13(*a*)], but river marks similar to those seen on cleavage cracks are visible at greater depth [Figs. 4.13(*b*) and 4.13(*c*)]. An attempt to remove the remaining oxide, without causing significant degradation of the underlying fracture, is being made.

Specimen DD-4HAZ, tested under the same conditions as CQ2-HAZ, exhibits significantly different fractography. Figure 4.14(*a*) shows the end of the fatigue precrack and the branching at the start of the crack whose fracture morphology is not obvious at this point. However, within 5 mm the cracking is obviously integranular [Fig. 4.14(*b*)]. The duplex grain size of this specimen is readily apparent in Fig. 4.15. In Fig. 4.15(*b*), some small regions of transgranular cracking can be seen and the transgraularity becomes more evident at longer crack lengths. Figures 4.16 and 4.17(*a*) can be compared with the river pattern, cleavagelike appearance seen on specimen CQ2-HAZ; however, a significant amount of intergranular cracking is still present [Fig. 4.17(*b*)].

4.5 Characterization of Test Environments Through Free Corrosion Potential Measurements

The objective here is to monitor the environment/material interaction with time by continuous measurement of electrochemical potential. Different reference electrodes have been incorporated into the corrosion fatigue test loops: an external silver/silver chloride (Ag/AgCl) reference electrode and two palladium/hydride (Pd/H) reference electrodes. One Pd/H reference electrode has been placed in the corrosion fatigue chamber. The current approach and experimental arrangement were discussed in the last progress report.[3] The electrode chamber presently

ORNL PHOTO 5788-84

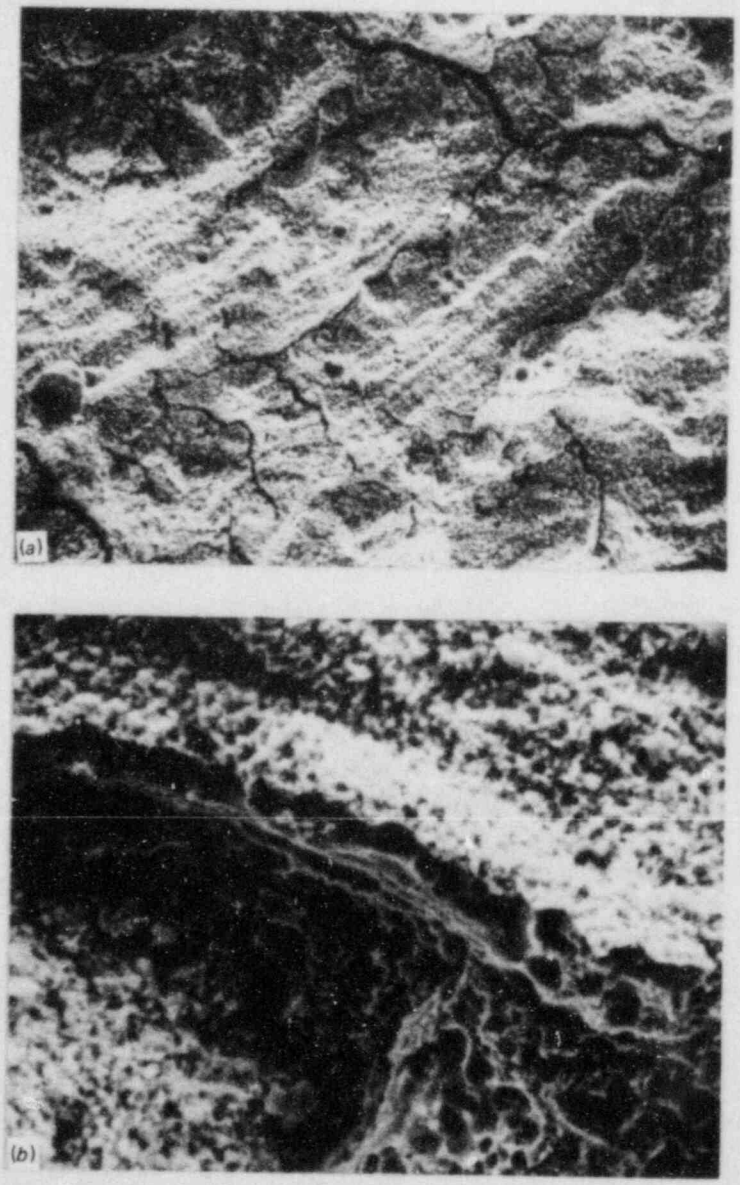

Fig. 4.10. SEM fractographs of specimen W72-C9. Similar fractography was observed on W72-C7 and TW1. (*a*) 400×, (*b*) 1600×.

ORNL PHOTO 5789-84

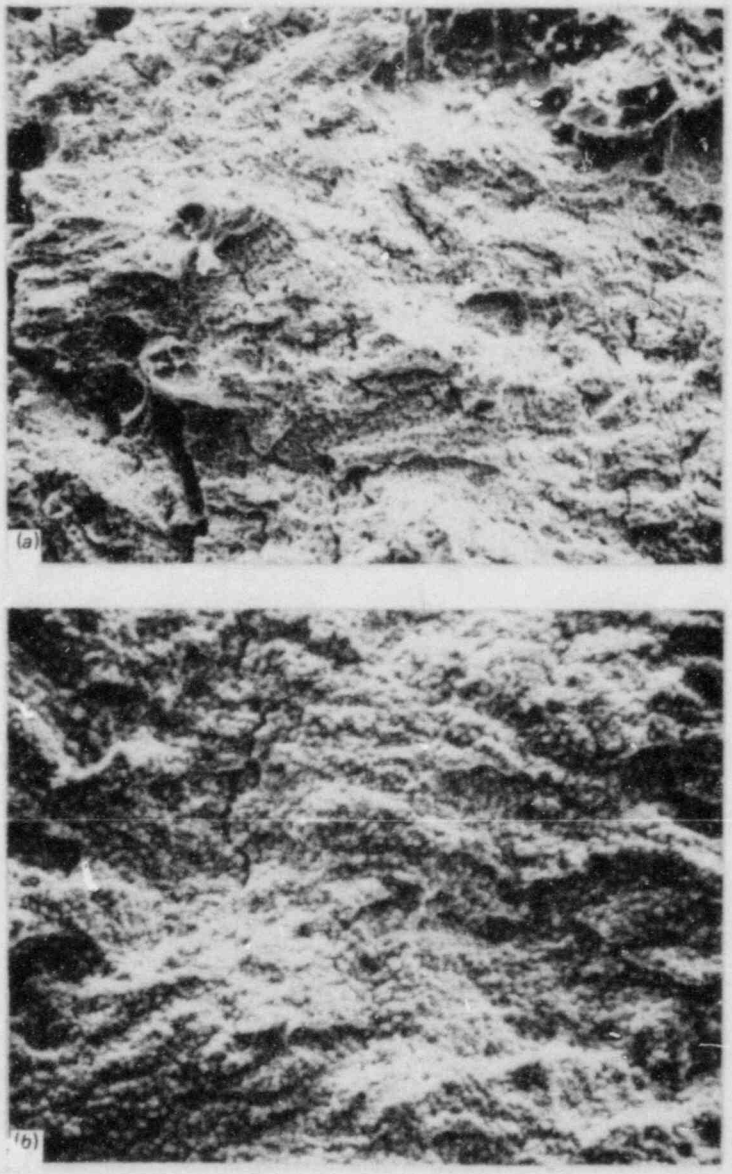

Fig. 4.11. SEM fractographs of (*a*) CQ-2-HAZ at 20 mm and (*b*) DD-1HAZ at 10 mm from root of notch. 800×

ORNL PHOTO 5790-84

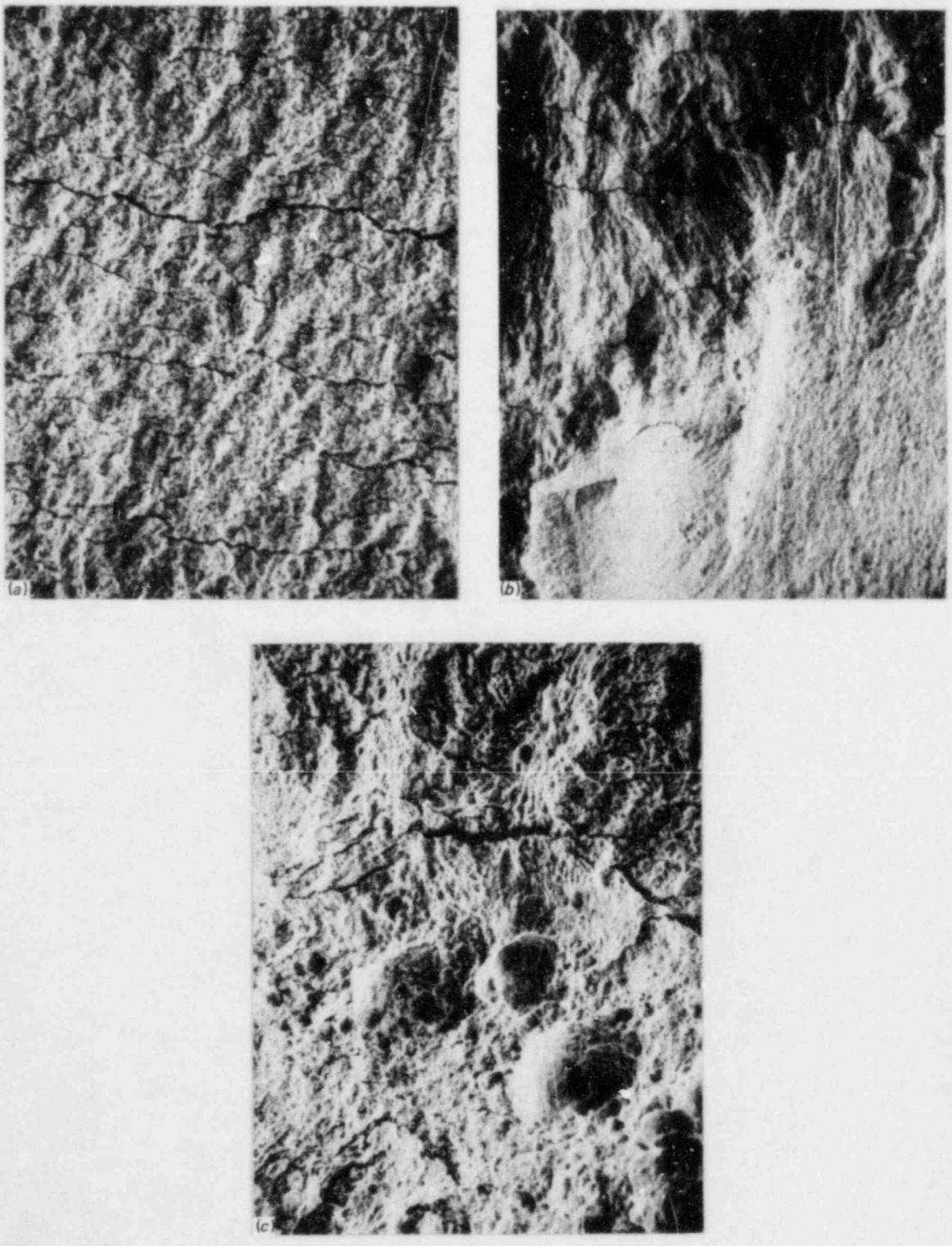

Fig. 4.12. SEM fractographs of specimen DD-2HAZ. (*a*) 400×, (*b*) 40×, and (*c*) 400× at 15 mm from root of notch.

ORNL PHOTO 5791-84

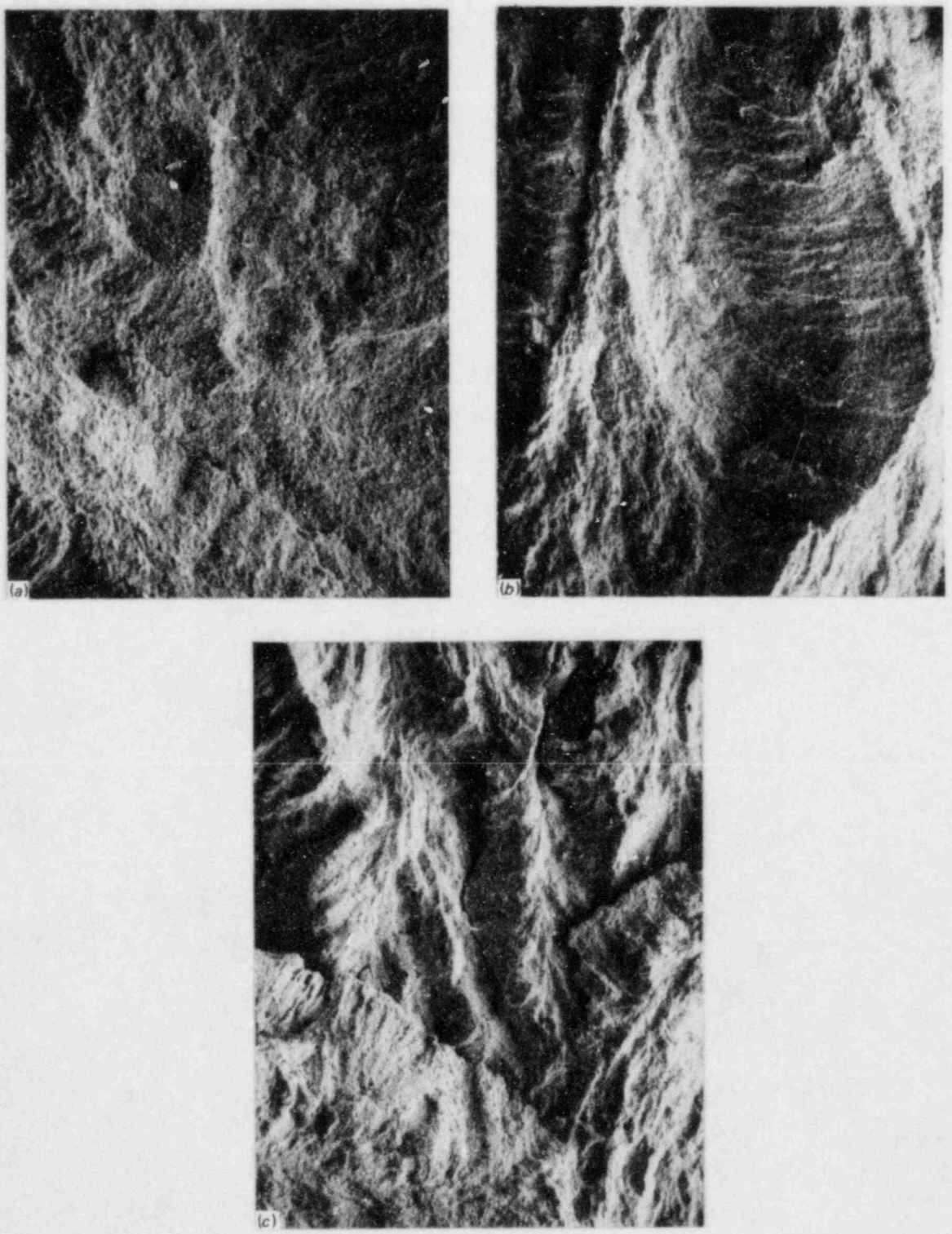

Fig. 4.13. SEM fractographs of bolt-loaded specimen CQ-1-HAZ. (*a*) 20 mm (160×), (*b*) 25 mm (80×), and (*c*) 25 mm (80×) from root of notch.

ORNL PHOTO 5792-84

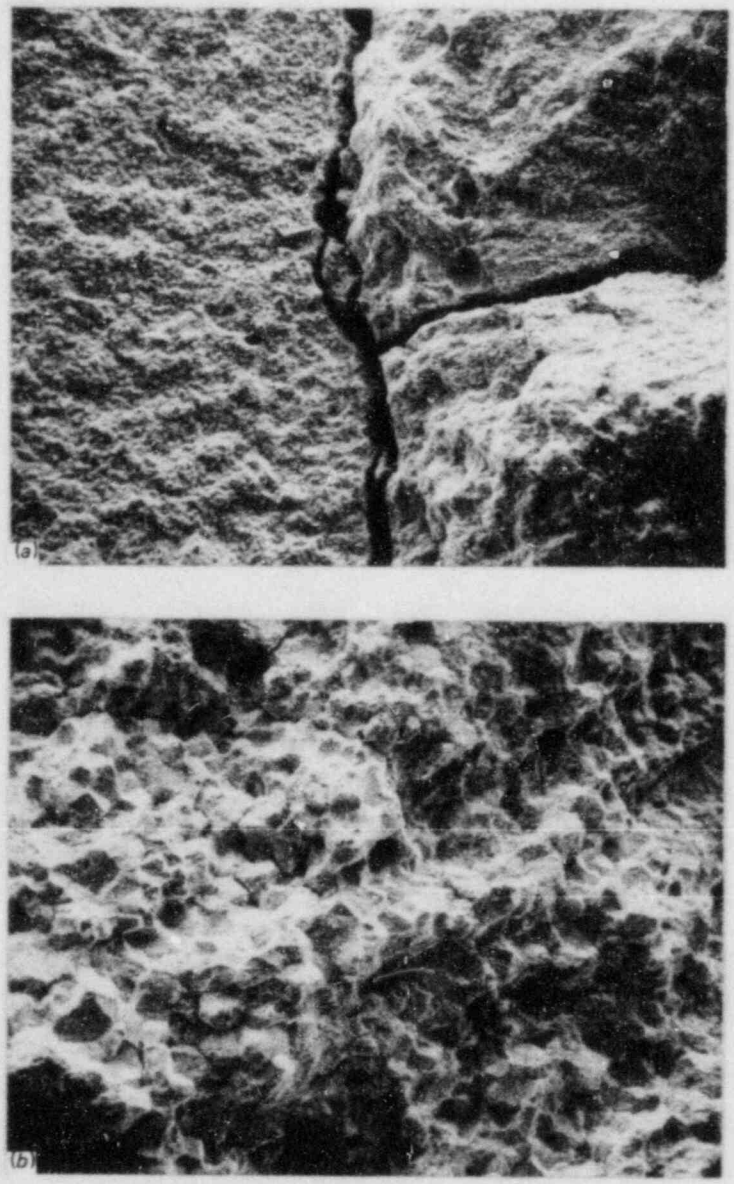

Fig. 4.14. SEM fractographs of specimen DD-4HAZ. (*a*) End of pre-crack and start of SCC at 5 mm below root of notch (160×); and (*b*) SCC at 10 mm below root of notch (80×).

ORNL PHOTO 5793-84

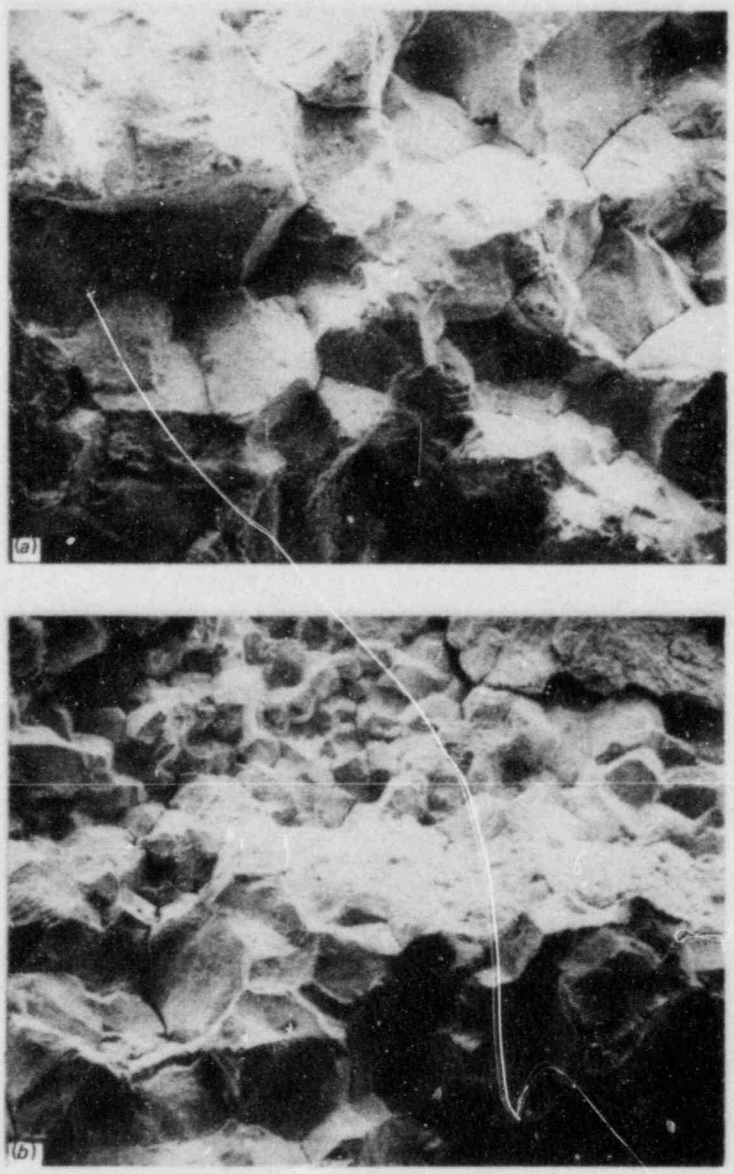

Fig. 4.15. SEM fractograph. of specimen DD-4HAZ at 10 mm below root of notch. 80×

ORNL PHOTO 5794-84

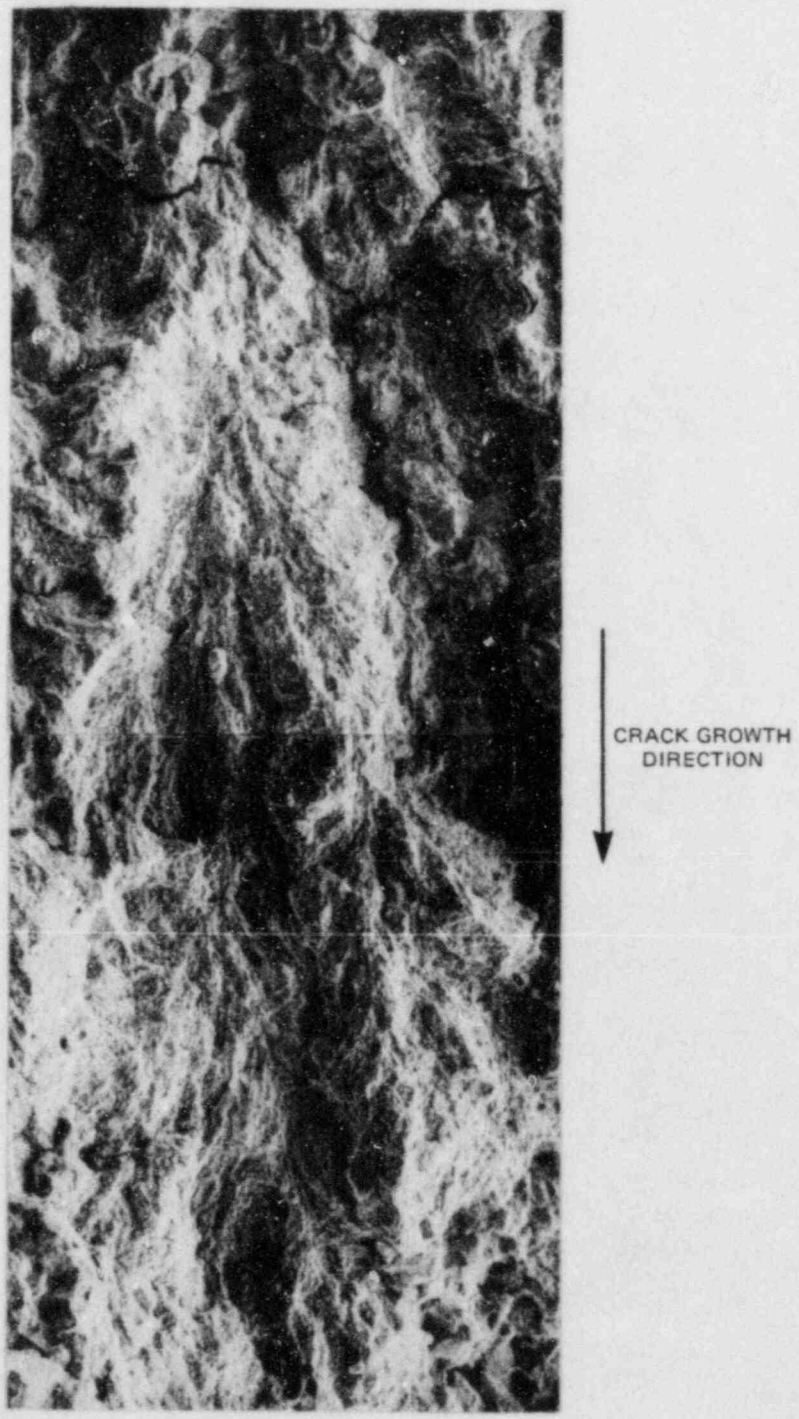

Fig. 4.16. SEM fractograph of specimen DD-4HAZ at 19 mm below root of notch. 160×

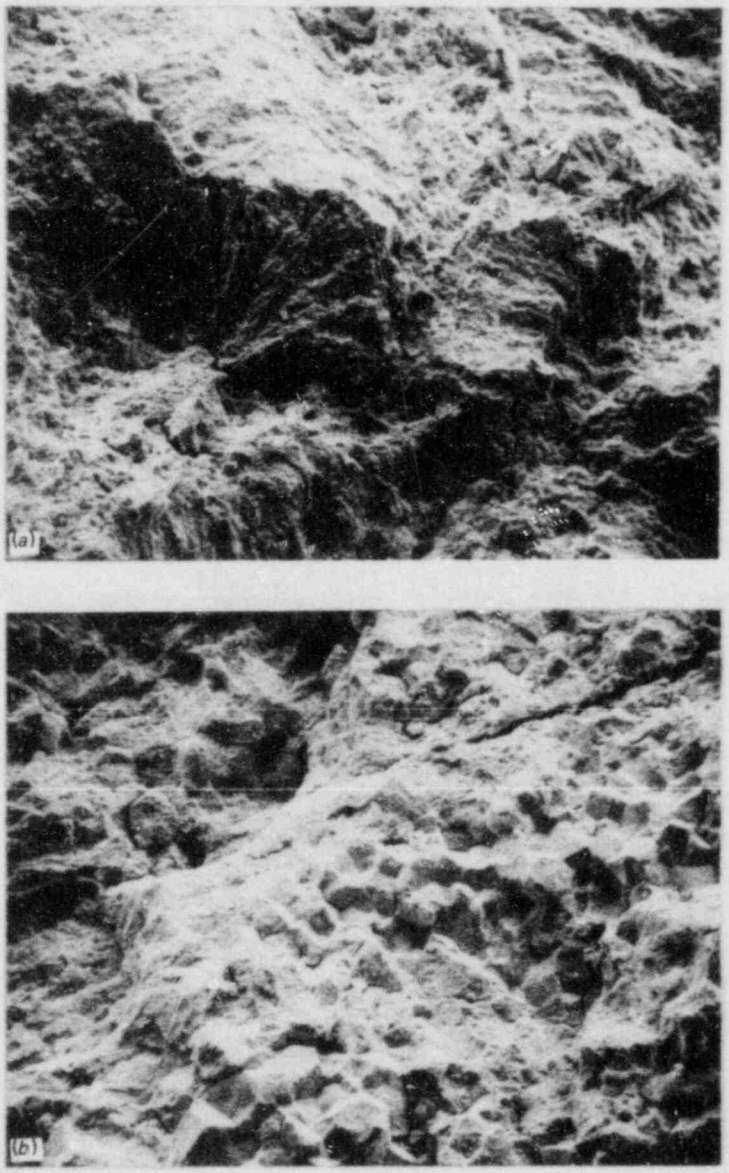

Fig. 4.17. SEM fractographs of specimen DD-4HAZ at 20 mm below root of notch. 160×

contains an Ag/AgCl reference electrode, a Pd/H reference electrode, an A508 steel sample, a thermocouple, and a platinum (Pt) counter electrode.

Two experiments were conducted during this reporting period. The first experiment was a confirmation test of the electrodes in a high-temperature environment containing deionized water with a 138-kPa hydrogen overpressure on the room temperature makeup tank. Lithium hydroxide (LiOH) additions were made to the test solution to adjust the room temperature pH to 9.0. The free corrosion potential of the A508 coupons was measured vs the Pd/H and Ag/AgCl reference electrodes in the test chamber. During the second experiment, a corrosion fatigue crack-growth test was conducted on test specimen CQ2-8 in a solution with the same water chemistry, which is typical of the other tests conducted in this program in nonborated water.

The potential measurements that were conducted for the first test are shown in Fig. 4.18. The potential readings listed are uncorrected. The equilibrium potential of the 0.01 M potassium chloride (KCl) Ag/AgCl reference electrode is 25 mV with respect to the standard hydrogen potential at temperature. The Pd/H reference electrodes behave as reversible hydrogen electrodes at temperatures which are in equilibrium with the test solution of that high-temperature pH. Calculations of the high-temperature pH of this test solution indicate that the pH is 6.33 at 288°C and 6.25 at 275°C. The reference electrodes appeared to operate satisfactorily during the initial 4 weeks of the test. However, careful examination of the figure shows that the two Pd/H reference electrodes did

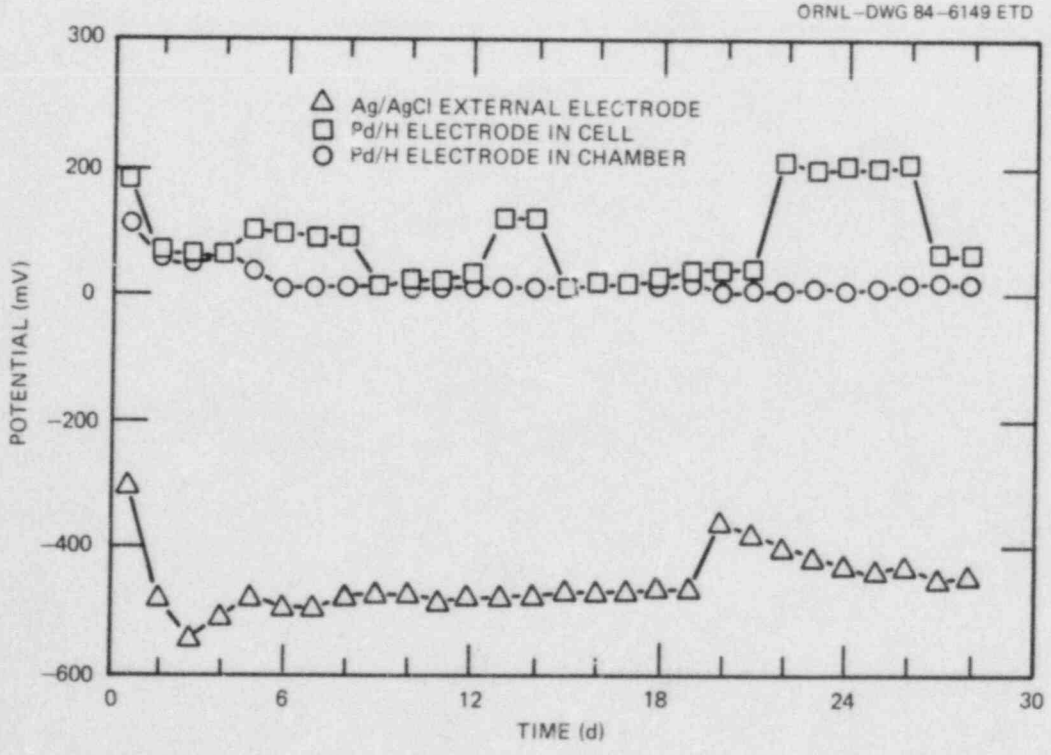

Fig. 4.18. Summary of potential readings from experiment No. 1.

not behave in an identical manner during the exposure. The Pd/H reference electrode, which was in the monitoring cell in the effluent line, would become depleted in H_2 more rapidly than the Pd/H reference electrode in the chamber. When the hydrogen pressure inside the reference electrode was recharged, the measured potential quickly dropped ~100 mV. The reference electrode in the fatigue chamber measured the corrosion potential of the static compact tension (CT) specimen that was in the fatigue chamber. Note that this test specimen in the stand is galvanically coupled to the grips and the test chamber. The area of the specimen is small with respect to the total area exposed to the high-temperature solution. Therefore, the specimen potential response is more determined by the test chamber and the grips than the A508 test specimen.

The most consistent readings during this interval were made using the Ag/AgCl reference electrode in the effluent line measuring cell. The readings were stable and appeared to predict changes in the solution chemistry during the exposure. Note the decay of the corrosion potential during the first 4 d of the experiment shown in Fig. 4.18. This decrease was attributed to two separate factors: the slow increase in temperature from 149 to 288°C and the consumption of dissolved oxygen in the system. The system had reached a stable test temperature of 288°C by 5 d, and the corrosion potential maintained a stable value of ~−480 mV for the next 14 d. After 19 d, the test solution reservoir was refilled with fresh makeup solution and the potential of the A508 increased by +120 mV. This increase in potential was attributed to a higher level of dissolved oxygen in the makeup water. This potential slowly approached the previous steady state value of −480 as the oxygen inventory of the system was reduced.

Significant findings for this set of potential readings include:

1. The external Ag/AgCl reference electrode was judged the most reliable of the three reference electrodes in the chamber. The readings were reliable and consistent with the operation of the test system.
2. The potential of the CT specimen in the test chamber may be compromised by the galvanic coupling with the test chamber. Possible ground loops between the CT specimen and the loading part of the fatigue system could also influence the readings. In future experiments, an electrically isolated coupon of A508 will be included so that the uncoupled potential of the CT specimen can be recorded.

Electrochemical potential measurements were made during the corrosion fatigue experiment for specimen CQ2-8. The data are shown in Fig. 4.19. The trends are comparable to those reported during the previous experiment. There appeared to be a slight difference between the potential measured by the Pd/H reference electrode and the electrically isolated steel coupon in the fatigue chamber and the Pd/H and steel samples in the monitor cell in the effluent line. As the experiment continued, the two potential readings appeared to converge. The potential readings given by the Ag/AgCl electrodes were stable. Note that this experiment was interrupted at 5860 cycles for ~10 weeks because of equipment malfunctions. During this interval the system was cooled to room temperature until restarted. During this 10-week interval, the Ag/AgCl

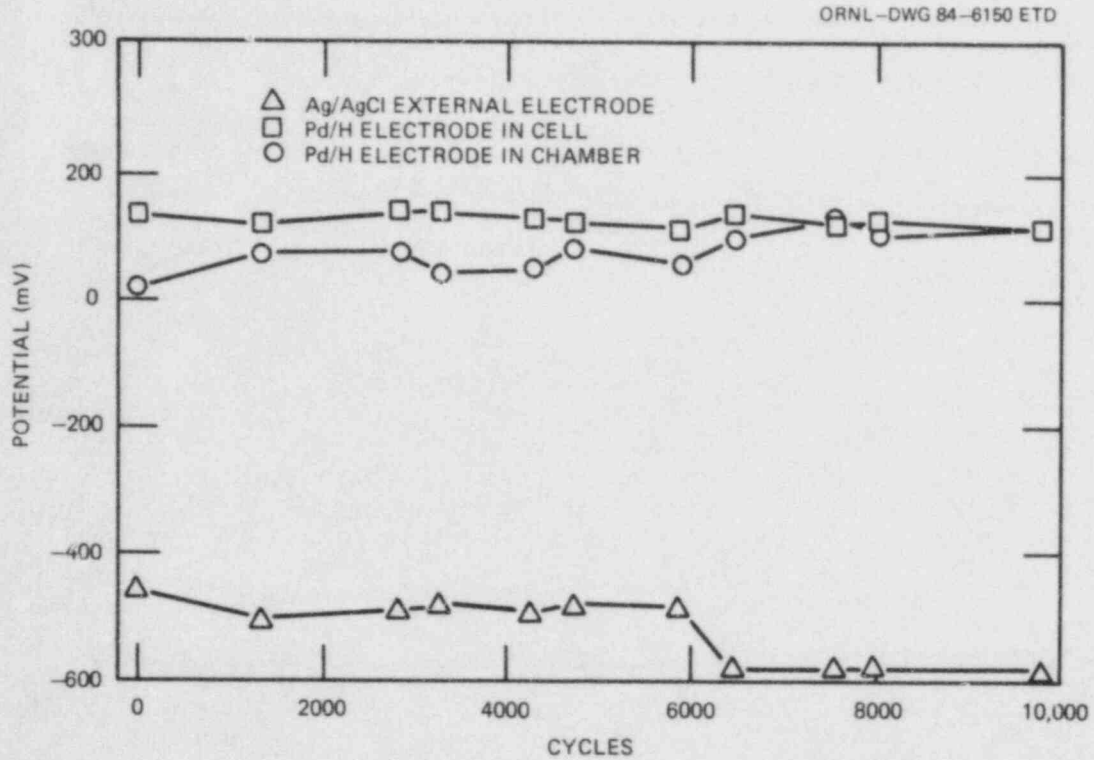

Fig. 4.19. Summary of potential readings observed during testing of CQ2-8.

reference electrode remained in the effluent cell. When the test was restarted, the corrosion potential measurements were ~80 mV more active than before. When the experiment was over, the electrode was calibrated against a commercial standard. The posttest calibration indicated that the equilibrium potential of the Ag/AgCl reference electrode was +200 mV, which can be correlated with an internal chloride concentration of 0.001 M KCl, showing that the electrolyte had become somewhat diluted. Presumably, a large portion of this shift in potential occurred during the system pressure changes from high pressure to ambient and the 10-week exposure to the dilute test environment during shutdown.

This series of potential readings demonstrated the usefulness and feasibility of measuring corrosion potential during actual corrosion fatigue experiments. The importance of pretest and posttest calibration of the reference electrodes vs a commercial standard was also emphasized. Additionally, the Ag/AgCl reference electrode should be removed from the test solution if downtimes in excess of a few days are anticipated. Properly maintained, the Ag/AgCl electrode appears to be a more sensitive monitor of the environment than the others.

In an effort to optimize the Ag/AgCl electrode performance, impedance tests have been performed to optimize the zirconia plug that acts as an ion exchange barrier between the test environment and the dilute KCl internal electrolyte. Alternating current impedance studies have been performed on several batches of porous zirconia that were purchased

and other lots that were fabricated using parameters identified by Andresen.[7] The objective of the testing is to determine a qualification test that will index the behavior of the plug. This will be correlated with the plug stability and the long-term electrode performance. The experimental procedure for the ac impedance measurements was detailed earlier.[3]

Impedance measurements have been made on a number of zirconia plugs representing six lots of material. Initial lots of material demonstrated impedance values >1 MΩ. These high impedance values were attributed to insufficient porosity. Andresen has recommended plugs with impedance ranging from 20 kΩ to 200 kΩ give acceptable performance. Plugs from lots E and F were pressed and sintered, using Zircoa B powder and conditions specified by Andresen. These plugs had impedances greater than the recommended range. The pressing conditions and the sintering temperature will be altered to fabricate plugs that give lower impedance. Plots of impedance vs frequency are shown in Fig. 4.20. Note that several plugs from the C and D lots of zirconia gave impedances that were in the recommended range, and the plug used in the experiments reported here had a measured impedance of 115 to 120 kΩ. Initial studies indicated that plug geometry (diameter and length) and outside surface finish played an important role in determining the impedance. Several of these plugs will be fabricated into reference electrodes and evaluated during the next reporting period.

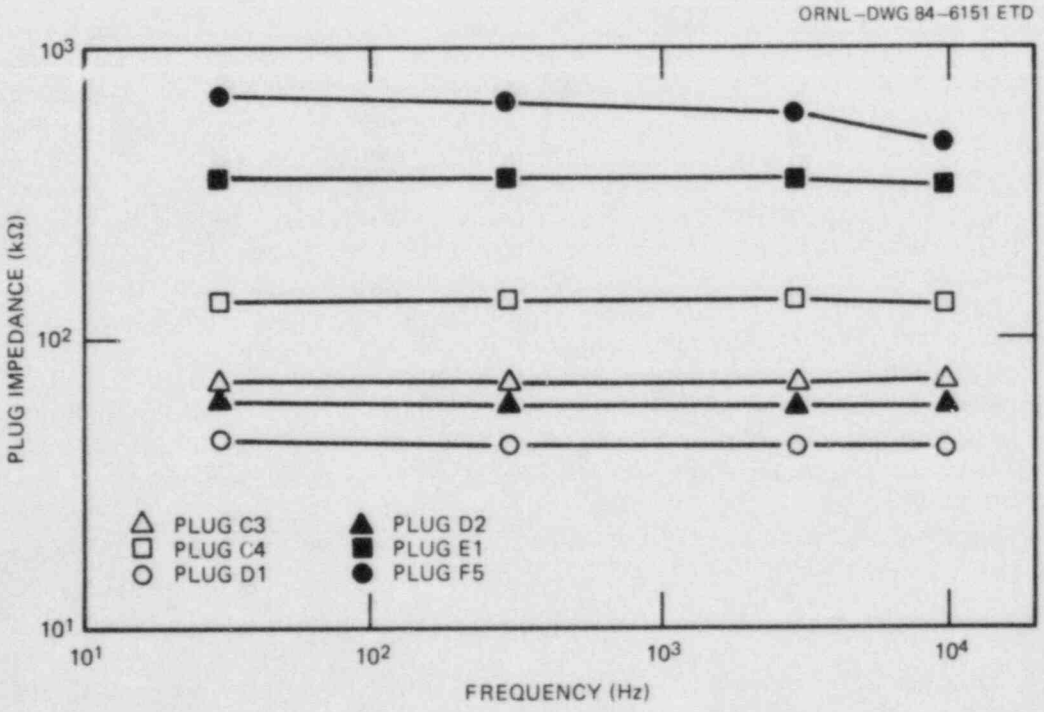

Fig. 4.20. Alternating current impedance measurements of zirconia plugs.

4.6 International Cyclic Crack-Growth Rate Group

Under this task, membership is maintained in the International Group on Cyclic Crack Growth Rate, which is an interdisciplinary group set up to share information on corrosion fatigue. The background of this group was included in the last progress report.[3] The status of subgroup activities is reviewed periodically in these reports. The most recent meeting was held in Daresbury, United Kingdom in May 1984. This section reviews the discussions of technical interest.

4.6.1 Test methods and results subgroup

This subgroup develops standard test methods and promotes more reliable and consistent testing by members. Group meetings also provide a forum for the exchange of recent test results.

In the area of new test results, the recent meeting resulted in a number of important conclusions. Apparently, two major parameters influence the results of the corrosion fatigue tests: (1) the chemistry and microstructure of the material and (2) the chemistry and flow rate of the water environment. Recent results have added considerable confirmation to the postulate that the sulfur content of the steel is an indicator of environmental acceleration. Evidence of this has now come from many laboratories. There is little question of this effect, because it has been confirmed by both macroscopic and microscopic observations. For materials that show environmental acceleration, there is also a clear effect of temperature, with several laboratories showing higher crack-growth rates as temperature increases from room temperature to reactor operating temperature, 288°C.

The effect of flow rate on the level of crack growth is now somewhat uncertain with some different conclusions being reported by different laboratories (in some cases, higher flow rates cause lower growth rates). The interaction with the environmental chemistry appears to be increasingly important and may eventually help explain observed differences.

To this end, extensive efforts have been undertaken to develop electrochemical potential measurement systems that are reliable. Such measurements highlight changes in chemistry that occur during a test and allow better, more reliable comparison of results from different laboratories. There have been two member surveys on this subject and many presentations. The most reliable measurement method to date is the cold Ag/AgCl electrode as described earlier in this report, although another good candidate is the Pd/A electrode. These electrodes have been found to be very accurate in characterizing environmental changes that can occur during a test. It is also very important to take complete chemical measurements of the bulk test medium both before and after testing.

4.6.2 Mechanisms subgroup

This subgroup provides mechanistically based explanations of the differences on observed fatigue crack-growth results for water environments. It now appears that the interactions between potential and pH

at the crack-tip region are fairly well understood, and the location of sulfates and other sulfur species on the Pourbaix diagram has been confirmed. The role of dissolution kinetics and the interaction with the flow rate are not yet well known, however. The mechanism of cracking, whether it be anodic dissolution or hydrogen assistance, has not been settled. There are indications that both may be acting, because some rate-determining steps and characteristics of observed growth are common to both.

4.6.3 Data collection and evaluation subgroup

This subgroup is establishing a data base of exiting corrosion fatigue data and developing reference laws. The status of the existing carbon and low alloy steel data base was reviewed. A brief report was presented on the development of reference fatigue crack-growth curves for stainless steel in both air and water environments. A series of recent results for different laboratories showed remarkable agreement. Testing is beginning on the first spectrum loading test for validation of reference crack-growth laws.

References

1. W. H. Bamford, R. Jacko, and L. J. Ceschini, "Environmentally Assisted Crack Growth in Light Water Reactors," in *Heavy-Section Steel Technology Program Quart. Prog. Rep. July–September 1983*, ORNL/TM-8787/V3 (NUREG/CR-3334, Vol. 3), Union Carbide Corp. Nuclear Div., Oak Ridge Natl. Lab., February 1984.

2. W. H. Bamford, "Environmental Cracking of Pressure Boundary Materials, and the Importance of Metallurgical Considerations," *Aspects of Fracture Mechanics in Pressure Vessel and Piping*, ASME Publication PVP-vol. 58, 209–28, 1982.

3. W. H. Bamford, R. J. Jacko, and L. J. Ceschini, "Environmentally Assisted Crack Growth Technology," in *Heavy-Section Steel Technology Program Semiannual Prog. Rep. October 1983–March 1984*, ORNL/TM-9154/V1 (NUREG/CR-3744, Vol. 1), Martin Marietta Energy Systems, Inc., Oak Ridge Natl. Lab., June 1984.

4. W. H. Bamford, "Application of Corrosion Fatigue Crack Growth Rate Data to Integrity Analyses of Nuclear Reactor Vessels," *Trans. ASME J. Eng. Mater. Technol.* 101, 182–90 (July 1979).

5. W. H. Cullen, "Characterization of Environmentally Assisted Crack Growth in LWR Materials," in *Structural Integrity of Water Reactor Pressure Boundary Components, Annual Report for 1982*, USNRC Rep. NUREG/CR-3228, April 1983.

6. W. H. Bamford, D. M. Moon, and L. J. Ceschini, "Studies of Statically and Dynamically Loaded Cracks in Simulated Pressurized Water Environment," presented paper No. 12, *Corrosion* 83, Anaheim, Calif., to be published in *Corrosion*.

7. P. L. Andresen, *Innovations in Experimental Techniques for Testing in High Temperature Aqueous Environments*, Rep. 81CRD088, General Electric Company, Schenectady, New York, May 1981.

5. CRACK ARREST TECHNOLOGY

5.1 Wide-Plate Crack-Arrest Test Definition

C. E. Pugh B. R. Bass

The Heavy-Section Steel Technology (HSST) Program plans include the performance of three series of wide-plate crack-arrest tests at the National Bureau of Standards (NBS), Gaithersburg, Maryland, in their 6 million-pound capacity tensile machine. The first series uses A533B steel in a quenched and tempered condition; the second will use low upper-shelf weldments, and the third will use A533B steel in a quenched-only condition. The first test (WP-1.1) of the first series is described below. The specimen design, specimen instrumentation, the loading sequence for a benchmark case, and a "reference analytical experiment" are described in this section, while the specimen material and properties (to the degree known) are discussed in Sects. 5.2 and 5.3 below. Several analysts were asked to perform pretest analyses of WP-1.1 according to this information; their results are given in Sect. 5.4. Finally, the work at the NBS to perform these tests is discussed in Sect. 5.5.

5.1.1 Specimen design for WP-1.1

The overall specimen design is shown in Fig. 5.1 to be a 1 m × 1 m × 0.1 m plate with a single-edge notch that gives a crack-depth to plate-width ratio (a/w) of 0.20. The notch, which is 20 cm deep, is composed of a 2.54-cm-wide gap that is machined to a depth of 18.7 cm ("X" in Fig. 5.1) and an electron-beam (EB)-weld-generated crack with a depth of 1.27 cm at the end of the gap. The sides of the specimen are side grooved to a depth equal to 12.5% of the plate thickness, and the grooves have a 0.025-cm root radius. The initial crack is perpendicular to the rolling direction. The specimen is welded to the pull-plate assembly, which is made up of two sections as shown in Fig. 5.2. The specimen and pull plates are 10.16 cm thick, and the pull tabs are 15.24 cm thick. The side grooves are 1.27 cm deep, so that the specimen is 7.62 cm thick along the crack plane.

5.1.2 WP-1.1 specimen instrumentation

The specimens are instrumented with three basic types of devices: (1) thermocouples, (2) strain gages, and (3) timing gages. In the first case, surface temperatures are measured using 11 pairs of thermocouples located as shown in Figs. 5.3 and 5.4. Thermal readings are made during the loading sequence, test, and posttest to ensure that intended thermal conditions are met. The strain gages serve two purposes. They provide (1) dynamic strain-field measurements to allow determination of crack propagation velocity and (2) far-field strain measurements for determining loading boundary conditions. The specimen is instrumented with nine pairs of single-direction strain gages and five rosettes as shown in

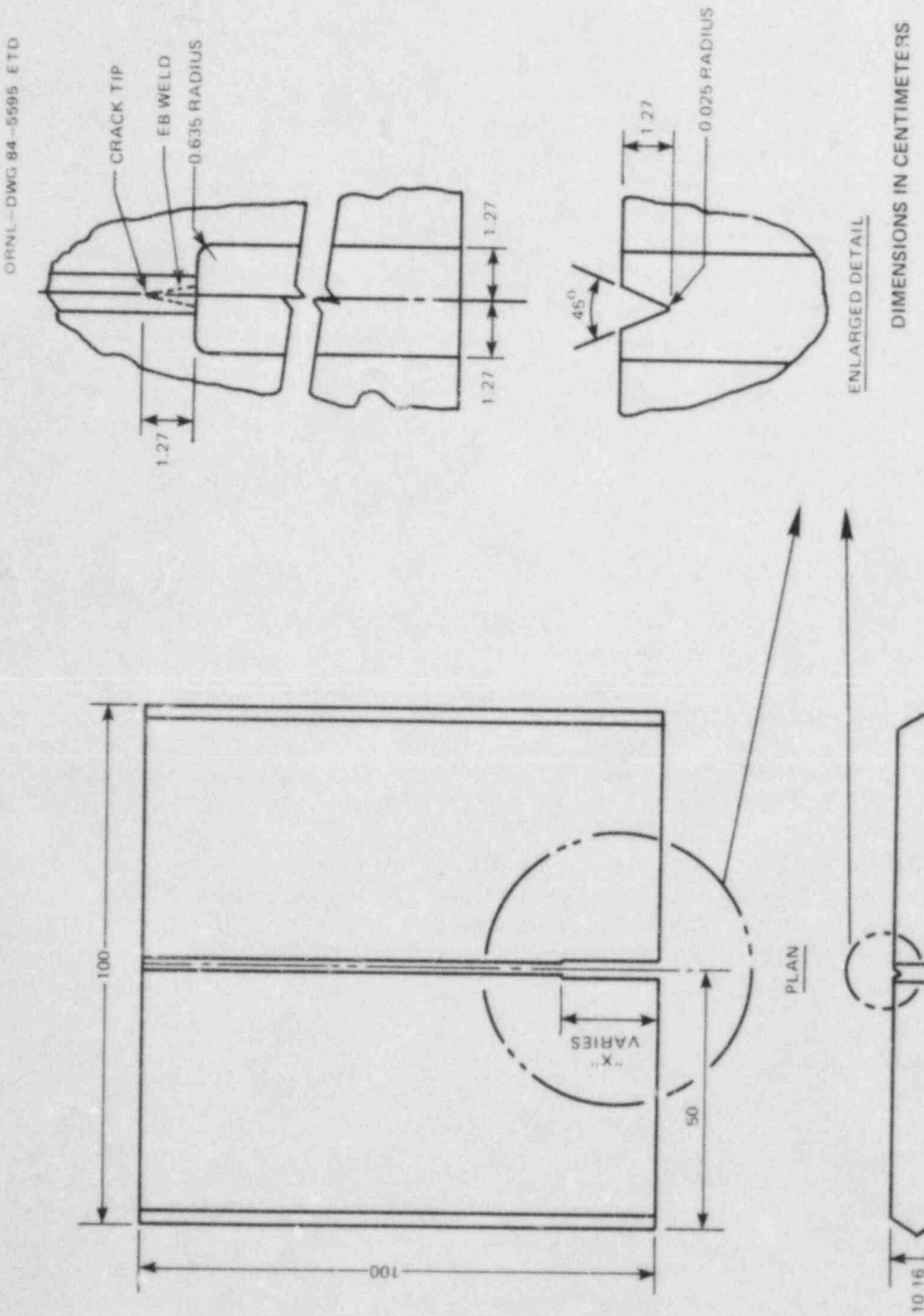

Fig. 5.1. Design of wide-plate specimen for first HSST crack-arrest experiment WP-1.1; A533 Grade B Class 1 steel in quenched and tempered condition.

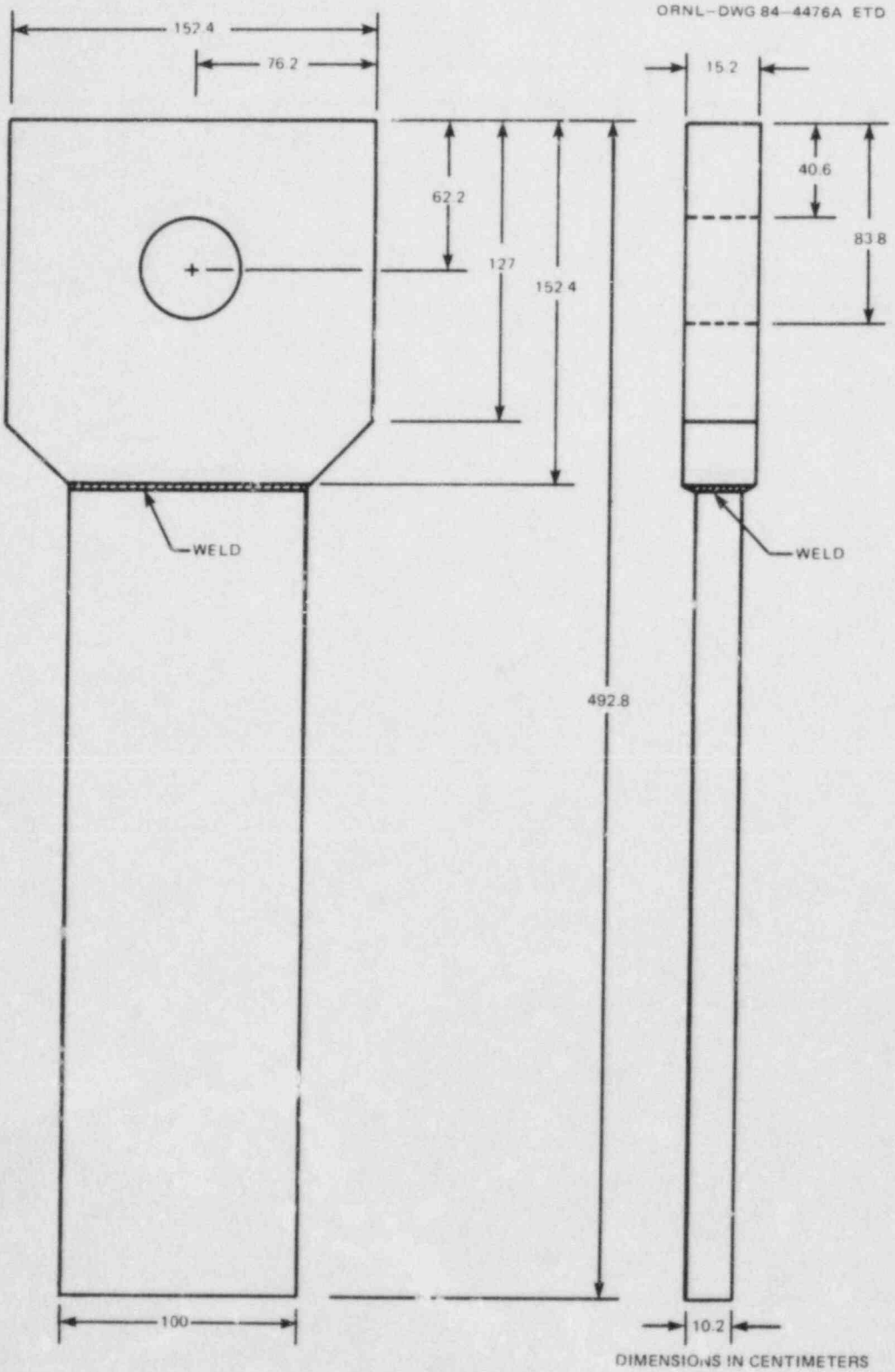

Fig. 5.2. Pull-plate assembly to be used in NBS tensile machine to perform HSST crack-arrest experiment WP-1.1.

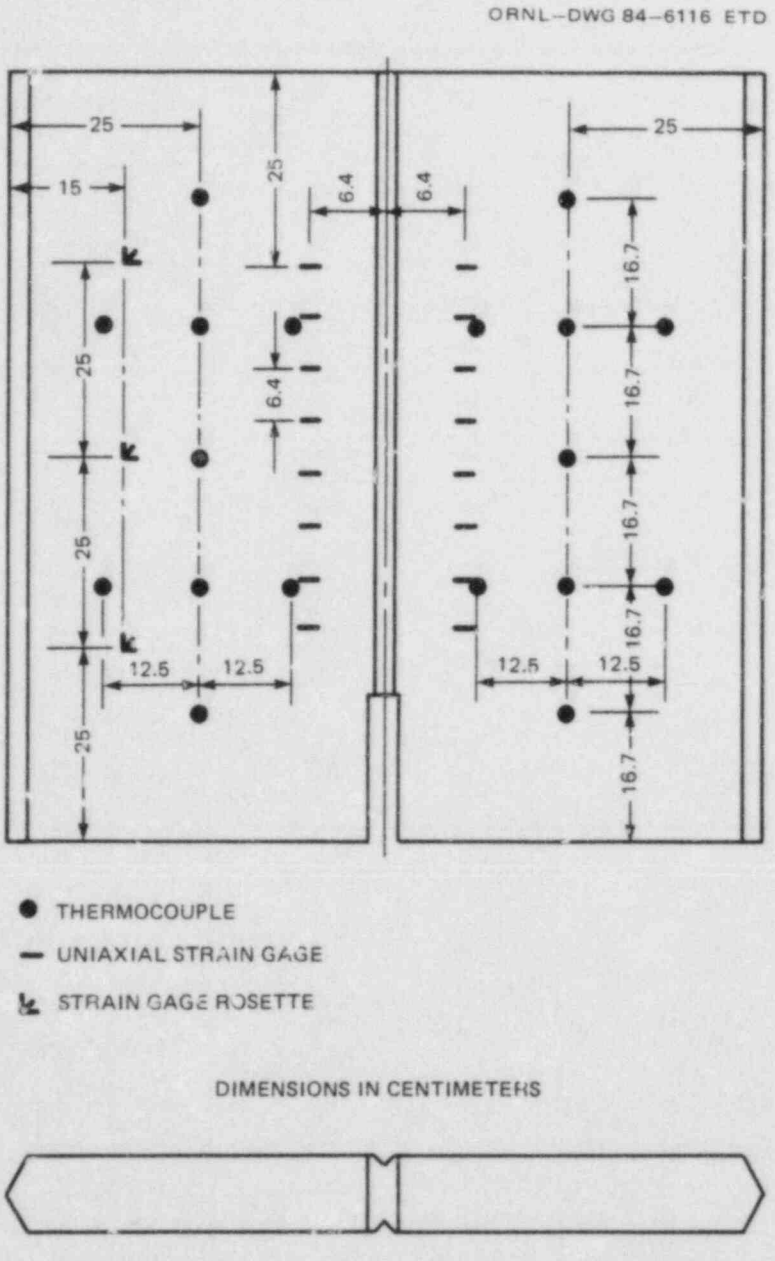

Fig. 5.3. Minimum strain gage and thermocouple placements on the wide-plate specimen to be used in first HSST wide-plate crack-arrest test WP-1.1.

Figs. 5.3 and 5.4. Finally, the side grooves are instrumented with conducting-paint grids which serve as timing gages during crack propagation. The data from the grids provide an additional measure of the crack propagation velocity. The grid lines are applied by Battelle Columbus Laboratories (BCL) (see Subsect. 5.3.2.4). All the instrumentation shown here is on one side of the specimen and pull plates. However, limited instrumentation is on the other side to check on specimen bending and through-the-thickness temperature variations.

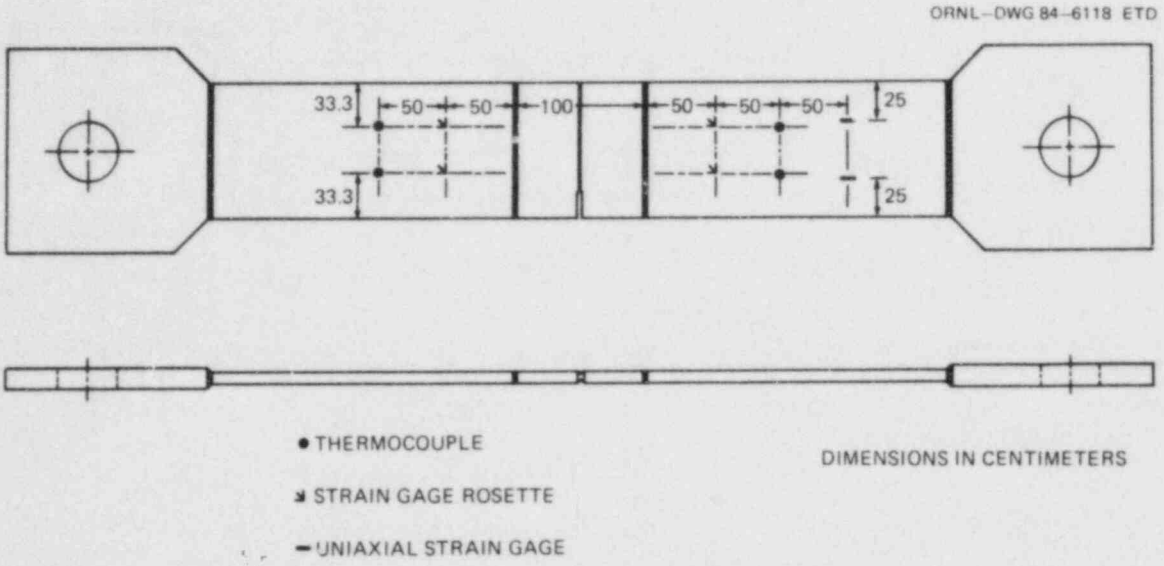

Fig. 5.4. Strain gage and thermocouple locations on pull plates in HSST wide-plate crack-arrest experiments.

5.1.3 Thermal and mechanical loading sequence for WP-1.1

One objective of WP-1.1 is to obtain crack-arrest toughness K_{Ia} data at temperatures near or above those corresponding to the onset of Charpy upper shelf. To accomplish this, the test specimen is to have a linear transverse temperature distribution with the initial crack in the cold side of the plate. Cleavage crack initiation is to occur, and the crack is to arrest in the higher-temperature ductile region of the plate. The target conditions were first defined for WP-1.1 as shown in Fig. 5.5, on the basis that static analyses suggested that arrest would occur at $a/w = 0.45$ and $K_{Ia} = 164.8$ MPa$\cdot\sqrt{m}$. Static analyses here are based on $K_{Ia} = K_I = \sigma\sqrt{\pi a}\,[\sec(\pi a/2w)]^{1/2}$. Note that the temperature distribution was selected by setting the initial crack-tip temperature equal to the estimated RT_{NDT} (−17°C) and specifying arrest to occur at $a/w = 0.45$ with $K_{Ia} = 164.8$ MPa$\cdot\sqrt{m}$. The expression used for K_{Ia} gave the temperature at the arrest point (39.5°C), and it was based on adjusting the expression used for the PTSE-1 material[1] according to the RT_{NDT} of the respective materials. That expression is given below, along with a corresponding K_{Ic} correlation,

$$K_{Ia} = 35.0 + 33.279\ \text{EXP}\ [0.02408\ (T - RT_{NDT})]\ \text{MPa}\cdot\sqrt{m}\ (T\ \text{in}\ °C)\ , \quad (5.1)$$

$$K_{Ic} = 51.276 + 51.897\ \text{EXP}\ [0.036\ (T - RT_{NDT})]\ \text{MPa}\cdot\sqrt{m}\ (T\ \text{in}\ °C)\ . \quad (5.2)$$

Using the static expression given above, the load required for these conditions is 10.64 MN.

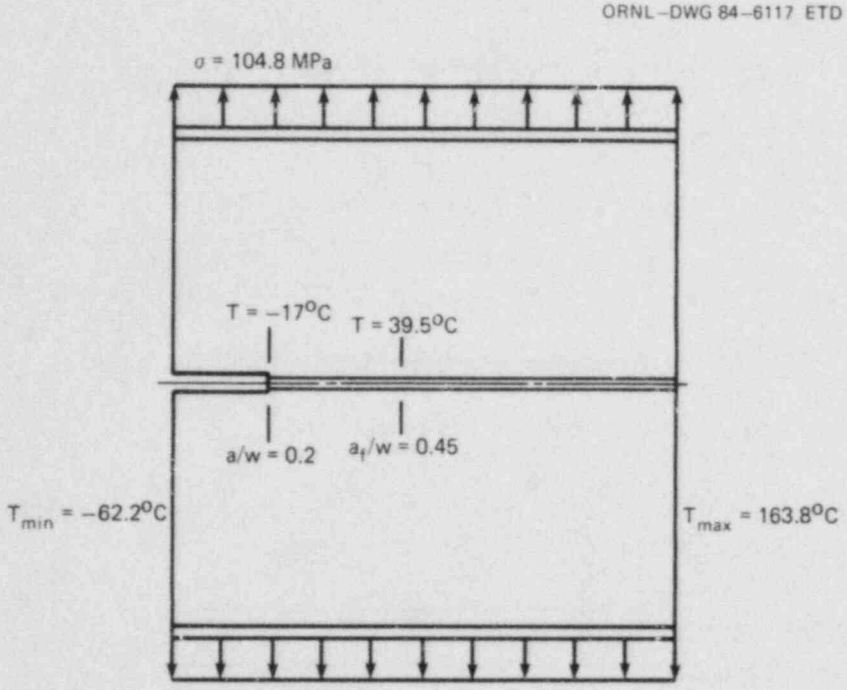

Fig. 5.5. Thermal and mechanical loading conditions tentatively defined for first HSST wide-plate crack-arrest test WP-1.1.

The stress-intensity factor K_0 for the initial crack (a/w = 0.20) when test load equals 10.64 MN is 131 MPa$\cdot\sqrt{m}$. This single-edge-notch value exceeds K_{Ic} for the crack-tip temperature of −17°C. Specifically, Eq. (5.2) gives, at T = −17°C, K_{Ic} = 103.2 MPa$\cdot\sqrt{m}$. To permit the specimen to support this high initial load, the region around the crack tip is warm prestressed (WPS) by application of the test load at a relatively high temperature prior to the test. Accordingly, the entire thermal and mechanical loading sequence is described below:

Step 1. Place specimen assembly into the test machine.
Step 2. Heat the specimen so that the crack-tip temperature (T_{WPS}) is slightly higher than the static-arrest temperature; for WP-1.1, T_{WPS} = 50°C.
Step 3. Apply 100% of the test load and hold for a period of time; for WP-1.1, P_1 = 10.64 MN.
Step 4. Reduce the load by 15%; for WP-1.1, P_2 = 9.04 MN.
Step 5. Very slowly, apply the temperature gradient while under load P_2; for WP-1.1, T_{min} = −62.2°C and T_{max} = 163.8°C.
Step 6. Increase the load from P_2 to P_1 or to the point of crack initiation.

Note that Steps 2 through 5 should warm prestress the region near the crack tip so that initiation does not occur until a load near P_1 is reached.

5.1.4 Benchmark analytical experiment

Several investigators were asked to analyze the common problem given here for benchmark purposes. The specimen was as defined in Subsect. 5.1.1, the loading was described in Subsect. 5.1.3, and the properties were then given by Eqs. (5.1) and (5.2):

Yield strength	434 MPa
Ultimate tensile strength	586 MPa
NDT	−28.8°C
RT_{NDT}	−17°C
Specific gravity	7.86
Coefficient instantaneous thermal experiment	11×10^{-6}/°C

The analytical boundary conditions were those shown in Fig. 5.6. Because of symmetry about the crack plane, only one-half of the plate is modeled. The lower boundary ahead of the crack tip was fixed with roller boundary conditions (zero y-displacement, no restraint in the x-displacement). The side boundaries of the plate are stress free, and the linear temperature distribution across the plate is maintained. The plate is free of thermal stress, and all surfaces other than the left and right edges are assumed to be insulated. After application of the static load (P_1), the top surface is fixed against y-displacement for the dynamic analysis.

Since the pretest analyses include dynamic considerations, a dynamic fracture-toughness relation was taken from Ref. 2 by estimating that the RT_{NDT} for the material in that study was −6.1°C (21°F) and is written as

$$K = K_{Ia} + A\,(\dot{a})^2 \ , \tag{5.3}$$

where K_{Ia} is given above, and for temperatures above (RT_{NDT} − 14°C),

$$A = \left\{ 32.97 + 1.625\,[T - RT_{NDT}] \right\} \times 10^{-5}\ \frac{MPa\cdot\sqrt{m}}{m^2/s^2} \ , \tag{5.4}$$

where T is in °C and $\dot{a}$ is in m/s.

Results of pretest analyses are discussed in Sect. 5.4.

5.1.5 Second benchmark experiment

After the initial mechanical properties data for HSST plate 13A became available (see Sects. 5.2 and 5.3), preliminary correlations were specified to define a refinement to the benchmark experiment for WP-1.1. Three changes were made to the reference case given in Subsect. 5.1.4:

1. $RT_{NDT} = -23.3°C$; (5.5)
2. $K_{Ia} = 49.957 + 32.970\ EXP\ (0.028738T)\ MPa\cdot\sqrt{m}$, T in °C; (5.6)
3. pull-plate length = 340.4 cm (see Fig. 5.1); pull-tab length = 152.4 cm.

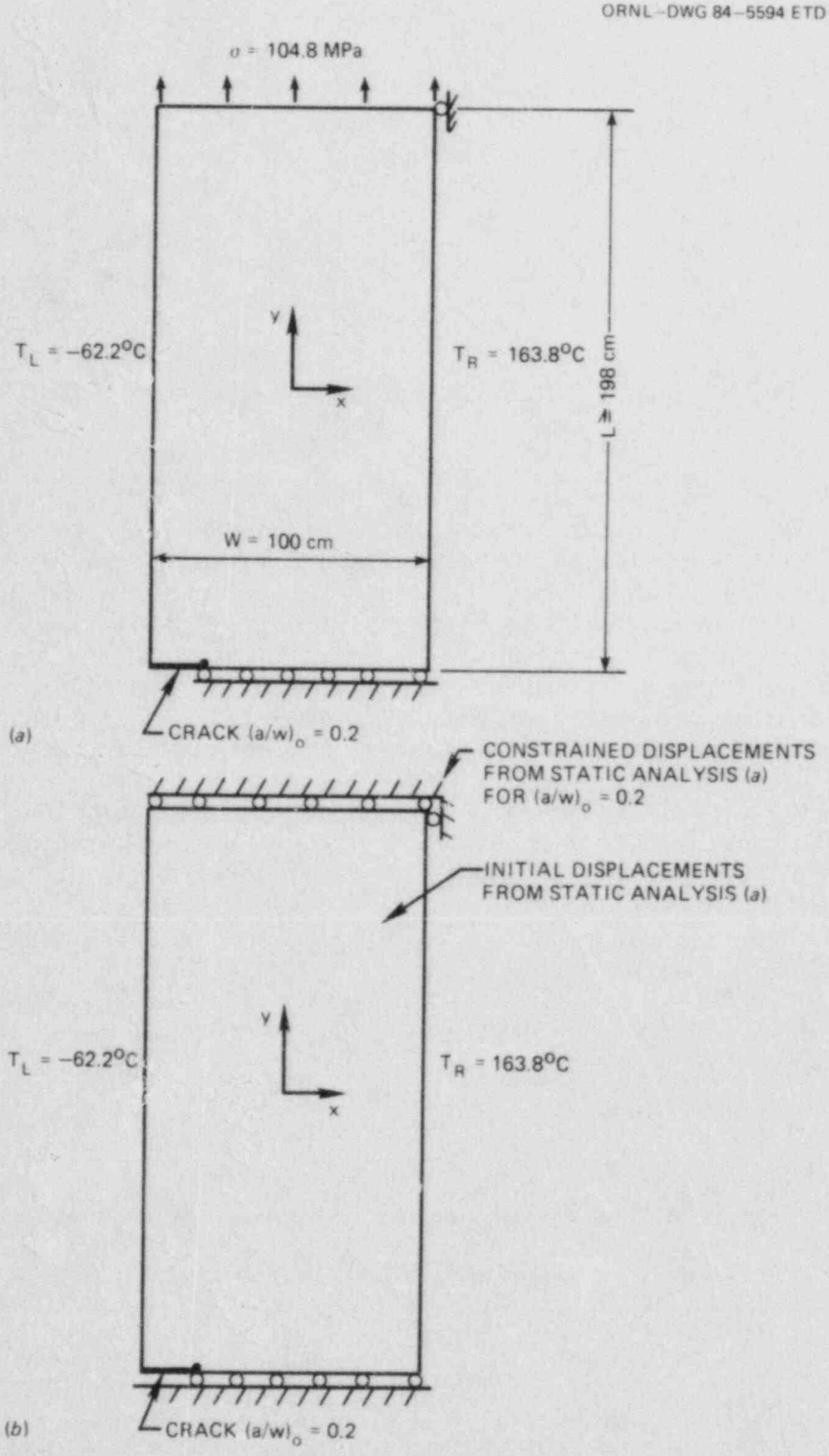

Fig. 5.6. Analytical model for benchmark problem solutions in support of first HSST wide-plate crack-arrest test.

The specimen temperature distribution and loading remained unchanged. Note Eq. (5.6) for K_{Ia} is a nonlinear least-squares fit to the data obtained at BCL (see Subsect. 5.3.2) and is not expressed in terms of the RT_{NDT}. However, upon including $RT_{NDT} = -23.3°C$ in Eq. (5.6) one has

$$K_{Ia} = 49.957 + 16.878 \text{ EXP } [0.028738 (T - RT_{NDT})]. \quad (5.7)$$

Analysts were asked to perform pretest analyses with these modifications.

5.2. Wide-Plate Crack-Arrest Specimens

G. C. Robinson S. E. Bolt
C. E. Pugh

5.2.1 Material allocation

The first series of wide-plate crack-arrest test specimens are taken from HSST plate 13A, which is of A533B Class 1 steel that is in a quenched and tempered condition. Usages of this material include the wide-plate specimen, characterization test specimens, WPS beam specimens, viscoplastic test specimens, and a modified moment K_{Ia} specimen for Combustion Engineering, Inc. The plate layout to cover these needs is shown in Fig. 5.7, and Table 5.1 identifies the allocation, purpose, and responsible person for the various parts. Distribution has been made to the various users. However, prior to cutting the plate, each part was identified by stamping in accordance with the HSST Guide for Material Control and Data Control[3] to maintain cognizance of position and identity throughout the subsequent machining operations.

5.2.2 Wide-plate specimens

The first two of the series of six wide-plate crack-arrest specimens from plate 13A were completely machined at ORNL and shipped to NBS for testing. Figure 5.1 shows the dimensions of these specimens. A sharp crack, which extends 1.3 cm from the 18.7 cm (X = 18.7 cm in Fig. 5.1) notch, was introduced by hydrogen charging an EB weld that had been laid at the bottom of the notch. The specimens were prepared for welding to the pull plates before shipment to NBS. Figure 5.8 shows the specimen while the EB welds were undergoing hydrogen charging. These specimens are designated 13A-01 and 13A-02.

5.2.3 Warm-prestressing beam specimens

The loading scenario for wide-plate crack-arrest tests is discussed in Sect. 5.1 above and includes a WPS phase to increase the K_Q level that the crack can sustain prior to initiation. To confirm the effectiveness

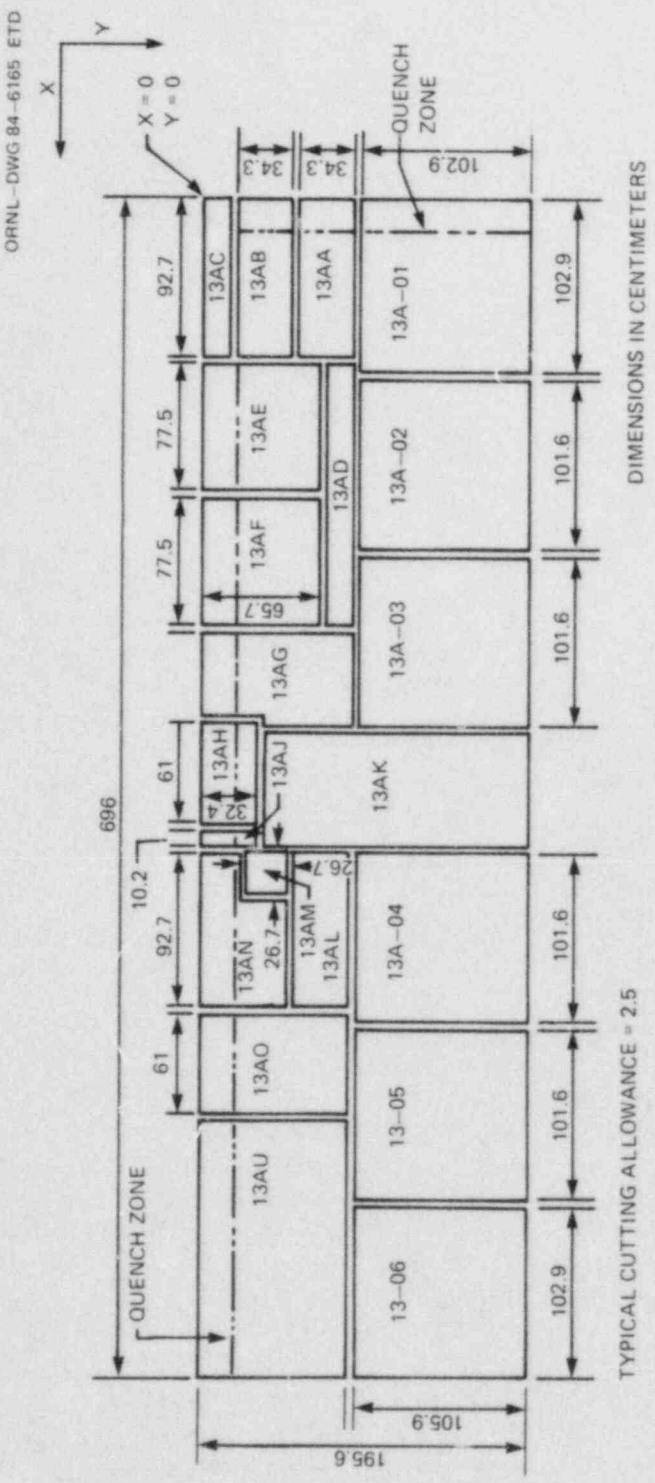

Fig. 5.7. Flame cutup of HSST plate 13A.

Table 5.1. Allocation of wide-plate task material from HSST plate 13A

Plate section or specimen	Purpose	Designee	Principal investigator
13A-01	Wide-plate test	National Bureau of Standards Gaithersburg, Md.	Richard Fields
13A-02	Wide-plate test	National Bureau of Standards Gaithersburg, Md.	Richard Fields
13A-03	Wide-plate test	National Bureau of Standards Gaithersburg, Md.	Richard Fields
13A-04	Wide-plate test	National Bureau of Standards Gaithersburg, Md.	Richard Fields
13A-05	Wide-plate test	National Bureau of Standards Gaithersburg, Md.	Richard Fields
13A-06	Wide-plate test	National Bureau of Standards Gaithersburg, Md.	Richard Fields
13AA	Warm prestress tests	National Bureau of Standards Boulder, Colo.	Dave Read
13AB	Warm prestress tests	National Bureau of Standards Boulder, Colo.	Dave Read
13AC	Quench zone Return to HSST storage		
13AD	1T crack-arrest tests	Battelle Columbus Laboratories Columbus, Ohio	A. R. Rosenfield
13AE	Development of 1T crack-arrest test	National Bureau of Standards Boulder, Colo.	Dave Read
13AF	Development of 1T crack-arrest test	National Bureau of Standards Boulder, Colo.	Dave Read
13AG	Dynamic tests	Southwest Research Institute San Antonio, Tex.	M. F. Kanninen
13AH	Cyclic properties	Oak Ridge National Laboratory Oak Ridge, Tenn.	R. W. Swindeman
13AJ	Plate characterization	Oak Ridge National Laboratory Oak Ridge, Tenn.	R. K. Nanstad
13AK	Plate characterization	Oak Ridge National Laboratory Oak Ridge, Tenn.	R. K. Nanstad
13AL	Warm prestress tests	National Bureau of Standards Boulder, Colo.	Dave Read
13AM	Dynamic tests	Southwest Research Institute San Antonio, Tex.	M. F. Kanninen
13AN	Return to HSST storage		
13AO	Modified moment K_{Ia}	Combustion Engineering, Inc. Windsor, Conn.	D. A. Peck
13AU	Return to HSST storage		

ORNL-PHOTO 7176-84

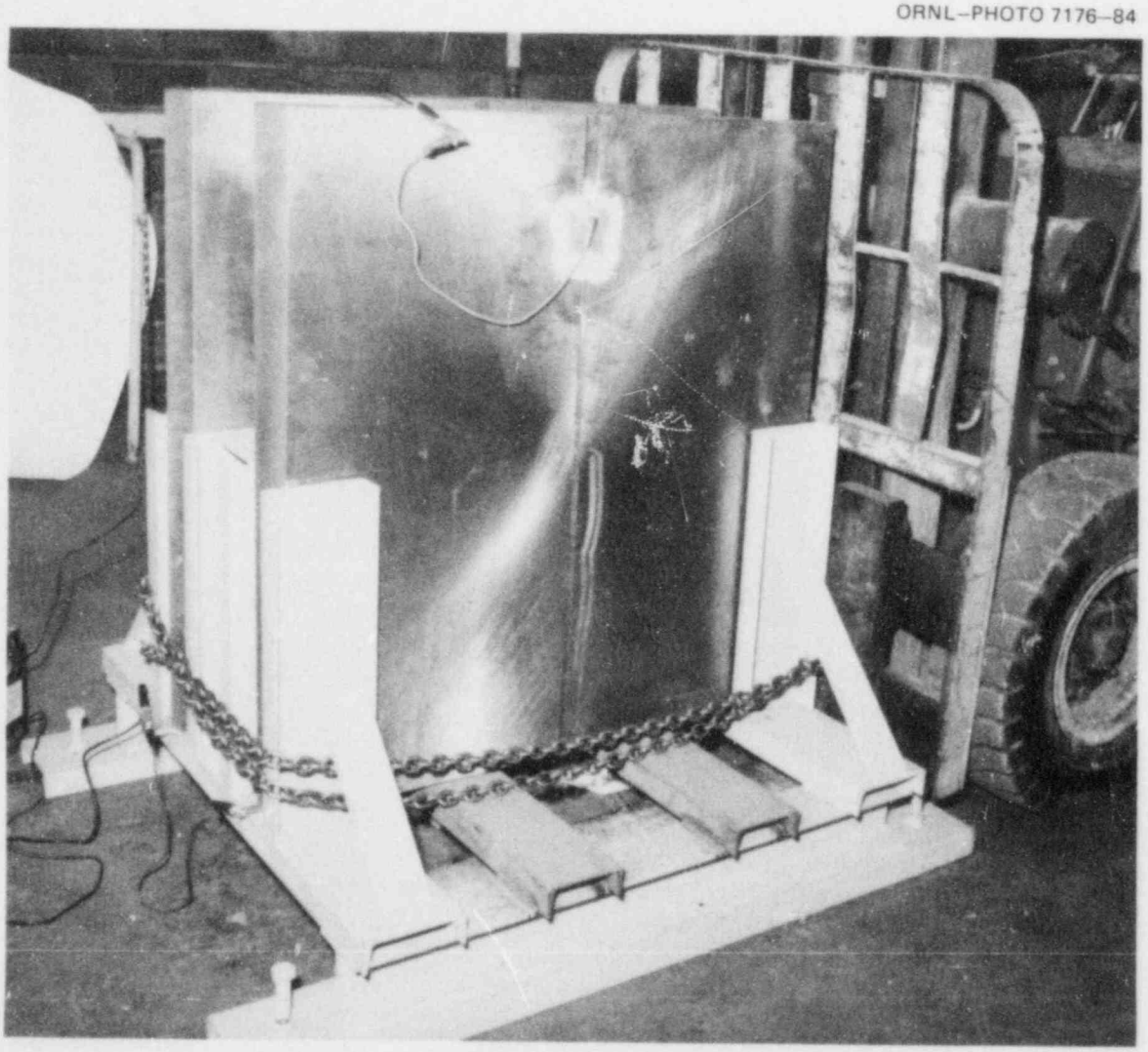

Fig. 5.8. Wide-plate test specimens 13A-01 and 13A-01 undergoing hydrogen charging.

of the proposed technique, six beam specimens were prepared for WPS testing. (Three have been tested by NBS, and the results are reported in Subsect. 5.4.4 below.) These beams were 10.2 cm thick, 15.2 cm deep, and 91.4 cm long and were side-grooved along the crack plane in the same manner as the wide-plate specimens. Cracks (1.3 cm deep) were placed in the 3.8-cm-deep notch by the same EB weld technique as was used for the plate specimens. These specimens are shown in Fig. 5.9, just prior to shipment to NBS. The designation numbers given to these beams are 13A-100 through 13A-105.

5.2.4 EB welding magnetic shield development

Residual magnetism has presented recurring difficulties in the HSST program in EB welding within narrow slots on ferritic materials, such as

ORNL–PHOTO 7172–84

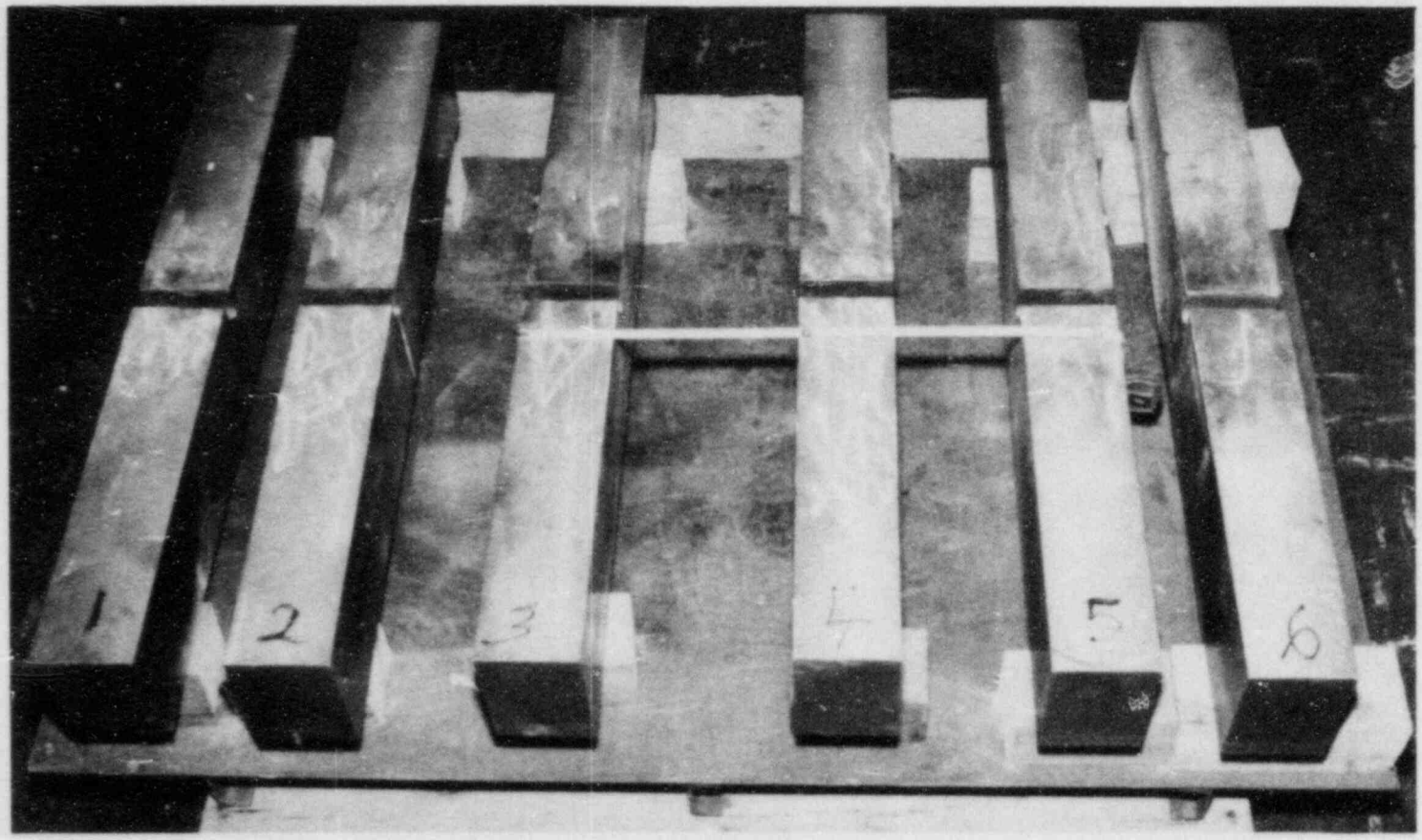

Fig. 5.9. Beam specimens prepared for testing by NBS to verify warm prestressing behavior.

the beams and plates cited above. We have conventionally resorted to degaussing techniques with varying success. On occasion, even though the residual magnetic field has been reduced to a 5- to 10-Gauss level by degaussing, the asymmetry of the field has caused an appreciable misalignment of the EB weld. We recently designed a shield fixture using a proprietary material "Ronetics" and tested its effectiveness. Figure 5.10 shows a slot mock-up similar to the wide-plate specimen slot design and the magnetic shield fixture in the approximate position used during the EB welding test. The mock-up piece residual magnetism varied from 50 to 60 Gauss at the mouth of the slot down to ~5 to 8 Gauss at the bottom of the slot. An initial EB weld was made with the shield in place. The resulting EB weld was straight and properly aligned. Then a second EB weld was placed in the slot without the shield. Although some deviation occurred, the second pass was surprisingly straight. A view of the juxtaposed EB welds is shown in Fig. 5.11. The welds were then H_2 charged until cracked and the mock-up separated into two halves. Figure 5.12 shows the resulting cracked EB welds. The second juxtaposed EB weld resulted in a displacement of the flaw path at one end; otherwise the flaw remained in plane and uniform in depth (0.95 cm) as intended. This exercise was somewhat disappointing in that more dramatic evidence of the effectiveness of the shield was expected; nevertheless, it will be used in future EB welds placed in slots.

5.3 Properties Data and Test Methods

5.3.1 Preliminary characterization of wide-plate test material at ORNL (D. P. Edmonds, J. J. McGowan)

A preliminary characterization has been completed for the A533 Grade B Class 1 steel from HSST plate 13A, which is being used for wide-plate crack-arrest testing. The 18.7-cm-thick plate (melt C4453) was produced by Lukens Steel Company and has the following chemical composition (wt %): 0.19% C, 1.28% Mn, 0.012% P, 0.013% S, 0.21% Si, 0.64% Ni, and 0.55% Mo. An average grain size of ASTM 7–8 was measured for the material. The plate was quenched and tempered as follows: 893°C (1640°F) for 7.5 h, water quenched; 671°C (1240°F) for 8.5 h, water quenched; 565°C (1050°F) for 4 h, air cooled; 621°C (1150°F) for 50 h; and furnace cooled to 316°C (600°F).

Hardness for the material was found to be 89 to 91 DPH (average) and did not vary through the thickness. The lack of surface effect on the through-thickness hardness is felt to result from the extended stress relief and tempering treatments to which the material was subjected. There is also no real variation in room temperature tensile properties through the plate thickness, as can be seen in Fig. 5.13. The average room temperature tensile properties (longitudinal orientation) are ultimate tensile strength, 597 MPa; yield strength, 445 MPa; total elongation, 24%; and reduction of area, 69%. Variations of longitudinal tensile properties with temperature for the plate center are shown in Fig. 5.14. Ultimate tensile strengths decrease from 747 MPa at –129°C to 554 MPa at

ORNL-PHOTO 7245-84

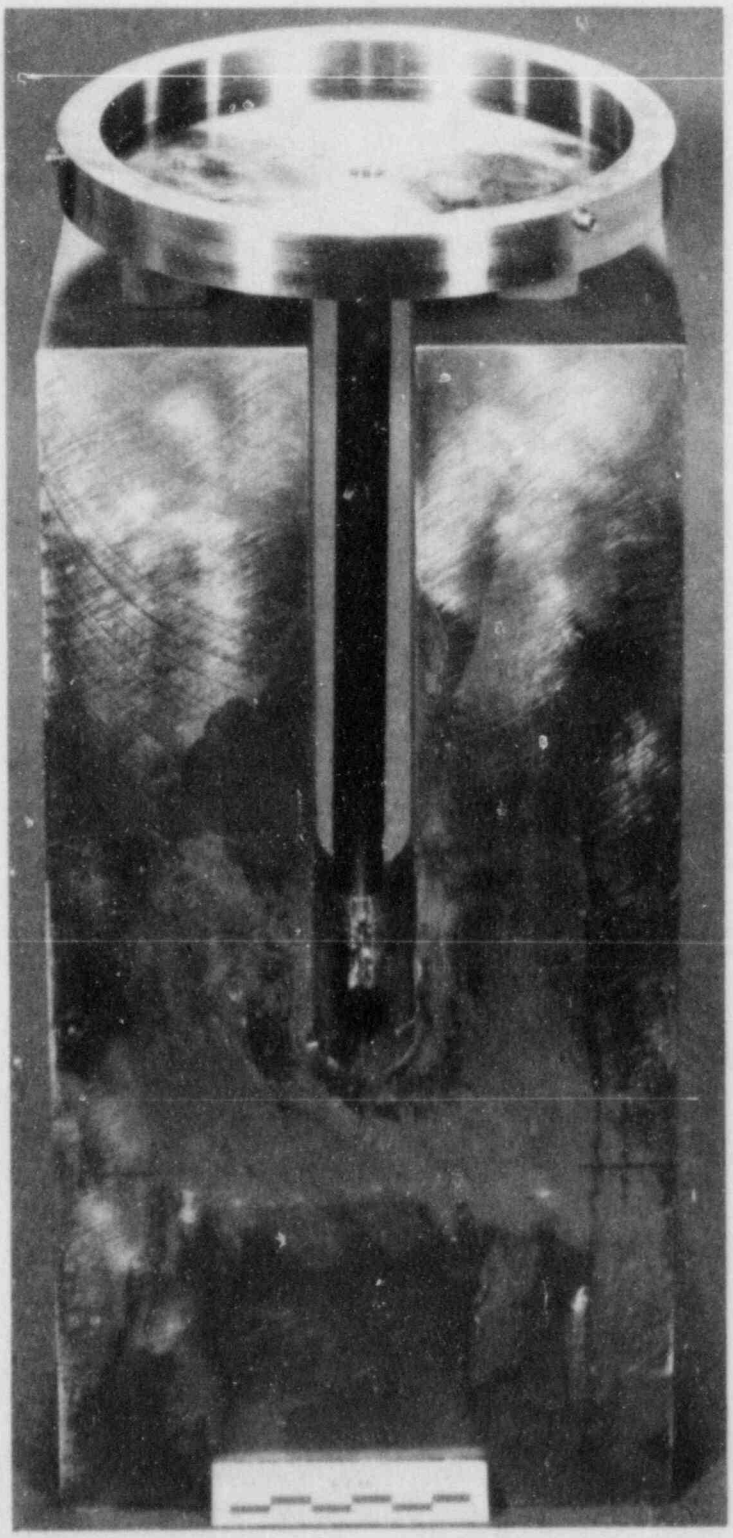

Fig. 5.10. View of EB-weld mockup using magnetic shield in slot configuration.

ORNL–PHOTO 7243–84

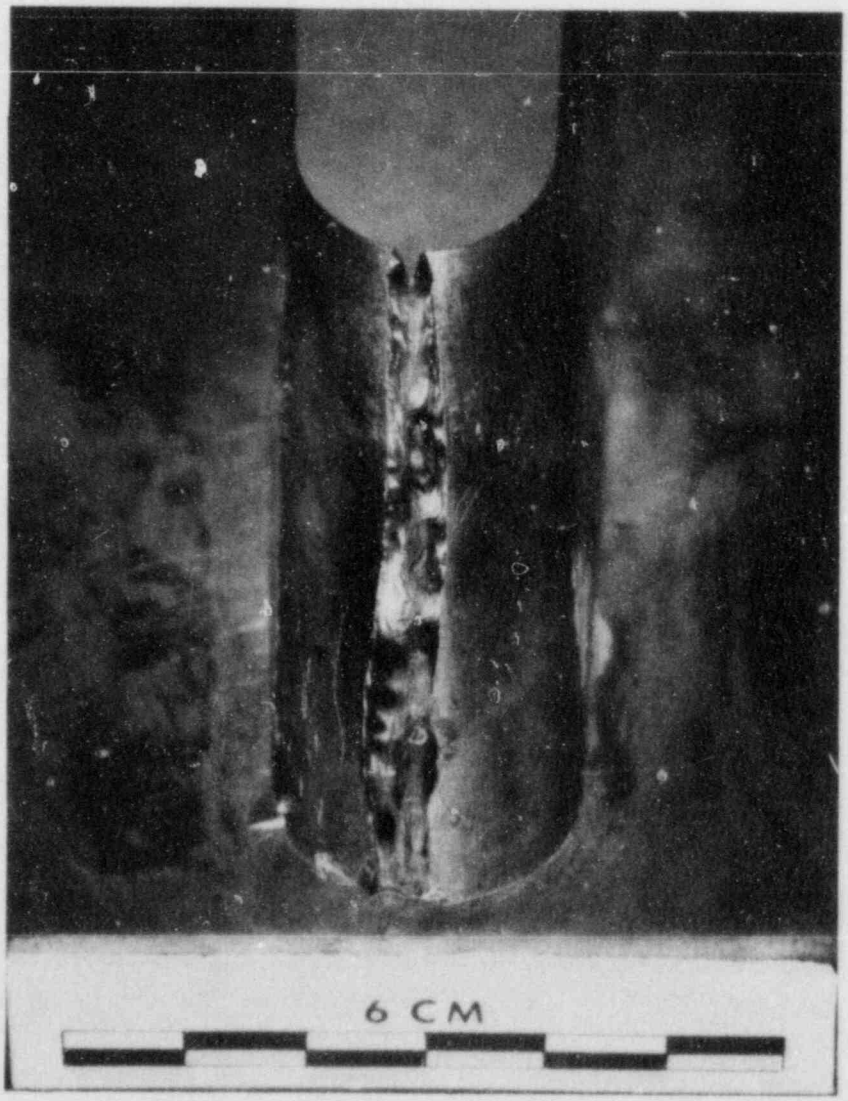

Fig. 5.11. View of juxtaposed EB welds placed in the bottom of slot with and without magnetic shield.

149°C, then increase to 600 MPa at 316°C, as a result of strain aging. Yield strengths decrease from 555 MPa at –129°C to 406 MPa at 316°C.

Figure 5.15 shows that the Charpy V-notch properties in the longitudinal orientation were also found not to vary appreciably through the plate thickness. The LT orientation has the specimen parallel to the rolling direction and the notch (crack propagation) transverse to the rolling direction, similar to the large wide-plate crack-arrest test. For the center 100 mm of the plate, the portion that will be used for wide-plate testing, the average 40-J transition temperature is –30°C, and 35 mils lateral expansion is obtained at –13°C. The RT_{NDT} (ASME reference nil-ductility temperature), as measured by drop-weight/Charpy testing in this orientation, was determined to be –23°C.

ORNL PHOTO 7350-84

Fig. 5.12. Broken half of mockup showing flaw path of H_2-charged juxtaposed EB welds.

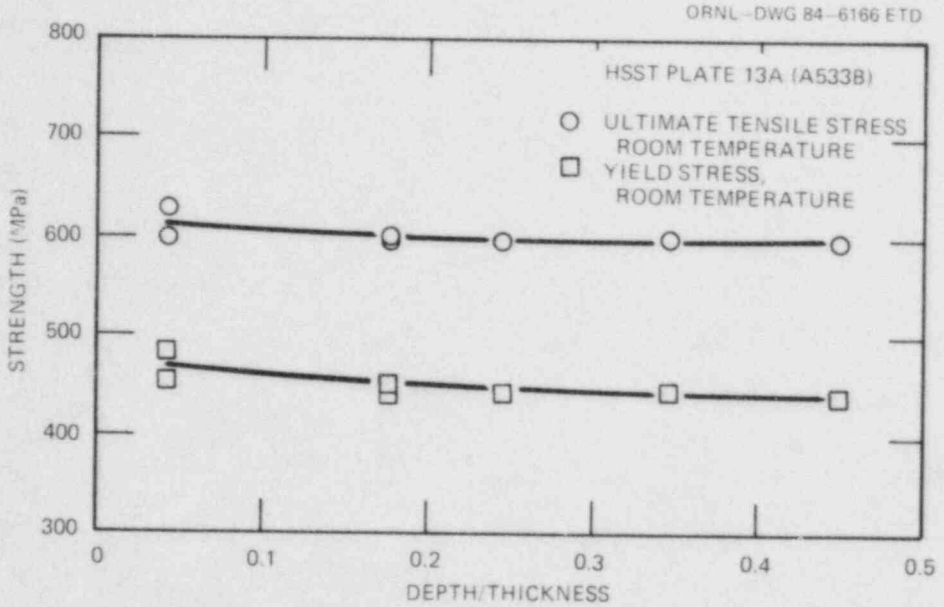

Fig. 5.13. Longitudinal tensile properties through 18.7-cm thickness of HSST plate 13A, A533 Grade B Class 1 steel at room temperature.

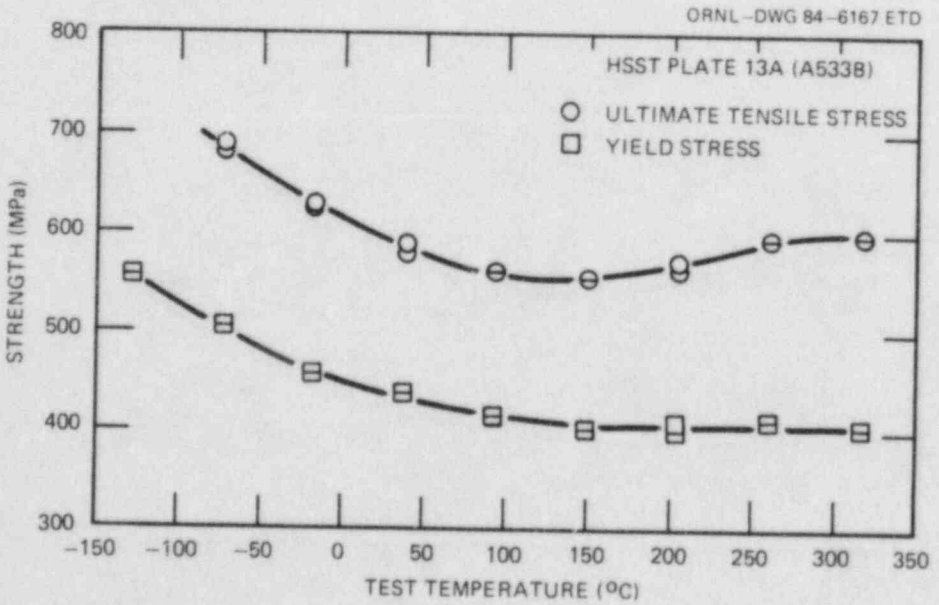

Fig. 5.14. Effect of temperature on longitudinal tensile properties for HSST plate 13A, A533 Grade B Class 1 steel (specimens from center half of 18.7-cm-thick plate).

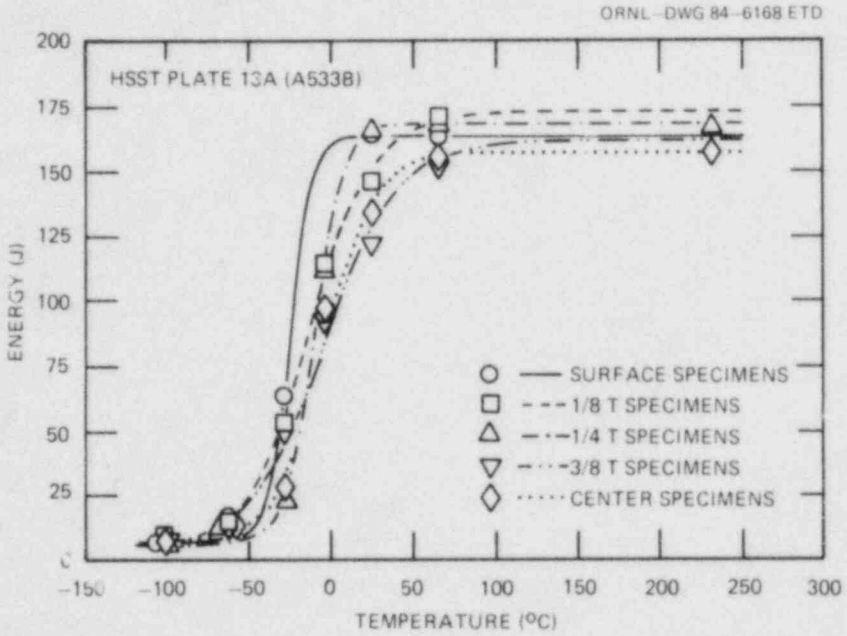

Fig. 5.15. CVN through-thickness results for LT specimens from HSST plate 13A, A533 Grade B Class 1 steel in quenched and tempered condition.

Limited compact specimen testing has been completed for 1T specimens taken from the center 100 mm of the plate in the LT orientation. Results of these tests are summarized in Table 5.2. None of the K_J values represent valid K_{Ic} values. The table shows that substantial stable crack growth occurred in the specimens at higher temperatures. All specimens

Table 5.2. Results for 1T compact specimen tests for A533 Grade B Class 1 steel melt C4453 (HSST plate 13A) in LT orientation

Specimen No.	Test temperature (°C)	K_J[a] (MPa·√m)	$K_{J\beta}$[b] (MPa·√m)	PZS[c]	Δa[d] (mm)
K53B	−50	122.95	78.03	2.05	0.046
K54C	−50	125.27	78.70	2.11	0.048
K51D	−18	167.99	86.22	1.95	0.084
K54E	−18	131.06	77.71	2.14	0.053
K51A	−18	321.94	110.35	2.51	0.818
K52F	26	328.72	109.02	2.23	2.540
K54D	26	312.82	107.09	2.26	3.071

[a] K_J calculated from the J-integral at maximum load using $K^2 = EJ$.

[b] β adjusted K_J.

[c] PZS, plastic zone size factor = $2.5(K_J/YS)^2$/thickness.

[d] Δa, stable crack growth measured on specimen fracture surface using nine-point averaging technique.

experienced conversion to cleavage following stable crack growth. Presently, unloading compliance testing is under way for 2T specimens from the same orientation.

5.3.2 Crack-arrest studies at Battelle Columbus Laboratories* (A. R. Rosenfield,† C. W. Marschall,† C. R. Barnes,† P. N. Mincer†)

5.3.2.1 Crack-arrest test results. The activity at BCl focused on crack-arrest toughness measurements for the A533B steel that is to be used in the wide-plate crack-arrest test series that the NSB—Gaithersburg will conduct (see Sect. 5.2) for ORNL. The material was provided by ORNL from HSST plate 13 A (see Table 5.1), and K_{Ia} values were obtained at temperatures up to those corresponding to the Charpy upper shelf. This is the fifth set of compact-specimen data for reactor-pressure-vessel steels generated at BCL to reach such a high temperature.

Compact crack-arrest specimens were fabricated from the plate segment designated 13AD by ORNL (see Fig. 5.7). Unlike all previous crack-arrest tests at BCL, the LT orientation (ASTM E-399 notation) was specified to be consistent with the NBS tests. The specimens were fabricated from the central 115 mm of the 187-mm-thick plate. An initial estimate of $RT_{NDT} = -17°C$ was provided for the purpose of preliminary planning.[4] Since past experience had shown that weld-embrittled specimens could be used successfully up to about 20—40°C above RT_{NDT}, this design was selected for use below room temperature; the duplex specimen, more suited for high temperatures,[5] for use above room temperature. The goal of the experiments was to obtain small-specimen crack-arrest data from the planned initiation point for WP-1.1 (—18°C) to temperatures at the estimated arrest point in the wide-plate experiment (at the time of BCL experiments the available estimates were 40°C by conventional static analysis[4] and 51°C by both static and dynamic finite-element analyses[6]).

Three problems were encountered. First, attempts to initiate rapid cracks in weld-embrittled specimens at temperatures above —18°C were unsuccessful. This may be due either to the existing temperature guideline being inappropriate for the LT orientation or to the RT_{NDT} estimate being too high. The second problem was that some of the duplex specimens contained surface cracks along the weld line. These were removed by grinding, and the resulting thinner specimens were tested successfully. The final problem was that some of the duplex specimens tested at 0 and 10°C displayed severe ligamentation and/or the crack ran out of the side groove. The corresponding K_{Ia} values were close to, or above, 2.5 K_{IR} (based on the estimated RT_{NDT} value). Past experience has shown that such observations may be a symptom of too high a ratio of initiation-stress-intensity to arrest toughness. As a result, later specimens were equipped with a smaller-diameter starting notch and tested successfully.

---

*Work sponsored by HSST Program under Subcontract 85X-17624C between Martin Marietta Energy Systems, Inc., and BCL.

†Battelle Columbus Laboratories, Columbus, Ohio 43201-2693.

The data, given in Table 5.3 and plotted in Fig. 5.16, show that the compact-specimen results span the intended temperature range. The table also provides inputs into two separate equations to describe the data. The pretest estimate,[4] numerically evaluated in the fourth column, is close to 1.75 times the estimated K_{IR} curve for this plate. In turn, the data average 96 ± 14% of this estimate. The second equation in the table is based on the ASME K_{IR} relation. It was found that the data fit the same relation if −48 ± 10°C is substituted for RT_{NDT}. Interestingly, the Charpy-impact-energy curve for this steel reaches 41 J (30 ft-lb) within this range (at about −40°C).

As was the case for the previous series of experiments on steel from PTSE-1,[7] the highest-temperature data were obtained using inverted-split-pin loading. It is possible that even higher-temperature values could be measured using contoured side grooves, but this option was not explored. Even so, data were obtained above the onset of the Charpy upper shelf, which occurs at about 50°C. These new data are compared with previous upper-shelf values in Table 5.4. The major points of interest are that

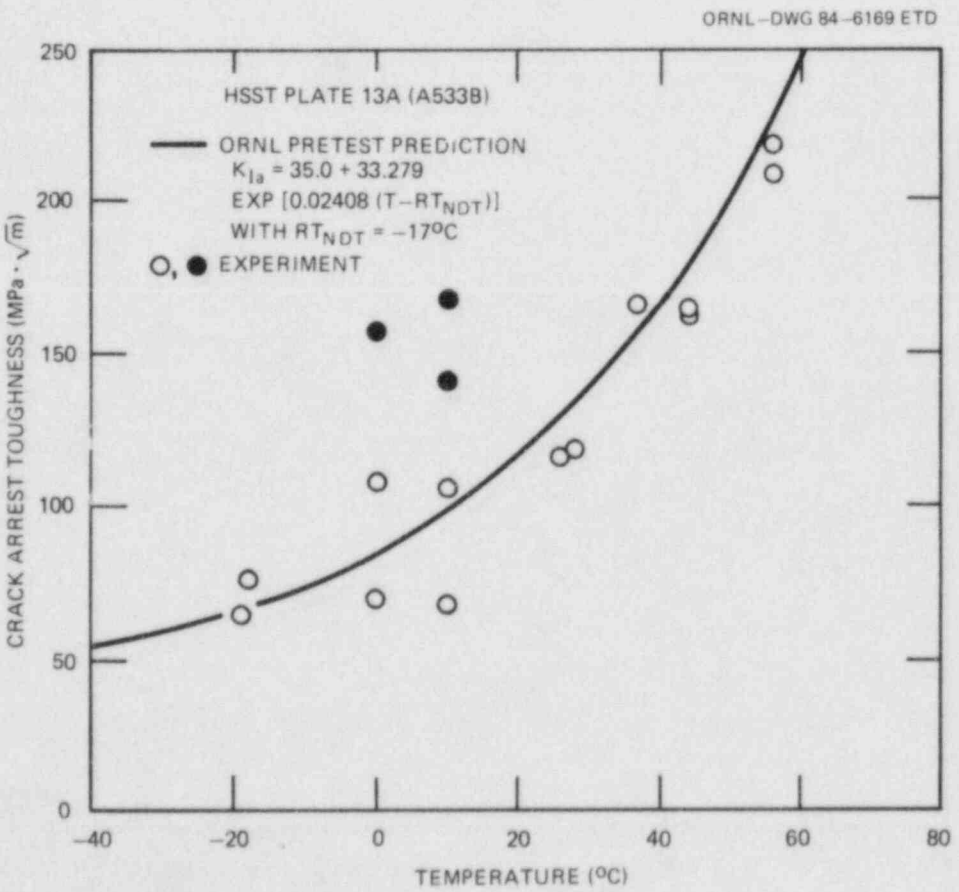

Fig. 5.16. Compact-specimen crack-arrest toughness for A533 Grade B Class 1 steel from HSST plate 13A. Solid line is pretest estimate and solid points are from specimens with unusually high K_{Ic}/K_{IR} values.

Table 5.3. Compact-specimen crack-arrest toughness data for A533B steel from HSST plate 13A

Specimen No.	Temperature (°C)	Crack-arrest toughness (MPa·√m)		T_0[b] (°C)
		Measured	ORNL[a]	
WP1-7	26	115.8	128.7	−44.3
WP1-15[c]	−18	75.5	67.5	−64.2
WP1-8	44	162.3	179.6	−42.8
WP1-5	44	164.6	179.6	−43.5
WP1-14[c]	−19	63.7	66.7	−52.9
WP1-1	28	118.1	133.3	−43.3
WP1-3	37	166.1[d]	157.1	−50.9
WP1-9[e]	0	69.3	85.1	−40.7
WP1-10[e]	10	67.6	98.8	−29.0
WP1-16[e,f]	56	219.0	228.0	−44.4
WP1-17[f]	10	167.6[d,g]	98.8	[g]
WP1-18[e]	56	208.8	228.0	−42.3
WP1-12[f]	10	140.0[d,g]	98.8	[g]
WP1-11[f]	0	156.4[g,h]	85.1	[g]
WP1-20[f]	0	107.0	85.1	−66.2
WP1-23[f]	10	105.3	98.8	−55.3
			Average	−48

[a] Estimate based on PTSE-1 data correlation: $K_{Ia} = 35.0 + 33.279 \text{ EXP } [0.02408(T - RT_{NDT})]$, where estimated RT_{NDT} is −17°C.

[b] T_0 is a reference temperature calculated from the equation: $K_{Ia} = 29.45 + 13.787 \text{ EXP } [0.0261(T - T_0)]$.

[c] Weld-embrittled specimen, all others are duplex.

[d] Severe ligamentation observed.

[e] Inverted split pin; all others normal-pin geometry.

[f] Specimen thickness = 25.4 mm, all others = 35 mm.

[g] Value suspect due to excessively high K_{Ic}/K_{IR} ratio; not counted in averaging.

[h] Crack ran out of side groove.

Table 5.4. Compact-specimen crack-arrest-toughness data for various steels tested at Charpy-upper-shelf temperatures

Steel[a]	Charpy upper shelf		K_{Ia} tests, highest	
	Energy (J)	Approximate temperature (°C)	Temperature (°C)	Toughness (MPa·$\sqrt{m}$)
TSE-5A (9)	160	70	70	152
TSE-6 (9)	106	100	121	157
TSE-6R (9)	150	70	71	260
PTSE-1 (7)	110	140	150	140
WP-1.1[b]	170	50	56	219

[a]Reference in parentheses.

[b]Present report.

the arrest-toughness value at the upper shelf varies strongly with composition and heat treatment and that there is no strong correlation between Charpy-shelf-energy and arrest toughness at the onset of the Charpy shelf. This is not surprising because the fracture mechanism is primarily cleavage in the crack-arrest experiment and completely shear in the Charpy specimen at the same test temperature. In addition, it should be noted that, similar to Fig. 5.16, the arrest-toughness curve shows no sign of leveling off at the highest temperatures reached in the experiments reported in Table 5.4. Indeed, the PTSE-1 cylinder crack-arrest data rise sharply at temperatures higher than those cited in the table.[8]

5.3.2.2 ASTM round robin. Specimen blanks of ASTM A514, A533, and A588 steels were received from the University of Maryland (UM), who is serving as the coordinator of the round-robin test program in support of establishing an ASTM standard on K_{Ia} testing. The blanks were machined into compact specimens following the proposed K_{Ia} test method.[10] Extra specimens of A533B steel were tested using an inverted split pin. In addition, half-size and quarter-size specimens of A533B steel were machined to provide further information concerning size requirements. Test temperatures had been previously fixed by the ASTM task force on K_{Ia} testing.

Complete test results have been provided to UM; these results are summarized in Table 5.5. Note that the toughness data in Table 5.5 do not include a plasticity contribution. The major reason for reporting the data in this way is that it is believed to be correct based on the excellent agreement between compact-specimen and thermal-shock data.[11] However, in the event strong evidence is accumulated that plastic displacements can drive elastic cracks, the current BCL procedure will have been proven to be conservative.

Table 5.5. Summary of BCL results for the ASTM crack-arrest round robin

Steel	Test temperature (°C)	BCL data		Other data	
		Number of specimens[a]	K_{Ia} (MPa·$\sqrt{m}$)[b]	Number of specimens[a]	K_{Ia} (MPa·$\sqrt{m}$)[b]
A514	−30[c]	3 (1)	85	8 (4)	85 (41)[d]
A588	−30[c]	3 (3)	61 (5)	6 (6)	82 (12)[d]
A533B	10	3 (3)	86 (9)	5 (4)	81 (11)[e]
A533B	10	2 (1)	95[f]	NA	NA
A533B	10	2 (2)	46 (14)[g]	NA	NA
A533B	25	3 (1)	63	5 (5)	79 (13)[e]
A533B	25	3 (3)	68 (13)[g]	NA	NA

[a]Number in parentheses is number of successful run-arrest events.

[b]Standard deviation in parentheses.

[c]Other data involve tests at −26 and −34°C.

[d]Lehigh University pretest data provided by W. L. Fourney (Jan. 12, 1984).

[e]ORNL pretest data plus results from first participant.

[f]Small specimen (101.6-mm face dimension).

[g]Inverted split pin.

A514 was characterized as "likely to give trouble" in the Participant Instruction Memorandum as evidenced by the Lehigh University pretest experience of extremely low success rate (50%) in arresting cracks. In addition, the toughness values for their arrested cracks exhibited extreme scatter. Similarly, in only one of the three specimens was the crack arrested; the other two exhibited complete fracture. The successful specimen exhibited marked delamination in the mid-thickness region, which apparently retarded the crack to the extent that its length was less in the center than at the side grooves. Conversely, the nonarrest specimens exhibited markedly less evidence of delamination. For this reason the irreproducibility of crack-arrest data for A514 steel may be judged to be caused by material inhomogeneity.

A588 presented no particular problems. Our data were on average 25% lower than the Lehigh values, presumably because Lehigh included the plasticity component of the measured displacement value in their computation. Because one of the objectives of the round robin is to provide

insight into the question of plasticity contributions to K_{Ia}, this result should help provide evidence concerning the magnitude of the errors arising from improper treatment of nonlinear records.

A533B data are compared with very preliminary results from other participants in Table 5.5. Overall, the table contains only about 10% of the estimated response to the round robin. Accordingly, the comparisons presented there must be treated with caution. Several trends are clear, however. For the "standard" tests listed in the table (i.e., full-size, normal split-pin) the success rate for rapid-crack initiation is 88%. This rate is lower than anticipated based on previous BCL experience but still considerably higher than the value of 50%, which has been cited[11] as justifying alternative starter designs. As noted above, there is an upper-temperature limit for successful crack initiation using the brittle-weld starter. Guidelines used at BCL suggest that most specimens in the round robin should exhibit unstable fracture, provided the steel plate is reasonably uniform and that the Charpy data are representative of all crack-arrest samples.

The BCL success rate for rapid-crack initiation using the inverted-split-pin was 100%, again in accord with previous BCL experience that this geometry facilitates initiation. In contrast, the results for subsize specimens were disappointing, since similarly sized specimens had given no trouble in the past (not included in the table are two 50.8-mm and one 101.4-mm face-size specimens, none of which produced rapid fracture).

The inverted-split-pin K_{Ia} data are also consistent with previous experience. Several years ago, the first of these experiments on steel revealed large dynamic effects and very low apparent toughness values,[12] particularly at a temperature close to RT_{NDT}. The subsequent recognition that this geometry facilitated unstable crack initiation led to its adoption at BCL as the most useful method for extending upwards the usable temperature range of the compact specimen. The successful comparison between our data and the first jump in ORNL experiment PTSE-1 (Ref. 8) is an example of the usefulness of this design modification. It appears that the dynamic effects, which are so bothersome at low temperatures, become less important at high ones. The reason for this was discovered by Rahka,[13] who found that unbroken ligaments inhibited arm vibrations during a run/arrest event. Ligaments are a feature of high-temperature crack propagation, which tend to prevent the specimen arms from flying apart. They apparently serve the same purpose as friction does at low temperature in forcing the specimen to behave in close to a fixed-grip manner. Thus, the postinitiation displacements associated with inverted-split-pin loading at high test temperatures tend to be comparable to those associated with normal-pin loading at moderate test temperatures. In the present experiments, the inverted-split-pin data for specimens tested at 25°C are much more comparable to the normal-split-pin data than is the case at 10°C.

5.3.2.3 BCL crack-arrest data base. During this report period, 134 new points have been added to the data base, bringing the total to 478. The distribution percentages are close to those reported in Table 5.5 of the previous HSST report,[7] with the exception of wide-plate tests whose representation has almost doubled to 9%. Three new laboratories

have been added (one in Italy, one in the United States, and one in Japan), bringing the total to ten. In addition, data for unirradiated base-plate plus irradiated and unirradiated welds are now included. Table 5.6 summarizes the contents.

Table 5.6. Contents of BCL crack-arrest data base

Condition	Base plate	Weld	Total
Unirradiated	427	17	444
Irradiated	19	15	34
Total	446	32	478

The percentage of unirradiated-base-plate data falling below K_{IR} is still close to the 4% level, reinforcing the use of K_{IR} as a good estimate of the fifth percentile of the K_{IR} distribution function.[14] Three percent lie above 2.5 K_{IR}, suggesting that the 95th percentile is slightly less than that value. These percentile estimates appear reasonable at least up to RT_{NDT} + 80°C, and possibly up to the highest temperatures reached (RT_{NDT} + 100°C), a region where compact- and ESSO-specimen data diverge with the small specimens producing more conservative values.[9]

The other data are considered too fragmentary to provide useful percentiles. However, the situation with respect to irradiated materials has been described in detail elsewhere, where it is suggested that the *Regulatory Guide* 1.99 radiation-induced temperature shift may be overconservative.[15]

5.3.2.4 BCL instrumentation of wide-plate specimens. Two techniques are used to monitor crack speeds in the series of NBS wide-plate crack-arrest tests. In the first, NBS applies strain gages along the projected crack path. As a propagating crack advances, a detectable change in the strain gage outputs will be produced and recorded to determine crack-tip position changes with time. Thus, the speed of an advancing crack can be accurately determined.

The importance of these tests argues for redundancy in crack speed monitoring systems. Accordingly, an additional crack speed monitoring technique is being used in conjunction with the strain gages. The selected technique, based on the one used by BCL researchers for the past 15 years,[16] involves the vapor deposition of a platinum-carbon composite through a pattern cut in tin foil that is taped to the insulated specimen surface. This deposition results in a pattern of four conducting grids. Each of these is connected to an individual leg of a Wheatstone bridge powered by 12 V. As connected, an advancing crack successively severs individual lines (and ultimately an individual grid), which produces voltage changes. After each grid is severed, the voltage changes polarity. Thus, assuming all four grids are severed, a complete record is

produced consisting of a series of voltage changes in the plus direction followed by a series of voltage changes in the minus direction. This cycle is repeated once again to indicate that all grid lines are severed.

For the wide-plate tests, however, the vacuum deposition of grids is difficult, because the specimens are too large to be placed inside the generally available vacuum chambers. Consequently, alternate methods of producing the conducting grids have been explored.

The best method employs grids formed from a conducting paint. As a check, a vapor-deposited grid (as in the conventional technique) was applied to one side of a Plexiglas (PMMA) specimen. Insofar as possible, the vapor-deposited grid position coincided with a painted grid on the opposite side. In addition, the painted grid was applied over an insulator as would be necessary in an actual metallic specimen test. This technique worked very well as shown in Fig. 5.17. The output from the top grid indicates a crack speed of 211 m/s; whereas the bottom grid indicates a crack speed of 208 m/s. Considering the possibility of errors introduced during line position measurement, this agreement is probably as good as can be expected.

Thus encouraged, two more specimens were prepared with side grooves. These two tests were not quite as successful as the first. However, it is believed that the new system is a viable technique that has been proven against a demonstrably reliable method. Therefore, efforts are under way to fine tune the technique for use in the WP tests.

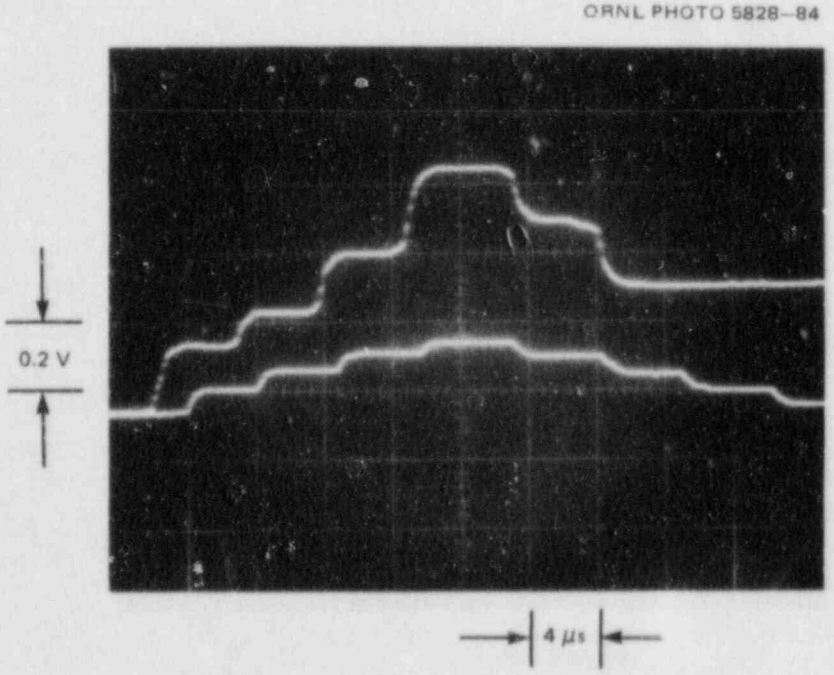

Fig. 5.17. Output of conventional vapor deposited grid (top) as opposed to newly developed painted grid (bottom).

5.3.3 ASTM round robin on K_{Ia} testing* (W. L. Fourney,† G. R. Irwin,† and R. Chona†)

5.3.3.1 Program participation. Twenty-five laboratories had originally indicated their interest in participating in the ASTM round-robin program. Of these, one had to drop out because of a lack of available funding (Stig Wastberg, Norway). However, three other participants have been added — Richard Fields of NBS (Gaithersburg) and Steve Hudak of SwRI, whose requests were received after planning for the wide-plate crack-arrest tests were initiated, and E. Klausnitzer of Kraftwerke Union, Federal Republic of Germany (FRG), whose request followed the Committe on the Safety of Nuclear Installations Crack Arrest Meeting held in June. The total participation therefore stands at 27 laboratories, of which 11 are located in the United States, 1 in Canada, 2 in Japan, and the remaining 13 in Europe.

5.3.3.2 Current status. A meeting of Task Group E24.01.06 was held in Jacksonsville, Florida, in April in conjunction with the E-24 meetings. Presentations were made by BCL (C. W. Marschall) and ORNL (W. R. Corwin) on their preliminary test results. An informal presentation was also made by G. Angelino of Centro Informazion Studi Esperienze, Milan, Itlay, on alternative techniques for starter notch embrittlement. Subsequently, additional tests at BCL and ORNL suggested that the A533B material should be tested at 10 and 25°C. This information was communicated to the participants. An estimated testing timetable was requested from all the participants.

Test results have been received from Dr. Susukida of Mitsubishi Heavy Industries, Japan, and Dr. Gillot of MPA-Stuttgart, FRG, C. W. Marschall of BCL, W. R. Corwin of ORNL, and Dr. Kawahara of Nippon Steel, Japan. Based on the above information, it should be possible to present a preliminary compilation of tests results at the next meeting of ASTM E14.01.06 on October 22—24 in Dallas.

5.4 Wide-Plate Benchmark Problem Solutions

As discussed in Sect. 5.1, ORNL identified two benchmark problems for analytical solutions in support of defining wide-plate crack-arrest tests. Three organizations performed static and dynamic fracture analyses, and the results are discussed below. The three organizations are ORNL, SwRI, and UM.

---

*Work sponsored by HSST Program under Subcontract No. 7778 between Martin Marietta Energy Systems, Inc., and the University of Maryland.

†Department of Mechanical Engineering, University of Maryland, College Park, Maryland.

5.4.1 Analyses at ORNL (B. R. Bass)

During this report period, the SWIDAC dynamic crack analysis code was received by ORNL from the SwRI, and was converted to run on the Oak Ridge IBM system. The two test cases obtained from SwRI were analyzed with the IBM version of SWIDAC, and the results agree with those reported by SwRI. Subsequently, the IBM version of SWIDAC was used at ORNL for elastodynamic finite-element analyses of the first wide-plate crack-arrest test (WP-1.1). A description of WP-1.1, including the benchmark analytical problems, has been given earlier in this section. The results reported here are for the benchmark problem with and without modified material properties and for the analysis of the complete wide-plate test assembly.

5.4.1.1 Analysis of the benchmark problem. The geometry and dimensions of the test specimen pull-plate assembly to be used in the wide-plate test WP-1.1 are depicted in Figs. 5.1 and 5.2. For benchmark analysis purposes, the portion of the plate assembly shown in Fig. 5.6 was recommended for analysis by interested participants. Because of symmetry conditions, only one-half of the plate is modeled. Material properties for the assembly are discussed in Sects. 5.2 and 5.3. The ORNL finite-element model of the benchmark problem is shown in Fig. 5.18. The model consists of 398 nodes and 108 8-noded isoparametric elements. The finite-element model includes 25 coupled nodes along the initially uncracked ligament that are gradually released as the crack advances through the plate.

The first step in the analysis of the benchmark problem involved a static computation of the displacement field corresponding to the initial applied stress of 104.8 MPa. For this boundary condition, a static stress-intensity factor $K = 127.7$ MPa$\cdot\sqrt{m}$ was computed with the SWIDAC code. This computation is performed in SWIDAC by first evaluating the J-integral, modifying J to account for the 25% side grooves in the specimen, and then using the relationship $K = (EJ)^{1/2}$, where E is Young's modulus.

The dynamic analysis of the plate was carried out with the loading surface displacements fixed at the static analysis values. Then, propagation of the crack was modeled by the relation $K = K_{ID}$, where K is the computed dynamic stress intensity factor, and K_{ID} is the dynamic fracture-toughness relation. The analyses reported have utilized the updated material properties defined by Eqs. (5.5) and (5.6). A time step of 4 μs was used in conjunction with the unconditionally stable Newmark-Beta time integration scheme. The results of the SWIDAC analysis are depicted in Figs. 5.19 and 5.20, which give the variations of crack-depth ratio a/w and stress-intensity factory K as functions of time t. In Fig. 5.19, crack arrest is predicted at $a/w = 0.538$, with crack tip temperature $T = 59.3°C$, and with time of arrest at 1.52 ms. From Fig. 5.20, the stress-intensity factor corresponding to the time of arrest is $K_{Ia} = 231.1$ MPa$\cdot\sqrt{m}$. In the two figures, the shaded circles indicate times at which successive elements in the initially uncracked ligament were released to advance the crack tip. The open circles denote potential release of nodal point forces on the crack plane to model crack propagation within an element. In Fig. 5.19, the small dots represent intermediate values of the variable computed by the crack growth modeling scheme in SWIDAC.

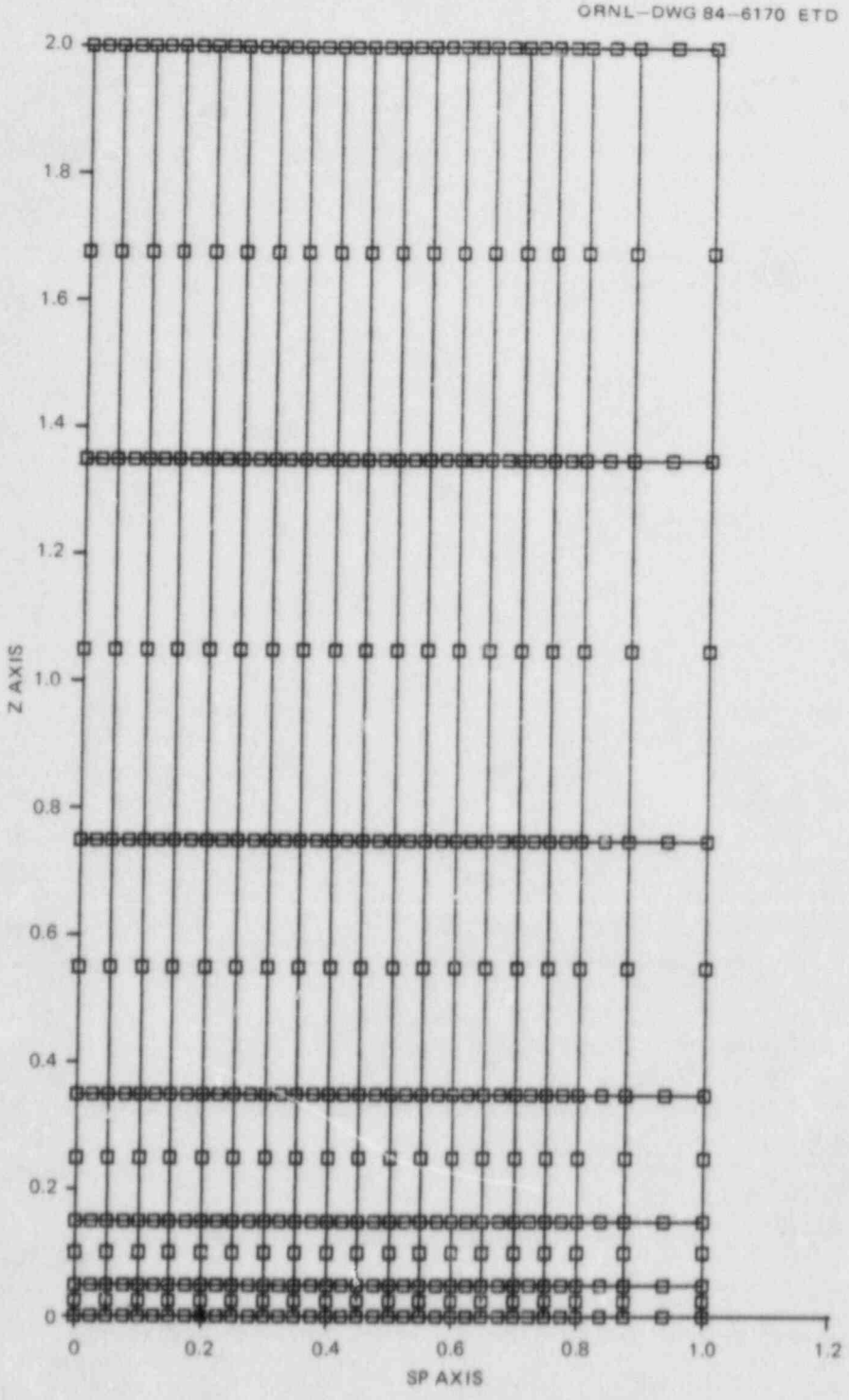

Fig. 5.18. Finite-element model employed in ORNL benchmark analytical solution.

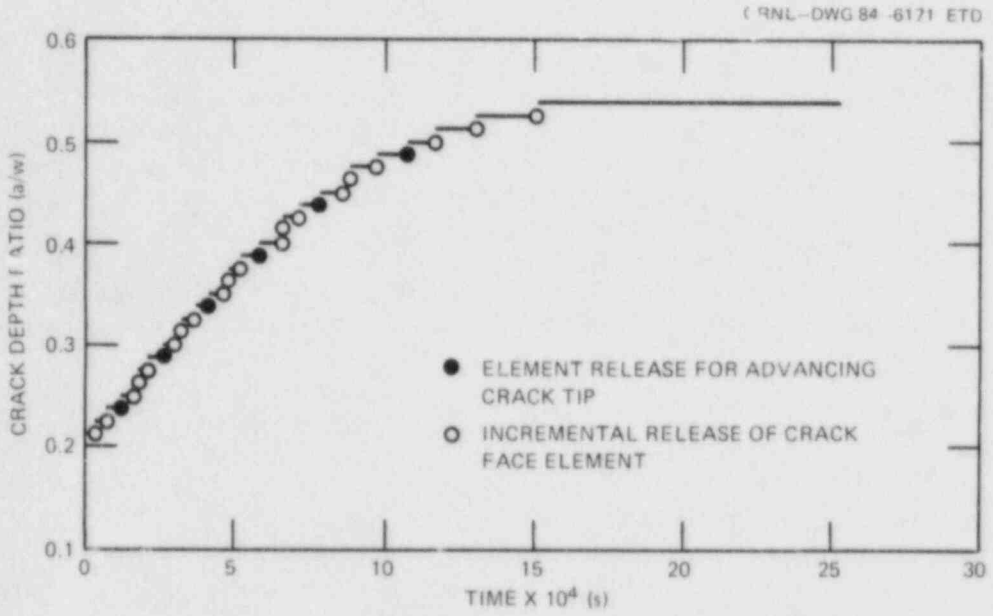

Fig. 5.19. Crack length vs time for ORNL benchmark solution.

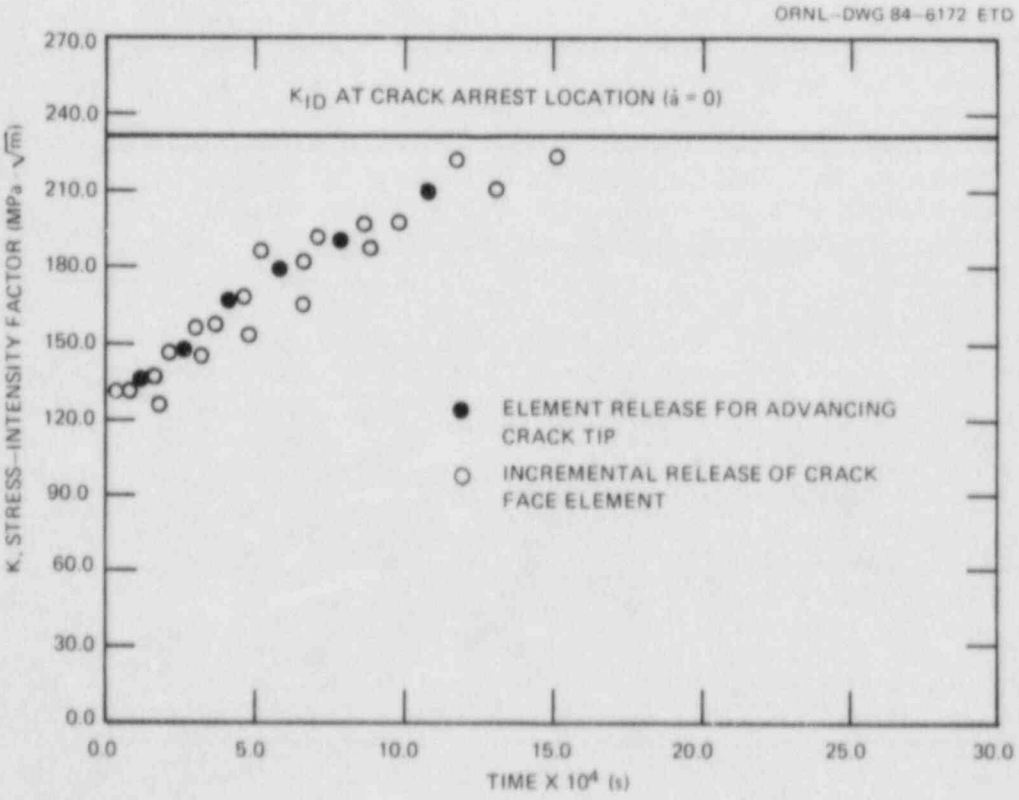

Fig. 5.20. Stress intensity factor vs time for ORNL benchmark solution.

5.4.1.2 Analysis of the complete plate geometry. A second analysis was performed at ORNL to assess the effects of including the complete pull-plate assembly (Fig. 5.2) in the finite-element analysis. The finite-element model employed in this analysis is depicted in Fig. 5.21 and incorporates 520 nodes and 148 8-nodal isoparametric elements. In the model, 21 coupled nodes are used in the uncracked ligament to model crack propagation. For the static analysis, a point load of 10.64×10^6 N was applied at the top of the loading hole (Fig. 5.2), yielding an initial stress-intensity factor of $K_0 = 125$ MPa$\cdot\sqrt{m}$. With the loading point fixed at the static displacement value, the dynamic analysis was performed with SWIDAC using the material properties of Eqs. (5.5) and (5.6) and a time step of 6 μs. Results from this analysis, depicted in Figs. 5.22 and 5.23, indicate that the complete geometry model predicts a longer crack jump than the benchmark case. The results imply arrest at crack-depth ratio a/w = 0.617, crack-tip temperature T = 77.2°C, time of arrest t = 2.19 ms, and stress-intensity factor $K_{Ia} = 353.4$ MPa$\cdot\sqrt{m}$.

5.4.2 Analyses at the University of Maryland* (W. L. Fourney, R. Chona, C. E. Schwartz, G. R. Irwin)†

Several analyses have been performed using the University of Maryland Dynamic Finite-Element Code, SAMCR, to assist in the planning of the first wide-plate test, WP-1.1. The detailed results obtained to date were communicated to ORNL in the form of letter reports.

The test geometry examined was as shown in Figs. 5.1 and 5.2. For the purposes of analysis, weld discontinuities were ignored. The initial analysis addressed the benchmark problem defined by Ref. 4 and described in Subsect. 5.1.4. The resulting finite-element mesh and the boundary conditions for the dynamic analysis are shown in Fig. 5.24. The relationships used for K_I as a function of temperature and K_I as a function of velocity are those given by Eqs. (5.1) and (5.3). Figure 5.25 shows the results obtained for crack length and stress intensity factor as functions of time. These results and those from the analysis of a longer section of the plate showed that computations were being influenced by reflections of stress waves from the top edge. Analysis of the full specimen geometry is currently in progress.

The computer code results have also been used to simulate data that will be recorded on near-field strain gages in the experiment and to recommend a gage layout that will provide optimal data-gathering capability during the test. The results from the full specimen geometry and the suggestions for strain gage locations have been factored into the plans for the first test (see Figs. 5.3 and 5.4).

---

*Work sponsored by HSST Program under Subcontract No. 7778 between Martin Marietta Energy Systems, Inc., and the University of Maryland.

†University of Maryland, College Park, Maryland.

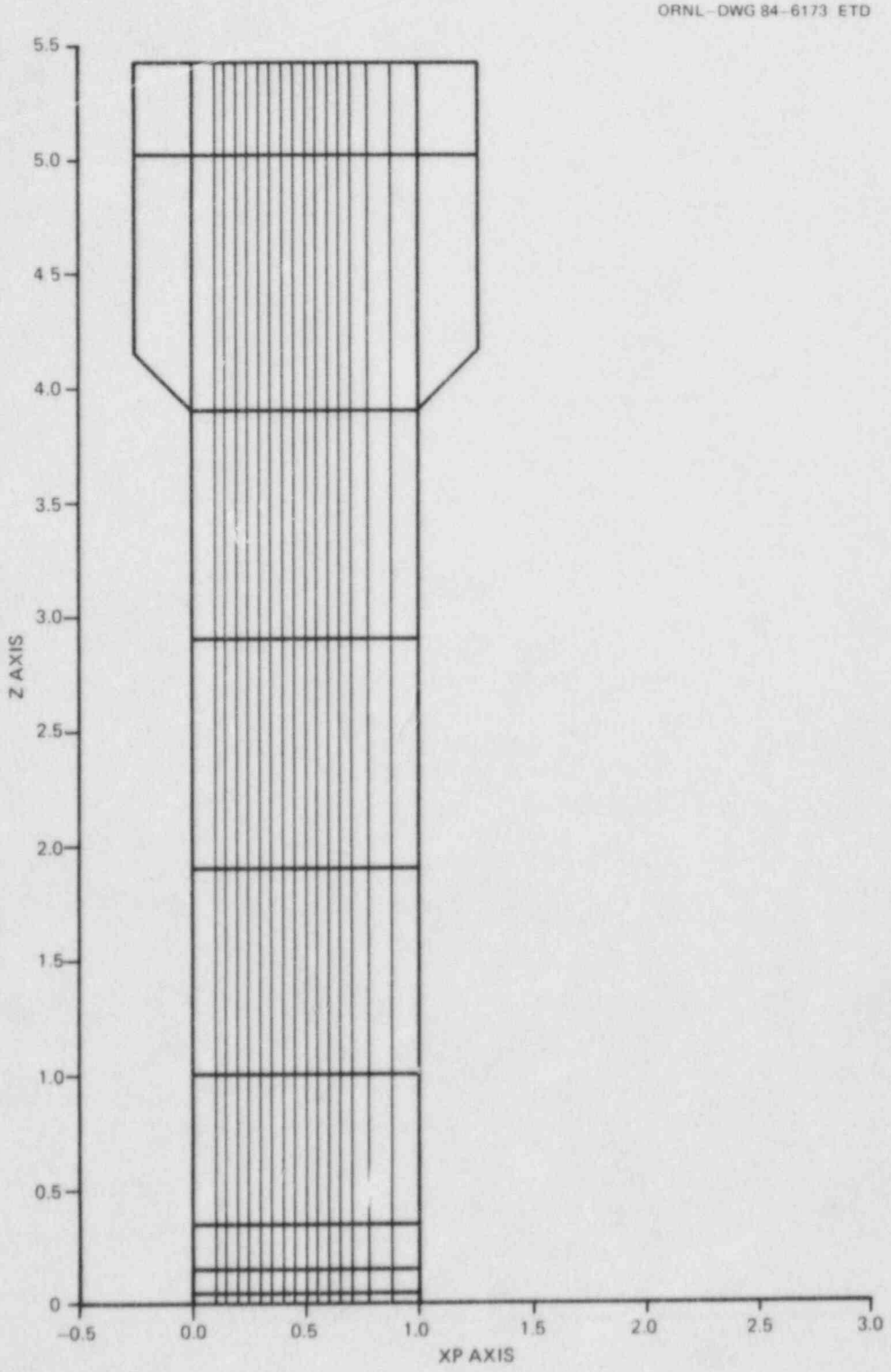

Fig. 5.21. Finite-element model employed in ORNL wide-plate pull tab solution.

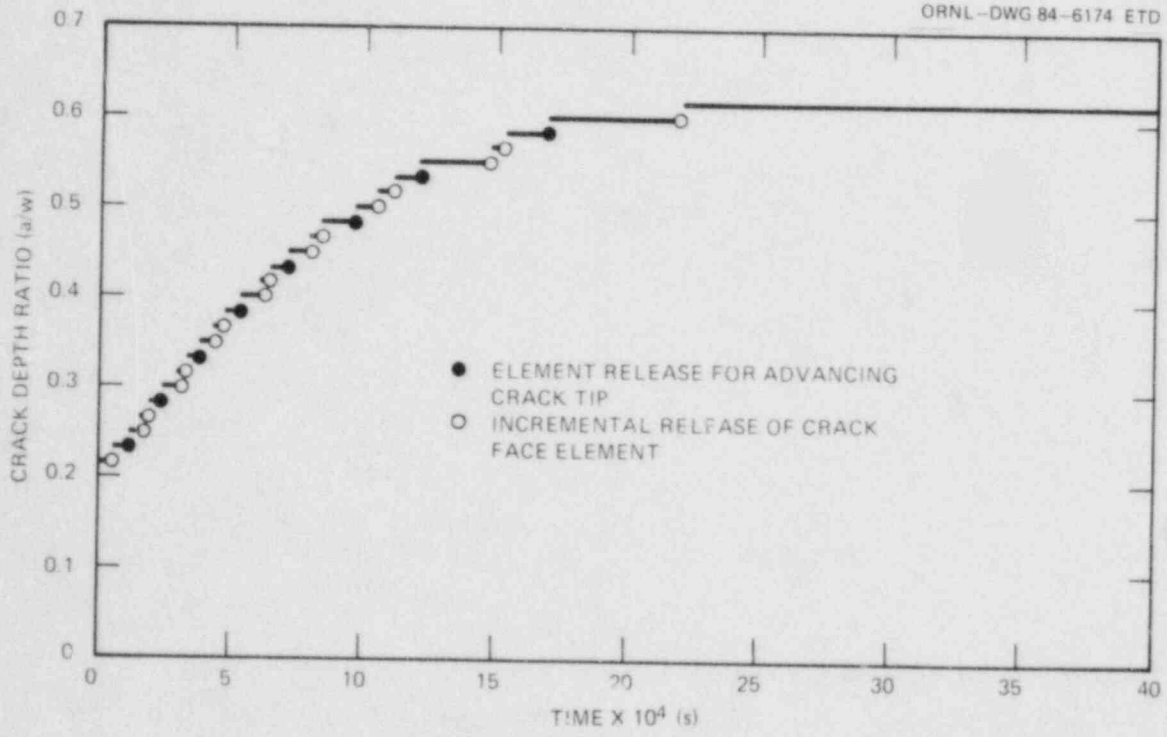

Fig. 5.22. Crack length vs time for ORNL wide-plate pull tab solution.

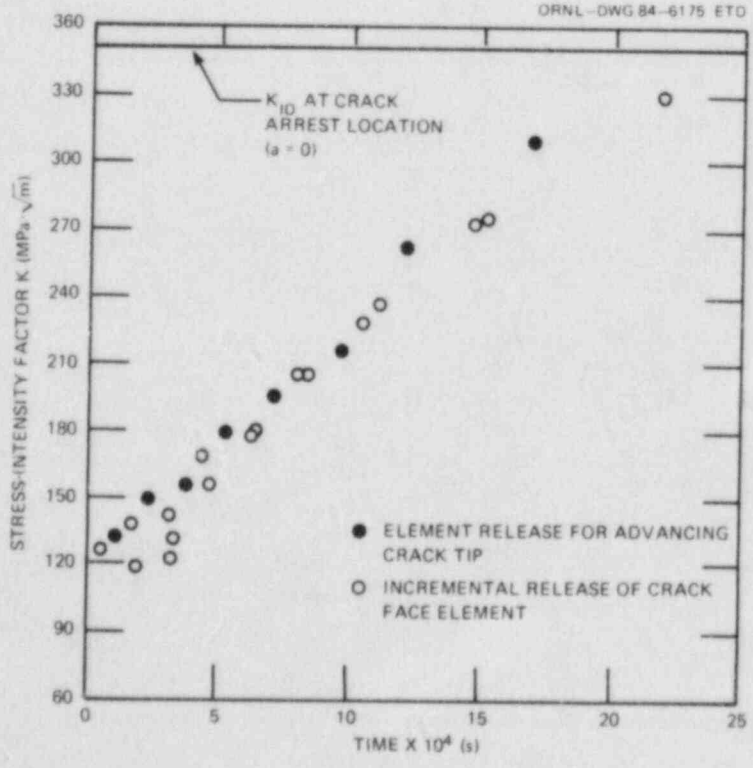

Fig. 5.23. Stress-intensity factor vs time for ORNL wide-plate pull tab solution.

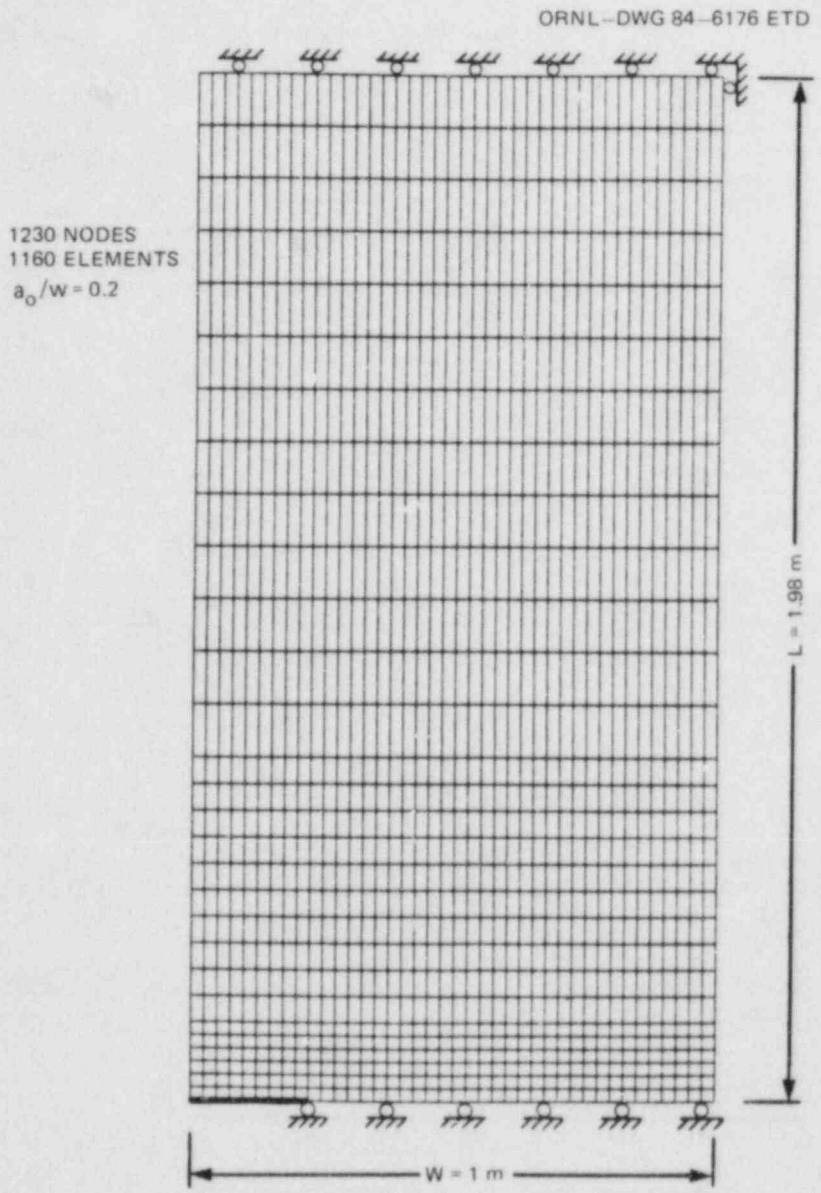

Fig. 5.24. Finite-element mesh and boundary conditions associated with analysis of benchmark problem.

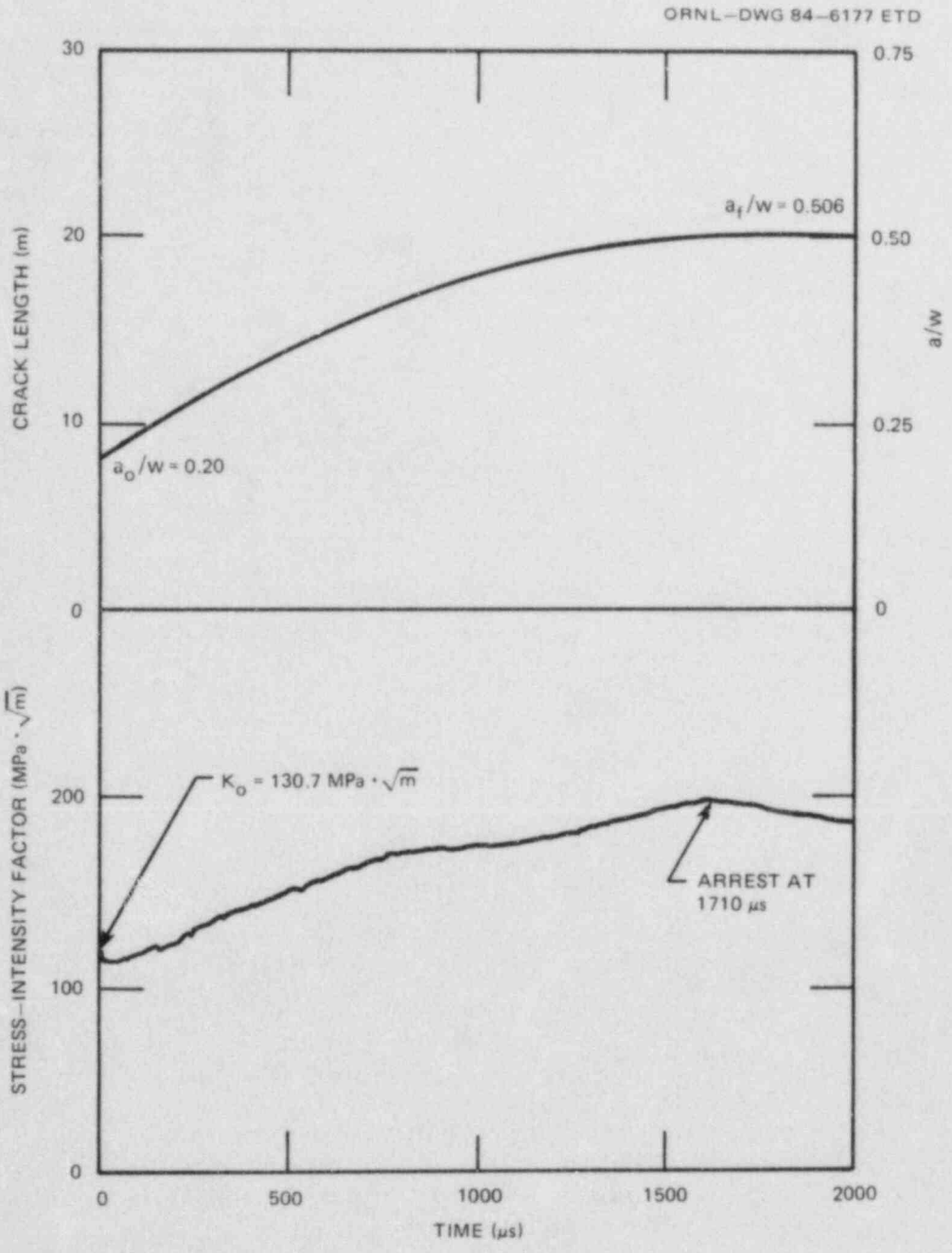

Fig. 5.25. Results obtained from dynamic finite-element analysis of benchmark (wide-plate test) problem for crack length and crack-tip stress-intensity factor as functions of time.

5.4.3 Analyses at SwRI* (M. F. Kanninen, J. Ahmad, V. Papaspyropoulos)†

Pretest elastodynamic finite-element analyses were performed on WP-1.1, which is to be conducted at NBS, Gaithersburg (see Sect. 5.1). Using the ORNL test descriptions given in Subsects. 5.1.4 and 5.1.5, analyses were performed to assess the effects of possible thermal stresses, remote boundary conditions, and the geometry of the test configuration.

The finite-element model used in the solution of this benchmark problem is shown in Fig. 5.26. The model contains 80 8-noded isoparametric elements with a total of 310 nodes, including 27 coupled nodes along the initially uncracked ligament. These coupled nodes are used to model crack propagation by gradually releasing the force between them as the crack advances from one pair of coupled nodes to the next.

The first benchmark problem included only a part of the pull-plate length in the experimental test configuration (see Fig. 5.6). To investigate whether including the complete pull-plate assembly in the finite-element model would have an effect on the predicted crack length vs time, a new model was generated. This model, shown in Fig. 5.27, contains 96 8-noded elements with a total of 348 nodes. There are 19 coupled nodes along the initially uncracked ligament. Like the first benchmark problem, this model does not contain the load-pin hole. This is tantamount to assuming that perfect contact exists between the plate and the load pin and that both the plate and the load pin are the same material. Detailed results of the analyses performed were transmitted to ORNL. Besides providing the results for the benchmark case, these analyses were performed to assess the effect of possible thermal stresses and the effect of pull-plate length (L) on the crack propagation behavior. Also, the effect of remote loading condition (fixed grip and fixed load) was investigated.

Analyses of the benchmark problem with and without the consideration of thermal stresses showed minimal effect of thermal stresses on the crack propagation and arrest behavior. Consequently, all the remaining analyses were performed without thermal stresses. These results are summarized in Table 5.7. It can be seen from these results that varying the problem formulation and the boundary conditions has a significant effect on the prediction of crack arrest.

---

*Work sponsored by the HSST Program under Subcontract 37X-97306C between Martin Marietta Energy Systems, Inc., and the Southwest Research Institute.

†Engineering and Materials Sciences Division, Southwest Research Institute, San Antonio, Texas.

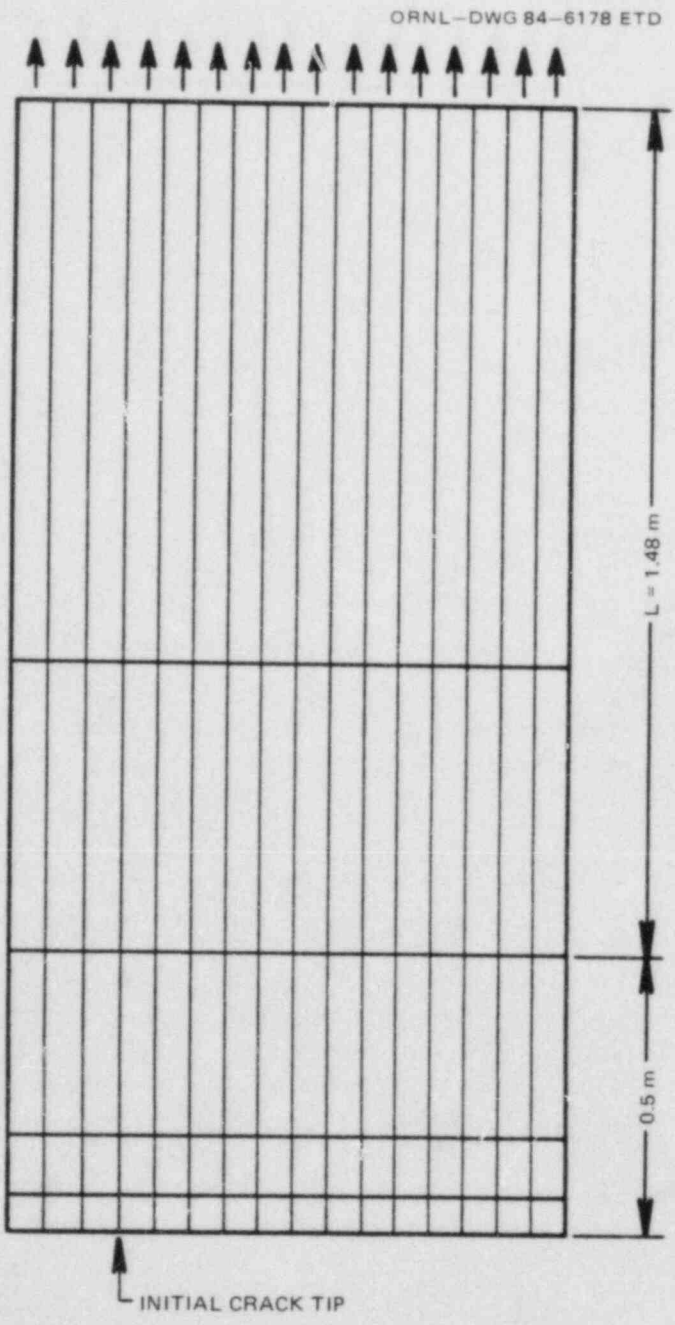

Fig. 5.26. Finite-element model used for benchmark problem.

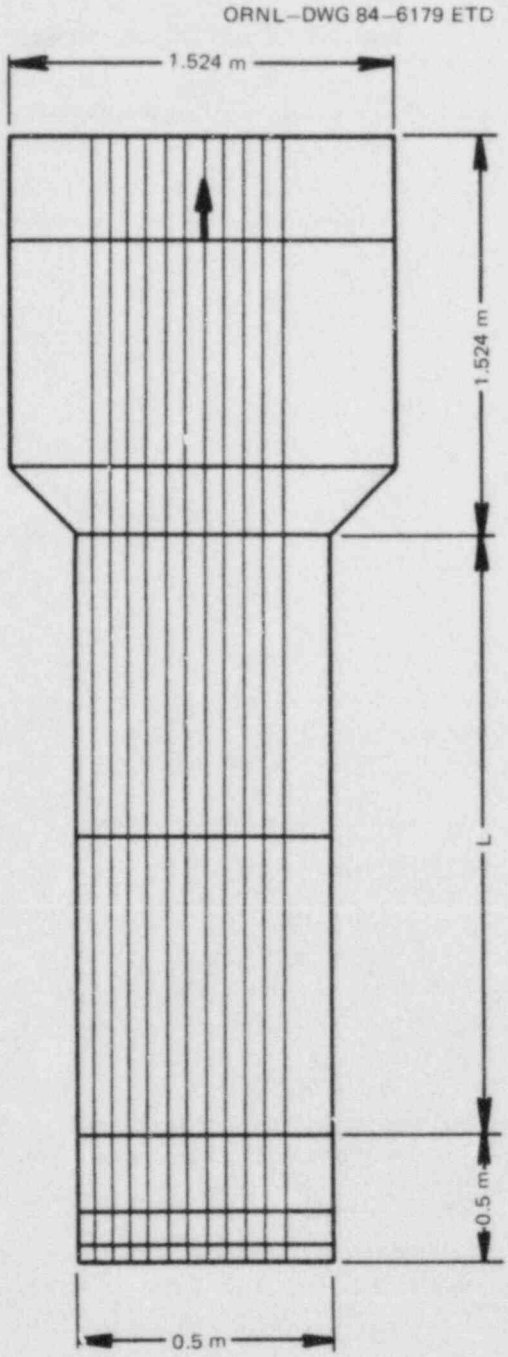

Fig. 5.27. Finite-element model used for optional (full geometry) problem.

Table 5.7. Summary of WP1.1 pretest analysis results

Pull-plate length (m)	Remote boundary condition	Crack length at arrest (m)	Crack-tip temperature at arrest (°C)
1.480 (Benchmark)	Fixed displacement	0.544	60.7
3.810	Fixed displacement	0.597	72.7
3.810	Fixed load	0.719	100.3
4.318	Fixed displacement	0.623	78.6

5.5 Wide-Plate Crack-Arrest Testing*

R. deWit† G. E. Hicho†
S. R. Low III† D. E. Harne†
R. J. Fields†

5.5.1 Introduction

As a part of the HSST program efforts to develop data and validated analysis methods for crack-arrest behavior of reactor vessel steels, NBS has initiated a task on dynamic tests involving crack propagation and arrest. The purpose of the work is to provide data from wide plates that are fracturing at temperatures up to the upper-shelf region. This is the first NBS contribution to an HSST progress report.

Six single-edge-cracked wide-plate specimens are to be tested under a tensile load and a transverse thermal gradient. The specimens, shown in Fig. 5.1, were supplied by ORNL, while the pull plates and pull tabs, shown in Fig. 5.2, were designed and constructed by NBS. The transverse thermal gradient that the NBS facilities have been prepared to accommodate can range from −101 to 260°C across the 1-m-wide specimen. To establish this gradient, a heating and cooling system was constructed. The temperature gradient will cause a slight in-plane bending of the specimen. When a load is applied to this bent specimen, a moment results that will affect the stress state of the specimen. NBS has estimated the magnitude of this effect.

An important part of this study is data acquisition from the numerous strain gages, thermocouples, and timing wires that are mounted on the specimen. BCL is responsible for installing one system of instrumentation for measuring crack velocity and acquiring the data from it. NBS is responsible for all other data acquisition. Low reactance bridges,

*Work sponsored by the HSST program under Interagency Agreement No. DE-AI05-84OR21432 between the U.S. Department of Energy and the National Bureau of Standards.

†Fracture and Deformation Division, National Bureau of Standards, Gaithersburg, Maryland.

wide-range dynamic amplifiers, and high-speed digital oscilloscopes will monitor the strain gage response to crack propagation and arrest.

To ensure a meaningful crack run and arrest event, it is necessary to achieve a significant elevation in K above K_{Ic}. The technique chosen by ORNL is warm prestressing, and they have provided a suggested warm prestressing procedure. This procedure has been tried on two, full-thickness bend bars with success.

5.5.2 Pinhole design

Tests were run to assess the possibility of yielding at the pinholes in the pull tabs. The configuration of a pinhole is shown in Fig. 5.2. Fifteen tests were run for various plate thicknesses, widths, distances between pinholes and end of plate, pinhole diameter, pin-to-pinhole clearance, and yield stress value. Loads were recorded that corresponded to yielding at the pinhole. The observed yield loads vs the predicted values are shown in Fig. 5.28.

From these studies it was predicted that the pull-tab configuration shown in Fig. 5.2 would have a yield load of about 45 MN. This load is about 65% greater than the 27-MN capacity of the NBS tensile machine if the tabs are of A533B steel. These observations, along with potential beneficial effects of material-hardening characteristics, lead to the conclusion that the pinhole design is sufficiently conservative for the planned tests.

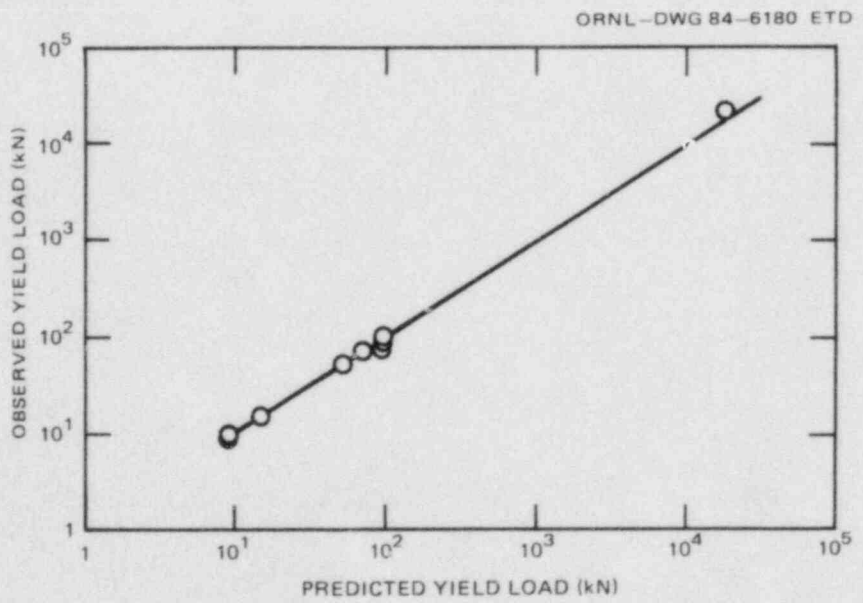

Fig. 5.28. Observed yield load vs predicted yield load for NBS pinhole design.

5.5.3 Fabrication of pull plates and pull tabs

For reasons of compatibility (both welding and mechanical), it was decided to construct the pull plates and tabs from the same type of steel as the ORNL wide-plate specimens (A533B).

Five steel companies were contacted and asked to submit bids for the four plates. American Alloy Plate of Houston, Texas, was chosen to be the supplier. The mechanical properties, chemistry, and heat treatment, as reported by American Alloy Plate, are shown in Tables 5.8 and 5.9.

Following the procurement of the steel plates, the next step was to find a welding company that could attach each tab end plate to the pull plate. This involved heavy section welding, and requests for bids were sent to three companies that perform this type of work. Included in the bid were requests for the machining of a 0.425-m hole in each tab end plate and the beveling of the plate adjacent to the welded region. General Welding Works of Houston, Texas, was chosen to perform the welding. Welding particulars, rod, wire, flux, and certification of the welder all met accepted nuclear construction codes. The welding rod was E10018 D2, the welding wire was F98-EF1-F1, and the flux was Oerliken OP121TT.

During the welding of the first tab end plate to the pull plate, difficulties were encountered. Initially, General Welding decided not to put a 26° bevel on the 0.152-m-thick plate. This proved to be an error, as the welder could not make a good weld using an automatic welder. The

Table 5.8. Mechanical properties[a] and heat treatment[b] for A533 Grade B Class 2 steel (Melt No. E18832) used for the tab ends and pull plates for the wide-plate test

(Manufacturers reported results)

Item	Pull plate	Tab ends
Thickness, cm	10.2	15.2
Slab No.	C275	C274
Ultimate tensile strength, MPa	730	768
0.2% Yield stress, MPa	596.7	637.3
Elongation, 5.1 cm, %	20	19
Reduction of area, %	48	37.5

[a]ASTM A533 Grade B Class 2: tensile strength: 620–792 MPa; specifications: yield stress, min: 482 MPa, elongation 5.1 cm, min %: 16.

[b]Heat treatment: all material 927°C for 1 h per 2.54 cm of thickness, quenched; tempered at 632°C for 1 h per 2.54 cm of thickness.

Table 5.9. Chemistry for the tab ends and pull tabs: A533 Grade B Class 2 quenched and tempered steel

Element	Content (wt %)	
	Mill report	ASTM A533-84 specification
Carbon, max	0.23	0.25
Manganese	1.31	1.15–1.50
Phosphorus, max	0.011	0.035
Sulfur, max	0.020	0.040
Silicon	0.35	0.15–0.40
Chromium	0.18	Not recorded
Nickel	0.60	0.40–0.70
Molybdenum	0.53	0.45–0.60

remainder was hand-welded, and radiographic and ultrasonic (UT) examinations were performed. Regions were totally unacceptable, and it was necessary to cut plates, put a bevel on both pieces, and reweld using automatic techniques. After rewelding, the plate was given an intermediate stress relief at 593°C. The second tab end and pull plates were also welded using automatic welding techniques and given an intermediate stress relief. Both welds were radiographed and UT examined, and the flaws found were repaired.

The final radiographic and UT results for these finished welds were then sent to NBS for examination. Two very thin cracks, about 0.0127 m and 0.025 m in length, were observed in one weld. The depth was estimated, using film density techniques, to be no greater than 0.002 m. The radiograph from the other weld was examined, and this weld was judged to be good.

It was estimated that the largest of these cracks should withstand a critical stress of 517 MPa, which corresponds to a fracture load in excess of 53 MN. Because this is two times the load capacity of the NBS test machine, it was decided not to have the cracks repaired, and the welds were accepted. Both weldments were given a postweld stress relief at 607°C for 2 h by General Welding.

Once the postweld stress relief was completed, the wide-plate test specimen, already sent to General Welding by ORNL, was welded to the pull plates. However, at the recommendation of NBS there was a change in the welding materials. The flux was Lincoln 860, and rod E7018 was used in the first pass and then EM12K. These changes reduced the possibility of weld cracking. The preheat temperature was the same, but the postweld heat treatment was at 232°C for at least 2 h. There was no postweld stress relief at 607°C. During the welding and postweld heat treatment, the temperature at the precracked region in the specimen was monitored;

it did not exceed 142°C. Two 0.05-m by 2.5-m plates were attached to the front and rear of the specimen to prevent the crack from being disturbed during the welding and subsequent shipment to NBS. NBS authorized the specimen pull-plate assembly to be shipped on August 29.

5.5.4 Temperature gradients system

The heating and cooling systems required must be capable of producing a linear temperature distribution across the specimen's width at the crack plane. Achieving and maintaining the temperature gradient is accomplished by controlled heating and cooling of the left and right edges of the plate surface, while the front and back surfaces are insulated. NBS was requested to develop a system that could maintain a linear thermal gradient across the specimen having a minumum temperature of --101°C at the cold notched edge and a maximum temperature of 260°C at the hot edge. A major consideration is the heat sink effect from the pull plates and test machine clevis devices. To maintain the desired linear thermal distribution within the area of interest (a/w = 0.2 to 0.8), the specimen edges may have to be heated or cooled beyond the required levels. Therefore, the thermal system can achieve temperatures beyond those requested in the initial requirements.

For heating, electrical resistance strip heaters were chosen. They are constructed of coiled nickel-chrome resistor wires embedded in a refractory material and sheathed in stainless steel. Each heating element is 61 cm long and 3.8 cm wide and has a maximum working temperature of 371°C. Either two or three heaters are attached side by side, longitudinally along the edge of a test specimen. Heating and cooling takes place along a 2440-mm length centered about the notched region of the specimen. The temperature will be maintained by powering each strip heater separately through a variable transformer controlled by a temperature controller.

A system to achieve and maintain a temperature of --101°C on the cold edge of a specimen was designed using liquid nitrogen (LN_2) as the coolant. A series of insulated chambers capable of either spraying gas and vaporizing liquid nitrogen onto the specimen surface or actually holding a reservoir of LN_2 in contact with the specimen edge were constructed. The cooling chamber is constructed of standard building lumber. Leakage is prevented at the wood joints and specimen by squeezing either rubber hose or rubber tape between the interfaces. The chamber is mounted onto the edge of a specimen and clamped tightly to seal the contact areas. Cooling is accomplished by pumping the LN_2 through a copper tube manifold affixed to the inside of the cooling chamber. The liquid or gas is sprayed across the specimen thickness at about 150-mm intervals down the length of the chamber. Control of temperature is maintained by starting and stopping the flow of LN_2 into the cooling chamber with an electrically activated solenoid valve. The valve is opended and closed by a temperature controller having a thermocouple sensor to monitor the specimen temperature. Additionally, the flow rate of the LN_2 can be varied by pressure valves that control the output from the LN_2 tanks. Provisions are to be available for filling the cooling chamber reservoir with LN_2 if that becomes necessary to obtain the low temperatures. The

performance of the insulation material is also important for maintaining a linear thermal gradient. Two different materials were chosen for the cold and hot sides of the specimen. Styrofoam sheeting used in building construction was chosen to insulate the cold half of the plate up to about 93°C. The styrofoam insulation is in sheet form, 25.4 mm thick, which can be stacked as needed for greater insulation. For temperatures on the specimen above 93°C, a mineral wool insulation blanket will be used. These blankets consist of a 50.8-mm-thick insulation material with a 25.4-mm wire mesh on both sides to retain insulation, form, and heat resistance. The insulation is suitable for temperatures to 566°C.

Thermal gradient readings of the test specimen will be taken during the entire course of the thermal and mechanical loading sequences with a data acquisition system capable of accessing at least 22 temperature sensors. The system consists of a data logger that can randomly access up to 40 channels that couple with an internal digital voltmeter. The data logger is interfaced with a computer for program control, data reduction, and output. Thermal readings can be taken at the operator's request or at a given time interval and provide hard copy output and data storage.

Certified type K (Chromel-Alumel) thermocouples were chosen for the temperature sensors. These thermocouples are bonded to a paper-thin laminate backing that can be glued to the specimen surface using a thermally conductive epoxy adhesive. Two different epoxies are used depending on the temperature range that the thermocouple will encounter. Glue-on thermocouples have the advantage of simple application and do not require holes to be drilled into the specimen. A disadvantage, however, is that temperature can be measured only at the surface of specimen. Two or three thermocouples will be mounted in 50.8-mm-deep holes to measure the internal temperatures and compare it with the surface.

To test the various heating and cooling systems that were developed, a test specimen mock-up was constructed. A hot-rolled steel plate — 1830 mm long, 1220 mm wide, and 12.5 mm thick — was used. The 22 cm of width in excess of an actual test specimen was used for attaching the heating and cooling systems. The extra width provides about the same area of heating and cooling during an actual test. For the mock-up tests, 1220 mm of the plate length (610 mm above and below the centerline) was used for heating and cooling the plate. The set-up is shown in Fig. 5.29.

An additional purpose of the mock-specimen test, other than to test prototype heating and cooling systems, was to obtain a linear thermal gradient along the centerline. Seventeen thermocouples were attached to one side of the plate along the centerline. As much of the exposed plate as possible was covered with insulation. The test began with the plate at ambient temperature. Figure 5.30 shows the temperatures after about 3.5 and 6.75 h. The test was stopped at 6.75 h. At that point, the thermal gradient was continuing to approach linearity at an extremely slow rate. Although perfect linearity was not achieved in the test, the results were good, and no further tests were scheduled before an actual specimen test.

In the first actual test, heating and cooling systems similar to those tested on the mock-up specimen will be used. The major difference will be in the area of heating and cooling on the test specimen. This

ORNL PHOTO 5946-84

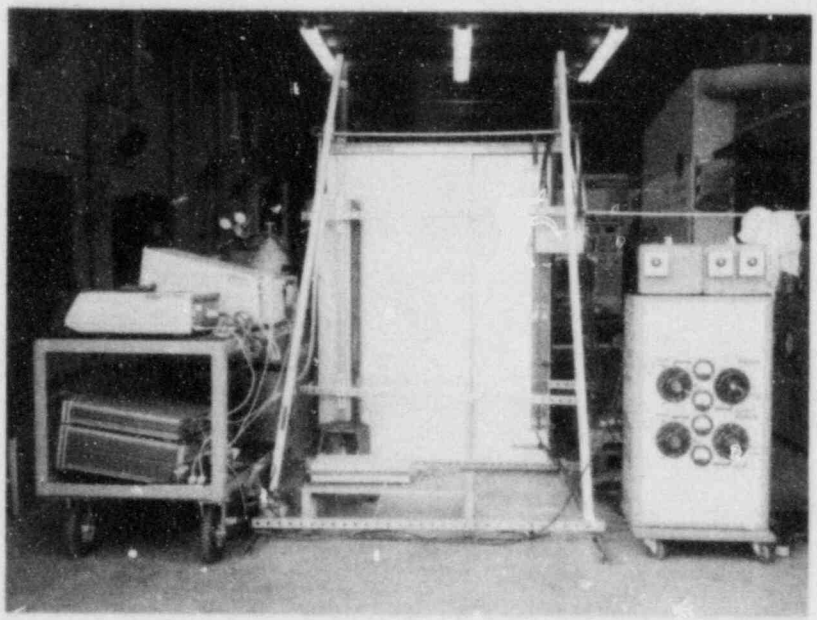

Fig. 5.29. Test specimen mockup with cooling, heating, and instrumentation systems attached.

ORNL-DWG 84-6181 ETD

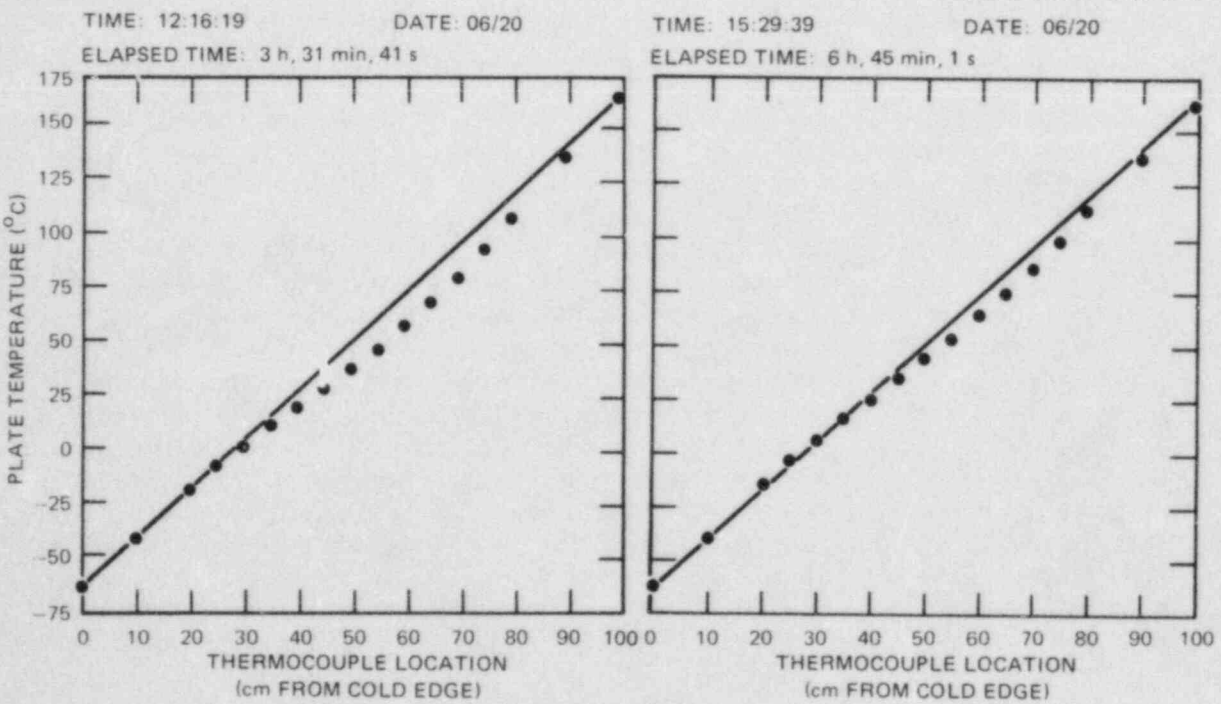

Fig. 5.30. Temperature as function of position along mockup specimen after 6.75 h of cooling and heating.

area will be doubled in length from 1200 mm to 2440 mm. This increase in area required that the number of strip heaters used be increased from 4 to 8 or 10. A modified cooling chamber is also required. The new cooling chamber will similarly be increased in length to 2440 mm. It will incorporate two separate coolant manifolds, each controlled independently and supplied from separate LN_2 tanks. The specimen and pull plates will be insulated as much as is feasible. With the increase in the heating and cooling areas and the results of the mock-up specimen test, we are confident that a nearly linear thermal gradient can be maintained in the specimen throughout the test sequence.

5.5.5 Effect of temperature gradient on thermal strain and stress state

5.5.5.1 No load case. The effect of the temperature gradient on the configuration of the specimen was investigated. As shown in Fig. 5.31, the "notch-edge" of the test plate will be cooled to a temperature T_{min}, and the "crack-arrest" edge will be heated to a temperature T_{max}. The extent of the temperature control along the height of the specimen is

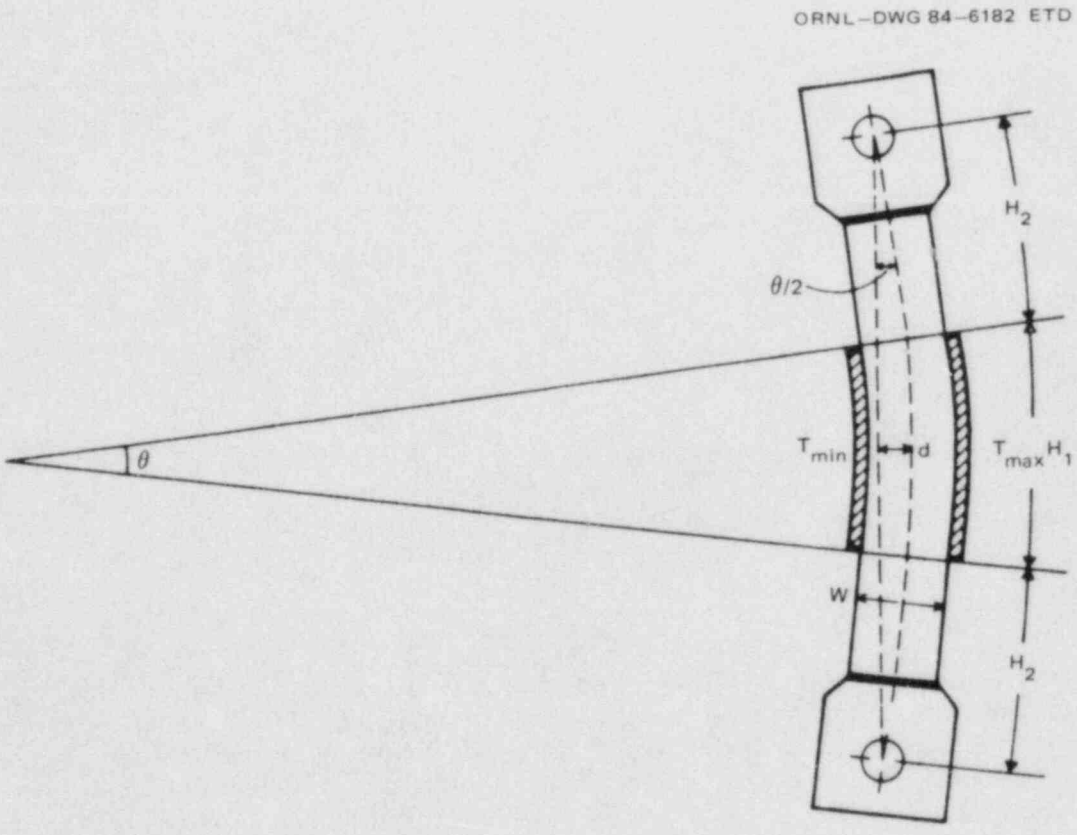

Fig. 5.31. Effect of temperature gradient on configuration of specimen (note in-plane bending).

given by H_1. An attempt will be made to establish a constant temperature gradient between the edges over this region, resulting in a uniform strain. Hence, the hot edge will increase in length over the cool edge by an amount

$$\Delta H = H_1(T_{max} - T_{min})\alpha \ , \tag{5.7}$$

where α is the coefficient of instantaneous thermal expansion. As a result, the section of the specimen with the temperature gradient will bend through an angle of $\theta = \Delta H/W$, where W is the specimen width. Figure 5.31 shows that H_2 is the length of each pull plate from the pinhole to the region of temperature control. Though this part of each pull plate remains unstrained, each is tilted with respect to the vertical by an angle of $\theta/2$. Therefore, the vertical line between the two pinholes will be offset from the centerline of the specimen. This offset will be a maximum at the notch position and is given by

$$d = H_1\theta/8 + H_2\theta/2 = (H_1/8W)(H_1 + 4H_2)(T_{max} - T_{min})\alpha \ . \tag{5.8}$$

For the first wide-plate crack-arrest test WP-1.1, the preliminary conditions and values were defined as

$$\begin{aligned} \alpha &= 11 \times 10^{-6}/°C, \\ T_{min} &= -62.2°C, \\ T_{max} &= 163.8°C, \\ W &= 1 \text{ m}, \\ H_1 &= 2.44 \text{ m}, \\ H_2 &= 3.70 \text{ m}. \end{aligned}$$

Hence, we find from Eq. (5.8) that

$$d = 13.1 \text{ mm} \ . \tag{5.9}$$

5.5.5.2 With load case. If a load P is applied to the pinholes of the specimen, the stress developed through the cross section of the specimen is given by

$$\sigma = (P/BW) - (Mx/I) \ . \tag{5.10}$$

The first term is the average stress, and the second term gives the stress variation due to the applied moment that results from the curvature of the sepcimen. The distance x is measured from the centerline of the specimen. The moment, which results from the applied load and the curvature offset, is $M = Pd$, and the moment of inertia for the plate is taken here to be given by $I = BW^3/12$, where B is the plate thickness.

Substituting this information into Eq. (5.10) gives

$$\sigma = (P/BW)\ \{1 - (12dx/W^2)\}\ . \tag{5.11}$$

For the preliminary WP-1.1 load of P = 10.65 MN and a thickness B = 101.6 mm, this results in

$$\sigma = 103.5(1 - 0.00015x)\ \text{MPa}\ . \tag{5.12}$$

At the extremities of the plate where $x = \pm W/2 = \pm 508$ mm, $\sigma = 103.5$ MPa ±7.7%.

5.5.6 Data acquisition system

The specimen will be instrumented with thermocouples, strain gages, and timing wires as shown in Fig. 5.3. BCL will be responsible for installing and monitoring crack velocity instrumentation. NBS will handle all other data acquisition. Most of the certified Type K (Chromel-Alumel) thermocouples will be mounted on the surface of the specimen but underneath the insulation. Two or three will be inserted into 50.8-mm-deep holes drilled adjacent to surface thermocouples to provide a comparison between surface and internal temperatures. All thermocouples will be monitored serially on a regular and frequent time basis during heating and cooling of the specimen to measure thermal gradients in the specimen. The data will be acquired by a data-logger/computer system and simultaneously printed out and recorded on magnetic tape to provide a thermal history of the specimen.

Strain gages (Micromeasurements Corp. designation CEA-06-250UW-350) will also be mounted as shown in Fig. 5.3. In particular, a row of eight strain gages will be mounted on each side of the crack plane; each pair of gages will form one arm of a full bridge circuit. The bridges used have been specially designed and constructed at NBS to have the lowest reactance possible. The outputs of the bridges are amplified by wide range, dynamic amplifiers designed and constructed by NBS in Boulder. Their gain is 113. The amplified signals are fed to high-speed digital oscilloscopes capable of resolving 0.5 μs. When the crack begins to move, it will activate a trigger setting of an oscilloscope which monitors a selected gage. The trigger setting is established by prototype fracture bars and compact-tension specimen tests. Once triggered, this oscilloscope will trigger all the rest within 5 ns. All strain gages will then be monitored for 2 ms. Once the data have been acquired, it will be automatically recorded onto magnetic disks within seconds of the event and then off-loaded to magnetic tape on the main computer for further analysis.

Besides the above temperature and strain data, the only other data recorded will be the load. This will be read off the testing machine dial and will also be monitored digitally along with the thermocouple data.

5.5.7 Validation of warm prestressing procedure

Before performing the first wide-plate crack-arrest test, three full-thickness precracked bend bars were tested to demonstrate that the planned WPS procedure was satisfactory. The bend bars, provided by ORNL (see Fig. 5.9), were machined from the same plate stock as the wide-plate specimens. Sharp cracks were introduced into these specimens by hydrogen charging an EB weld at the root of the notch. ORNL also estimated the crack length using UT testing. The desired WPS procedure was determined by ORNL. Testing of the bend bars was carried out in the Fracture and Deformation Division of NBS in Boulder, Colorado.

The relevant dimensions and actual (not UT) crack lengths of the three bars are given in Table 5.10. The spans for the three-point bend tests are also given in this table. Based on these dimensions, specimens 1 and 2 had been warm (50°C) prestressed to 129.3 and 135.6 MPa$\cdot\sqrt{m}$, respectively. ORNL had requested a prestress of 131 MPa$\cdot\sqrt{m}$. Thus, these specimens were warm prestressed at stress-intensity factor levels very close to the desired value. The actual loading history is given in Table 5.11. The heating took about 2 h, and the specimens were allowed

Table 5.10. Warm prestressing beam specimens

Specimen No.	Loading[a] span (cm)	Width (cm)	Thickness (cm)	Total side groove depth (cm)	Total crack[b] length (cm)
1	81.3	14.1	10.2	2.54	5.18
2	81.3	15.2	10.2	2.46	4.99
3	81.3	15.2	10.2	2.59	4.93

[a] Three-point bend.

[b] Includes machined notch depth.

Table 5.11. Loading history for warm prestressing beam test

Specimen No.	WPS[a] load[b] (kN)	WPS[a] K_I (MPa$\cdot\sqrt{m}$)	Reduced load (kN)	Reduced K_I (MPa$\cdot\sqrt{m}$)	Fracture[c] load[b] (kN)	Fracture[c] K_I (MPa$\cdot\sqrt{m}$)
1	403.0	129.3	342.5	109.9	403	129.3
2	532.0	135.6	452.2	115.3	665.0	169.4
3	0	0	0	0	327.8	83.7

[a] Warm prestressing at 50°C.

[b] All loading at 1.5 kN/min.

[c] Fracture took place at −17°C.

to thermally equilibrate for one-half hour prior to testing. The temperature was monitored using thermocouples on the surface and inserted into holes drilled to the midplane of the specimen. After equilibration, the temperatures on the surface and internally were within 1°C of each other.

After WPS, the specimens were unloaded by 15%: to 109.9 MPa$\cdot\sqrt{m}$ in the case of specimen 1 and to 115.3 MPa$\cdot\sqrt{m}$ for specimen 2. At this point, the specimens were cooled to room temperature and dry ice was packed around the ends of the specimens. After about 6 to 7 h the specimens reached −17°C.

Reloading at 1.5 kN/min was started once the specimens had been at −17°C for one-half hour. As noted in Table 5.11 specimen 1 broke just as it reached the WPS load. No evidence of plasticity was apparent on the load-crack-opening displacement (COD) record. A photograph of the fracture surface is shown in Fig. 5.32. Specimen 2 exceeded the WPS load by 25% at the point of fracture. There was considerable nonlinearity in the load-COD curve, indicating plasticity. The fracture surface is shown in Fig. 5.33. It should be noted that, at about 110% of the prestressing load, the testing machine cut out. Specimen 2 had to be completely unloaded and reloaded to fracture. The unloading probably increased the required fracture load by introducing compressive residual stresses near the crack tip. Therefore, the actual fracture load would have been anywhere between 10 and 25% over the WPS load had unloading not taken place.

Specimen 3 was not warm prestressed. It was simply cooled to −17°C, in the same manner as above, and loaded to fracture. This occurred at 83.7 MPa$\cdot\sqrt{m}$ and should represent the K_{Ic} at −17°C for this material. Comparing this value with the 129.3 and 169.4 MPa$\cdot\sqrt{m}$ required to break the warm prestressed specimens, significant K elevations are noted. Such

ORNL PHOTO 5947-84

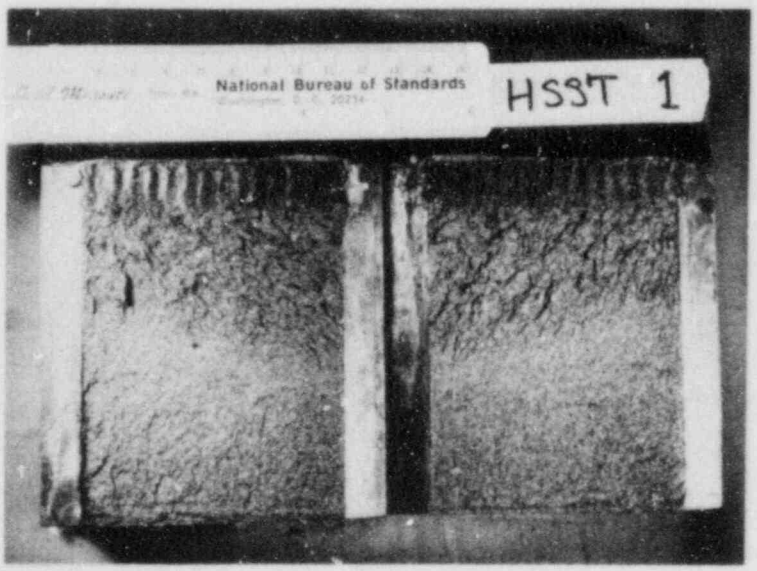

Fig. 5.32. Fracture surface of bend test specimen No. 1.

ORNL PHOTO 5948-84

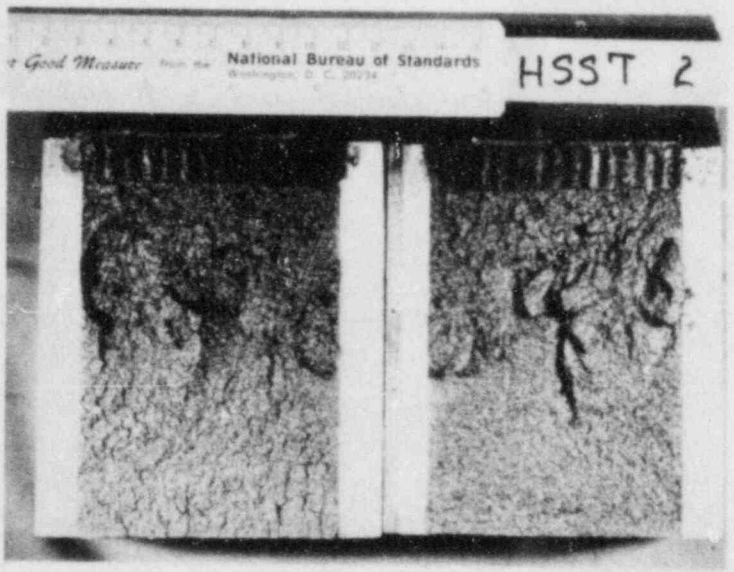

Fig. 5.33. Fracture surface of bend test specimen No. 2.

K elevations are necessary to produce the long run and arrest events required for the wide-plate tests. The fracture surface of specimen 3 is shown in Fig. 5.34.

In conclusion, the bend bar tests have validated, in principle, the WPS procedure planned for the wide-plate tests. Using WPS K levels similar to those applied here, it is expected that fracture may commence at between 1.5 to 2 times K_{Ic} at −17°C in the wide-plate tests.

The stress-intensity factors reported here for the beam specimens were calculated from the following equation:

$$K_I = (t/t_n)^{0.5}(1.5Ps/b^2t)(\pi a)^{0.5}F(a/w) \quad , \tag{5.13}$$

where

t = full thickness,
t_n = grooved thickness,
P = load,
s = span,
b = width,
a = total crack length,
$F(a/w)$ = geometric factor.

The geometric factors for s/b = 4 and 8 are given in Ref. 17. (Geometric factors appropriate for the s/b ratios used here were obtained by linear interpolation.)

ORNL PHOTO 5949-84

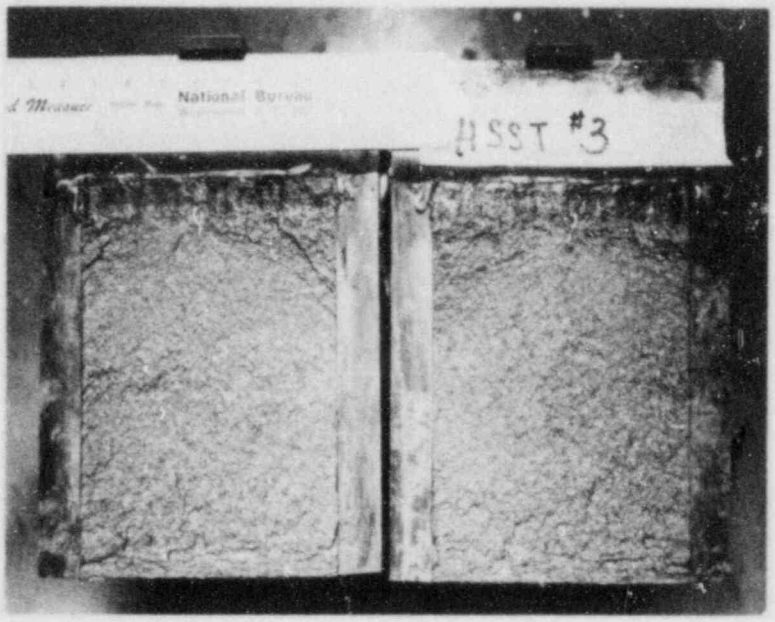

Fig. 5.34. Fracture surface of bend test specimen No. 3.

5.5.8 Status of wide-plate tests

For report scheduling purposes, the above sections were written in early September and reflect the status as of that time. All of the preparatory work was completed in the 6 months since this project began, and the first test (WP-1.1) was actually performed on September 28. Fine details of strain gage data acquisition were checked out as the first test specimen was arriving. The clevises were installed and instrumentation, thermal gradient system, and insulation were attached after mounting the specimen. Final confirmation of test conditions was established by ORNL for WP-1.1. The second wide-plate test, WP-1.2, should follow the first by about two months.

The first test will be reported in detail in the next progress report. However, the test was run under a linear temperature gradient of $T_{min} = -72°C$ and $T_{max} = 202°C$. After application of the warm prestressing sequence, crack propagation did not initiate at the expected 10.6-MN load ($K_I = 139$ MPa$\cdot\sqrt{m}$). The loading was continued to 19.0 MN before unloading to 11.9 MN and lowering the temperature of the cold side until the crack tip was at $-55°C$. Upon reloading, initiation occurred at 20.1 MN ($K_I = 269$ MPa$\cdot\sqrt{m}$). The crack exhibited an apparent arrest at $a/w = 0.49$, where $T = 51°C$, before the crack propagated through the remainder of the specimen in a ductile manner.

References

1. R. H. Bryan et al., *Quick-Look Report on the First Pressurized-Thermal-Shock Test, PTSE-1*, ORNL/PTSE-1, Union Carbide Corp. Nuclear Div., Oak Ridge Natl. Lab., March 7, 1984.

2. M. F. Kanninen et al., *Preliminary Analysis of Japanese Wide Plate Dynamic Crack Propagation Arrest Experiments*, Subcontract report from Battelle-Columbus Laboratories to Oak Ridge National Laboratory, December 1983.

3. ORNL Inspection Engineering Department, *Heavy-Section Steel Technology Program Guide for Material Control and Data Control*, Oak Ridge National Laboratory, June 15, 1968.

4. C. E. Pugh, "Description of an HSST Wide-Plate Crack-Arrest Test for Use in Pretest Benchmark Analysis," Martin Marietta Energy Systems, Inc., Oak Ridge Natl. Lab., Letter Communication CEP-05-84-87 (1984).

5. P. B. Crosley et al., *Cooperative Test Program on Crack Arrest Toughness Measurements*, NUREG/CR-3261, University of Maryland, College Park (1983).

6. C. W. Schwartz et al., University of Maryland, letter to C. E. Pugh, Martin Marietta Energy Systems, Inc., July 25, 1984.

7. A. R. Rosenfield et al., "Crack-Arrest Studies at BCL," in *Heavy-Section Steel Technology Program Semiannual Prog. Rep. Oct. 1983—March 1984*, NUREG/CR-3744, Vol. 1 (ORNL/TM-9154/V1), Martin Marietta Energy Systems, Inc., Oak Ridge Natl. Lab.

8. R. H. Bryan et al., *Quick-Look Report on the First Pressurized-Thermal-Shock Test, PTSE-1*, ORNL/PTSE-1, Martin Marietta Energy Systems, Inc., Oak Ridge Natl. Lab. (1984).

9. A. R. Rosenfield et al. "Battelle-Columbus HSST Support Program," pp. 12—37 in *Heavy-Section Steel Technology Program Quart. Prog. Rep. January—March 1983*, NUREG/CR-3334, Vol. 1 (ORNL/TM-8787/V1), Union Carbide Corp. Nuclear Div., Oak Ridge Natl. Lab.

10. "Proposed ASTM Test Method for Crack-Arrest Fracture Toughness of Ferritic Materials," Revised: June 1984, working document of ASTM Task Group E24.01.06, 1984.

11. E. T. Wessel, "Contribution by E. T. Wessel," pp. 12—22 in *ORNL Foreign Trip Report*, ORNL/FTR-1786, Martin Marietta Energy Systems, Inc., Oak Ridge Natl. Lab. (1984).

12. A. R. Rosenfield et al., "Battelle-Columbus HSST Support Program," pp. 3–30 in *Heavy-Section Steel Technology Program Quart. Prog. Rep. April–June 1982*, NUREG/CR-2751, Vol. 2 (ORNL/TM-8369/V2), Union Carbide Corp. Nuclear Div., Oak Ridge Natl. Lab.

13. K. Rahka, "Vibrations in Compact Specimens During Crack Arrest Testing," *J. Testing Eval.* 8, 318–23 (1980).

14. R. D. Cheverton and D. G. Ball, "The Role of Crack Arrest in the Evaluation of PWR Pressure Vessel Integrity During PTS Transients," presented at the CSNI Meeting on Crack Arrest, Friebourg, Germany (1984).

15. C. W. Marschall et al., "Crack Arrest Behavior of Pressure Vessel Plates and Weldments as Influenced by Radiation and Copper Content," presented at the Twelfth International Symposium on Effects of Radiation on Materials, Williamsburg, Va., June 1984.

16. G. T. Hahn et al., "A Preliminary Study of Fast Fracture and Arrest in the DCB Test Specimen," pp. 649–62 in *Dynamic Crack Propagation*, ed. G. C. Sih, Noordhoff, Leyden (1973).

17. H. Tada, P. Paris, and G. Irwin, *Stress Analysis of Cracks Handbook*, Del Research Corp., Hellertown, Pennsylvania (1973).

6. IRRADIATION EFFECTS STUDIES

R. K. Nanstad

6.1 Fourth HSST Irradiation Series

J. J. McGowan T. N. Jones
R. G. Berggren R. L. Swain

The cooperative testing program with Materials Engineering Associates (MEA) on specimens from the first three capsules of the Fourth HSST Irradiation Series is continuing. Testing of all unirradiated 1T-CS specimens has been completed, and testing of the irradiated 1T-CS specimens is continuing. Testing of the 1T-CS specimens in the transition region has been completed, and testing of the 1T-CS specimens in the upper-shelf region is one-third complete. All of the 1T-CS specimen tests are expected to be completed within the next reporting period.

Both Oak Ridge National Laboratory (ORNL) and MEA used unloading compliance to measure crack length, and all specimens had razor blades mounted at the load line. The ORNL testing system used an HP-9836 microcomputer to control the test and acquire data; as a result, the crack length could be determined within 0.02 mm during each unloading. The specimen was loaded under load-line displacement control at a rate of 0.2 mm/min. A 1-min hold at constant load-line displacement was performed prior to each unloading to minimize hysteresis problems. Smooth-sided specimens were used in the transition region; 20% side-grooved specimens, however, were used in the upper-shelf region. When applicable, K_{Ic} according to ASTM E399 (Ref. 1) was determined; otherwise, the modified Ernst J-integral[2] was used to infer $K_J = \sqrt{EJ_c}$, where $E(GPa) = 207.2 - 0.057\ T(°C)$. If there was no significant crack growth (the J_I vs Δa curve did not intersect the 0.15-mm exclusion line), J to maximum load was used to determine K_J. If there was significant crack growth (the J_I vs Δa curve did intersect the 0.15-mm exclusion line), J_{Ic} was used to determine K_J. J_{Ic} is determined both with the power law and ASTM E813 procedure.[3] A summary of results from all the irradiated tests with nonsignificant crack growth is shown in Table 6.1 for ORNL. A summary for all irradiated tests with significant crack growth is shown in Table 6.2 for ORNL. The $K_{\beta c}$ values were calculated using the Merkle method[4] to estimate lower-bound fracture toughness in the transition region. Results obtained with unirradiated specimens are given in the most previous progress report.[5]

A comparison of the fracture toughness data for the two laboratories is shown in Figs. 6.1–6.5. Note that there is no significant variation between the two laboratories.

The data scatter among all materials is comparable both for irradiated and unirradiated conditions (the degree of scatter depends upon the temperature regime). The lower transition and upper shelf have low scatter ($\pm 15\ MPa\cdot\sqrt{m}$), while the upper transition regime has high relative scatter ($\pm 50\ MPa\cdot\sqrt{m}$).

A summary of the material properties is shown in Table 6.3 (taken from Ref. 6) after neutron irradiation to a target fluence of 2×10^{23}

Table 6.1. ORNL transition region test data summary for irradiated 1T-CS specimens

Specimen No.	Test temperature (°C)	Fluence, 10^{22} (neutrons/m^2)	Irradiation temperature (°C)	$(a/w)_i$	J_{max} (kJ/m^2)	K_{Jc} (Mpa·$\sqrt{m}$)	K_{Ic} (MPa·$\sqrt{m}$)	$K_{\beta c}$ (MPa·$\sqrt{m}$)	Yield stress (MPa)
02GA-288	79	20.4	288	0.624	84.6	131.0		89.5	591
-401	−25	12.9	288	0.609	16.7		58.9		647
-406	−25	19.5	288	0.602	14.4		45.1		647
-407	50	20.5	288	0.611	18.3	61.2		56.6	604
-414	−25	21.8	288	0.593	7.1		36.2		647
68W-BB	−75	10.2	288	0.593	84.8	133.9		102.2	757
-HC	−130	12.1	288	0.601	13.9		52.5		833
-MB	−130	17.4	288	0.598			39.8		833
69W-113	29	12.4	288	0.617	54.2	105.5		86.9	714
-119	−35	15.1	288	0.593	15.3		57.0		784
-142	−36	13.4	288	0.594	12.9		55.0		785
-143	50	12.3	288	0.597	68.3	118.2		92.2	703
-149	−35	8.8	288	0.581	24.3		69.8		784
70W-123	−25	24.9	288	0.539	19.4	63.6		57.7	579
-126	−125	26.0	288	0.547	6.3		37.9		692
-140	−125	17.7	288	0.541	6.4		36.9		692
-148	−25	14.5	288	0.539	123.4	160.4		97.2	579
71W-108	−70	13.1	288	0.545	20.2	65.3		59.9	622
-122	−13	20.5	288	0.546	57.4	109.2		79.8	563
-133	0	27.3	288	0.538	74.9	124.6		84.3	552
-141	−70	22.9	288	0.549	21.8	67.9		61.9	622
-143	−73	19.4	288	0.548	5.6		36.6		625
-144	0	19.0	288	0.540	125.4	161.2		94.8	552

Table 6.2. ORNL upper-shelf J-R curve data summary for irradiated 1T-CS specimens

Specimen No.	Test temperature (°C)	Fluence, 10^{22} (neutrons/m^2)	Side groove (%)	Irradiation temperature (°C)	$(a/w)_i$	Δa_m (mm)	$\Delta a_p - \Delta a_m$ (mm)	J_{Ic} (kJ/m^2)		K_{Jc} (MPa$\sqrt{m}$)		T_{avg}		Flow stress (MPa)	J = 8.8T (kJ/m^2)	E813 validity
								Power law	ASTM	Power law	ASTM	Power law	ASTM			
02GA-329	80	26.0	0	288	0.612	7.60	−7.34	151.1		175.0				657	1330	Invalid
-344	80	10.5	0	288	0.607	9.07	−8.79	131.0		162.9				657	1153	Invalid
-421	80	17.7	0	288	0.603	9.17	−8.75	148.1		173.2				657	1303	Invalid
69W-116	52	14.0	0	288	0.580	0.89	−0.251	77.7	56.2	125.9	107.1	60.8	67.5	739	684	Invalid
-165	50	19.0	0	288	0.592	2.26	0.21	95.5	85.6	139.7	132.2	59.2	60.7	740	840	Invalid
71W-140	16	21.2	0	288	0.554	0.71	−0.33	151.3		176.7				595	1331	Invalid

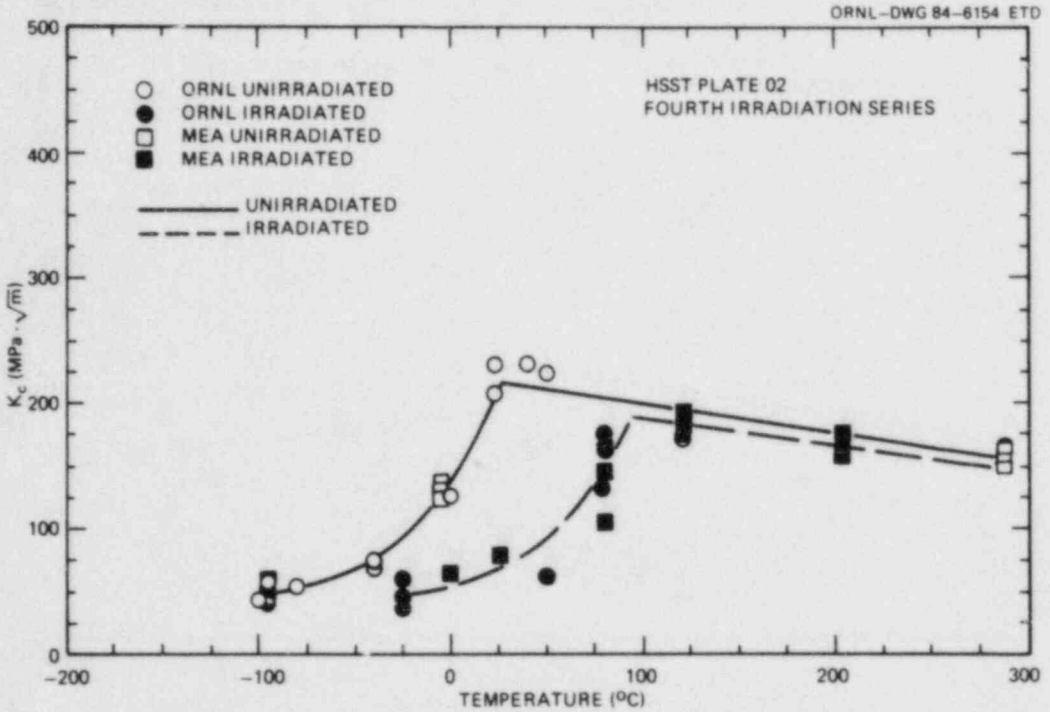

Fig. 6.1. Fracture toughness of irradiated and unirradiated HSST-Plate 02.

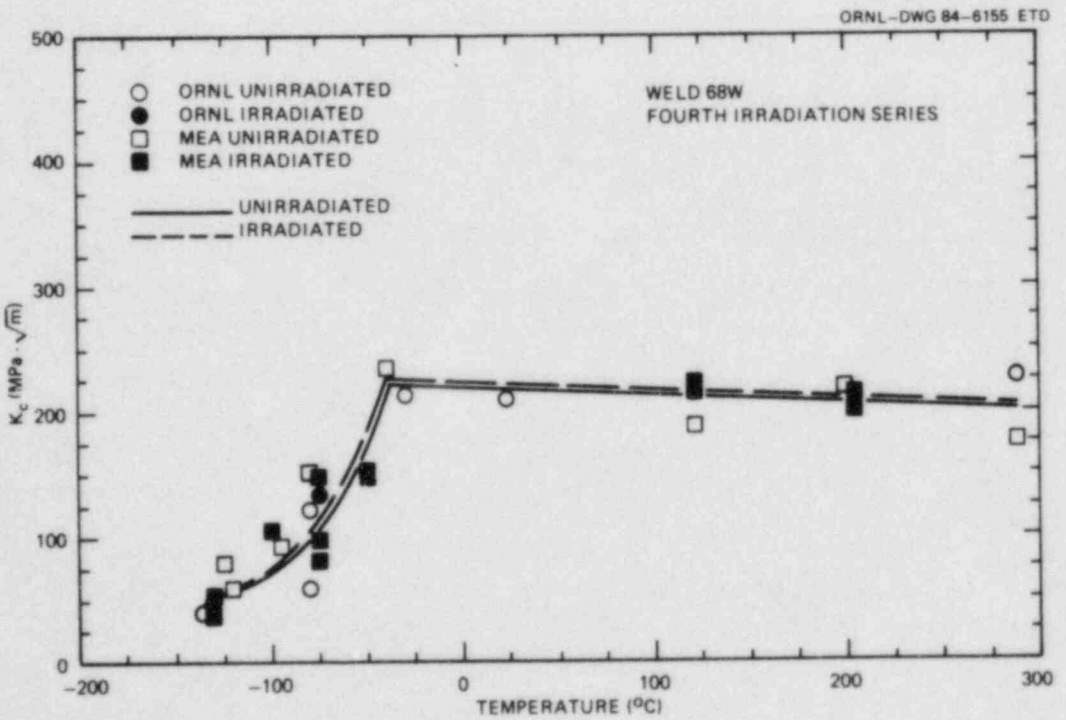

Fig. 6.2. Fracture toughness of irradiated and unirradiated weld 68W.

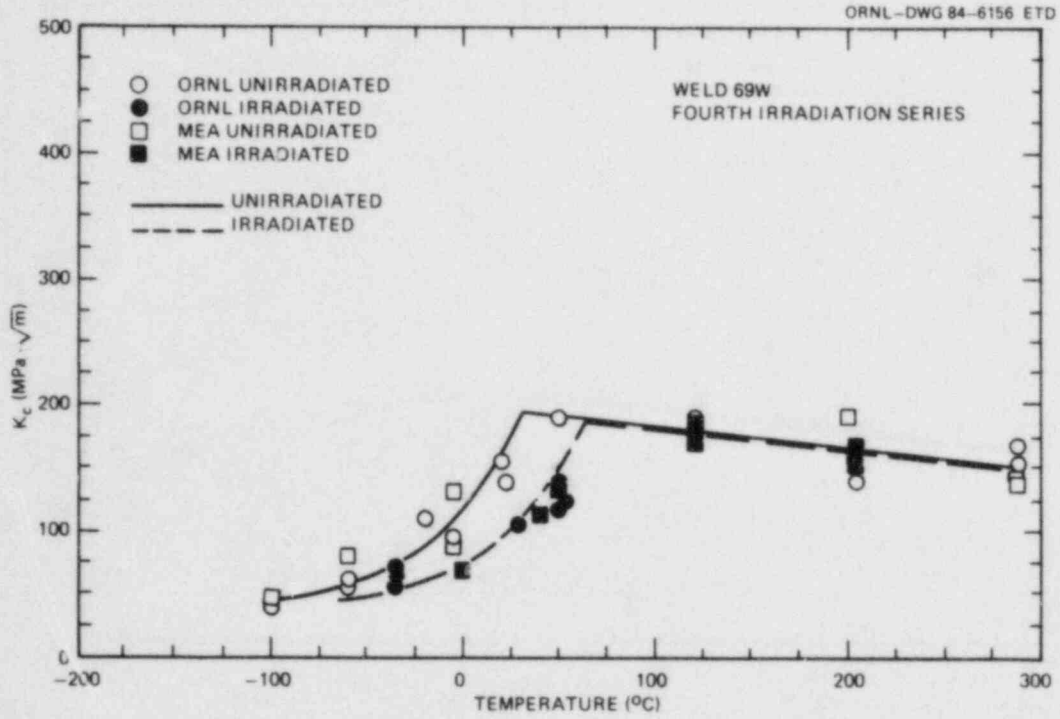

Fig. 6.3. Fracture toughness of irradiated and unirradiated weld 69W.

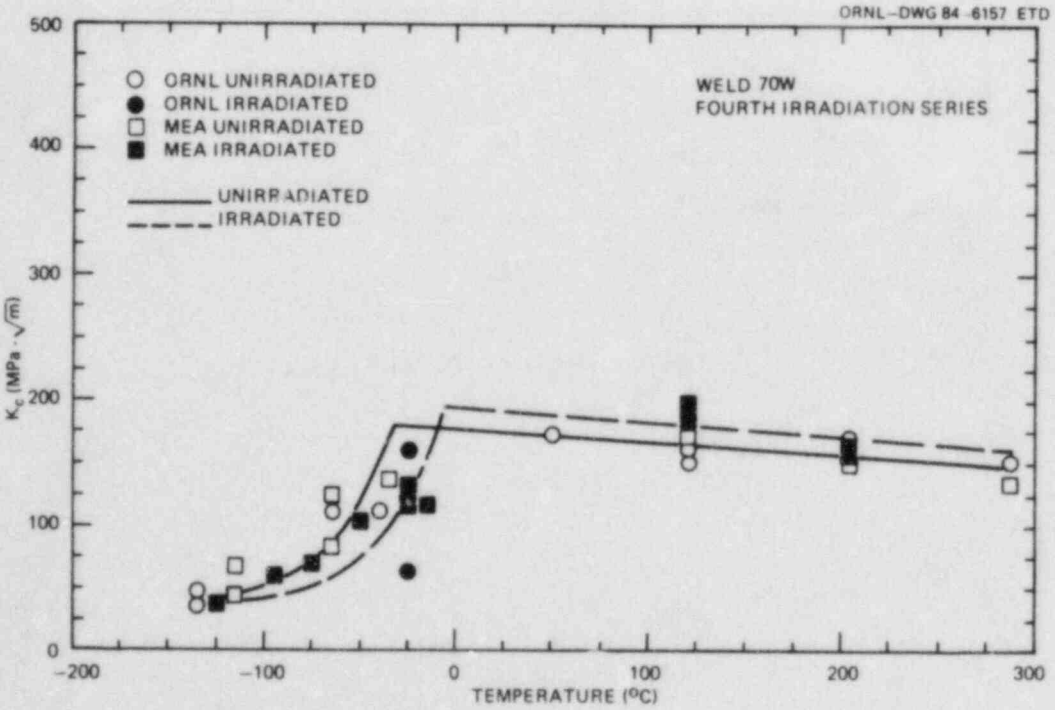

Fig. 6.4. Fracture toughness of irradiated and unirradiated weld 70W.

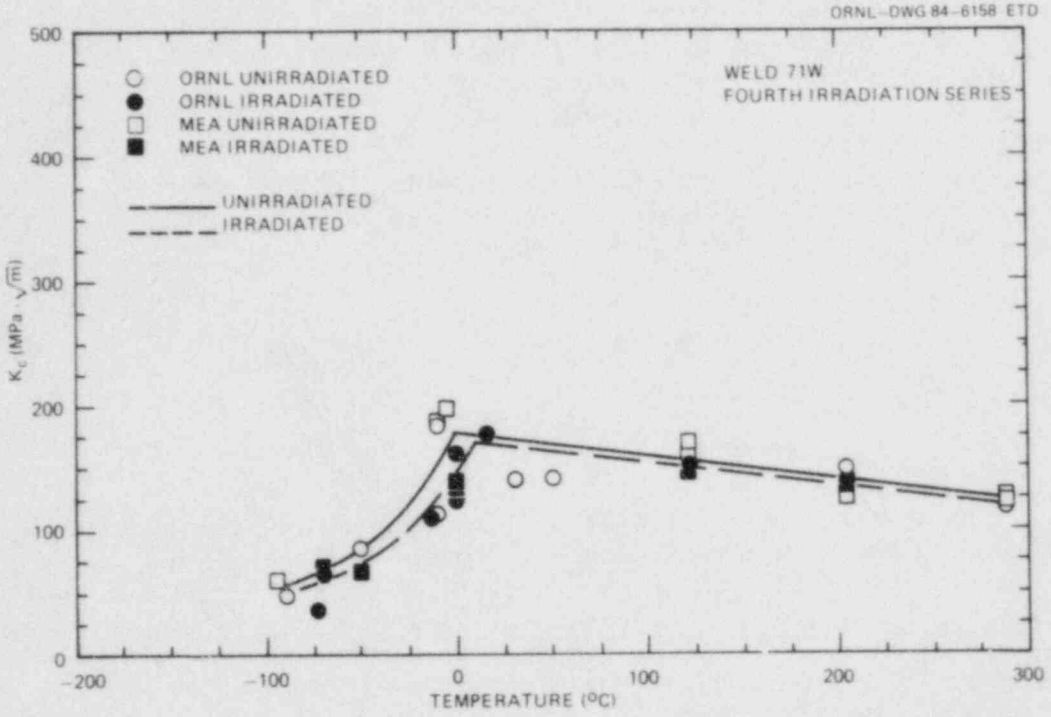

Fig. 6.5. Fracture toughness of irradiated and unirradiated weld 71W.

Table 6.3. Transition temperature shift after neutron irradiation to a target fluence of 2×10^{23} neutrons/m^2

Material	Transition temperature shift (°C)		Composition (wt %)	
	Charpy V-notch[a]	K_c	Cu	Ni
Plate 02	68	75	0.14	0.67
Weld 68W	6	−2	0.04	0.13
Weld 69W	34	35	0.12	0.10
Weld 70W	31	24	0.056	0.63
Weld 71W	26	13	0.046	0.63

[a]Source: R. G. Berggren et al., "An Analysis of Charpy V-Notch Impact Toughness of Irradiated A533 Grade B Class 1 Plate and Four Submerged-Arc Welds," *Proceedings of the Twelfth International Symposium on the Effects of Radiation on Materials*, Williamsburg, Va., June 18–22, 1984, American Society for Testing and Materials, Philadelphia.

neutrons/m^2 (>1 MeV). Note that there is good agreement for the transition temperature shift between the Charpy V-notch and fracture toughness results. The transition temperature is ordered from low to high by the amount of copper present. Comparison of welds 68W and 71W shows the effect of nickel on transition temperature shift.

From the preliminary results of testing on the upper shelf, it does not appear that the fracture toughness upper shelf in these materials is affected significantly by irradiation.

6.2 Fifth HSST Irradiation Series

R. G. Berggren K. R. Thoms
R. K. Nanstad F. B. Kam

The primary objective of the Fifth HSST Irradiation Series is to obtain valid fracture toughness K_{Ic} curves for two nuclear pressure vessel materials irradiated at 288°C and to as high a toughness level as practical. The program has been described previously.[7-9] However, completion of neutron dosimetry results (prototype exposures) and detailed irradiation capsule designs have led to some minor changes in the program. This report summarizes the present program.

Currently, estimates of the K_{Ic} curve shift are based on results from Charpy impact testing with the assumption that the shift of a Charpy toughness curve to higher temperatures can be applied directly to a K_{Ic} curve. To test this assumption, this program includes Charpy V-notch impact test specimens and drop-weight test specimens, in addition to the compact fracture toughness specimens. Tensile specimens are included in the program to provide data for determining test parameters for the fracture toughness tests and for analysis of the fracture toughness data.

Irradiation and material parameters were chosen to (1) provide significant separation of unirradiated and irradiated properties (i.e., a significant radiation-induced temperature shift of toughness properties), (2) represent, as closely as possible, materials used in early nuclear pressure vessel construction (high copper and nickel contents), and (3) permit program conclusion in a reasonable time. The chosen irradiation parameters are an irradiation temperature of 288°C (550°F) — most significant for both the industry and regulatory bodies — and a neutron fluence of 1.5×10^{23} neutrons/m^2 (>1 MeV) to complete irradiations in a reasonable time. The chosen materials are submerged-arc weldments of 0.23% and 0.32% Cu content (0.60% Ni in both weldments). The predicted temperature shifts of fracture toughness for these two weldments are 86 and 121°C (155 and 217°F), respectively, for the above irradiation parameters. The lower bounds (95% confidence level) are 58 and 93°C (105 and 167°F), respectively. These predictions are based on the Metal Properties Council analyses[10] of weld metals irradiated in test reactors.

The plan provides sufficient numbers of specimens to permit meaningful statistical analyses of test results.

6.2.1 Materials

To provide as uniform a test material as possible, submerged-arc weldments were fabricated using two special heats of AWS type EF-2 welding wire with copper added in the ladle to achieve the two levels of copper content. One lot, well mixed, of Linde 124 flux was used for all the welds. The weldments were fabricated and stress-relieved according to commercial practice. The base plate for the weldments is a single 220-mm-thick plate of SA533 Grade B Class 2 steel. The submerged-arc welding was done by the tandem-arc, alternating-current procedure, using a 0° bevel weld groove. The width of the deposited weld metal is about 30 mm. All welds were stress-relieved at 607°C for 40 h. About 14 linear meters of each weldment were fabricated for the program. (This amount will also provide material for the Sixth HSST Irradiation Series on irradiation effects on crack arrest.)

6.2.2 Specimen complement

The largest practical compact K_{Ic} specimen that can be irradiated is a 4T-CS specimen. The irradiated yield stress will be about 620 MPa, resulting in a valid fracture toughness K_{Ic} measuring capacity of 130 MPa$\cdot\sqrt{m}$. To achieve this toughness level in the unirradiated specimens having a yield stress of about 480 MPa requires 8T-CS specimens, and these are provided for in the program. Smaller fracture toughness specimens are provided to measure toughness at lower levels and to obtain both K_{Jc} values for predicting test parameters for the larger specimens and data for comparisons of K_{Ic} and K_{Jc} results. The types, sizes, and number of specimens per material are presented in Tables 6.4 and 6.5. The total specimens are twice the number listed. The number of specimens is based on consideration of statistical analysis requirements and the constraints of the irradiation facility. Sufficient amounts of the weldments are available for fabrication of additional unirradiated specimens, if necessary.

6.2.3 Irradiation capsule design and operation

The Fifth HSST Irradiation Series consists of a total of 12 capsules to be irradiated in the poolside facility of the Oak Ridge Research Reactor (ORR). Neutron dosimetry studies in the facility were conducted in a dummy capsule, and a prototype of the 4T capsules was operated in the facility to obtain neutron and gamma heat parameters for final experiment design. A steel gamma shield was incorporated into the facility to allow control of specimen temperatures.

The final capsule designs provide for the irradiation of the specimens shown in Table 6.6, which also gives the predicted fast neutron fluences and ranges based on the results of the measurements conducted in the dummy capsule. Neutron dosimeter sets are also included in each capsule to verify the exposures.

The initial neutron characterization of the irradiation facility was completed, and the results indicated that the flux levels were significantly lower than the experiment design basis. Consequently, steps

Table 6.4. Compact specimen complement for the K_{Ic} curve shift program

Test/specimen types	Number of specimens per material						
Target K_{Ic} ($MPa\cdot\sqrt{m}$) and Estimated T-NDT (°C)	49 / −56	66 / −14	88 / 3	110 / 11	132 / 19	Spare specimen	Totals
Unirradiated							
K_{Ic}, 1T-CS[a]	10					[b]	10
K_{Ic}, 2T-CS[a]		4				[b]	4
K_{Ic}, 4T-CS[a]			4			[b]	4
K_{Ic}, 6T-CS[a]				2		2	4
K_{Ic}, 8T-CS[a]					2	2	4
K_J, 1T-CS		6	6	6	6	[b]	24
K_J, 2T-CS		4	4	4	4	[b]	12
K_J, 4T-CS				4[c]	4[c]	[b]	8[c]
Irradiated							
K_{Ic}, 1T-CS[a]	4	6				2	12
K_{Ic}, 2T-CS[a]			6			4	10
K_{Ic}, 4T-CS[a]				4	4		8
K_J, 1T-CS			6	6	6		18
K_J, 2T-CS				4	4		8

[a] Valid tests.

[b] Material for additional specimens is available.

[c] These tests would be valuable if material is available.

Table 6.5. Charpy V-notch impact, drop-weight, and tensile specimens for K_{Ic} curve shift program

Estimated test temperature relative to NDT (T-NDT) (°C)	Number of specimens per material					
	Charpy-V specimens		Drop-weight specimens		Tensile specimens	
	Unirradiated	Irradiated	Unirradiated	Irradiated	Unirradiated	Irradiated
Scoping tests[a]	16	1?	12	16		
−56					6	3
−28	5					
−14					6	3
0	10	10				
+24					6	3
+40	10	5				
+70	10	5			6	3
+111	10					
+167	10	5				
+222	10					
Spares		18				4
Totals (per material)	81	56	12	16	24	16

[a]Varied temperatures to determine NDT and "upper-knee" temperatures.

Table 6.6. Specimen complement and predicted neutron fluences for irradiation capsules

Capsule type	Number of capsules per material	Specimen[a] type	Number of specimens per capsule	Predicted neutron fluence [10^{23} neutrons/m^2 (>1 MeV)]		
				Maximum	Mean	Minimum
4T	4	4T-CS	2	1.54[b]	1.50[b]	1.46[b]
		CVN[c]	12	1.83	1.65	1.53
2T	1	2T-CS	18	1.78	1.50	1.07
		CVN	12	1.53	1.50	1.46
1T	1	1T-CS	30	1.64	1.50	1.36
		DW(F)[d]	8	1.51	1.46	1.41
		DW(B)[d]	8	1.14	1.10	1.06
		CVN	56	1.59	1.51	1.39
		MT	16	1.59	1.51	1.39

[a] 4T-CS, 2T-CS, and 1T-CS are compact specimens of 101.6-, 50.8-, and 25.4-mm thickness, respectively; DW are P-3 drop-weight specimens; CVN are standard Charpy V-notch specimens; and MT are miniature tensile test specimens.

[b] These fluence values are for the 1/4- and 3/4-thickness positions at the fatigue crack front. Due to neutron attenuation, there will be a fluence variation along the crack front with maximum variations of −7% at the center and +21% at specimen surfaces.

[c] The CVN specimens in the 4T capsules are nonstandard (10 × 9.5 × 55 mm) and will be used for initial scoping studies.

[d] "F" and "B" refer to front and back groups of drop-wieght specimens in the 1T capsule.

were taken to allow the entire facility to be moved closer to the reactor core. During this exercise, the facility was discovered to be 2.5 cm from the core box wall instead of the 2.0 cm reported previously[11] for the operation of the prototype. Following the relocation of the facility, which resulted in a 1.0-cm gap between the thermal shield and the core box wall, another neutron characterization run was made, indicating that a fast fluence (>1.0 MeV) of 1.5×10^{23} neutrons/m^2 could be obtained in about 60 d for the 4T capsules.

The first two 4T capsules, designated HSST5-1 and HSST5-2, were installed in the irradiation facility during the April 22 to May 2, 1984, shutdown of the ORR. Following extensive checkouts of both the capsules and the facility instrumentation, the irradiation facility was inserted, and irradiation began on May 11, 1984. A summary of the observed temperature along the crack tip of each specimen is presented in Fig. 6.6. The lower curves show the temperature profiles with no electric heat in the 18 heater zones of each capsule, while the upper curves show the profiles with the heat being applied to the capsules to achieve the desired 288°C at the 1/4T position. It should be noted that the peak-to-minimum temperature is significantly higher than that reported for the

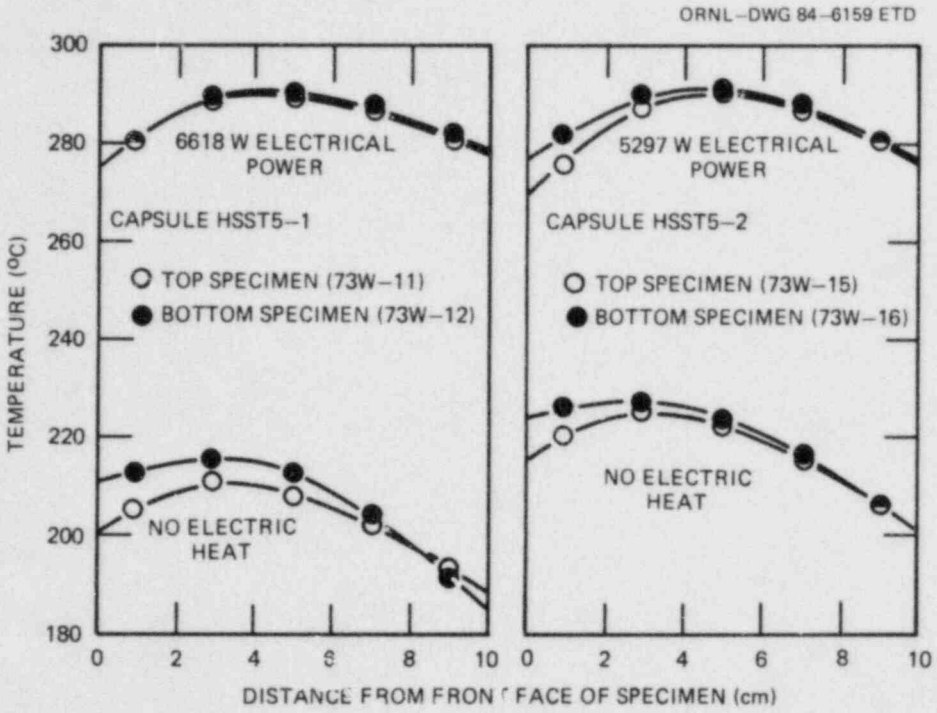

Fig. 6.6. Temperatures observed during initial startup of capsules HSST5-1 and HSST5-2 on May 11, 1984.

prototype.[11] The need to move the facility closer to the core results in a higher gamma heating rate that increases the temperature gradient. The use of a seven-element "A" row, put in place to increase the flux and reduce the horizontal flux gradient, also increases the gamma heating. The temperature patterns on the front and back surfaces of both capsules during startup are shown in Table 6.7, with the location of thermocouples and heater zones being shown in Fig. 6.7.

After 30 EFPD of irradiation, the capsules were rotated on June 11, 1984, and after an additional 30 d the irradiation was terminated on July 21, 1984. In general, the temperature control during irradiation was very good. Capsule HSST5-2 operated somewhat hotter than HSST5-1. Also, at times, the control of the front surface of the specimens was not very good, but the desired 288°C at the 1/4T position was easily maintained. The recorded temperature data are presently being reduced, and average temperatures for all thermocouples, as well as their variations with time, will be reported in the next semiannual progress report.

The second set of 4T capsules, HSST5-3 and HSST5-4, began irradiation on August 16, 1984. Temperature profiles along the crack tip of each specimen immediately after the beginning of irradiation are summarized in Fig. 6.8. The temperature patterns on the front and back surfaces of the specimens are shown in Table 6.8. Both capsules are being controlled very satisfactorily, with none of the problems experienced with HSST5-2 having materialized to date.

The assembly of the small specimen capsules will begin as soon as the fatigue cracking and remachining of the 1T compact specimens are

Table 6.7. Summary of observed specimen surface temperatures and electric heater input during the startup of HSST5-1 and HSST5-2 on May 11, 1984

Heater zone or thermocouple No.[a]	HSST5-1			HSST5-2		
	No electric heat	Total electric heat of 6618 W		No electric heat	Total electric heat of 5297 W	
	Temperature (°C)	Temperature (°C)	Power (W)	Temperature (°C)	Temperature (°C)	Power (W)
Front face						
1	203	279	404	198	277	454
2	205	280	145	220	275	15
3	188	280	532	223	276	197
4	226	281	0	219	277	103
5	218	280	25	232	284	0
6	210	281	91	240	285	0
7	207	280	366	204	276	280
8	213	280	19	226	282	0
9	197	279	409	222	277	138
Back face						
11	192	281	552	188	281	670
12	192	281	333	206	281	327
13	175	281	778	208	280	482
14	207	281	318	203	280	463
15	199	282	377	212	282	291
16	191	281	527	220	281	260
17	193	280	544	188	280	715
18	192	282	420	206	282	339
19	176	281	783	207	281	562

[a]Location of heater zones and thermocouples (TC) shown in Fig. 6.7.

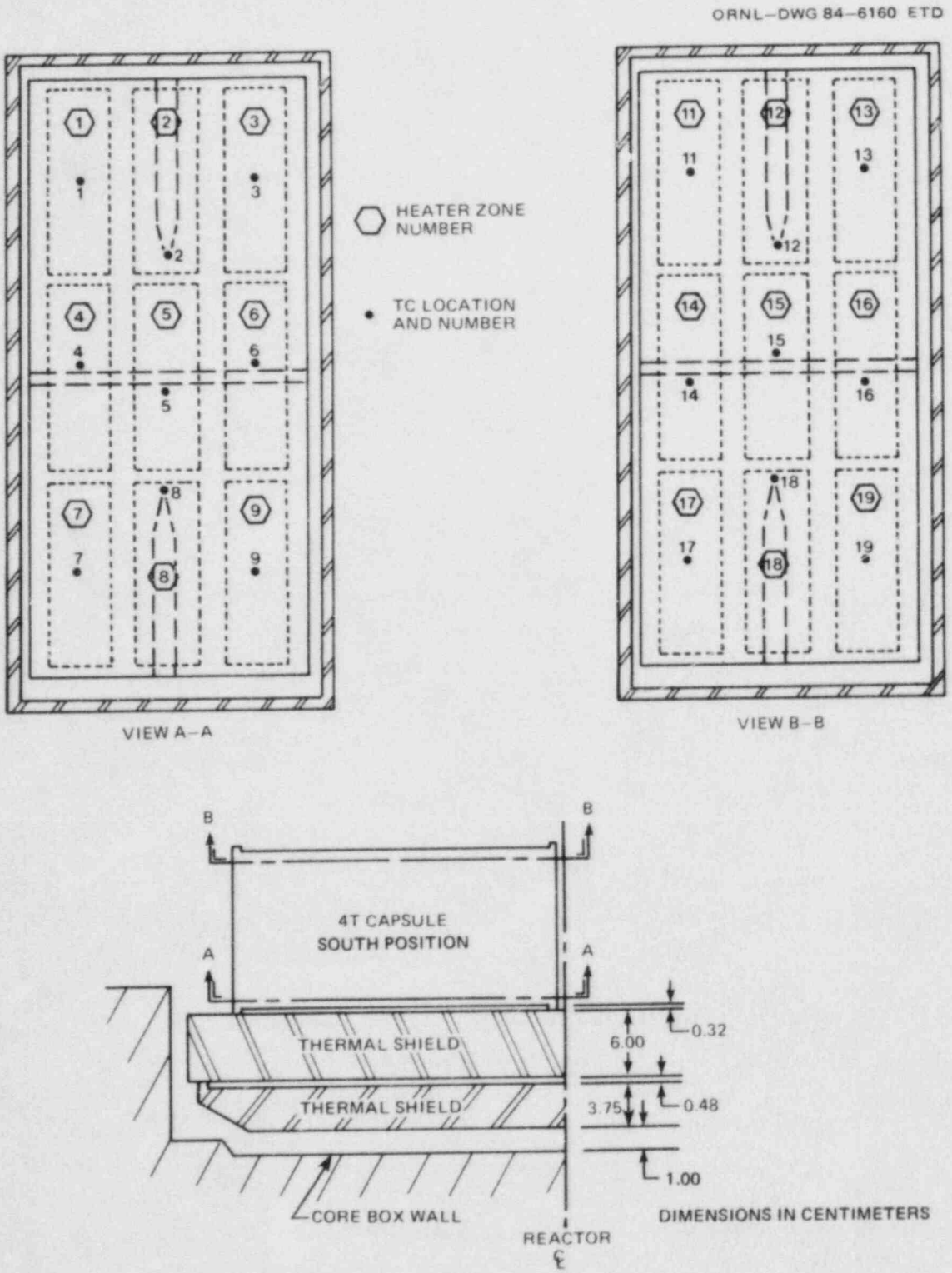

Fig. 6.7. Plan view of 4T capsule in southern position of ORR poolside facility and location of heater zones and specimen surface thermocouples. Identical configuration exists on north side of reactor centerline.

Table 6.8. Summary of observed specimen surface temperatures and electric heater input during the startup of HSST5-3 and HSST5-4 on August 16, 1984

Heater zone or thermocouple No.[a]	HSST5-3			HSST5-4		
	No electric heat	Total electric heat of 7501 W		No electric heat	Total electric heat of 6764 W	
	Temperature (°C)	Temperature (°C)	Power (W)	Temperature (°C)	Temperature (°C)	Power (W)
Front face						
1	189	281	532	188	280	532
2	196	281	142	207	280	101
3	178	281	616	206	280	364
4	213	281	74	209	280	199
5	209	281	73	218	280	88
6	202	281	145	226	280	14
7	199	282	445	200	280	423
8	204	281	21	219	282	0
9	188	281	474	218	280	222
Back face						
11	182	283	592	179	282	751
12	183	284	363	195	282	386
13	168	284	779	195	282	559
14	197	283	444	192	282	610
15	190	283	393	200	282	380
16	184	283	540	208	282	390
17	185	283	631	183	282	760
18	187	284	432	201	282	330
19	170	283	805	197	282	655

[a]Location of heater zones and thermocouples (TC) shown in Fig. 6.7.

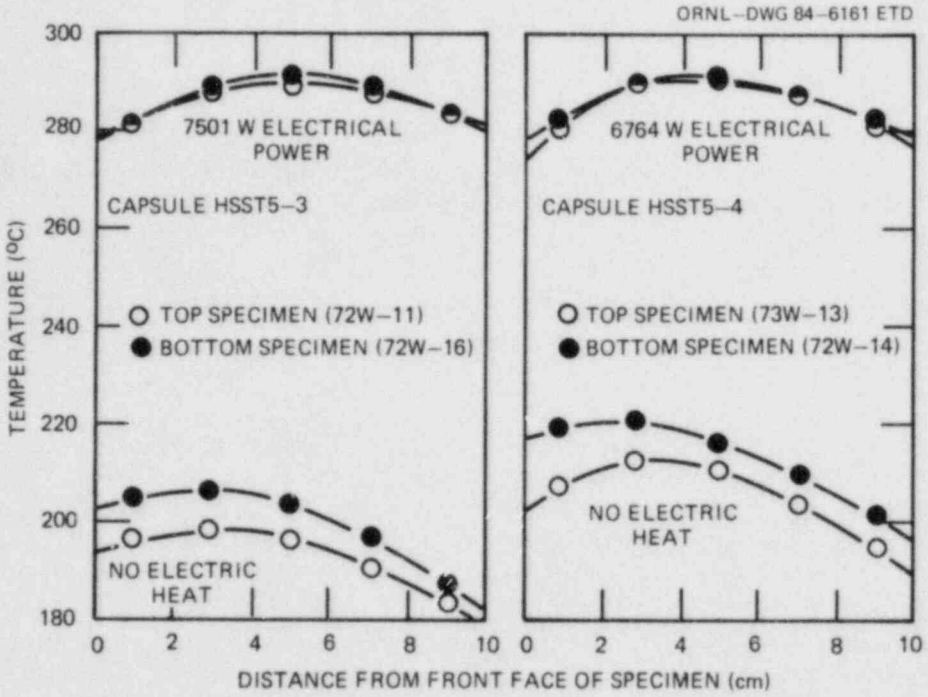

Fig. 6.8. Temperatures observed during initial startup of capsules HSST5-3 and HSST5-4 on August 16, 1984.

completed. The procurement process for the fabrication of parts for the 2T capsules has begun.

6.2.4 Test plan

MEA and ORNL will participate in the testing program. Because of testing equipment limitations, all testing of irradiated 4T-CS specimens and unirradiated 6T-CS and 8T-CS specimens will be conducted by MEA, and all tensile tests will be conducted by ORNL (testing of the other types of specimens will be shared). The sequence of testing will be

1. materials characterization,
2. testing of unirradiated Charpy V-notch, tensile, and drop-weight specimens,
3. testing of unirradiated compact specimens, smaller specimens being tested first and K_{Jc} tests preceding the large specimen tests,
4. testing of irradiated Charpy V-notch, tensile, and drop-weight specimens, and
5. testing of irradiated compact specimens, smaller specimens being tested first and K_{Jc} tests preceding the large specimen tests.

6.2.5 Program status

All the weldments are on hand, and a major portion of the test specimens have been fabricated. Designs for all irradiation capsules are complete. Irradiation of the first two 4T capsules was completed, irradiation of the second two 4T capsules is in progress, and assembly of the two 1T capsules is in progress.

6.3 Seventh HSST Irradiation Series: Stainless Steel Cladding

W. R. Corwin R. J. Gray

The previous metallographic studies[12] of the three layers of cladding from which the specimens were fabricated for the cladding irradiation[13] revealed radically different microstructures in each layer. The upper layer (type 308 stainless steel) was composed of small amounts of δ-ferrite dispersed in an austenitic matrix, typical of good quality cladding applied to existing reactor pressure vessels. The lowest layer (type 309 stainless steel) is a three-phase structure consisting of austenite, martensite, and ferrite. This structure was caused by high dilution of the weld puddle (~50%) from excessive melting of the base plate. Similar cladding has been shown to exist in light-water reactors where inadequate control has also allowed excessive dilution of the cladding to occur.[14,15] Amounts of dilution in good practice are typically in the range of 10 to 25%. The middle layer of cladding (type 308 stainless steel) was similar to the austenite-δ-ferrite structure of the top layer with isolated islands of martensite.

To verify the tentative conclusions regarding the composition of the lower layer and examine the δ-ferrite-to-sigma-phase transition during postweld heat treatment (PWHT), transmission electron microscopy and additional optical microscopy involving magnetic etching and color staining techniques were performed.[16]

The most revealing studies regarding the apparent three-phase microstructure of the lowest layer were those using ferrofluid etching techniques. In this technique a colloidal suspension of magnetic particles is applied to the specimen surface and viewed with and without the presence of a magnetic field. Examining the lowest layer in this manner (Fig. 6.9) shows that of the three optically different phases visible with the magnet off, two are clearly magnetic. When examined by transmission electron microscopy, the light-gray phase was determined to be martensite and the black phase ferrite decorated with $M_{23}C_6$ carbides.

The ductile-to-brittle transition observed in both the irradiated and unirradiated Charpy impact testing of the different layers of cladding[13] was also investigated further. Though consistent with the work of other researchers,[17-19] who have shown fully ductile fracture in as-welded austenitic weld metal to occur as low at 4 K, and though quasi-cleavage can occur in weld metal that has received a PWHT in the temperature range in which carbide precipitation and sigma formation occur, a better understanding of the mechanism involved was desired. Selected unirradiated Charpy specimens were sectioned and metallographically prepared such that the central plane of the specimen perpendicular to the

ORNL–PHOTO Y198644

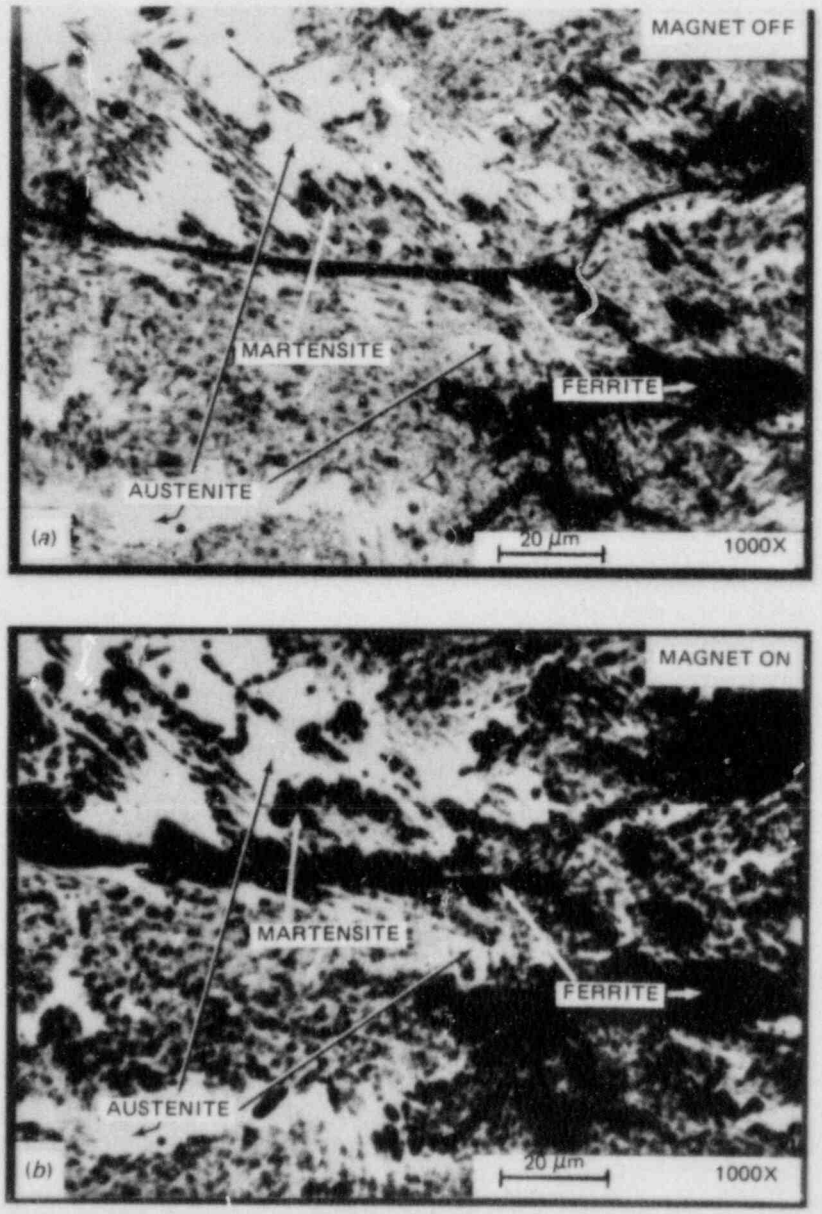

Fig. 6.9. Examination of lowest layer of cladding with magnetic etching techniques shows gray and black phases, visible with magnet off, to be ferromagnetic.

fracture face was visible, providing an "edge-on" view. Two specimens are examined here: (1) CPL 539 tested at −73°C on the lower knee of the transition and (2) CPL 530 tested at −30°C low in the transition. Both specimens contain both types 309 and 308 layers with the notch located in the type 309, the lowest layer of cladding.

The reasons for the transition behavior become immediately obvious when the photomicrographs of specimen CPL 530 are examined. An overview of the edge of the fracture is shown in Fig. 6.10. The fracture initiated in the type 309 highly diluted cladding in which the notch is located. Close examination of the fracture in the type 309 at location 1 (Fig. 6.11) shows the fracture path follows the ferrite (dark phase) in the structure. Note that the martensite and austenite are not differentiated by the etching technique used here. Once the fracture progresses into the type 308 to locations 2 and 3 (Figs. 6.12 and 6.13), the fracture path strictly follows the δ-ferrite islands. Clearly, in both materials the fracture is dominated by the ferritic phases.

These results are verified in specimen CPL 539 (Fig. 6.14). Again, the fracture in the type 308 cladding at locations 1 and 2 (Figs. 6.15 and 6.16) follows the δ-ferrite. At these higher magnifications the sigma phase transformed during PWHT can be resolved as dark spots or bands within the δ-ferrite islands. It does not appear that the brittle sigma phase particularly influences the fracture process. Examining the secondary crack at location 3, which opened in the type 309 cladding next to the main crack (Fig. 6.17), strongly reinforces the conclusion that the fracture progresses within the ferrite regions. Here, where both halves of the fracture are still visible, the crack can be seen to split the ferrite. Even the initiation of the crack in the Charpy notch, location 4 (Fig. 6.18), was moved well away from the bottom of the notch to the nearest patch of ferrite.

Obviously, the material governing the fracture process in the lower transition region of the Charpy curve is ferritic. Similar studies on specimens tested higher in the transition are under way to see if this behavior still exists or if the fracture transfers to the austenite. In any case, the mechanism responsible for the typically ferritic type ductile-to-brittle transition observed in our stainless steel cladding has been identified as the failure of δ-ferrite regions in both types 309 and 308 cladding rather than fracture within the bulk of the austenite. This behavior may also explain the rate sensitivity observed by Hawthorne and Watson[20] in their impact testing of stainless steel weldments since the ferritic phases controlling the fracture are inherently rate, as well as temperature, sensitive. If the cladding on the interior of a reactor pressure vessel is to be considered structural in nature, then the potential for its rate sensitivity should also be considered.

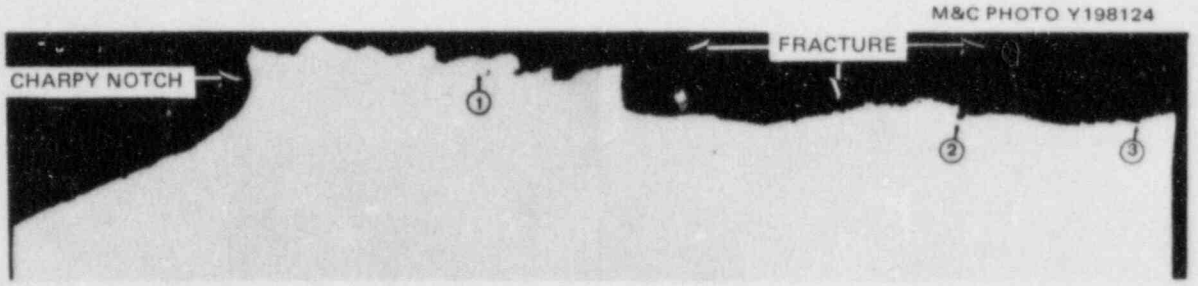

Fig. 6.10. Side view of fracture surface of Charpy specimen CPL 530 tested at −30°C low in transition region. Notch is located in type 309 weld metal; unnotched side is type 308.

Fig. 6.11. Detail of location 1 in Fig. 6.10 showing fracture path in type 309 cladding following patches of ferrite.

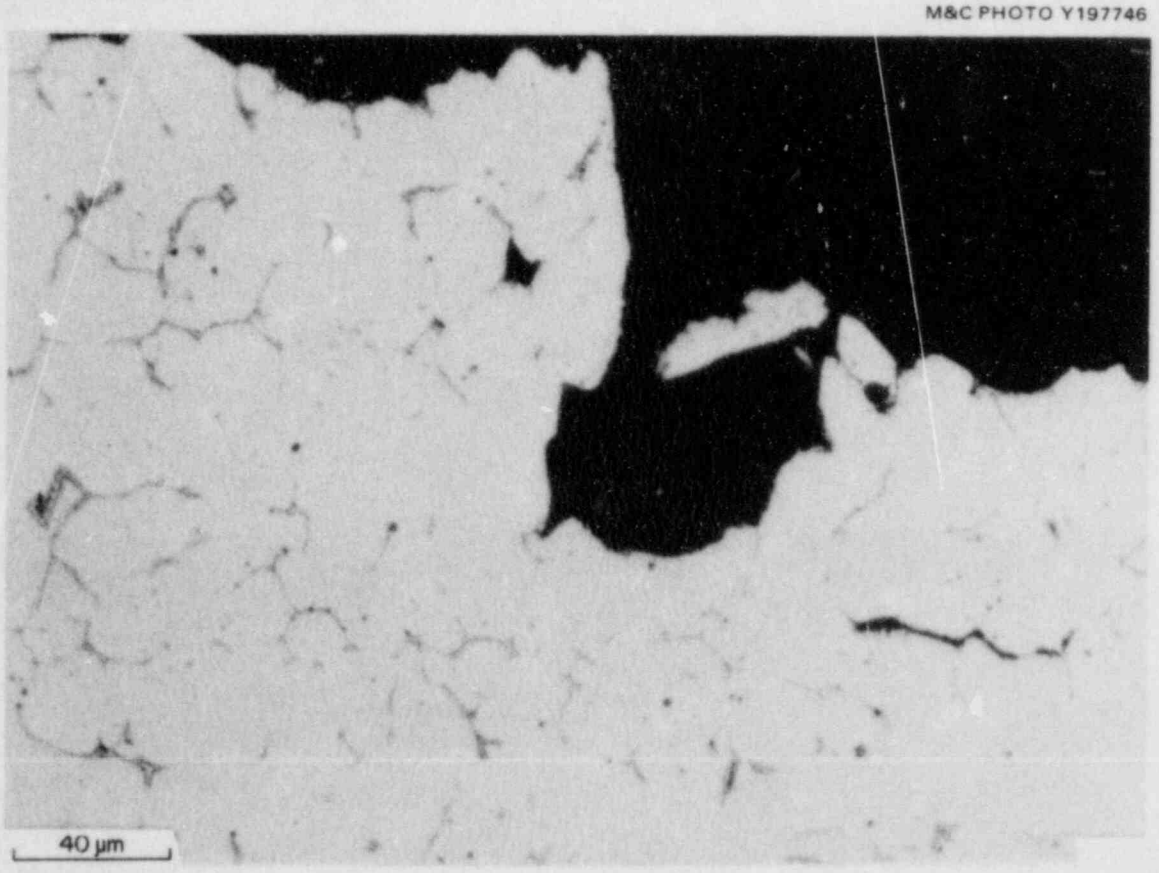

Fig. 6.12. Detail of location 2 in Fig. 6.10 showing fracture path in type 308 cladding following δ-ferrite islands.

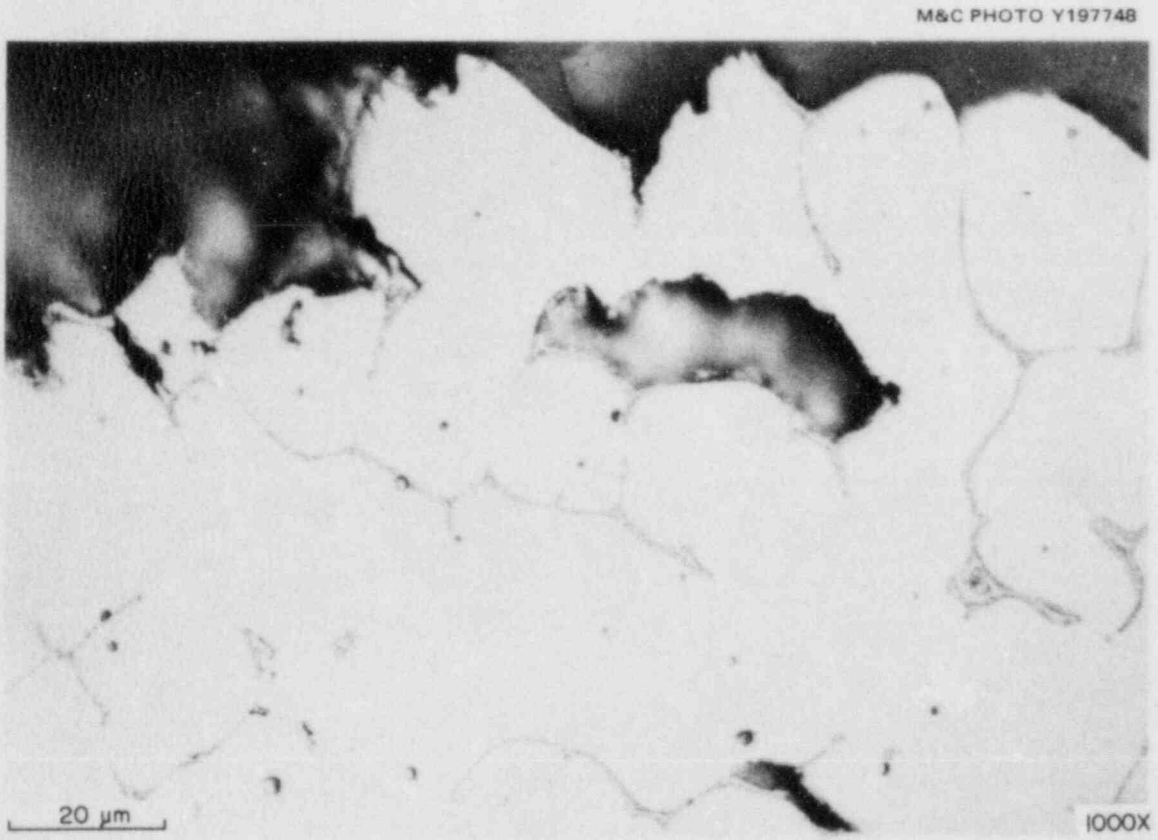

Fig. 6.13. Detail of location 3 in Fig. 6.10 showing fracture path following δ-ferrite islands.

M&C PHOTO Y198123

Fig. 6.14. Side view of fracture surface of Charpy specimen CPL 539 tested at −73°C in lower knee of transition region. Notch is located in type 309 weld metal; unnotched side is type 308 weld metal.

M&C PHOTO Y197762

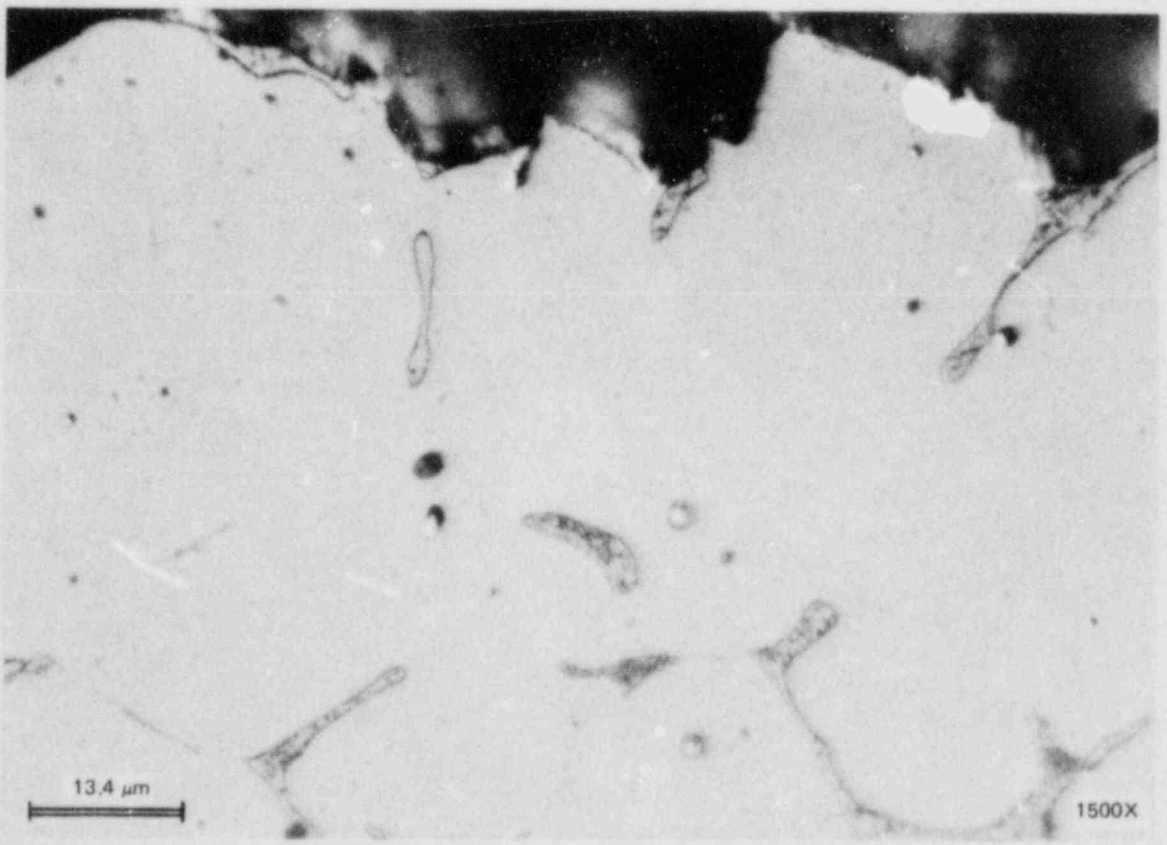

Fig. 6.15. Detail of location 1 in Fig. 6.14 showing fracture path following islands of δ-ferrite.

M&C PHOTO Y197761

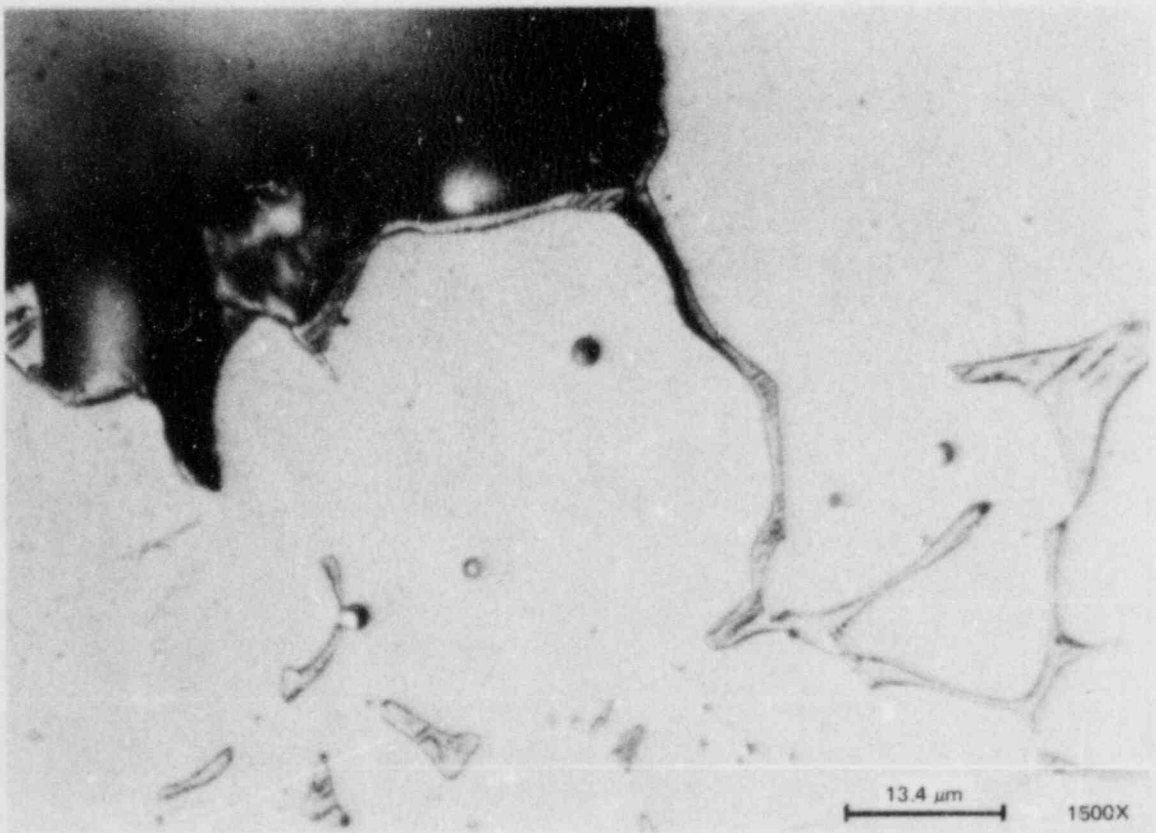

Fig. 6.16. Detail of location 2 in Fig. 6.14 showing fracture path following islands of δ-ferrite. Sigma-phase formed during PWHT, dark lines and dots within δ-ferrite islands, does not appear to influence fracture.

M&C PHOTO Y197759

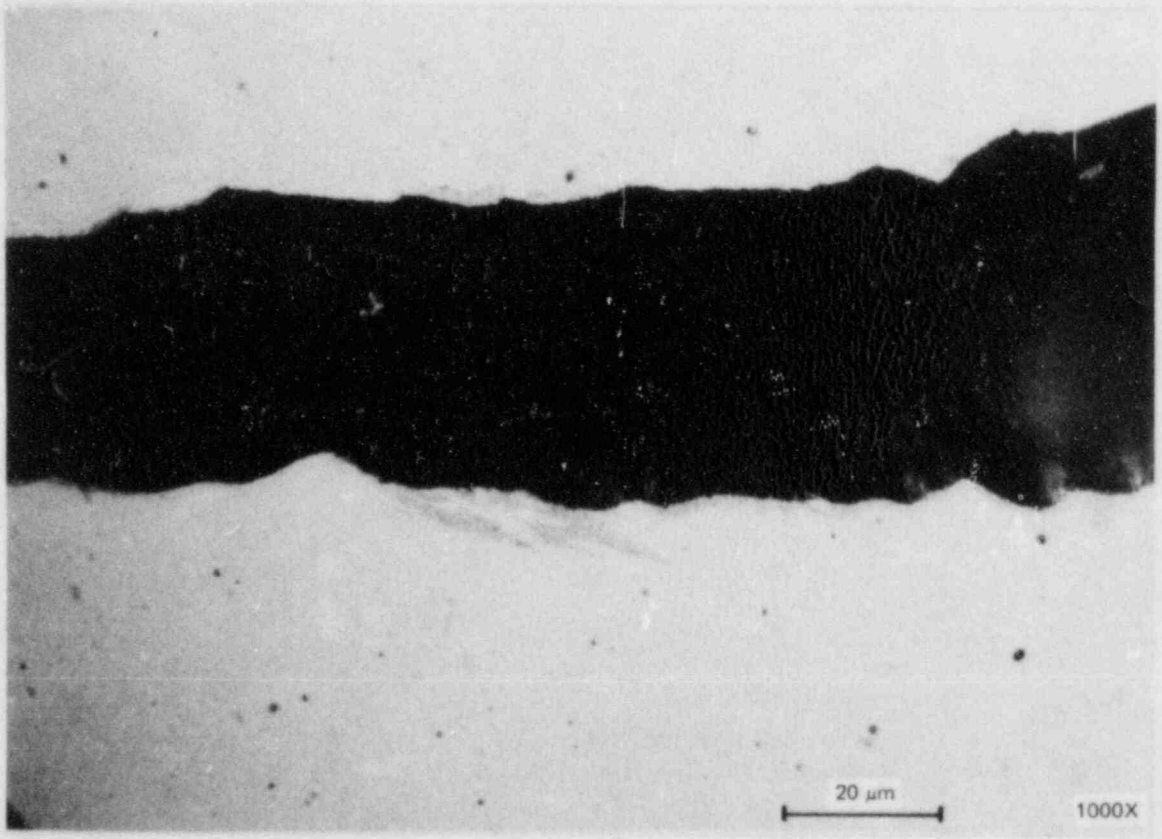

Fig. 6.17. Detail of location 3 in Fig. 6.14 showing splitting of ferrite in forming side crack in type 309 weld metal.

M&C PHOTO Y198125

Fig. 6.18. Detail of location 4 in Fig. 6.14 showing bottom of Charpy notch. (Note fracture initiated well up in flank of notch, presumably because that was nearest patch of ferrite.)

References

1. *Standard Test Method for Plane-Strain Fracture Toughness of Metallic Materials*, E-399-81, American Society for Testing and Materials, Philadelphia, 1981.

2. H. A. Ernst, *Material Resistance and Instability Beyond J-Controlled Growth*, 81-1D7-JINTF-P6, Westinghouse Research and Development Center, Pittsburgh, Dec. 3, 1981.

3. "J_{Ic}, A Measure of Fracture Toughness, ASTM Designation: E-813," *1983 Annual Book of ASTM Standards*, Sect. 3, Vol. 03.01, American Society for Testing and Materials, Philadelphia, 1983.

4. J. G. Merkle, "A New Method for Analyzing Small Scale Fracture Specimen Data in the Transition Zone," pp. 307–15 in *Proceedings of the U.S. Nuclear Regulatory Commission 10th Water Reactor Safety Research Information Meeting*, NUREG/CP-0041, Vol. 4, 1982.

5. J. J. McGowan et al., "Fourth HSST Irradiation Series," in *Heavy-Section Steel Technology Program Semiannual Prog. Rep. October 1983–March 1984*, NUREG/CR-3744, Vol. 1 (ORNL/TM-9154/V1), Martin Marietta Energy Systems, Inc., Oak Ridge Natl. Lab.

6. R. G. Berggren, J. R. Hawthorne, and R. K. Nanstad, "An Analysis of Charpy V-Notch Impact Toughness of Irradiated A533 Grade B Class 1 Plate and Four Submerged-Arc Welds," *Proceedings of the Twelfth International Symposium on the Effects of Radiation on Materials, Williamsburg, Va., June 18–22, 1984*, American Society for Testing and Materials, Philadelphia.

7. R. G. Berggren and R. K. Nanstad, "Irradiation-Induced K_{Ic} Curve Shift," in *Heavy-Section Steel Technology Program Quart. Prog. Rep. April–June 1982*, NUREG/CR-2751, Vol. 2 (ORNL/TM-8369/V2), Union Carbide Corp. Nuclear Div., Oak Ridge Natl. Lab.

8. R. G. Berggren and R. K. Nanstad, "Irradiation-Induced K_{Ic} Curve Shift," in *Heavy-Section Steel Technology Program Quart. Prog. Rep. October–December 1982*, NUREG/CR-2751, Vol. 4 (ORNL/TM-8369/V4), Union Carbide Corp. Nuclear Div., Oak Ridge Natl. Lab.

9. R. G. Berggren et al., "Irradiation-Induced K_{Ic} Curve Shift," in *Heavy-Section Steel Technology Program Semiannual Prog. Rep. October 1983–March 1984*, NUREG/CR-3744, Vol. 1 (ORNL/TM-9154/V1), Martin Marietta Energy Systems, Inc., Oak Ridge Natl. Lab.

10. Metal Properties Council Subcommittee 6 on Nuclear Materials, "Prediction of the Shift in the Brittle-Ductile Transition Temperature of Light-Water Reactor (LWR) Pressure Vessel Materials," *J. Test. Eval.* (11)4, 327–60 (July 1983).

11. R. G. Berggren et al., "Irradiation-Induced K_{Ic} Curve Shift," in *Heavy-Section Steel Technology Program Quart. Prog. Rep. July–September 1983*, NUREG/CR-3334, Vol. 3 (ORNL/TM-8787/V3), Union Carbide Corp. Nuclear Div., Oak Ridge Natl. Lab.

12. W. R. Corwin et al., "Stainless Steel Cladding Investigations," in *Heavy-Section Steel Technology Program Quart. Prog. Rep. January–March 1983*, NUREG/CR-3334, Vol. 1 (ORNL/TM-8787/V1), Union Carbide Corp. Nuclear Div., Oak Ridge Natl. Lab.

13. W. R. Corwin, R. G. Berggren, and R. K. Nanstad, "Irradiated Stainless Steel Cladding," in *Heavy-Section Steel Technology Program Semiannual Prog. Rep. October 1983–March 1984*, NUREG/CR-3744, Vol. 1 (ORNL/TM-9154/V1), Martin Marietta Energy Systems, Inc., Oak Ridge Natl. Lab.

14. E. B. Norris, D. R. Ireland, and C. E. Lautzenheiser, *The Second Inspection of the Elk River Pressure Vessel After Operation*, SwRI 122, pp. 9–13, Southwest Research Institute, San Antonio, Texas, July 21, 1967.

15. T. Kondo, H. Nakajima, and R. Nagasaki, "Metallographic Investigation of the Cladding Failure in the Pressure Vessel of a BWR," *Nucl. Eng. Design* 16, 205–22 (1971).

16. R. J. Gray, "Magnetic Etching with Ferrofluid," pp. 155–77 in *Metallographic Specimen Preparation*, ed. J. L. McCall and W. M. Mueller, Plenum, New York, 1974.

17. D. T. Read et al., "Metallurgical Factors Affecting the Toughness of 316L SMA Weldments at Cryogenic Temperatures," *Weld. J.* 59(4), 104–13-s (April 1980).

18. F. W. Bennett and C. P. Dillon, "Impact Strength of Austenitic Stainless Steel Welds at −320°F — Effects of Composition, Ferrite Content, and Heat Treatment," *J. Basic Eng.* 88, 33–36 (March 1966).

19. G. M. Goodwin, *Fracture Toughness of Austenitic Stainless Steel Weld Metal at 4 K*, ORNL/TM-9172, Martin Marietta Energy Systems, Inc., Oak Ridge Natl. Lab., August 1984.

20. J. R. Hawthorne and H. E. Watson, "Exploration of the Influence of Welding Variables on Notch Ductility of Irradiated Austenitic Stainless Steel Welds," pp. 327–36 in *Proceedings of the International Conference on Radiation Effects in Breeder Reactor Structural Materials, Scottsdale, Arizona, June 1977.*

7. CLADDING EVALUATIONS

W. R. Corwin G. C. Robinson
T. D. Owings

To provide baseline values on the material used as the base plate in the first series of clad-beam experiments,[1,2] crack-arrest testing was completed on Heavy-Section Steel Technology (HSST) plate 07. These data allow a direct comparison to be made between the values of crack arrest calculated for the clad beams and those of the base plate itself to determine if the cladding did indeed enhance the structural resistance of the clad structure.

Crack-arrest data were generated at several temperatures in addition to the test temperature of the clad beams in the expectation that they would be useful for the American Society of Testing and Materials (ASTM) round-robin crack-arrest testing, because the A533 Grade B Class 1 material for the round robin is also from HSST plate 07. While some guidance was gained from these data, the different orientation subsequently chosen for the round-robin specimens made direct comparisons less meaningful.

The crack-arrest specimens were fabricated from broken halves of the clad-beam specimens in the LT orientation. This corresponds to the extension of the flaw in the clad-beam experiments across the width of the plate. The material had received a postweld heat treatment (PWHT) of 40 h at 621°C. Details of mechanical properties on this material are provided elsewhere,[1,3] but its drop-weight nil-ductility temperature (NDT) is −18°C, and the 68-J Charpy V-notch impact energy transition temperature is 20°C, yielding an RT_{NDT} of −13°C. The clad-beam test temperature was −40°C, for comparison.

The specimens were of the weld-embrittled, transverse-loaded, split-pin type recommended by the latest draft of the proposed ASTM standard on crack-arrest testing. They were 25.4 mm thick with planar dimensions of 152.4 and 148.2 mm.

Comparing the results of the crack-arrest specimens and the clad-beam specimens (Fig. 7.1) shows that two of the values of arrest toughness calculated for the clad-beam experiments coincide closely with those obtained using crack-arrest specimens; the third value is slightly higher. Beam specimen CP5 did not arrest. The stress intensity calculated at the point where arrest would have been caused by the cladding if it had occurred was well in excess of the values obtained with the crack-arrest specimens. The values of stress intensity calculated for the clad-beam specimens were the maximum local values obtained using the ORVIRT finite-element code.[4]

The comparisons made between the crack-arrest specimens and the clad-beam experiments reinforce the primary conclusions made regarding the ability of the moderate toughness cladding examined in this study to enhance structural resistance to crack extension; the cladding may indeed help, but the present data are inconclusive. The second phase of the clad-beam tests, scheduled to begin in FY 1985, will utilize a different specimen design and tougher cladding more typical of the good quality cladding in the field.[5,6] This phase is expected to provide better insight for conditions relevant to the bulk of existing reactor pressure vessels.

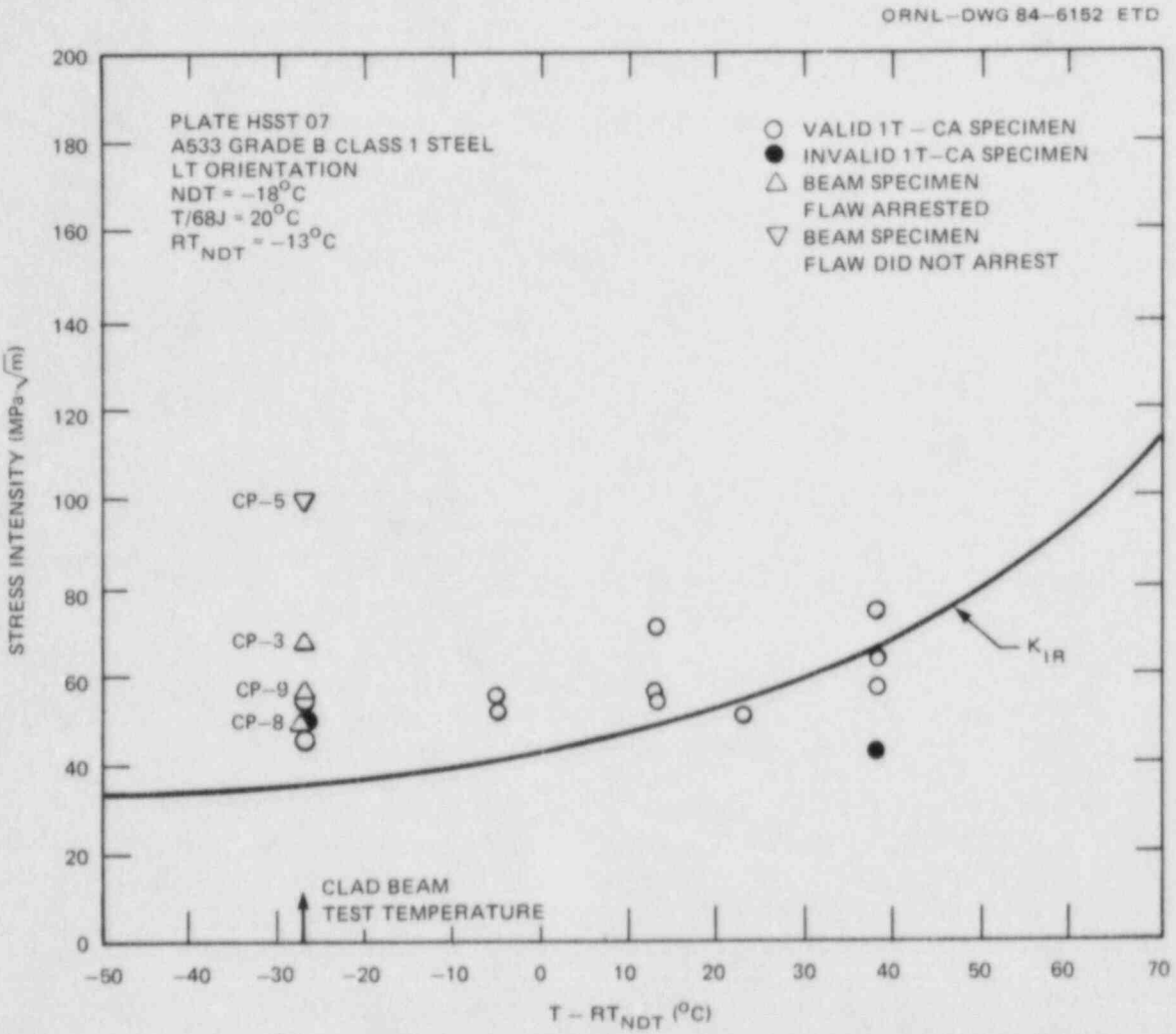

Fig. 7.1. Comparing crack-arrest values calculated for clad-beam specimens that arrested with those obtained from crack-arrest specimens indicate only possibility that cladding enhanced toughness of structure.

Efforts by Combustion Engineering, Inc., (CE) to produce the specimens and material for the second series of clad-beam experiments as well as the Seventh HSST Irradiation Series have progressed well but somewhat slower than anticipated. Working to an Oak Ridge National Laboratory (ORNL) specification, CE has developed a method for producing clad-beam specimen blanks that are composed of three-wire series-arc cladding, typical of that used in reactor pressure vessels, deposited on a base plate of pressure vessel steel that has a high ductile-to-brittle transition temperature. This combination of materials will allow testing of the clad beams in a temperature regime in which the cladding is appreciably tougher than the base plate. This will more closely simulate the materials properties expected to exist in good quality cladding in an operating vessel, as well as reduce the ambiguity that resulted from the

first series of clad-beam experiments regarding the ability of cladding to mitigate crack propagation. Testing of the first of these specimens is scheduled for the first half of FY 1985. A topical report covering the first series of clad-beam tests was drafted this period and will be published next report period.

References

1. G. C. Robinson et al., "Stainless Steel Cladding Investigations," in *Heavy-Section Steel Technology Program Quart. Prog. Rep. January–March 1982*, NUREG/CR-2751, Vol. 1 (ORNL/TM-8369/V1), Union Carbide Corp. Nuclear Div., Oak Ridge Natl. Lab.

2. R. K. Nanstad et al., "Stainless Steel Cladding Investigations," in *Heavy-Section Steel Technology Program Quart. Prog. Rep. April–June 1982*, NUREG/CR-2751, Vol. 1 (ORNL/TM-8369/V2), Union Carbide Corp. Nuclear Div., Oak Ridge Natl. Lab.

3. W. R. Corwin, R. G. Berggren, and R. K. Nanstad, "Irradiated Stainless Steel Cladding," in *Heavy-Section Steel Technology Program Semiannual Prog. Rep. October 1983–March 1984*, NUREG/CR-3744, Vol. 1 (ORNL/TM-9154/V1), Martin Marietta Energy Systems, Inc., Oak Ridge Natl. Lab.

4. G. C. Robinson, "Small-Scale Clad Effects Study," pp. 272–81 in *Proceedings of the U.S. Nuclear Regulatory Commission 10th Water Reactor Safety Research Information Meeting*, NUREG/CP-0041, Vol. 4, 1982.

5. W. R. Corwin, *Assessment of Radiation Effects Relating to Reactor Pressure Vessel Cladding*, NUREG/CR-3671 (ORNL-6047), Martin Marietta Energy Systems, Inc., Oak Ridge Natl. Lab., July 1984.

6. W. R. Corwin et al., "Stainless Steel Cladding Investigations," in *Heavy-Section Steel Technology Program Quart. Prog. Rep. January–March 1983*, NUREG/CR-3334, Vol. 1 (ORNL/TM-8787/V1), Union Carbide Corp. Nuclear Div., Oak Ridge Natl. Lab.

8. INTERMEDIATE VESSEL TESTS AND ANALYSES

B. R. Bass*

During this reporting period, work continued on preparation of the final report for the intermediate vessel test V-8A,[1,2] conducted earlier by the Heavy-Section Steel Technology (HSST) program. The objective of the test was to provide accurate quantitative data concerning growth by ductile tearing and final instability of a flaw in a low upper-shelf toughness weldment.

The objective of the V-8A test was attained, with a tearing instability observed at a pressure of ~139 MPa (~2 × design pressure). Exposure of the crack surface after the test indicated that the initial fatigue-sharpened notch, with an approximate semielliptical profile, grew into a canoe-shaped profile of 103-mm depth and 456-mm length. Stress and fracture-mechanics (FM) analyses of the posttest vessel were made by three-dimensional (3-D) finite-element methods, using the ORMGEN/ORVIRT[3,4] FM analysis system. Results obtained from finite-element models of the initial and the final configurations were compared with measured values of crack-mouth-opening displacement (CMOD) and with inner and outer surface hoop strains recorded 180° from the crack plane. These comparisons, described in Ref. 2, indicate that the stress-strain curve used to model the vessel material was overly stiff in the elastic region.

An adjusted stress-strain curve that more accurately reflects the posttest measured properties of the V-8A vessel material in the elastic region near the yield point is depicted in Fig. 8.1. This stress-strain

*Computer Services Division, Martin Marietta Energy Systems, Inc.

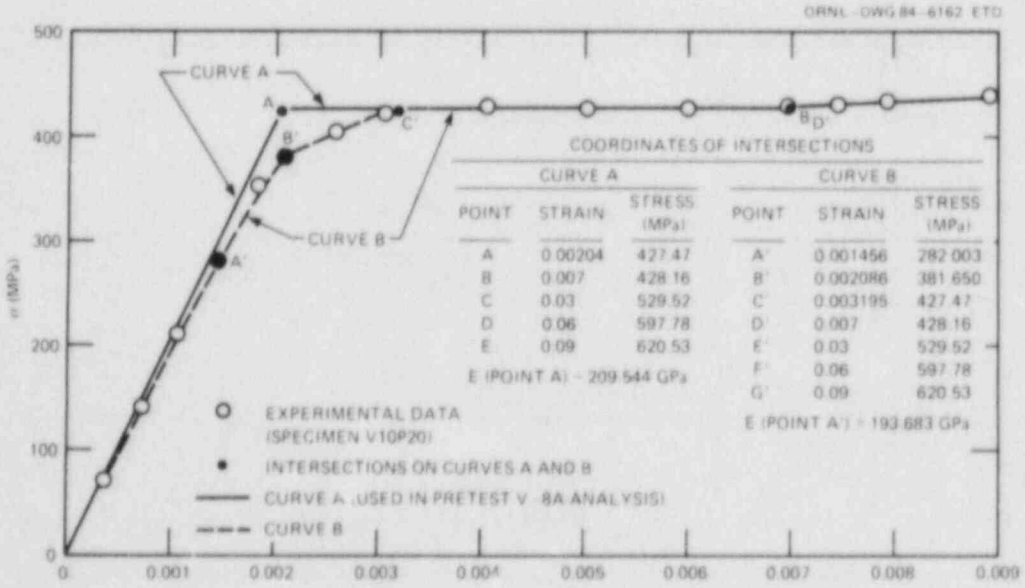

Fig. 8.1. Stress-strain relationships used in earlier V-8A analyses (curve A) and in present analysis (curve B).

curve was used with 3-D finite-element models that better approximate the initial and final crack configurations in a repetition of the stress and fracture analyses of Ref. 2. Computed results from this second set of analyses are compared with measured data in Fig. 8.2 (for CMOD) and in Fig. 8.3 (for inner- and outer-surface hoop strain) and indicate improved agreement over those of Ref. 2. A complete description of these analyses, including the updated J_I values for the initial and final crack configurations, will be forthcoming in the final report on the V-8A test.

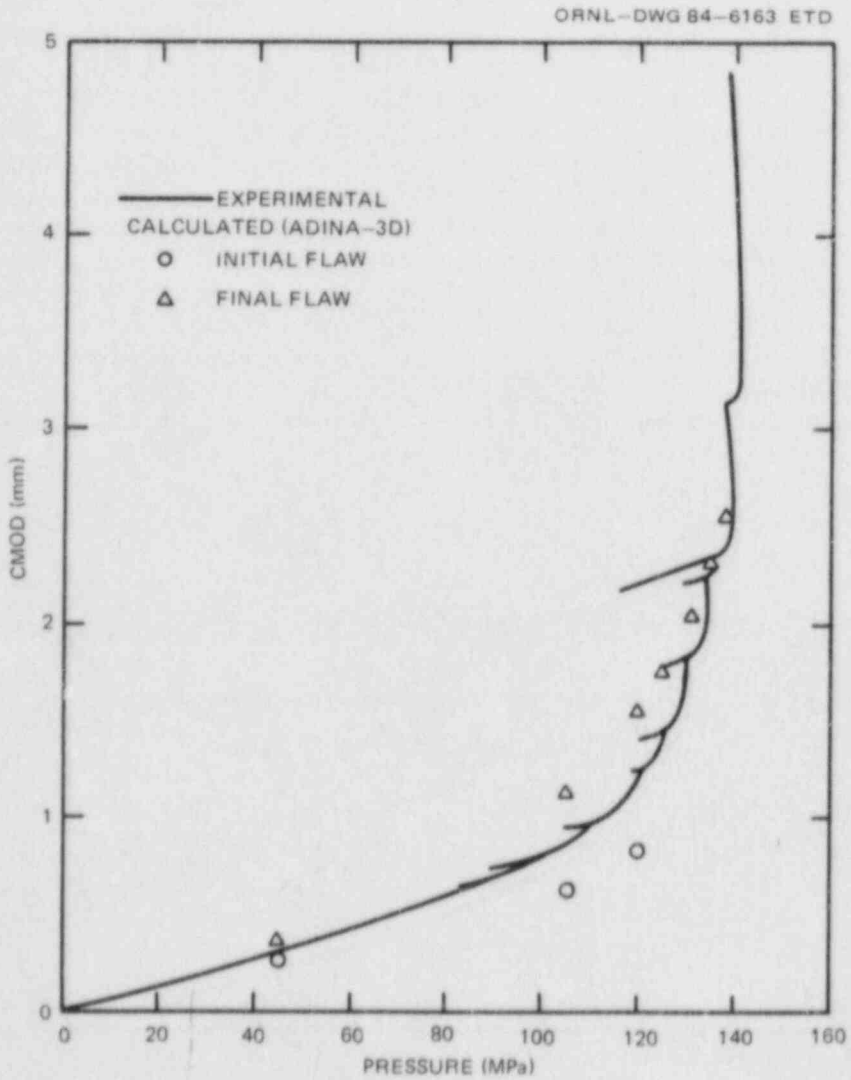

Fig. 8.2. Comparison of measured and calculated values of CMOD in V-8A at center of flaw. Almost all of crack growth occurred above 120 MPa.

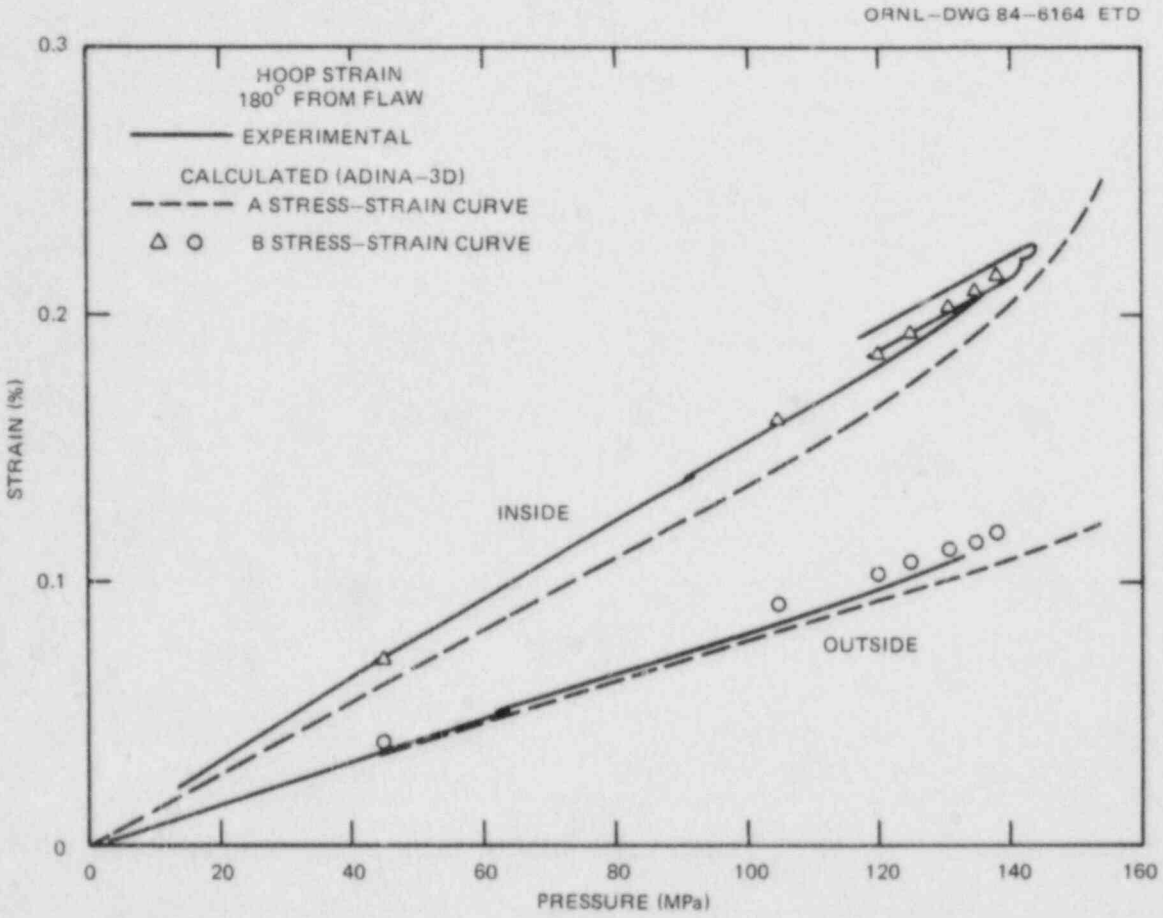

Fig. 8.3. Comparison of measured and calculated values of hoop strain 180° from flaw in V-8A.

References

1. R. H. Bryan et al., "Experimental Investigation of Tearing Behavior of a Flaw in a Thick Pressure Vessel," paper presented at the SMiRT Post Conference Seminar No. 6, Integrity of Reactor Pressure Boundary, Monterey, Calif., August 29–30, 1983.

2. B. R. Bass et al., "Computational Methods for Fracture Analysis of Heavy-Section Steel Technology (HSST) Pressure Vessel Experiments," pp. 264–311 in *Proceedings of the USNRC Eleventh Water Reactor Safety Research Information Meeting*, NUREG/CP-0048, Vol. 4, U.S. Nuclear Regulatory Commission, Washington, D.C., January 1984.

3. B. R. Bass and J. W. Bryson, *Applications of Energy Release Rate Techniques to Part-Through Cracks in Plates and Cylinders; Volume 1. ORMGEN-3D: A Finite Element Mesh Generator for 3-Dimensional Crack Geometries*, ORNL/TM-8527/V1, Union Carbide Corp. Nuclear Div., Oak Ridge Natl. Lab., December 1982.

4. B. R. Bass and J. W. Bryson, *Applications of Energy Release Rate Techniques to Part-Through Cracks in Plates and Cylinders; Volume 2. ORVIRT: A Finite Element Program for Energy Release Rate Calculations for 2-Dimensional and 3-Dimensional Crack Models*, ORNL/TM-8527/V2, Union Carbide Corp. Nuclear Div., Oak Ridge Natl. Lab., February 1983.

9. THERMAL-SHOCK TECHNOLOGY

R. D. Cheverton

9.1 Summary

As a part of the Integrated Pressurized Thermal-Shock (IPTS) Program, probabilistic fracture-mechanics (FM) calculations were made for the Calvert Cliffs-1 and H. B. Robinson-2 (HBR-2) reactor pressure vessels to obtain a best estimate of the conditional probability of vessel failure [P(F|E)] associated with numerous postulated transients. These studies indicated that warm prestressing (WPS) could be a significant factor and that P(F|E) was insensitive to the crack-arrest toughness, including the upper-shelf value.

The feasibility of conducting a thermal-shock experiment (TSE) with a clad test cylinder and a subclad crack was investigated. The studies included two-dimensional (2-D) and three-dimensional (3-D) linear-elastic fracture mechanics (LEFM) and elastic-plastic fracture mechanics (EPFM) calculations for a 19-mm-deep, 6/1 semielliptical, subclad crack in a clad TSE test cylinder subjected to a typical TSE (liquid nitrogen) thermal transient.

9.2 IPTS Program Studies

R. D. Cheverton D. G. Ball

The general purpose of the IPTS program is to estimate the frequency of failure of specific pressurized-water reactor (PWR) pressure vessels during overcooling accidents (OCAs) that are postulated for the specific plants. The effort includes defining transients, estimating the frequency of these transients, calculating the corresponding primary-system pressure and downcomer coolant-temperature transients, and, finally, conducting a probabilistic FM analysis of the pressure vessel. In addition, sensitivity and uncertainty analyses are performed, and the effects of proposed remedial measures are investigated. Studies of this type were recently completed for the Oconee-1 and Calvert Cliffs-1 nuclear plants and are under way for the HBR-2 plant. FM aspects of these studies have been reported previously[1,2] and are updated in the following paragraphs.

9.2.1 The role of crack arrest

9.2.1.1 FM model. The probabilistic FM calculations for the IPTS program are being performed with the computer code OCA-P,[3] which is based on LEFM and makes use of Monte Carlo methodologies for computing probabilities associated with flaw behavior. Two of the parameters simulated in the probabilistic analysis are the crack-initiation toughness K_{Ic} and the crack-arrest toughness K_{Ia}. Mean values of these parameters are required

for the probabilistic analysis and are obtained from

$$\bar{K}_{Ic} = 1.43\{36.5 + 3.084 \exp [0.036 (T - RT_{NDT} + 56)]\} , \quad (9.1)$$

$$\bar{K}_{Ia} = 1.25\{29.5 + 1.344 \exp [0.0261 (T - RT_{NDT} + 89)]\} , \quad (9.2)$$

where

K_{Ic}, $\bar{K}_{Ia}$ = mean values of initiation and arrest toughness, MPa$\cdot\sqrt{m}$;
T = temperature at tip of flaw, °C;
$RT_{NDT} = RT_{NDT_o} + \Delta RT_{NDT}$ = nil-ductility reference temperature,[4] °C;
RT_{NDT_o} = initial (zero fluence) value of RT_{NDT}, °C;
ΔRT_{NDT} = increase in RT_{NDT} due to radiation damage, °C.

Equations (9.1) and (9.2) represent the American Society of Mechanical Engineers (ASME) Sect. XI lower-bound curves[5] times a constant. The constants were derived by specifying a normal distribution, one standard deviation (σ) = 0.15 $\bar{K}_{Ic}$, 0.10 $\bar{K}_{Ia}$, and by assuming that the ASME lower-bound curves represent -2σ values. These specific values of σ were based on the data that were used to generate the ASME K_{Ic} and K_{IR} curves.

A provision is made in OCA-P for limiting K_{Ia} to some maximum value, $(K_{Ia})_{max}$. One way to select a value of $(K_{Ia})_{max}$ is to use a K_J value corresponding to the upper portion of an appropriate J vs Δa curve (J-resistance curve), as illustrated in Fig. 9.1. This figure shows the

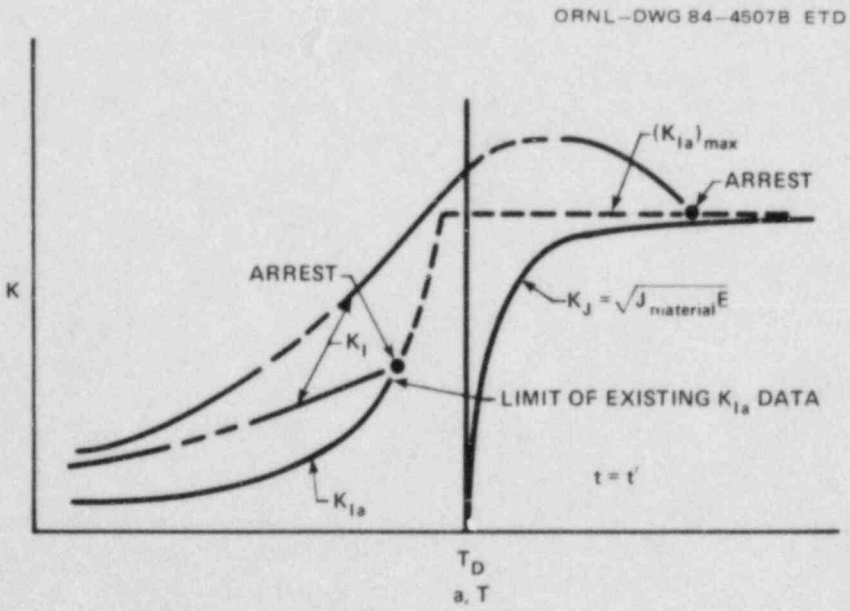

Fig. 9.1. Illustration of method for selecting $(K_{Ia})_{max}$.

radial distribution of fracture toughness through the wall of the vessel at some time during a typical postulated transient. At temperatures less than T_D, it is assumed that the flaw will behave in a frangible manner only; that is, ductile tearing is not permitted following arrest. [Depending on the value of $(K_{Ia})_{max}$ selected, tearing might actually occur and lead to failure.] In accordance with this model, the load line will not intersect the steeply rising portion of the J-Δa curve. Thus, it is sufficient to extend $(K_{Ia})_{max}$ across the T_D line as shown. It is then possible in the analysis for crack arrest to take place on the upper shelf if the load line rises steeply enough to miss the knee of the K_{Ia} curve and then drops back down again, as it does for some of the postulated pressurized thermal-shock (PTS) transients.

A particular J-Δa curve of interest corresponds to a specific high-copper low-upper-shelf weld [referred to as 61W (Ref. 6)] that was irradiated to a fluence of ~1.2×10^{19} neutrons/cm^2 at a temperature of ~290°C and was tested at ~200°C. The upper portion of the curve is essentially horizontal and equivalent to a K_J value of ~220 MPa•$\sqrt{m}$. This value has been used for $(K_{Ia})_{max}$ in the IPTS studies. As illustrated later, a value of 220 MPa•$\sqrt{m}$ nearly corresponds to the Charpy-V impact (CVN) onset of upper-shelf temperature; thus, minimal ductile tearing would be expected at lower values.

K_{Ia} data obtained from wide-plate tests in Japan[7] and PTS experiments with large cylinders at Oak Ridge National Laboratory (ORNL)[8] indicate that values of K_{Ia} substantially greater than 220 MPa•$\sqrt{m}$ might be achieved in a PWR vessel. However, the tearing resistance following arrest probably would not be sufficient to prevent ductile tearing up to the point indicated in Fig. 9.1. Additional experiments are planned as a part of the Heavy-Section Steel Technology (HSST) program to further explore the behavior of flaws under high loading conditions and at temperatures close to and above those corresponding to the onset of upper shelf. In the meantime, calculations have been made to determine the effect of higher values of $(K_{Ia})_{max}$ on the probability of vessel failure, assuming tearing does not follow crack arrest. The results of these calculations are discussed later (Sect. 9.2.1.3).

9.2.1.2. Validity of static crack-arrest concept for PTS studies. The validity of the static crack-arrest concept for application to the PTS issue has been investigated at ORNL by comparing small-specimen crack-arrest data with K_{Ia} values deduced from a series of thermal-shock and PTS experiments [TSE-4 (Ref. 9); TSE-5, -5A, and -6 (Ref. 10); and PTSE-1 (Ref 8)]. In most cases the lab K_{Ia} data were obtained using 25 × 151 × 151-mm wedge-loaded, compact, crack-arrest specimens, and the source of material was a prolongation from each of the test cylinders. [Battelle Columbus Laboratory (BCL) was responsible for making the small-specimen K_{Ia} measurements.]

The material used in the testing was a low-alloy forging-grade steel [A508 with Class-2 chemistry[11] (see Table 9.1)] that is used for light-water reactor (LWR) pressure vessels. Three different heats of material and four different heat treatments were involved. The test cylinders for TSE-5, -5A, and -6 came from one heat of material (a single long forging);

Table 9.1. Chemical composition for A508 Class 2 material

Composition[a] (wt %)								
C	Mn	P	S	Si	Cr	Ni	Mo	V
0.27	0.50/1.00	0.012	0.015	0.15/0.40	0.25/0.45	0.50/1.00	0.55/0.70	0.05

[a]Single values are maximum.

the other two test cylinders were from two other heats. The heat treatments differed only in the "tempering" temperature. Preceding tempering, the material was normalized for 8 h at 930°C, air cooled, austenitized for 9 h at 860°C, and then quenched in water. "Tempering" temperatures corresponding to each of the experiments are included in Table 9.2, which summarizes the test conditions and results. As indicated in the table, test cylinders for four of the five tests (TSE-4, -5, -6, and PTSE-1) were in essentially the quench-only condition. The test cylinder for TSE-5A was tempered at a high enough temperature to nearly satisfy the strength requirements for Class-2 material.

Following the water-quench and prior to tempering, sufficient surface material was removed from the test cylinders and their prolongations to avoid having significant residual stresses and gradients in toughness in the sections of material to be tested.[13]

Values of RT_{NDT} for the different test cylinders and their prolongations are also included in Table 9.2. Because of the different heat treatments and heats of material involved, there is a substantial range in values (10 to 91°C).

A total of 55 small-specimen K_{Ia} values were obtained as a part of the test-cylinder characterization studies,[14,15] and the TSEs produced 12 critical values of K_I corresponding to crack-arrest events. The small-specimen K_{Ia} values covered a range of testing temperatures ($T - RT_{NDT}$) of −66 to +59°C, while the corresponding range for the cylinder tests was −30 to +77°C. The 12 K_{Ia} values deduced from the TSEs are plotted in Fig. 9.2, where they are compared with the ASME Sect. XI K_{Ia} (K_{IR}) curve and the 5th and 95th percentile curves corresponding to a BCL data base of 233 K_{Ia} values for A533 and A508 material. With the exception of a few relatively high data points associated with fracture surfaces having a high density of uncracked ligaments, the BCL 5th and 95th percentile curves represent lower and upper bounds of the 55 K_{Ia} values obtained from the thermal-shock test-cylinder characterization studies (these 55 values are included in the BCL data base).

Also included in Fig. 9.2 are three K_{Ia} values deduced from a French TSE[16] and five values obtained by the Japanese from wide-plate tests,[7] which, like the ORNL PTS experiment (PTSE-1),[8] permit the investigation of crack arrest at relatively high temperatures.

Table 9.2. Test conditions and summary of results for ORNL thermal-shock and PTS experiments

	TSE-4	TSE-5	TSE-5A	TSE-6	PTSE-1
Cylinder dimensions, mm					
Outer diameter	533	991	991	991	991
Inner diameter	242	686	686	838	686
Length	914	1219	1219	1219	1372
Cylinder material					
Type	← SA 508 with Class-2 chemistry →				
Tempering temperature, °C	No tempering[a]	613[b]	679[b]	613[b]	561[c]
RT_{NDT}, °C	~90[d]	66[e]	10[f]	66[e]	91[e]
Flaw (initial)					
Type	← Long, inner surface →				Long, outer surface
Orientation	← Longitudinal →				
Length, mm	914	1219	1219	1219	1000
Depth, mm	11	16	11	8	11
Thermal shock					
Cylinder initial temperature, °C	291	96	96	96	290
Coolant initial temperature, °C	−25	−196	−196	−196	−25
Coolant	Alcohol and water	LN_2	LN_2	LN_2	Alcohol and water
Pressure, MPa	0	0	0	0	0–90
Initiation-arrest events					
Number	1	3	4	2	2
Arrest depth, mm	22	30, 96, 122	21, 30, 48, 82	21, 142	22, 37
Arrest temperature, °C					
T	126	36, 82, 89	22, 38, 51, 67	34, 64	157, 169
$T - RT_{NDT}$	36	−30, 16, 23	12, 28, 41, 57	−32, −2	66, 78
K_{Ia}, MPa·$\sqrt{m}$	127	86, 104, 92	76,[g] 86, 107, 130	63,[g] 105	177,[g] 265[g]

[a]Cylinder tested in quenched condition.

[b]Temperature maintained for 4 h, air cooled.

[c]Stress-relief treatment only.

[d]Corresponds to CVN energy of 40 J. No drop-weight testing; CVN upper shelf <68 J.

[e]Based on CVN data.[12]

[f]Based on drop weight.[12]

[g]Rising K_I field.

As indicated by Fig. 9.2, the scatter in the small-specimen data, with the exception of the few outliers mentioned above, is approximately ±45% over the temperature range shown, and only a small fraction of the data points falls below the K_{IR} curve. All of the K_{Ia} values deduced from the ORNL TSEs fall within the small-specimen scatter band and well above the K_{IR} curve, while the three French data points cluster about the K_{IR} curve.

The first crack-arrest events during TSE-5A and TSE-6 and both crack-arrest events during PTSE-1 took place in a rising K_I field ($dK_I/da > 0$), and it is not evident that this resulted in K_{Ia} values different from those obtained with $dK_I/da < 0$, which is the usual condition when obtaining small-specimen K_{Ia} values. Because of this and the good agreement

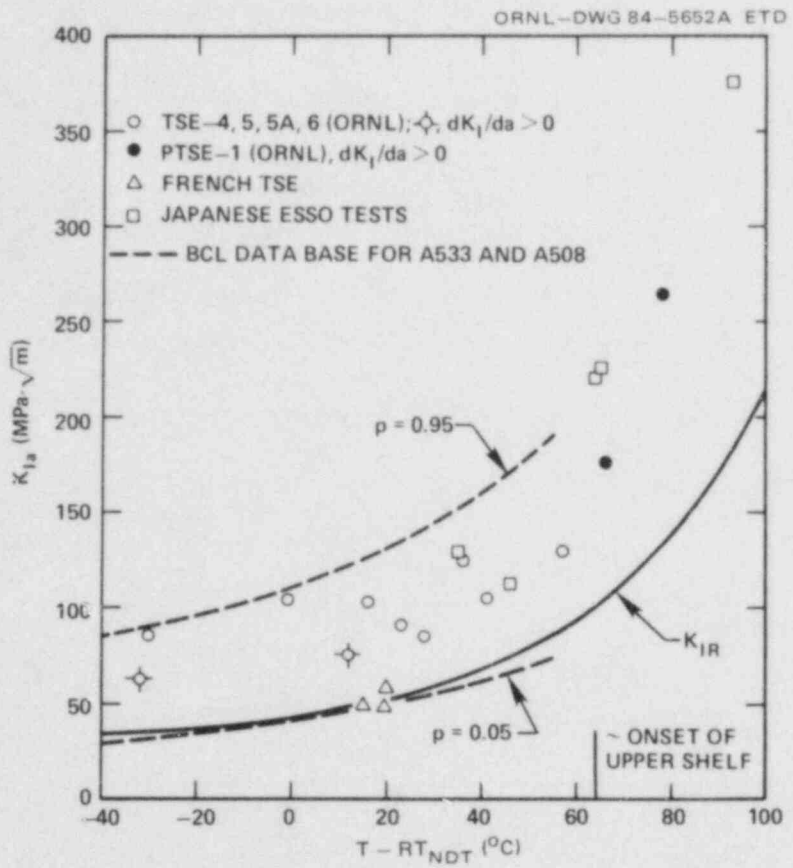

Fig. 9.2. Comparison of small-specimen and large-specimen K_{Ia} data.

between the small-specimen and large-cylinder data, it appears that the LEFM crack-arrest concept based on small-specimen data is reasonably valid and can be used with confidence in evaluating the integrity of PWR pressure vessels during postulated PTS transients. Furthermore, the data in Fig. 9.2 indicate that it would be appropriate to use a higher mean curve in the IPTS probabilistic FM analyses than that expressed by Eq. (9.2). The effect of using a higher value is discussed in Sect. 9.2.1.3.

With reference to Fig. 9.2, it is also of interest to note that the CVN onset of upper-shelf temperature corresponds to a mean value of K_{Ia}, based on the large-specimen data, of nearly 200 MPa·$\sqrt{m}$. This indicates that little, if any, ductile tearing would take place at K_I values less than the $(K_{Ia})_{max}$ value selected for the IPTS studies.

9.2.1.3. Behavior of inner-surface flaws during PTS transients. An FM analysis of the Oconee-1[17] vessel, based on the model described earlier, indicates that for some postulated high-pressure transients, axially oriented inner-surface flaws with a maximum surface length of ~2 m (height of a shell course) will propagate through the vessel wall without

arresti , as indicated by the set of critical-crack-depth curves in Fig. 9.3.* Furthermore, increasing the value of $(K_{Ia})_{max}$ above 220 MPa$\cdot\sqrt{m}$ does not affect this result, provided that Eq. (9.2) is appropriate for extrapolating to higher values of K_{Ia}. For an increase in $(K_{Ia})_{max}$ to have an ameliorating effect, the K_{Ia} vs T curve would have to turn up more abruptly.

For a somewhat more severe transient than that associated with Fig. 9.3, it is possible, as shown in Fig. 9.4, for crack arrest to take place if $(K_{Ia})_{max}$ is increased above 220 MPa$\cdot\sqrt{m}$. However, the arrest event would take place at or above a temperature corresponding to the onset of the Charpy upper shelf, and, thus, ductile tearing would be expected, as indicated in Fig. 9.5. If ductile tearing did not take place and if the particular transient extended for ~30 min or more beyond the minimum critical time (~35 min), the propagated flaw would reinitiate, and, presumably, arrest would not take place, as indicated in Fig. 9.4. Furthermore, if the transient extended as little as ~10 min or more beyond the

*The initiation and arrest curves ($K_I = K_{Ic}$, $K_I = K_{Ia}$) in Figs. 9.3 and 9.4 are based on the ASME Sect. XI K_{Ic} and I_{Ia} curves, and no maximum values were imposed. The inclusion of the 220 MPa$\cdot\sqrt{m}$ iso-K_I curve allows interpretation of the results as if this maximum value were imposed.

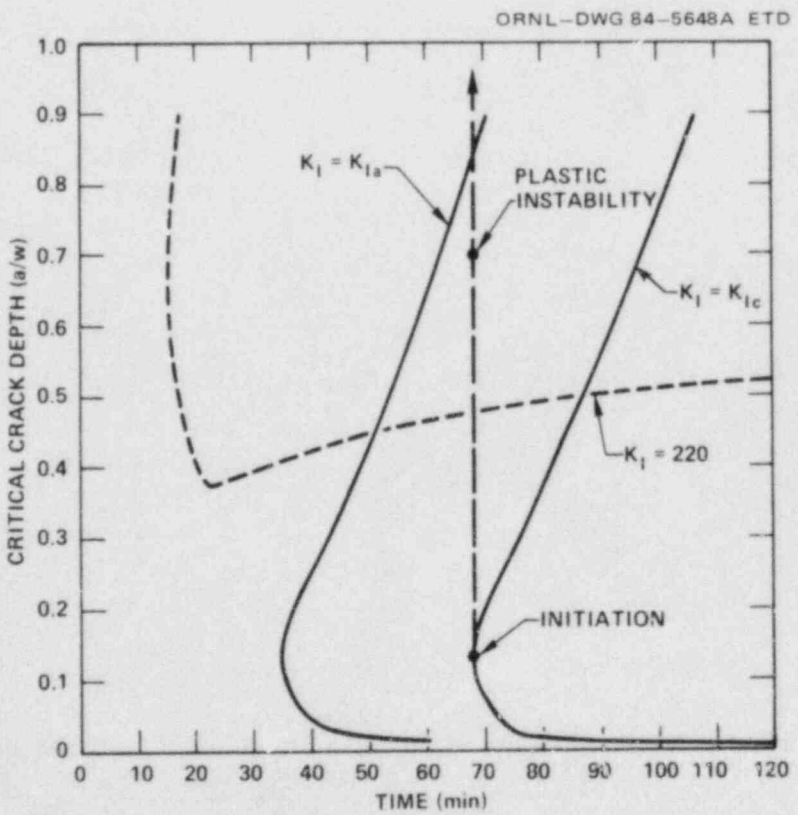

Fig. 9.3. Critical-crack-depth curves for Oconee-1 postulated transient No. 44, 32 EFPY, weld SA1430.

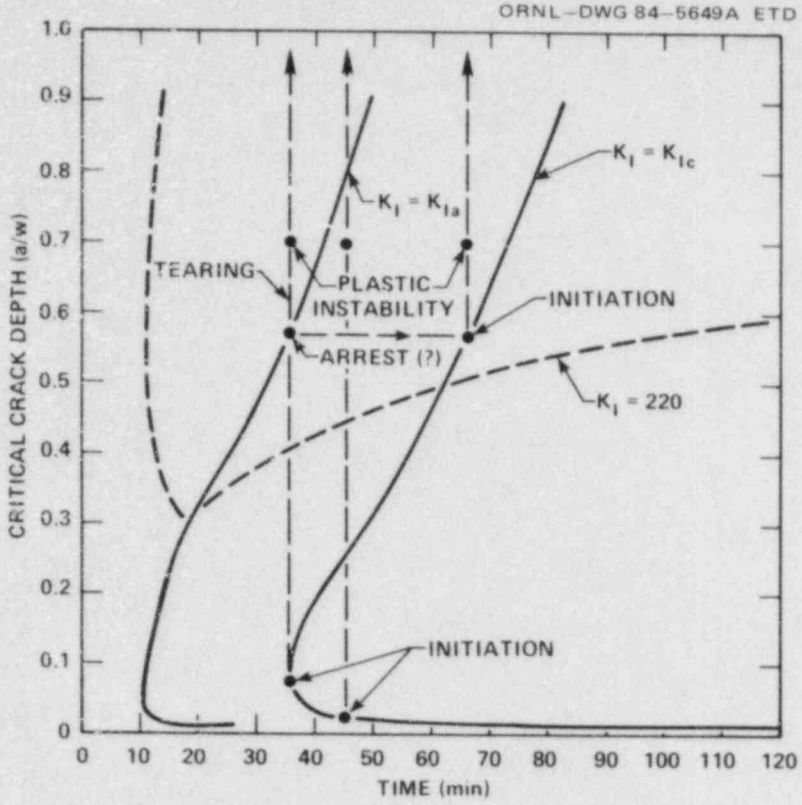

Fig. 9.4. Critical-crack-depth curves for Oconee-1 postulated transient No. 34, 32 EFPY, weld SA1430.

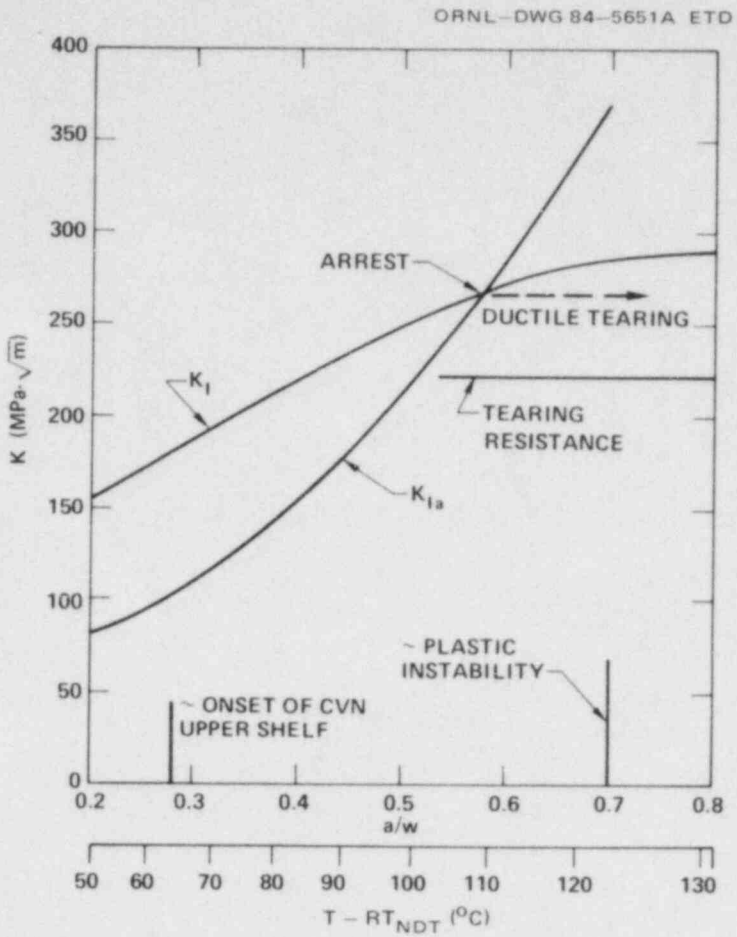

Fig. 9.5. Radial distribution of K_I and K_{Ia} in vessel wall at specific time in PTS transient.

minimum critical time, much shallower flaws could propagate without arresting. Thus, for this transient also, increasing $(K_{Ia})_{max}$ does not prevent failure, at least for the set of conditions assumed for the particular analysis regarding fluence, fracture toughness, copper and nickel concentrations, and warm prestressing (WPS). (Figures 9.3 and 9.4 indicate, by the minimum in the iso-K_I curve, that WPS would prevent crack-initiation events. For a number of reasons not discussed herein, no benefit was taken for WPS in the IPTS studies.)

In the probabilistic FM analysis, parameters that have significant uncertainties associated with them are simulated, resulting in a rather broad range of predicted flaw behavior for a given transient. It is not feasible to examine each of the thousands of cases involved in the manner described above, but it is possible, of course, and instructive to perform the probabilistic FM analysis using different values of $(K_{Ia})_{max}$ in conformance with the arrest model described in Fig. 9.1. This has been done for several typical Oconee and Calvert Cliffs postulated transients for a range of $(K_{Ia})_{max}$ values of 220 to 330 MPa$\cdot\sqrt{m}$. The results indicate a factor of 3 decrease in $P(F|E)$ for some transients and less for many others. Thus, it appears that increasing $(K_{Ia})_{max}$ will not substantially reduce the calculated frequency of vessel failure.

Since the data in Fig. 9.2, which are reproduced in Fig. 9.6 for illustrative purposes, indicate, when compared to Eq. (9.2), that a higher

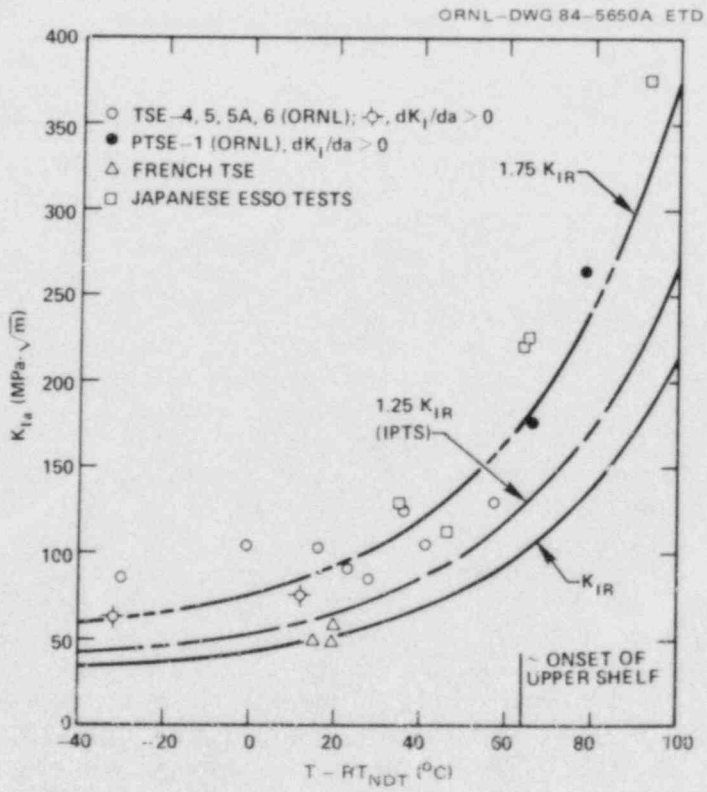

Fig. 9.6. Comparison of large-specimen K_{Ia} data and $\overline{K}_{Ia} = f(T - RT_{NDT})$ curves used in IPTS studies.

mean curve for $K_{Ia} = f(T - RT_{NDT})$ could be used in the IPTS studies, the effect on $P(F|E)$ of doing so was investigated. As indicated in Fig. 9.6, a better fit to the data is achieved with

$$\overline{K}_{Ia} = 1.75\ K_{IR} \ . \tag{9.3}$$

Using Eq. (9.3) for the probabilistic FM analysis of several of the IPTS transients, with $2\sigma = 0.45\ \overline{K}_{Ia}$ and $(K_{Ia})_{max} = 220\ MPa\cdot\sqrt{m}$, reduces $P(F|E)$ for some transients by only a factor of 4, and for other transients the reduction is less. Thus, increasing $\overline{K}_{Ia}$ in the IPTS studies to what appears to be a more realistic value does not substantially reduce the frequency of vessel failure.

9.2.2 Summary of results for Calvert Cliffs-1

A complete summary of results for the Calvert Cliffs-1 studies is beyond the scope of this report. Furthermore, the full significance of the FM results cannot be appreciated without combining these results with estimated frequencies of occurrence of the postulated transients, which is also beyond the scope of this report. However, a few points of particular interest will be discussed.

Although a million or so end points of event trees were considered, only 19 postulated transients were actually subjected to a probabilistic FM analysis. For most of the others, it was apparent that either the frequency or the conditional probability of vessel failure $P(F|E)$ was insignificant or that some transients were very similar to others. A detailed description of the transients calculated is included in Ref. 18.

Calculated values of $P(F|E)$, based only on flaws in the axial welds of the beltline region, are shown as a function of the number of effective full-power years of reactor operation (EFPY) in Fig. 9.7 for five dominant transients (those that contribute the most to the overall frequency of vessel failure). The contribution of flaws in the circumferential welds and of axial flaws in the plate segments was calculated for the two most dominant transients (8.2 and 8.3), the latter being a high-pressure transient and the former a low-pressure transient. Results of the analysis indicate that for transient No. 8.3 the circumferential flaws add ~5% to $P(F|E)$ and the plate segments ~50%. For transient No. 8.2, a less severe transient, the contributions were much less, being only 5% for the plate segments.

WPS was not included in the analysis that provided the results in Fig. 9.7. However, it was possible to estimate the effect of WPS on $P(F|E)$ from knowledge of the time of incipient WPS (time at which $\dot{K}_I = 0$) and the times at which failures occur. These estimates are presented in Table 9.3 for a number of transients. It is observed that $P(F|E)$ is reduced by several orders of magnitude for many of the transients, but for others the benefit is much less, and for transient 8.3, the most dominant transient, there is no benefit because of late repressurization, as indicated in Figs. 9.8 and 9.9. In arriving at this conclusion, the assumption is made that the increase in K_I at ~90 min for shallow flaws is sufficient to overcome WPS, and this may not actually be the case.

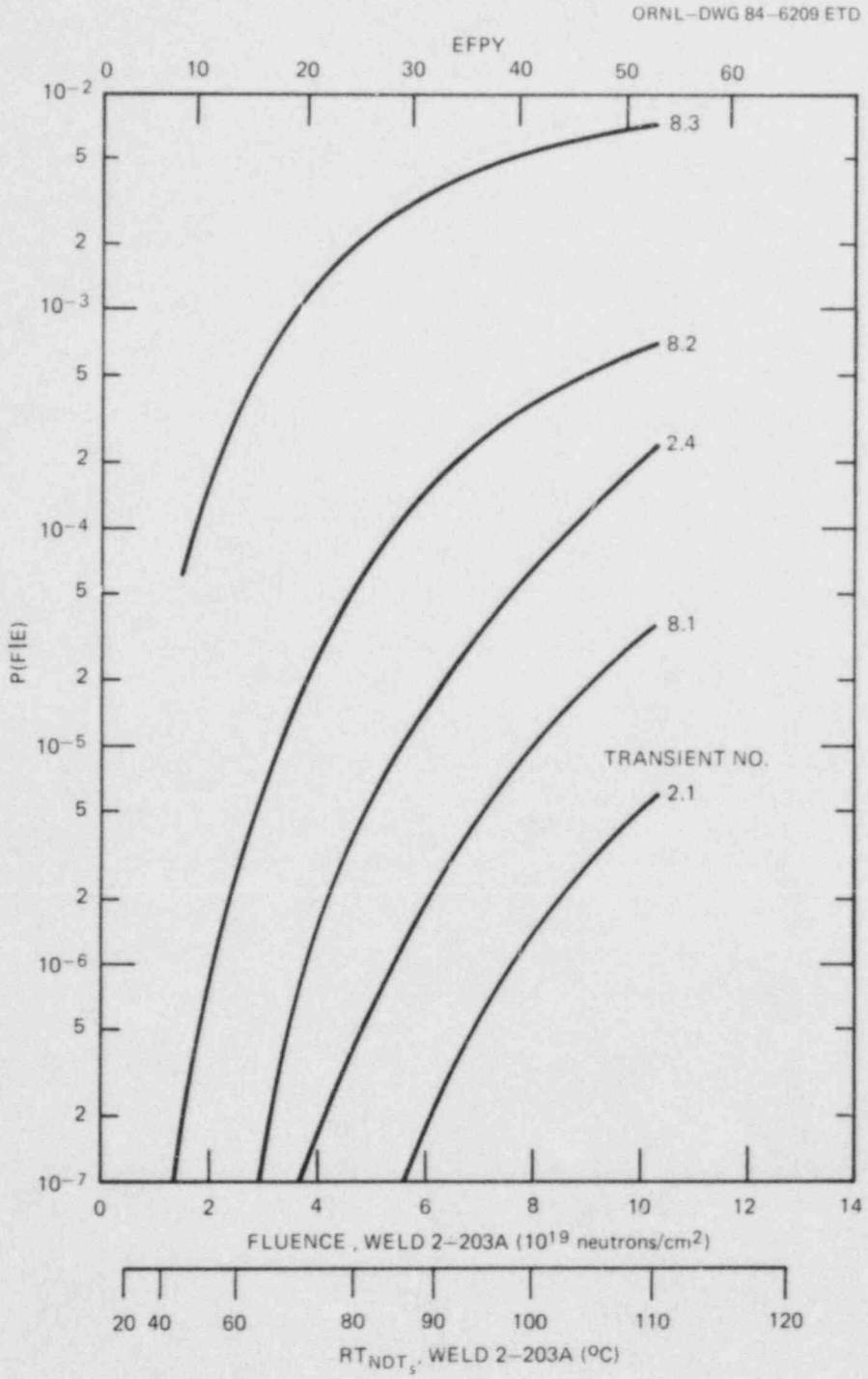

Fig. 9.7. P(F|E) vs EFPY for Calvert Cliffs-1 postulated PTS transients.

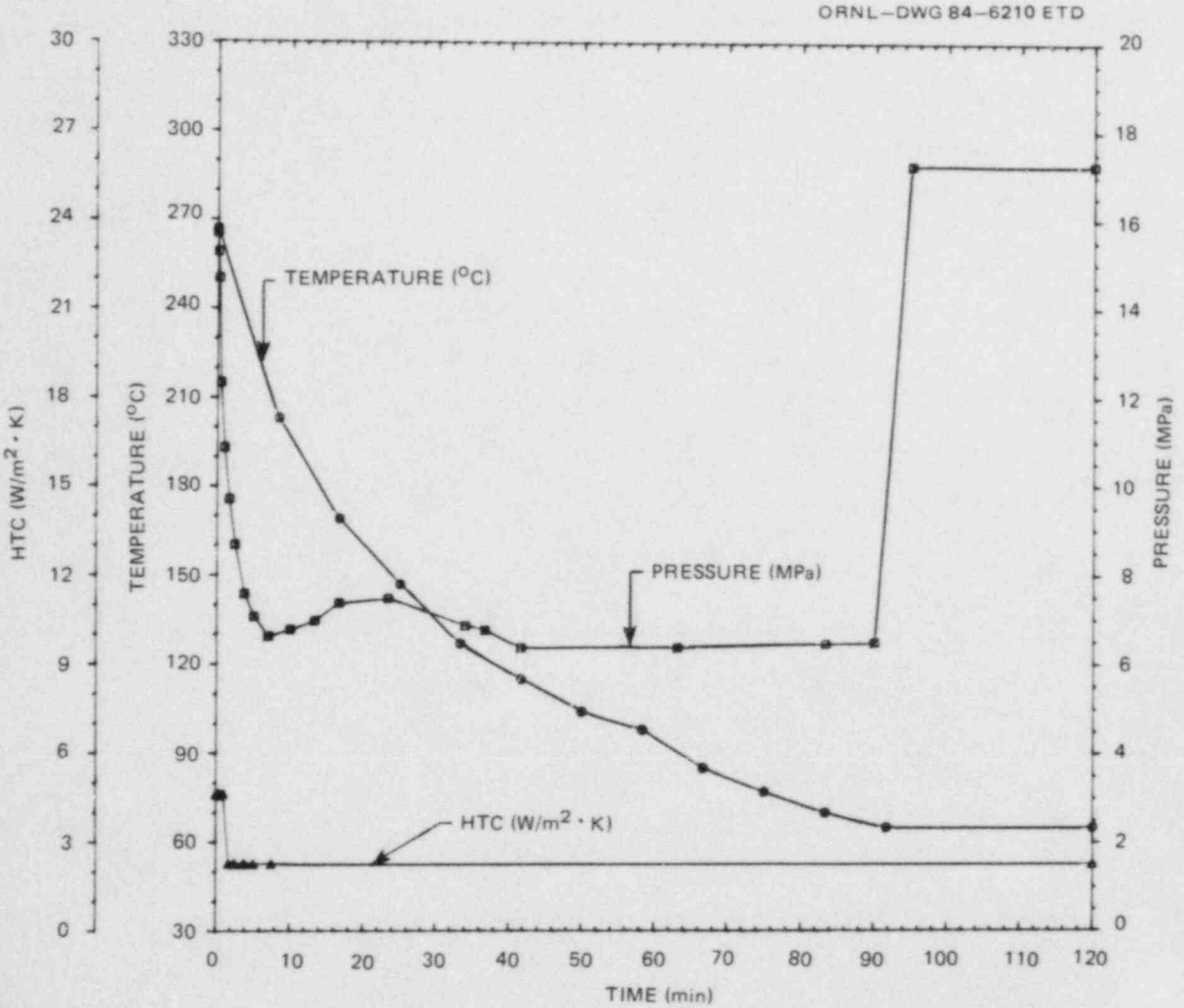

Fig. 9.8. Primary-system pressure, downcomer coolant temperature, and coolant-vessel interface fluid-film heat-transfer coefficient vs time for Calvert Cliffs-1 transient No. 8.3.

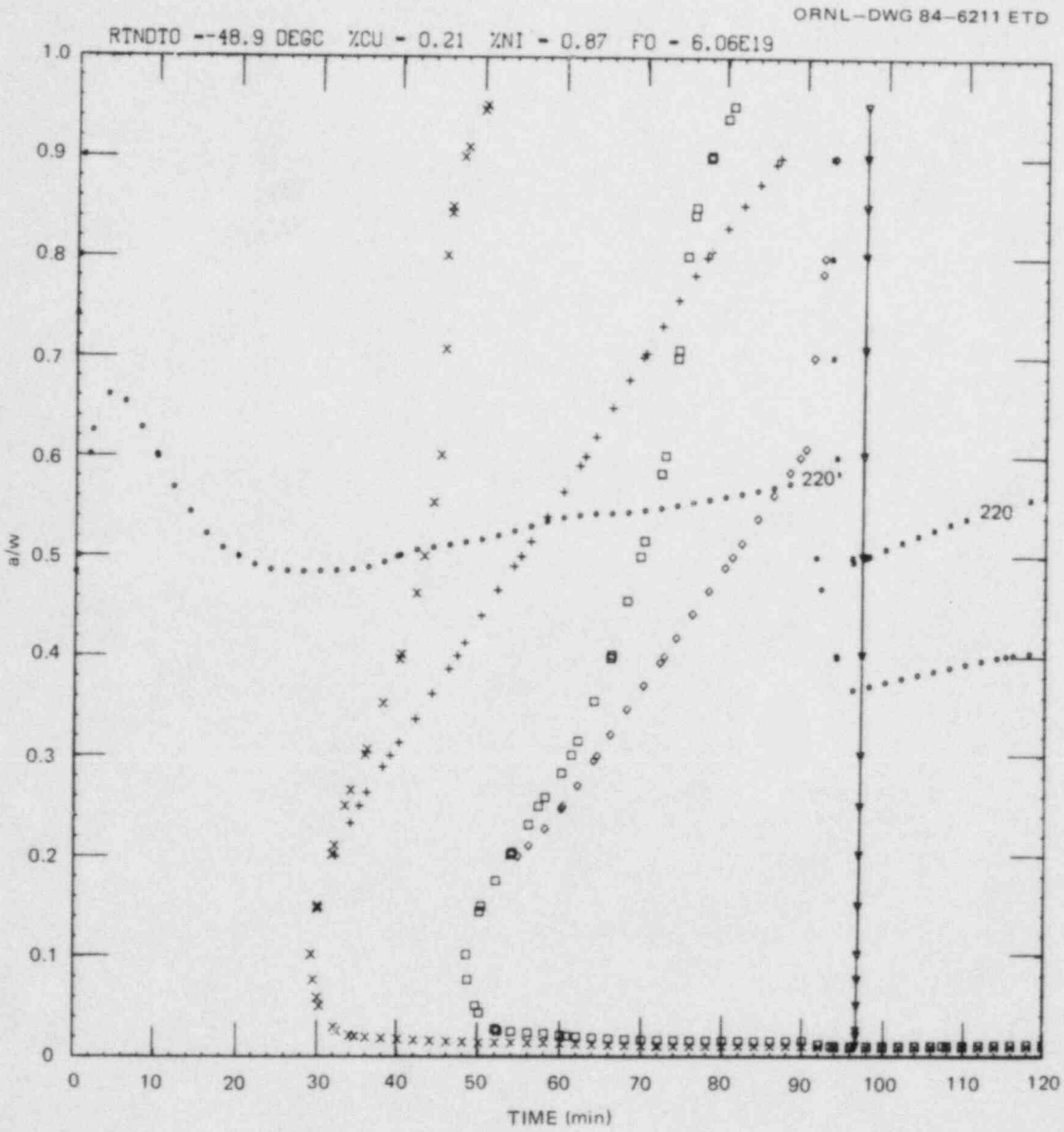

Fig. 9.9. Critical-crack-depth curves for Calvert Cliffs-1 transient No. 8.3 using -2σ K_{Ic} and K_{Ia} values and mean values of Cu, Ni, F_o, and RT_{NDT_o}.

Table 9.3. Effect of including WPS in calculation of P(F|E) at 32 EFPY

Transient	P(F|E) w/o WPS[a]	Time of WPS (min)	$\frac{P(F\|E)_{w/WPS}}{P(F\|E)_{w/oWPS}}$
1.3	6.0E-7	18	<5E-2
1.4	3.3E-6	18	<1E-2
1.5	3.0E-5	18	<2E-3
1.6	5.1E-5	20	<1E-3
1.7	1.9E-4	50	4E-1
1.8	2.5E-4	40	1E-1
2.1	2.0E-7	18	4E-1
2.4	1.7E-5	50	1E-1
2.5	7.6E-6	15	<4E-3
2.6	8.2E-6	20	<4E-3
2.7	1.8E-4	50	2E-1
2.8	2.3E-6	18	<1E-2
3.6	7.2E-5	15	<4E-3
3.10	6.7E-5		
4.6	2.0E-7	20	<2E-1
4.13	6.0E-6		
8.1	4.0E-7	40	1E-2
8.2	1.5E-4	70	1E-3
8.3	5.9E-3	100	1.0

[a] $P(F|E)_{w/WPS}$ is the value of P(F|E) with WPS included in the analysis, and $P(F|E)_{w/oWPS}$ is the value without WPS included.

9.2.3 HBR-2 studies

For the Oconee-1 and Calvert Cliffs-1 studies, the inner-surface fluence F_o, the initial nil-ductility reference temperature RT_{NDT_o}, and the concentrations of copper (Cu) and nickel (Ni) were used as independent variables in the calculation of P(F|E). However, greater flexibility in the use of the results is achieved if only RT_{NDT_o} and ΔRT_{NDT_s} are used as independent variables, where ΔRT_{NDT_s} is the increase in RT_{NDT} at the inner surface due to radiation damage. To make this choice, it is necessary to make a simplifying assumption regarding the radiation-damage trend curve [$\Delta RT_{NDT} = f(Cu, Ni, F_o)$] for high values of F_o. This assumption, discussed in Ref. 3, leads to a simple relation between ΔRT_{NDT_s} and $\Delta RT_{NDT}(a)$, where the latter quantity is the value of ΔRT_{NDT} at the tip of

the crack. The relation is

$$\Delta RT_{NDT}(a) = \Delta RT_{NDT_s} e^{-0.27\,ma} , \qquad (9.4)$$

where m is the fluence attenuation coefficient and a is the crack depth or radial position in the vessel wall relative to the inner surface. By specifying values of ΔRT_{NDT_s} and RT_{NDT_o}, values of K_{Ic} and K_{Ia} can be calculated without having to specify values of Cu, Ni, and F_o since K_{Ic}, $K_{Ia} = f(T - RT_{NDT})$, where the temperature T and RT_{NDT} correspond to the tip of the flaw.

Another problem with using RT_{NDT} as the independent variable in the calculation of $P(F|E)$ is that the uncertainty in the value of ΔRT_{NDT} associated with the uncertainties in Cu, Ni, and F_o must be determined. This was done by using Monte Carlo techniques and by simulating Cu, Ni, and F_o in the equation $\Delta RT_{NDT} = f(Cu, Ni, F_o)$. Normal distributions were used for Cu, Ni, and F_o, and the resultant distribution for ΔRT_{NDT} was very nearly normal. The standard deviation was somewhat dependent on the mean value of Cu but was insensitive to the mean value of F_o. An average standard deviation of 0.14 $\overline{\Delta RT_{NDT}}$ was used in the HBR-2 studies and corresponds to the standard deviations for Cu, Ni, and F_o given in Ref. 17.

When using RT_{NDT} as the independent variable, one must first specify values of $\overline{RT_{NDT_o}}$ and $\overline{\Delta RT_{NDT_s}}$. The next step is to simulate ΔRT_{NDT_s}, using $\sigma = 0.14\ \overline{\Delta RT_{NDT}}$ (this corresponds to simulating values of Cu, Ni, and F_o and then calculating ΔRT_{NDT_s} using these values). The final step is to simulate RT_{NDT_s} using $\sigma = \sqrt{\sigma_o^2 + \sigma_\Delta^2}$, where σ_o is one standard deviation for RT_{NDT_o} and σ_Δ is one standard deviation associated with the uncertainty in the correlation for ΔRT_{NDT}. Values of σ_o and σ_Δ used in the IPTS studies are given in Ref. 17.

As indicated above, it is necessary for both RT_{NDT_o} and ΔRT_{NDT_s} to be independent variables in the calculation of $P(F|E)$. However, once the calculations have been made, the sum of the two, RT_{NDT_s}, can be used as a single independent variable without introducing an excessive error. For instance, values of $P(F|E)$ were calculated for several different HBR-2 transients, assuming $\overline{RT_{NDT_s}}$ = 171, 143, and 116°C, and RT_{NDT_o} = −49, −18, and 10°C; for a given value of $\overline{RT_{NDT_s}}$, the largest variation in $P(F|E)$ over the indicated range of RT_{NDT_o} values was a factor of ~2.5. For all cases the factor increased with decreasing $\overline{RT_{NDT_s}}$ and was essentially unity for $\overline{RT_{NDT_s}}$ = 171°C. For lower values of $\overline{RT_{NDT_s}}$, the factor was sensitive to the type of transient and tended to decrease with increasing severity of the transient.

For HBR-2, three types of flaws were considered: 2-D axial flaws in the plate segments, 3-m-long axial flaws in axial welds, and 2-D circumferential flaws in circumferential welds. Values of $\hat{P}_j(F|E)$ — the conditional probability of failure for a flaw in the jth region, normalized to one flaw per simulated vessel — were calculated as a function of $\overline{RT_{NDT}}_s$ with $\overline{RT_{NDT}}_o = -49°C$. Typical results are shown in Fig. 9.10 for one of ~50 postulated transients analyzed for HBR-2.

To obtain the total P(F|E) for a specific transient, it is only necessary to sum the contribution from each type of flaw and/or region of

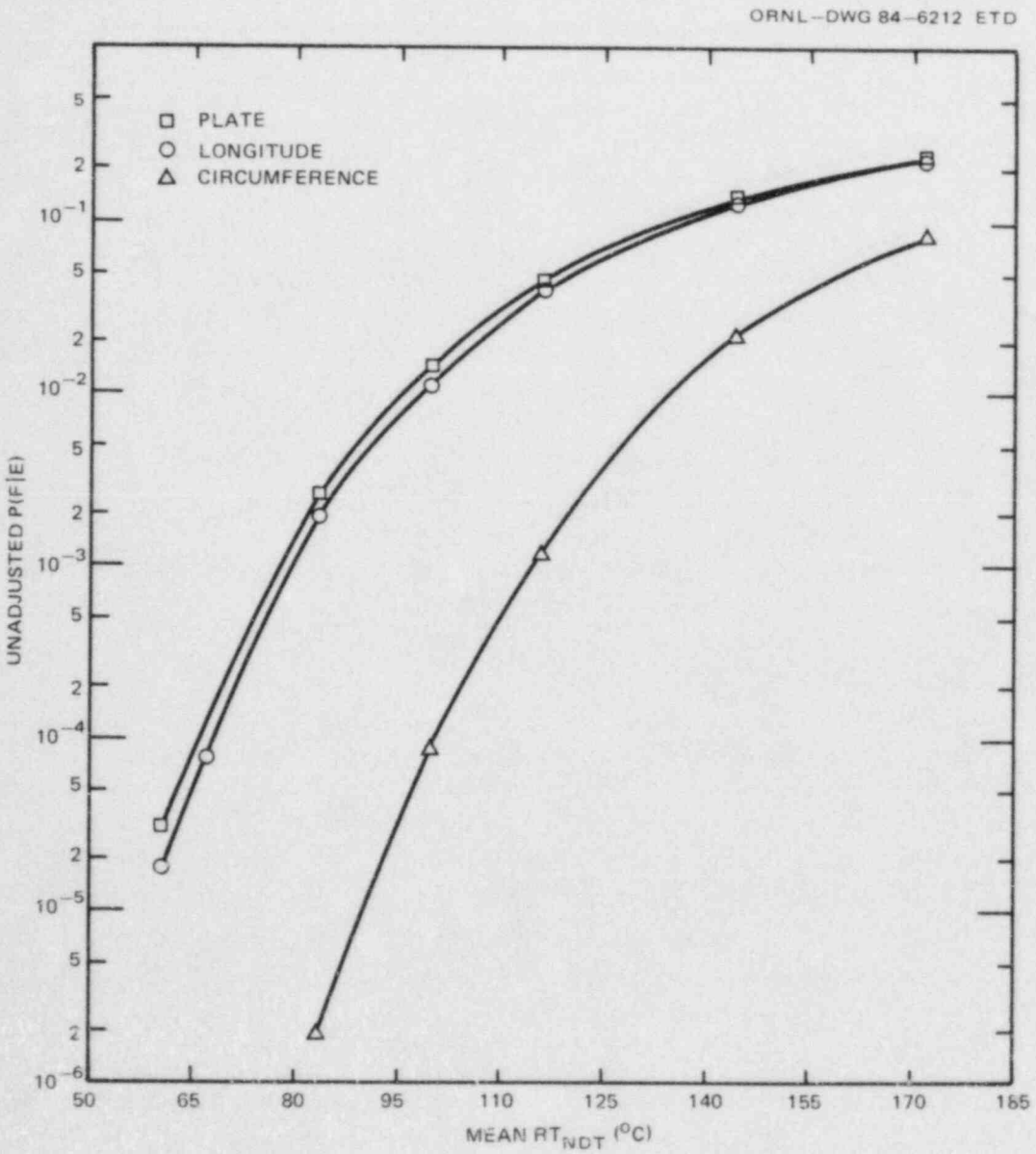

Fig. 9.10. $\hat{P}_j$ vs RT_{NDT} for H. B. Robinson transient 8.6.

the vessel:

$$P(F|E) = \sum_j \hat{P}_j(F|E)\ N_j V_j\ , \qquad (9.5)$$

where

N_j = flaw density in region j,
V_j = volume of region j.

Preliminary results for HBR-2 indicate that predicted values of RT_{NDT} at 32 EFPY are low enough that $\hat{P}_j(F|E) < 10^{-6}$ for all postulated transients. This implies a rather low frequency of vessel failure ($<10^{-8}$/ reactor year).

9.3 Subclad-Crack Thermal-Shock Studies

R. D. Cheverton J. W. Bryson
D. G. Ball

ORNL is proposing to conduct a TSE with a clad cylinder to investigate the behavior of subclad, finite-length flaws. Feasibility studies are under way to determine whether the existing ORNL TSE concept (1-m-OD test cylinder and liquid-nitrogen test facility)[10] is appropriate for the desired investigations.

A reason for concern over the adequacy of the present TSE concept is that subclad flaws tend to have much lower K_I values than those for surface flaws, which have been used exclusively in previous thermal-shock tests.[10] It is possible that the most severe thermal shock achievable in the present test facility will not be adequate to cause propagation of the desired initial shallow subclad flaw.

It is possible that the severity of the thermal shock achievable with liquid nitrogen can be increased, at least in the initial part of the thermal transient, by spraying the liquid nitrogen against the inner surface of the test cylinder rather than by simply dunking the test cylinder. The spray technique is being investigated on a lab scale, and a preliminary concept for a full-scale test is described in Ref. 2.

Under the present natural convection (dunking) conditions, the fluid-film heat-transfer coefficient tends to be low at the beginning of the transient, when the surface temperature is high, but then increases substantially and continuously as the surface cools.[19] This situation is made possible by the use of a special surface coating that tends to suppress film boiling and promotes nucleate boiling.[19] However, this tendency is greater as the surface temperature approaches the saturation temperature, and, furthermore, the initial test temperature is limited by the properties of the coating to ~120°C. It is believed that by spraying the liquid nitrogen, in which case the surface coating would not be used, liquid in the form of droplets would impinge on the surface. Thus, the

extent of nucleate boiling would be dependent only on the rate of droplet impingement, which, presumably, can be controlled. Results of preliminary lab tests with initial temperatures as high as 288°C look promising.

With regard to the analytical feasibility studies, LEFM and EPFM 2- and 3-D analyses are being performed, using the ORMGEN-ADINA-ORVIRT[20-22] system of finite-element fracture codes. A 19-mm-deep, 6/1 semielliptical, subclad flaw has been analyzed, assuming typical TSE test conditions.[10] A preliminary analysis indicated that WPS would occur at ~8 min into the transient. Thus, only earlier times (1, 3, 5, and 7 min) have been considered for a detailed analysis. Corresponding temperature distributions in the wall are shown in Fig. 9.11.

For subclad flaws the clad-base interface also becomes a crack front, and this requires a core of special crack-tip elements in the modeling at the interface. ORMGEN and ORVIRT are presently capable of considering only the curved portion of the semielliptical crack front for the calculation of the relevant fracture parameters (energy release rates and K_I values). Modifying the codes to calculate these quantities at the interface would be prohibitively time consuming for the feasibility studies; thus, 2-D models, which are capable of calculating the required K_I

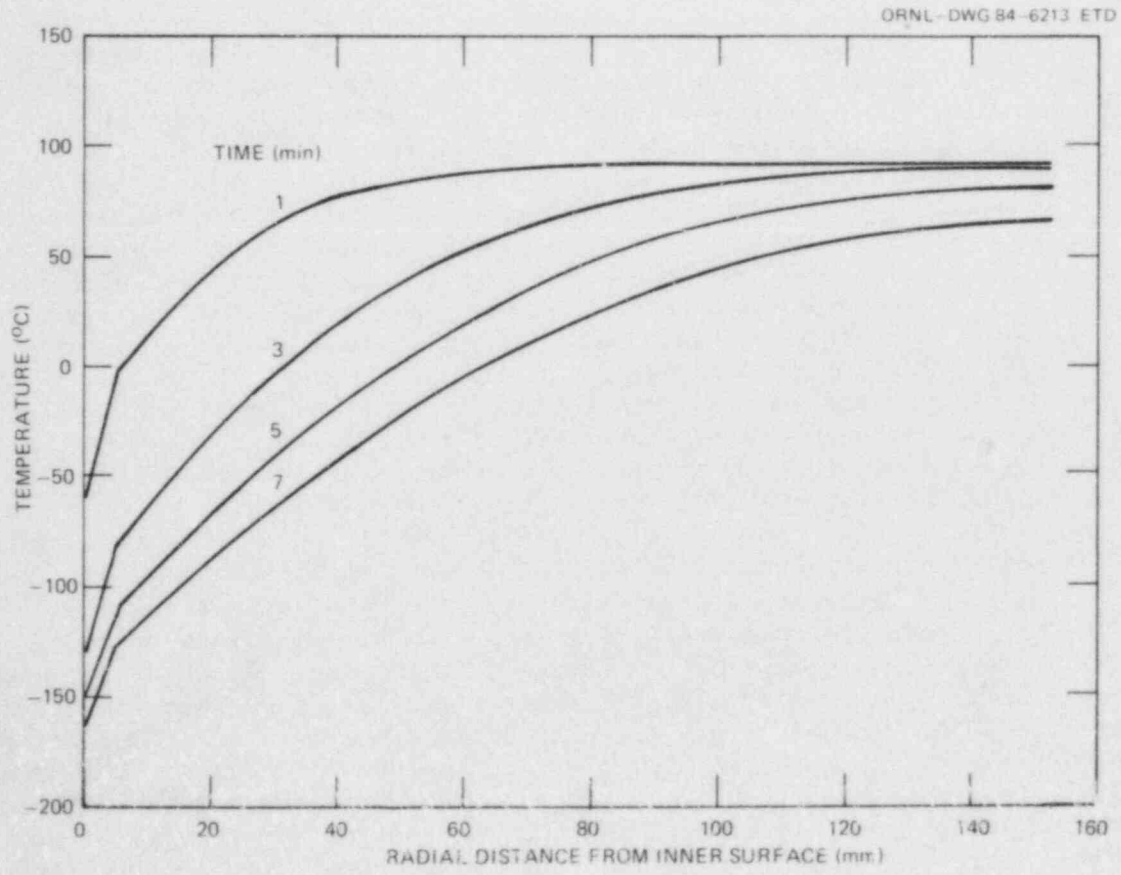

Fig. 9.11. Test-cylinder temperature distributions corresponding to typical TSE.

values at the base-clad interface, have been constructed and are being used to estimate the ratio of K_I values at the top and bottom of the flaw. Figures 9.12–9.15 show both the 3-D and 2-D finite-element models used for the present studies. Material properties used for the cladding and base material are shown in Table 9.4 and in Fig. 9.16, the latter including plots of the assumed stress-strain curves.

The fracture-toughness data (K_{Ic} vs T) used in the feasibility study are represented by the dashed curve in Fig. 9.17, which is the ASME Sect. XI lower-bound K_{Ic} curve[5] (solid curve in Fig. 9.17) times a factor of 1.8. The data points shown in Fig. 9.17 are those obtained from previous TSEs, and it is evident that the dashed curve is a reasonable mean for these data.

Results of the calculations of K_I for the four different times in the transient are shown in Table 9.5 and Fig. 9.18, while Table 9.6 and Fig. 9.19 compare the 3-D elastic-plastic K_I values with the corresponding values of $\overline{K}_{Ic}$ for RT_{NDT} = −18 and 66°C ($\overline{K}_{Ic}$ data from dashed curve in Fig. 9.17). The values of RT_{NDT} are typical extremes of interest in the feasibility studies and correspond proportionately to full-temper and quench-only heat treatments, respectively.

The data in Table 9.5 indicate that (1) for the deepest point of the flaw, there is little difference between the 2-D and 3-D K_I values for both the elastic and elastic-plastic analysis; (2) for the 2-D analysis the K_I values at the clad-base interface are substantially greater than those at the deepest point; and (3) the elastic-plastic analysis results

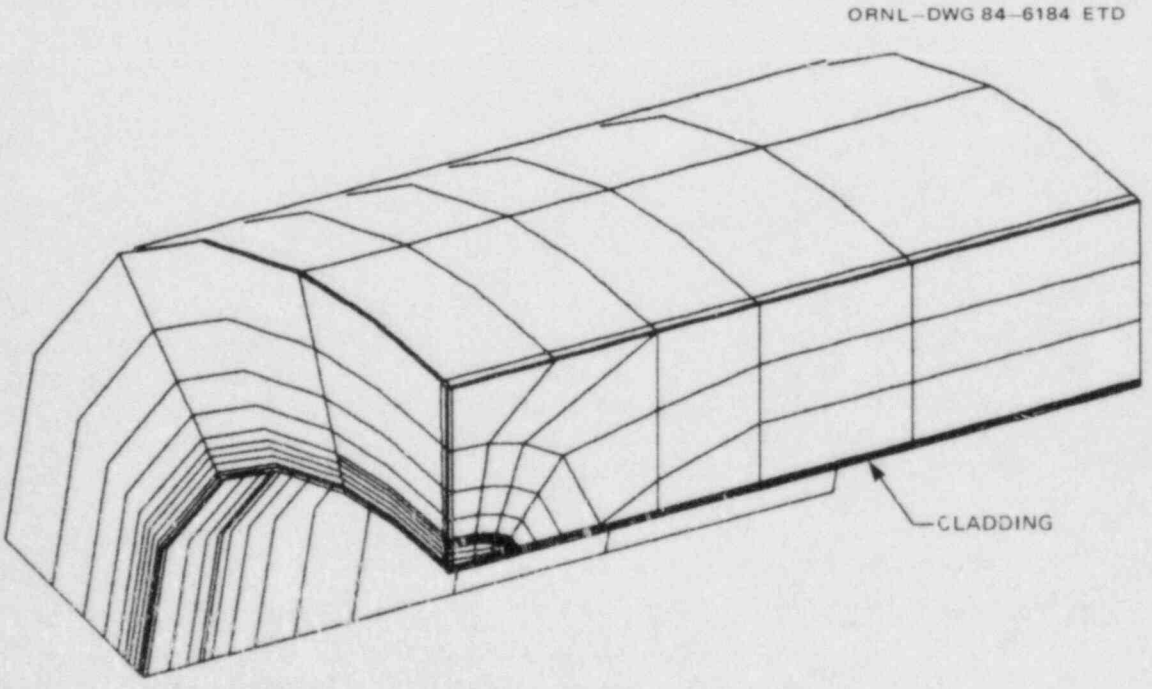

Fig. 9.12. Finite-element model for 3-D analysis of 6/1 semi-elliptical flaw in TSE test cylinder.

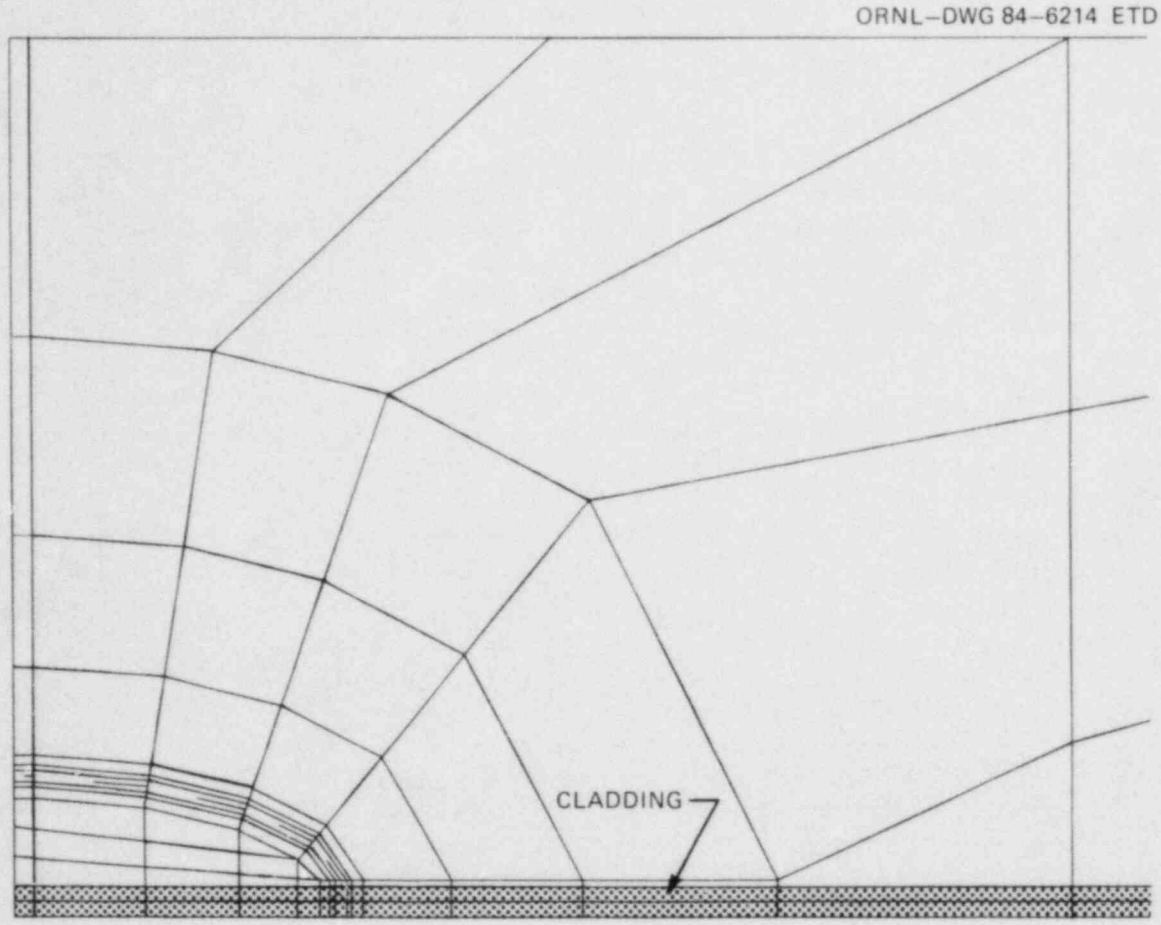

Fig. 9.13. Enlarged view of crack-tip region for 3-D finite-element analysis of subclad flaw in TSE test cylinder.

in substantially higher K_I values than the elastic analysis. Because of the good agreement between the 2-D and 3-D results for the deepest point of the flaw, it is reasonable to estimate the 3-D K_I value at midlength of the interface portion of the crack front by multiplying the 3-D deepest-point K_I value by the ratio of the 2-D values at the interface and deepest point. This was done to obtain the 3-D midlength interface values given in Table 9.6 and Fig. 9.19.

The comparison in Table 9.6 of the 3-D elastic-plastic K_I values with the corresponding $\overline{K}_{Ic}$ values indicates that for the deepest point of the flaw, $(K_I/\overline{K}_{Ic})_{max}$ = 0.95 and 0.89 for RT_{NDT} = 66 and −18°C, respectively, and, of course, the maximum ratio occurs at the time corresponding to the onset of WPS (larger ratios may occur afterwards, but not before). Considering all of the uncertainties in an experiment of this type, these results indicate that an experiment in the existing TSE test

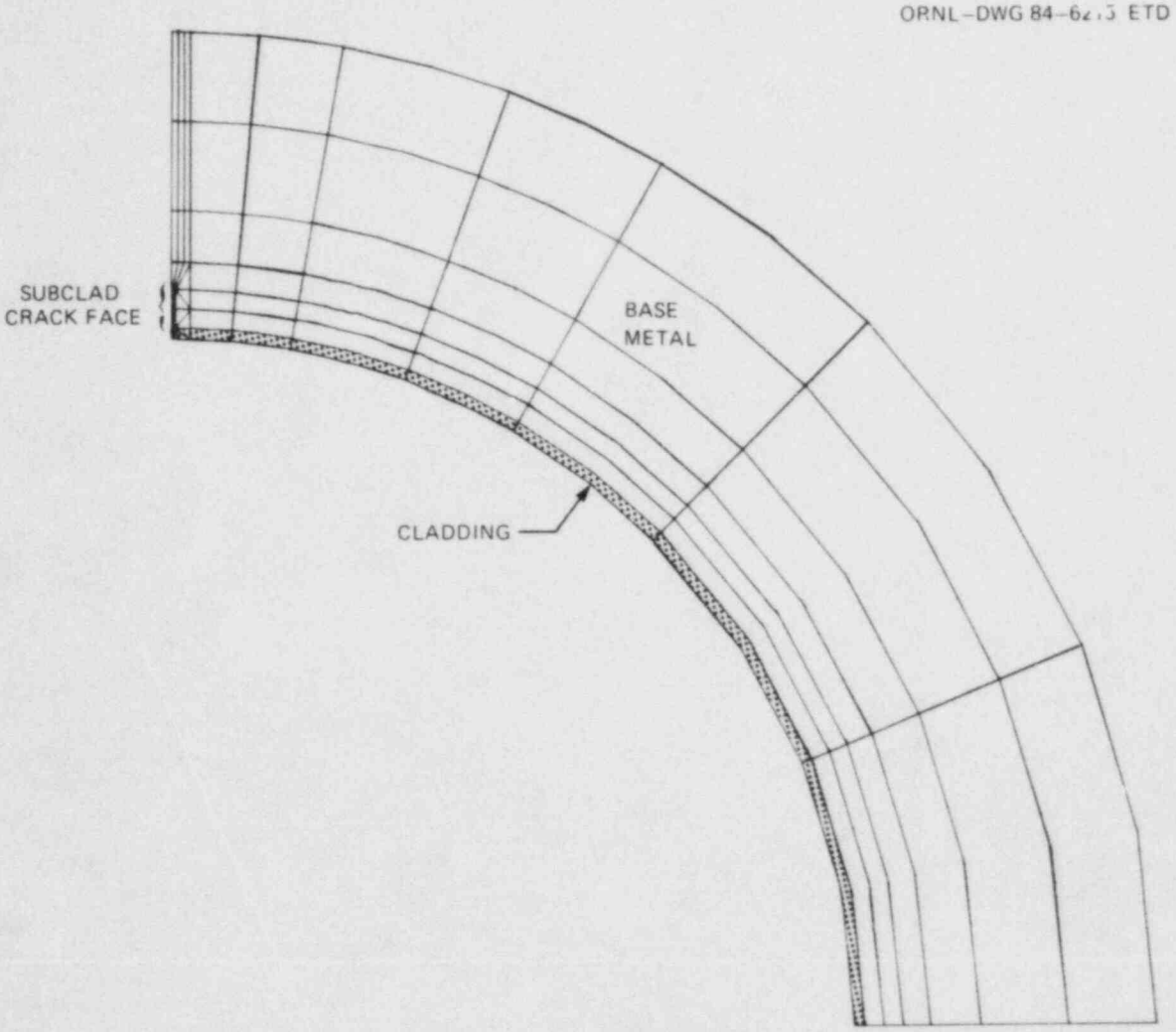

Fig. 9.14. Finite-element model for 2-D analysis of subclad flaw in TSE test cylinder.

facility would have a rather low probability of resulting in crack propagation in the base material. It is preferred that at the onset of WPS $(K_I/\overline{K}_{IC}) > 1.5$. Thus, different initial crack depths, a more severe thermal shock (liquid-nitrogen-spray concept), and combined thermal and pressure loading (PTSE facility) are being considered. It is not likely that RT_{NDT} can be increased above 66°C, which corresponds to a quench-only heat treatment for the A508 test-cylinder material.

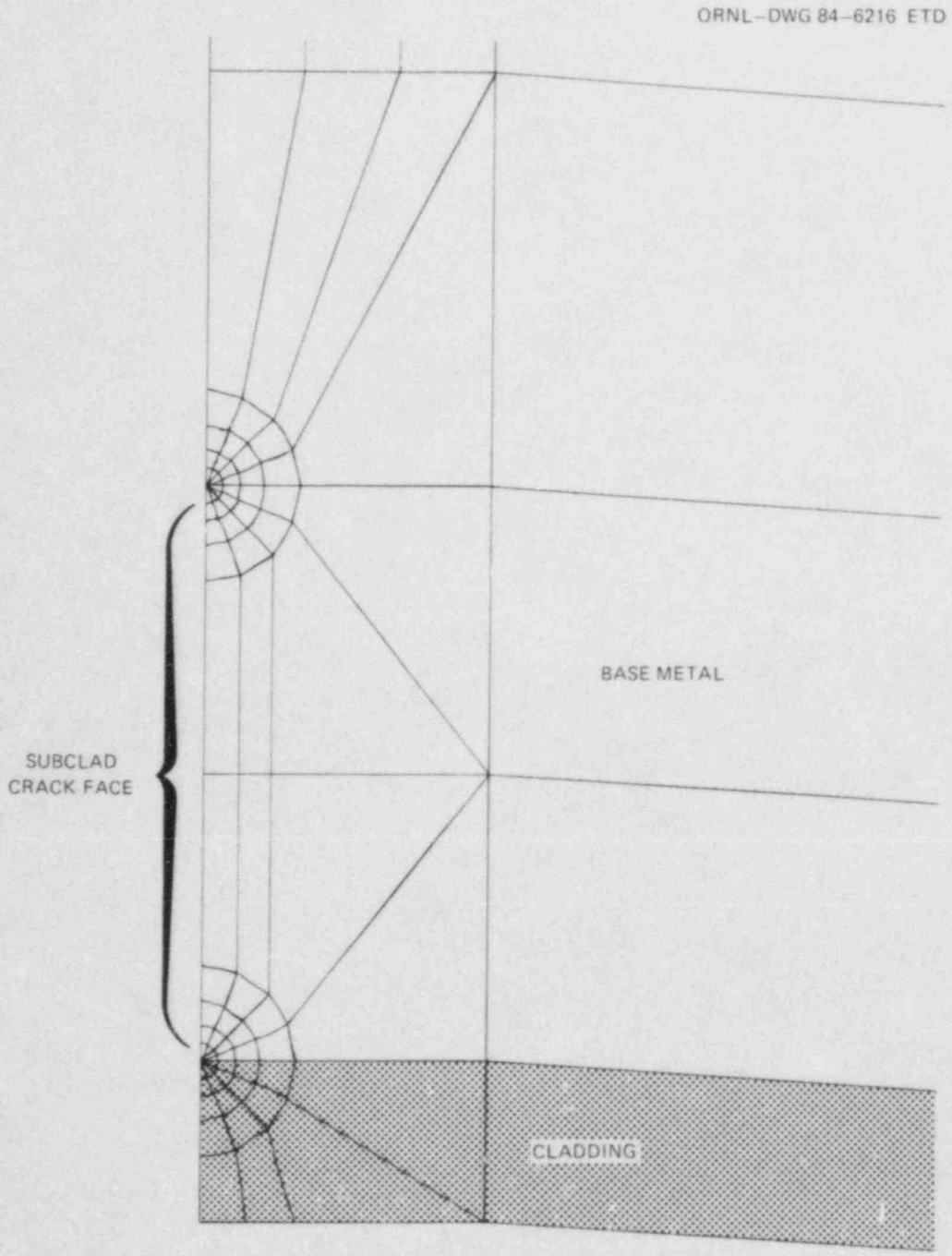

Fig. 9.15. Enlarged view of crack-tip region for 2-D finite-element analysis of subclad flaw in TSE test cylinder.

Table 9.4. Material properties used in FM analysis of proposed subclad-crack TSE

Property	Cladding	Base
Modulus of elasticity, MPa	207,000	193,000
Coefficient of expansion, $°C^{-1}$	14×10^{-6}	11.7×10^{-6}

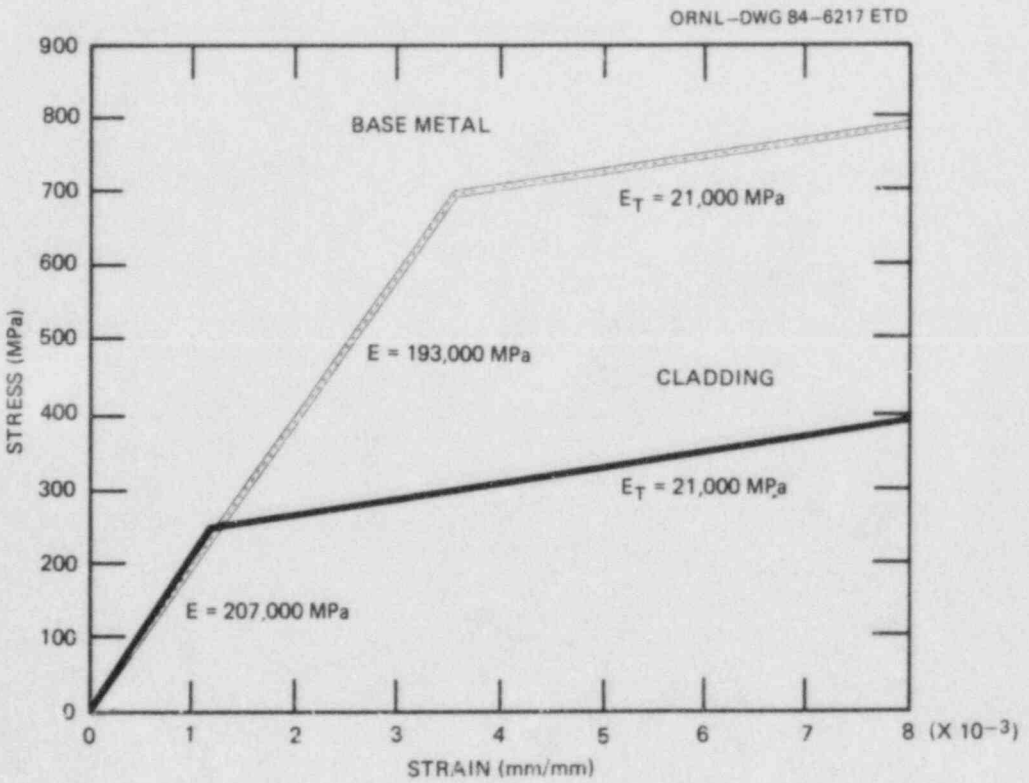

Fig. 9.16. Bilinear stress-strain curves for elastic-plastic subclad analysis.

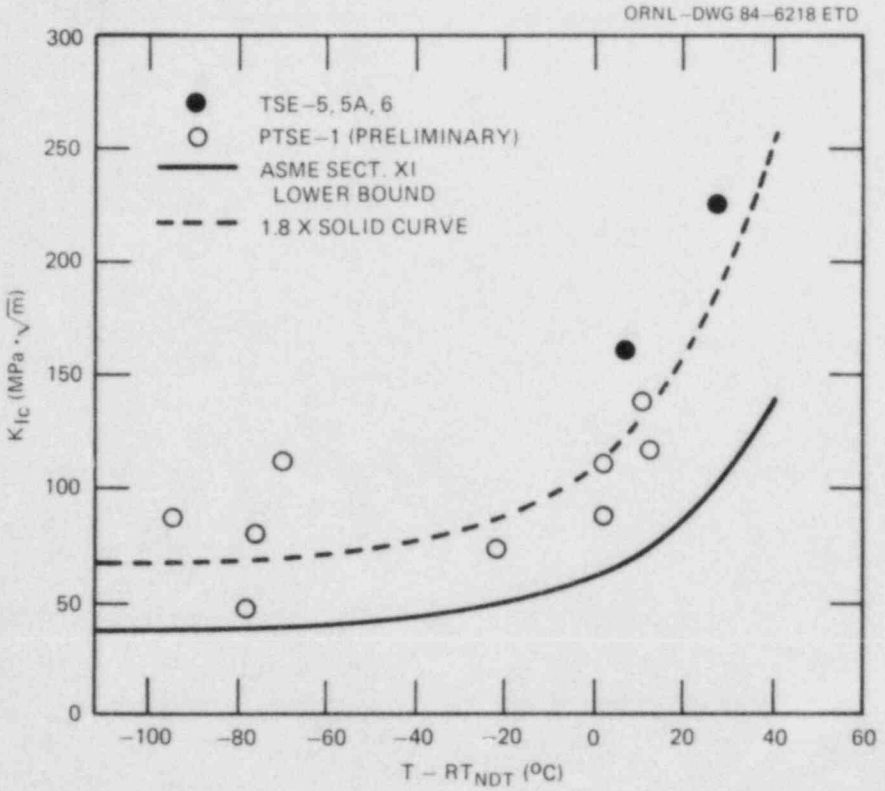

Fig. 9.17. (K_{Ic} vs T – RT_{NDT}) data deduced from TSE and PTSE experiments.

Table 9.5. K_I values for 19-mm-deep, 6/1 semielliptical and 2-D, subclad flaws under typical TSE test conditions

Time into transient (min)	K_I (elastic analysis) (MPa•√m)			K_I (elastic-plastic) (MPa•√m)		
	2-D		3-D	2-D		3-D
	Clad-base interface	Max depth	Max depth	Clad-base interface[a]	Max depth	Max depth
1	43	20	21		26	23
3	77	47	46		60	53
5	84	54	53		70	61
7	84	54	53		72	62

[a]Unstable values obtained for all times.

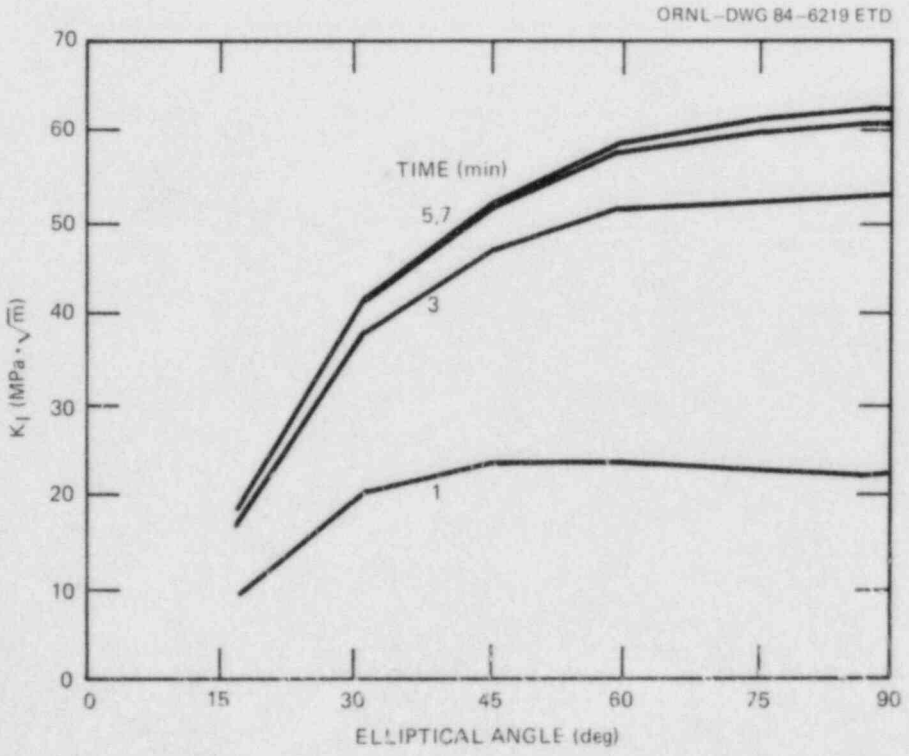

Fig. 9.18. K_I variation along crack front for 3-D elastic-plastic analysis.

Table 9.6. Crack-tip temperature, elastic-plastic K_I and K_{Ic} data for the 19-mm-deep, 6/1 semielliptical subclad flaw under typical TSE test conditions

Time in transient (min)	Crack-tip temperature (°C)		3-D K_I values (MPa·√m)		Crack-tip $\overline{K}_{Ic}$ values[a] (MPa·√m)	
	Interface	Max depth	Interface	Max depth	Interface	Max depth
1	−2	55	49	23	137/69	629/95
3	−79	−17	88	53	70/66	107/68
5	−108	−54	95	61	68/66	76/66
7	−126	−76	96	62	66/66	70/66

[a] RT_{NDT} = −18°C/66°C
K_{Ic} = 1.8 × ASME XI lower bound for base material only (cladding toughness not included.

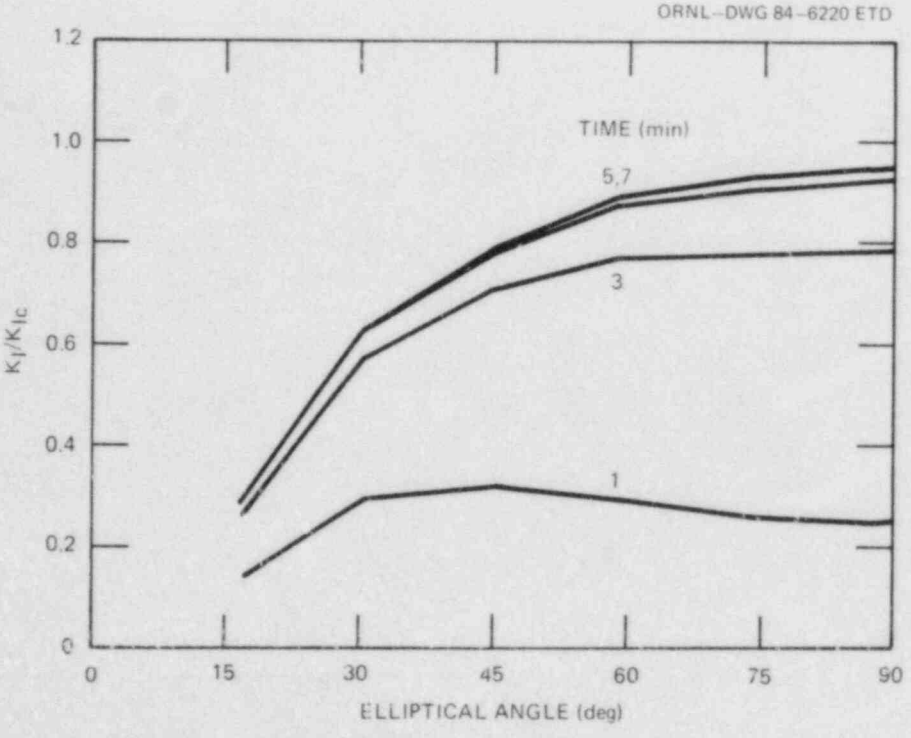

Fig. 9.19. K ratio along crack front for 3-D elastic-plastic analysis.

References

1. R. D. Cheverton and D. G. Ball, "Thermal-Shock Investigations," in *Heavy-Section Steel Technology Program Quart. Prog. Rep. July–September 1983*, NUREG/CR-3334, Vol. 3 (ORNL/TM-8787/V3), Union Carbide Corp. Nuclear Div., Oak Ridge Natl. Lab.

2. R. D. Cheverton et al., "Thermal-Shock Technology," pp. 134–37 in *Heavy-Section Steel Technology Program Semiannual Prog. Rep. October 1983–March 1984*, NUREG/CR-3744, Vol. 1 (ORNL/TM-9154/V1), Martin Marietta Energy Systems, Inc., Oak Ridge Natl. Lab.

3. R. D. Cheverton and D. G. Ball, *OCA-P, A Deterministic and Probabilistic Fracture-Mechanics Code for Application to Pressure Vessels*, NUREG/CR-3618 (ORNL-5991), Union Carbide Corp. Nuclear Div., Oak Ridge Natl. Lab., May 1984.

4. *ASME Boiler and Pressure Vessel Code*, Sect. III, Div. I, Subsection NA, Appendix I, American Society of Mechanical Engineers, New York, 1974.

5. T. U. Marston, ed., *Flaw Evaluation Procedures, ASME Section XI, Background and Application of ASME Section XI, Appendix A, Special Report*, EPRI NP-719-SR, American Society of Mechanical Engineers, Electric Power Research Institute, August 1978.

6. A. L. Hiser, F. J. Loss, and B. H. Menke, *J-R Curve Characterization of Irradiated Low Upper Shelf Welds*, NUREG/CR-3506 (MEA-2028), Materials Engineering Associates, Inc., April 1984.

7. Japan Welding Council, *Structural Integrity of Very Thick Steel Plate for Nuclear Reactor Pressure Vessels*, JWES-AE-7806, 1977 (in Japanese).

8. R. H. Bryan et al., *Quick-Look Report on the First Pressurized-Thermal-Shock Test, PTSE-1*, ORNL/PTSE-1, Union Carbide Corp. Nuclear Div., Oak Ridge Natl. Lab., March 7, 1984.

9. R. D. Cheverton and S. E. Bolt, *Pressure Vessel Fracture Studies Pertaining to a PWR LOCA-ECC Thermal Shock: Experiments TSE-3 and TSE-4 and Update of TSE-1 and TSE-2 Analysis*, ORNL/NUREG-22, Union Carbide Corp. Nuclear Div., Oak Ridge Natl. Lab., December 1977.

10. R. D. Cheverton et al., "Fracture Mechanics Data Deduced from Thermal-Shock and Related Experiments with LWR Pressure Vessel Materials," *J. Pres. Vessel Technol.* 105(2), 102 (May 1983).

11. American Society for Testing and Materials, "Standard Specification for Quenched and Tempered Vacuum-Treated Carbon and Alloy Steel Forging for Pressure Vessels," *1984 Annual Book of ASTM Standards*, Sect. 1, Vol. 01.04.

12. *ASME Code*, Section XI, Division 1, Subsection NB-2331.

13. D. A. Canonico, "Transition-Temperature Considerations for Thick-Walled Steel Nuclear Pressure Vessels," *Nucl. Eng. Des.* 17, 149–60 (1971).

14. A. R. Rosenfield, "Validation of Compact-Specimen Crack-Arrest Data," Technical Briefs, *J. Eng. Mater. Technol.*, Vol. 106/207 (April 1984).

15. A. R. Rosenfield et al., "Crack-Arrest Studies at BCL," *Heavy-Section Steel Technology Program Semiannual Prog. Rep. October 1983–March 1984*, NUREG/CR-3744, Vol 1 (ORNL/TM-9154/V1), Martin Marietta Energy Systems, Inc., Oak Ridge Natl. Lab.

16. A. Pellissier-Tanon, P. Sollougoub, and B. Houssin, "Crack Initiation and Arrest in an SA 508 Class-3 Cylinder Under Liquid Nitrogen Thermal-Shock Experiment," *Transactions of the 7th International Conference on Structural Mechanics in Reactor Technology*, Chicago, Vols G and H (August 1983).

17. T. J. Burns et al., *Pressurized Thermal Shock Evaluation of the Oconee-1 Nuclear Power Plant*, NUREG/CR-3770 (ORNL/TM-9176), Martin Marietta Energy Systems, Inc., Oak Ridge Natl. Lab. (in preparation).

18. R. D. Cheverton et al., *A Pressurized Thermal-Shock Evaluation of the Calvert Cliffs Unit 1 Nuclear Power Plant*, ORNL report in preparation.

19. R. D. Cheverton, "Thermal-Shock Investigations," pp. 61–62 in *Heavy-Section Steel Technology Program Quart. Prog. Rep. July–September 1978*, NUREG/CR-0476 (ORNL/NUREG/TM-275), Union Carbide Corp. Nuclear Div., Oak Ridge Natl. Lab., January 1979.

20. B. R. Bass and J. W. Bryson, *Applications of Energy Release Rate Techniques to Part-Through Cracks in Plates and Cylinders; Volume 1. ORMGEN-3D: A Finite-Element Mesh Generator for 3-Dimensional Crack Geometries*, NUREG/CR-2997, Vol. 1 (ORNL/TM-8527/V1), Union Carbide Corp. Nuclear Div., Oak Ridge Natl. Lab., December 1982.

21. B. R. Bass and J. W. Bryson, *Applications of Energy Release Rate Techniques to Part-Through Cracks in Plates and Cylinders; Volume 2. ORVIRT: A Finite-Element Program for Energy Release Rate Calculations for 2-Dimensional and 3-Dimensional Crack Models*, NUREG/CR-2997, Vol. 2 (ORNL/TM-8527/V2), Oak Ridge National Laboratory, Oak Ridge, Tennessee, February 1983.

22. K. J. Bathe, *ADINA – A Finite-Element Program for Automatic Dynamic Incremental Nonlinear Analysis*, Report 82448-1, Massachusetts Institute of Technology, Cambridge, Mass., September 1975 (revised December 1978).

10. PRESSURIZED-THERMAL-SHOCK TECHNOLOGY

R. H. Bryan

10.1 PTSE-1 Flaw Examination

R. H. Bryan S. E. Bolt

The pressurized thermal shocks in the PTSE-1 experiment produced two fast crack jumps to depths estimated during the tests to be 22.1 mm and 36.9 mm (Ref. 1). During the first crack propagation, the crack ran axially as well as radially. At the upper end of the 1000-mm-long initial flaw, the crack extended along an irregular path with an increment in length of 109 mm projected on the axis (Fig. 10.1). This extension ran along the initial plane of the crack for about 10 mm and then turned by about 21°. At the lower end, the crack branched near the end of the initial flaw (Fig. 10.2). Branches 1 and 2 had axial projections of 116 mm and 68 mm with directions deviating 30° and 34°, respectively, from the plane of the initial flaw.

The region of the flaw was surveyed ultrasonically to determine the depth and extent of the cracking, and a block containing the entire flaw was flame cut from the vessel and segmented (Fig. 10.3). The thickness of each segment was reduced to about 50 mm, and each piece was then chilled in liquid nitrogen and broken by bending to expose the mating fracture surfaces. Photographs were made of the fracture surface on each fragment to maintain the identity of features during further examinations of the flaw.

Visual examinations confirmed the results of the ultrasonic survey reported previously;[1] namely, the final flaw depth was ~40 mm over ~80% of the length of the flaw. The upper part of the flaw was relatively uniform (Figs. 10.4 and 10.5). The axial extension at the upper end (Fig. 10.4) occurred at the time of the first crack jump, which was in transient PTSE-1B, and was indicated by strain gages XE-51 and XE-52 (Fig. 10.1). The flaw extended in depth but not in length during the second crack jump, which occurred in PTSE-1C.

At the lower end of the flaw, the two branches extended axially at the time of the first crack jump. There was no further advance in either length or depth at this end of the flaw during the second crack jump. Side B of the fracture surfaces of each branch is shown in Figs. 10.6 and 10.7.

10.2 Fractographic Evaluation of PTSE-1 Fracture Surface

D. P. Edmonds R. K. Nanstad

To determine better the nature of crack propagation for this experiment, optical metallography and scanning electron fractography of the fracture have been performed. A montage showing both surfaces of the fracture is shown in Fig. 10.8. Also, typically different regions of the

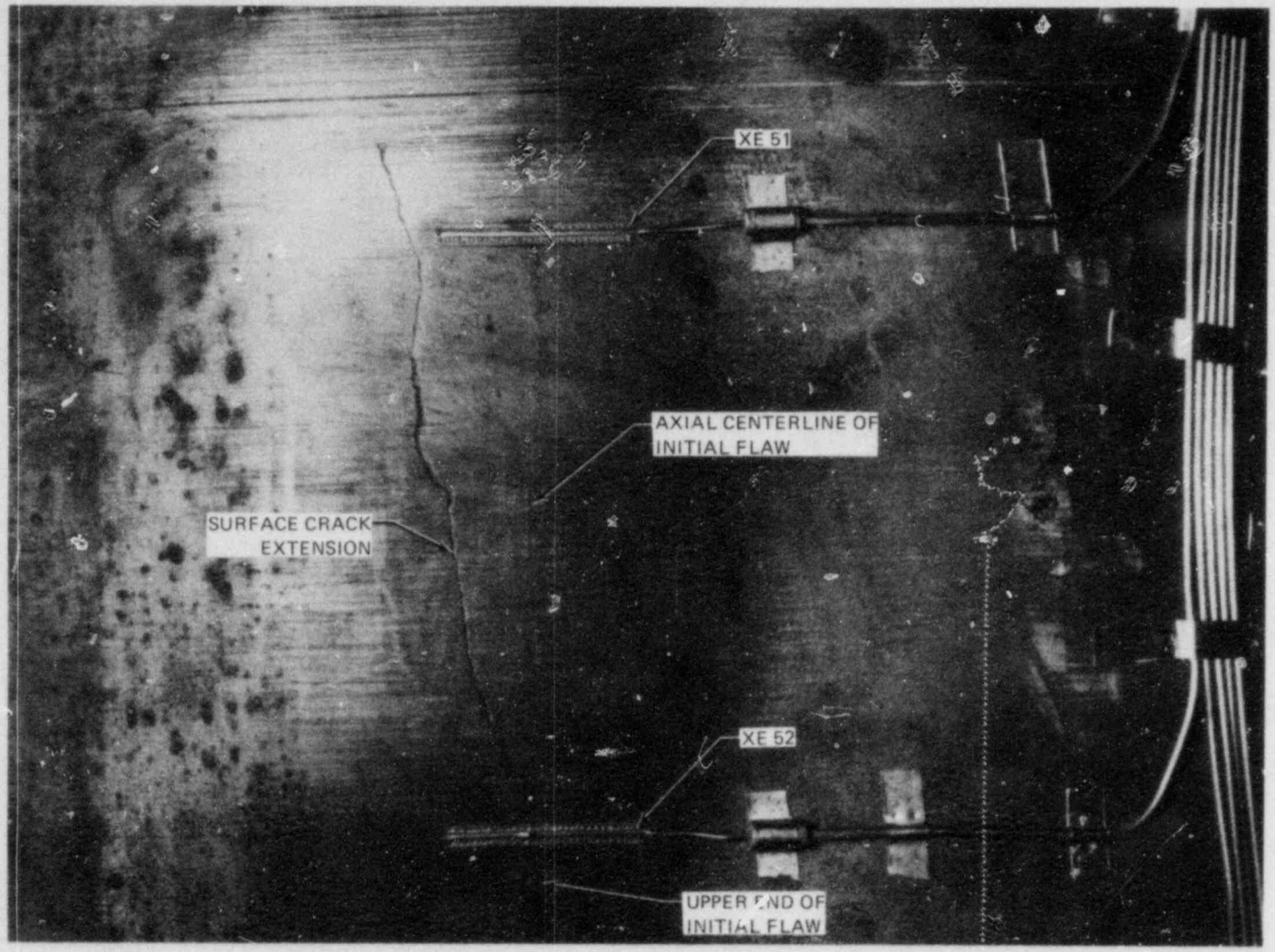

Fig 10.1. Posttest photograph of outside surface of PTSE-1 vessel at upper end of flaw.

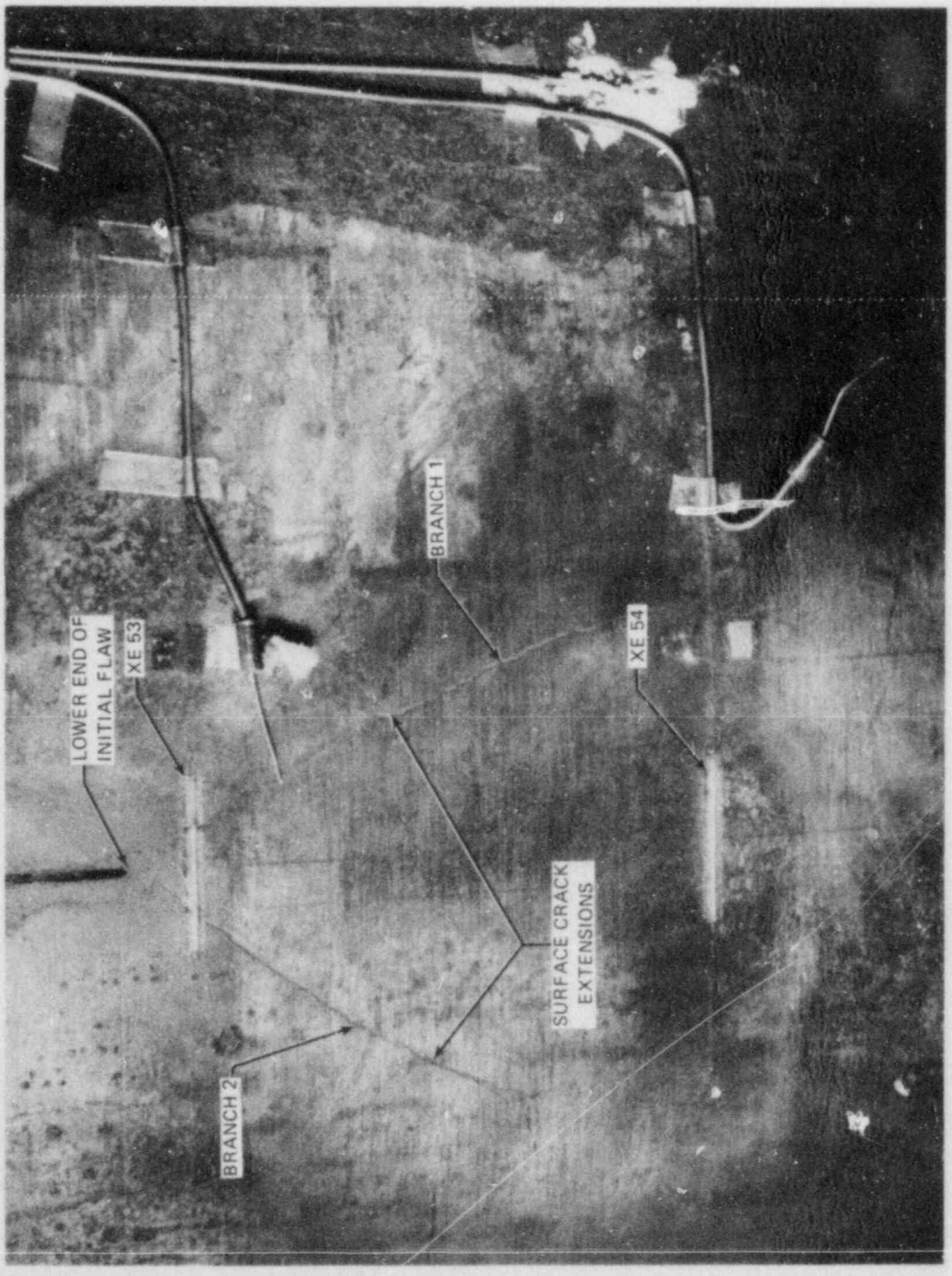

Fig. 10.2. Posttest photograph of outside surface of PTSE-1 vessel at lower end of flaw.

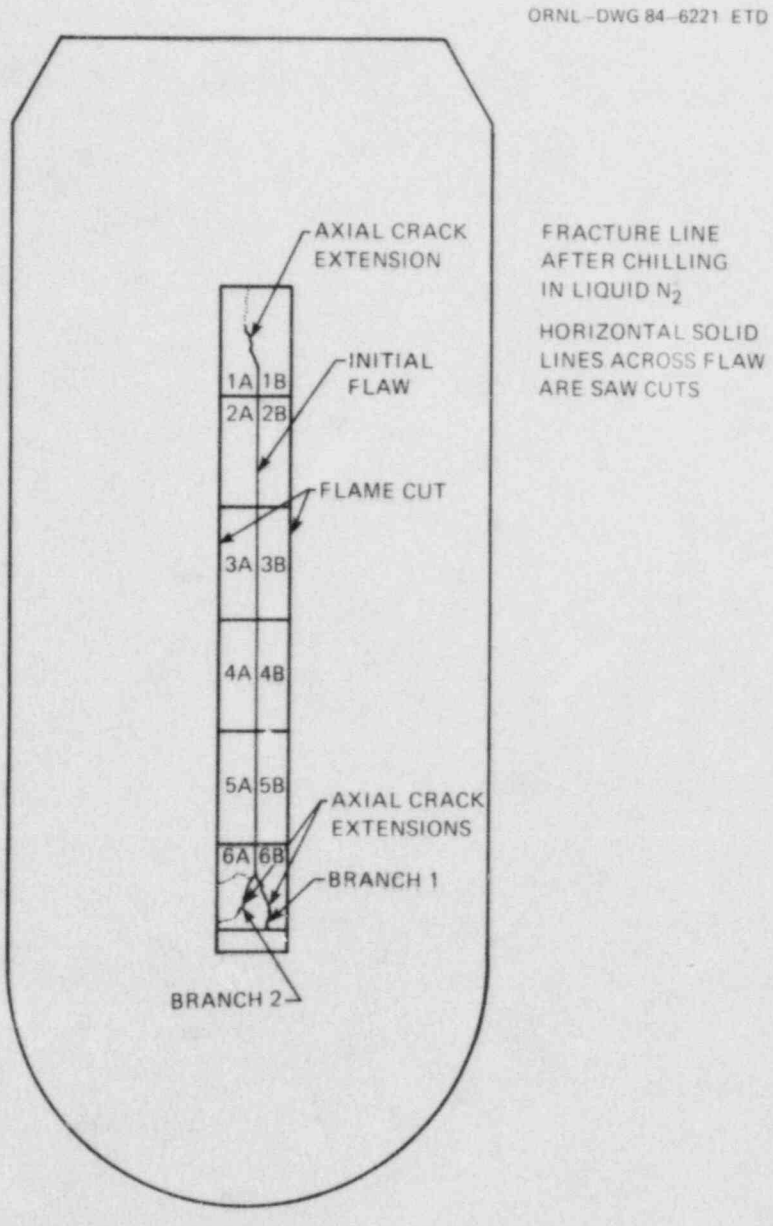

Fig. 10.3. Scheme for cutting and labeling PTSE-1 fracture surfaces. Surfaces labeled A are viewed toward left and B, toward right. Segment 6 contains two branches, designated by surfaces 1 and 2. Main crack and branch 1 mating surfaces are called 6A1 and 6B1, and branch 2 mating surfaces are called 6A2 and 6B2.

ORNL–PHOTO 6856–84A

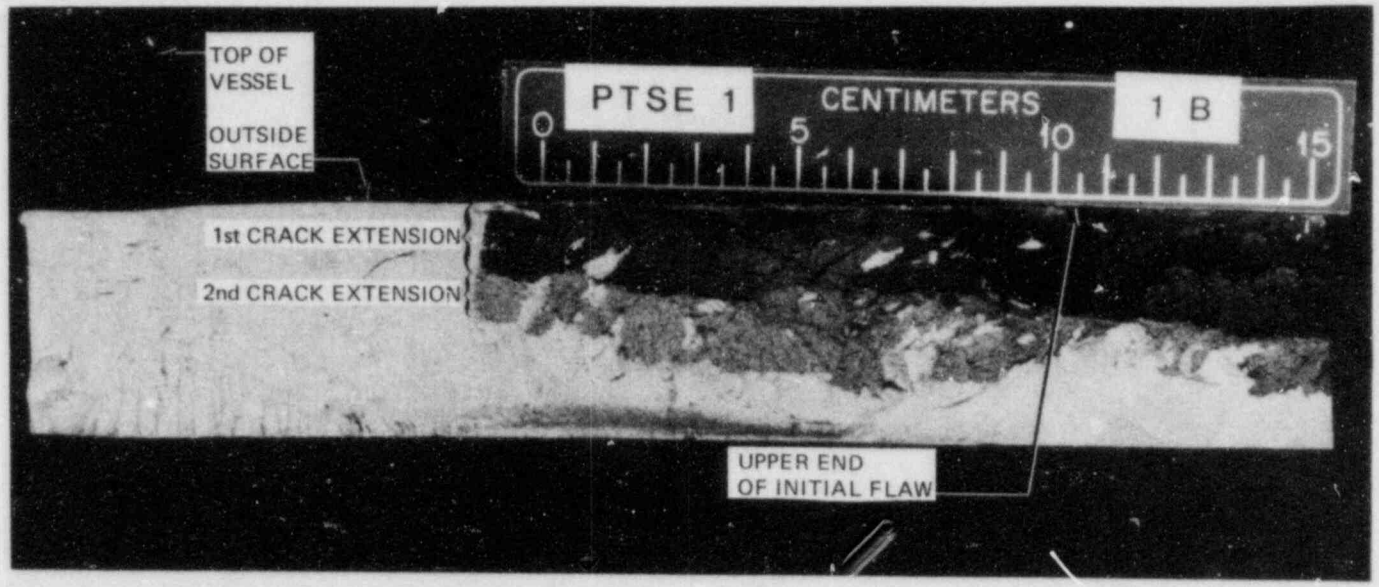

Fig. 10.4. Fracture surface B of segment 1 of PTSE-1 flaw showing axial extension at upper end of flaw. (See Fig. 10.3 for key to location.)

ORNL–PHOTO 6851–84A

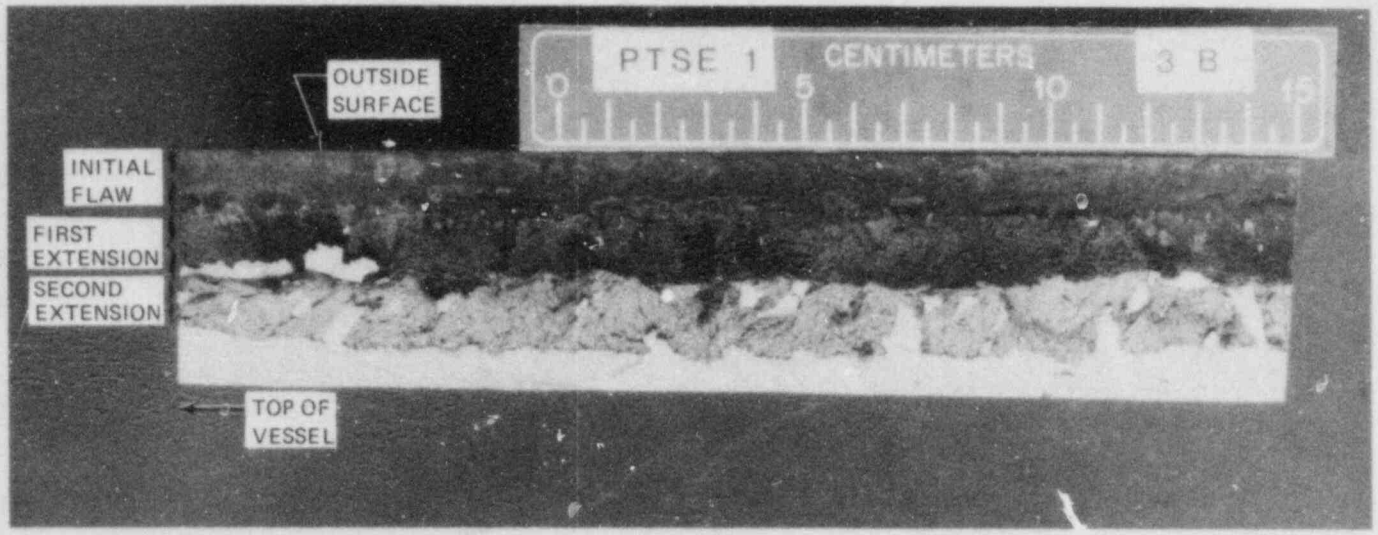

Fig. 10.5. Fracture surface B of segment 3 of PTSE-1 flaw is piece, next to midplane of flaw, shows deepest part of flaw. (See ig. 10.3 for key to location.)

ORNL–PHOTO 6854–84A

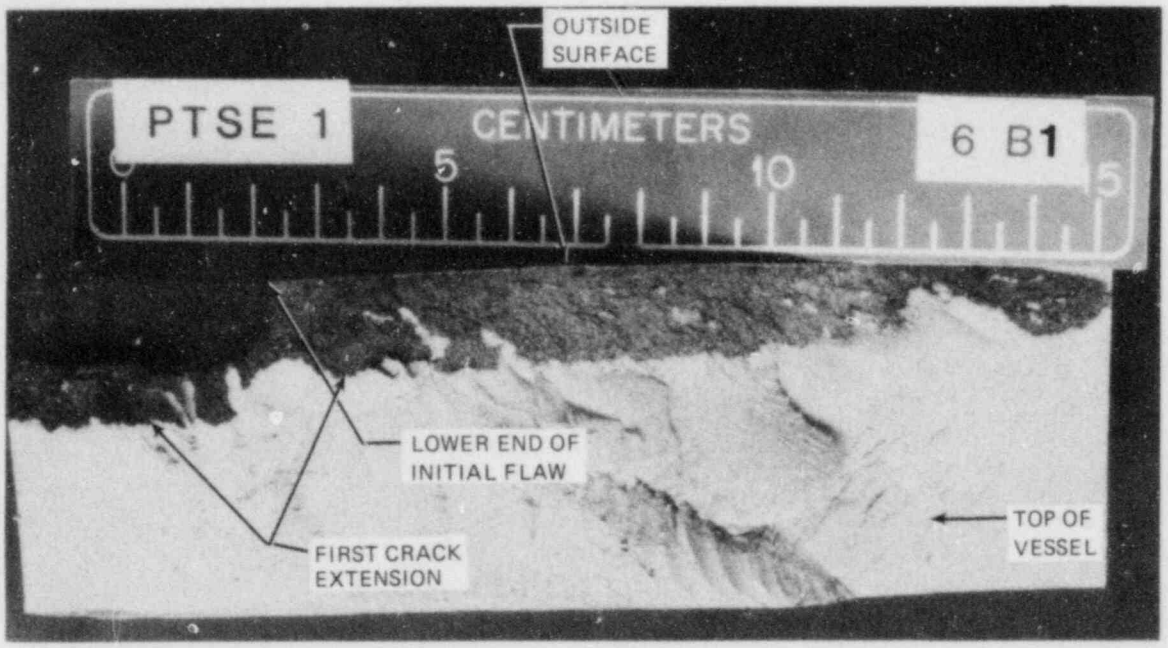

Fig. 10.6. Fracture surface B of main flaw and branch 1 in segment 6 of PTSE-1 flaw. Crack extensions in the piece occurred only during first crack jump, which was in PTSE-1B transient. (See Fig. 10.3 for key to location.)

ORNL–PHOTO 6846–84A

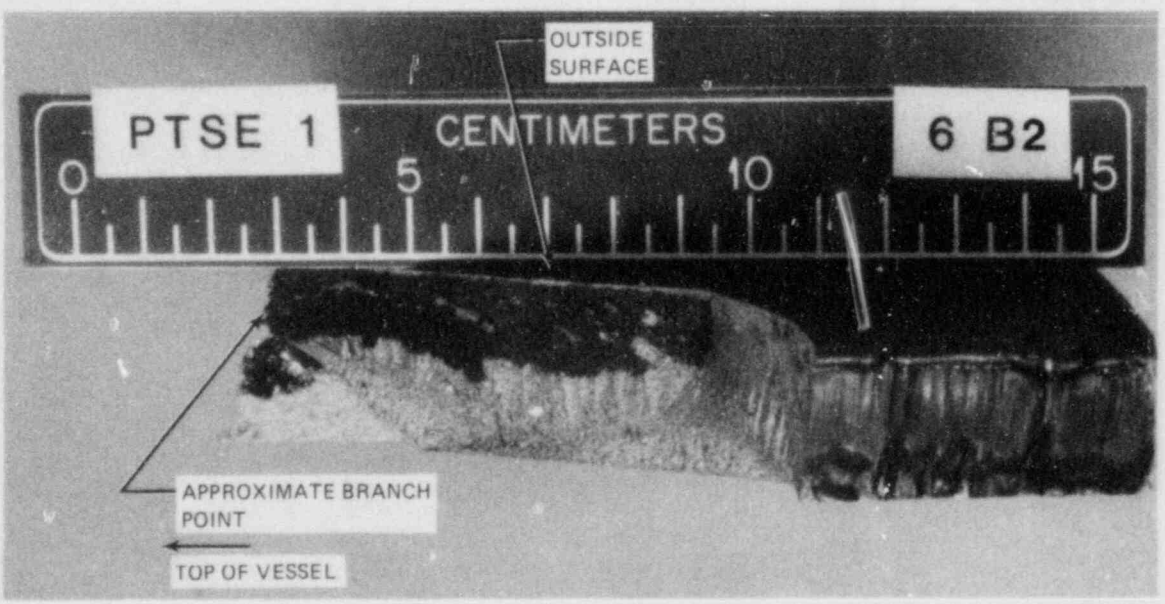

Fig. 10.7. Fracture surface B of branch 2 in segment 6 of PTSE-1 flaw. This crack extension occurred only during first crack jump, which was in PTSE-1B transient. (See Fig. 10.3 for key to location.)

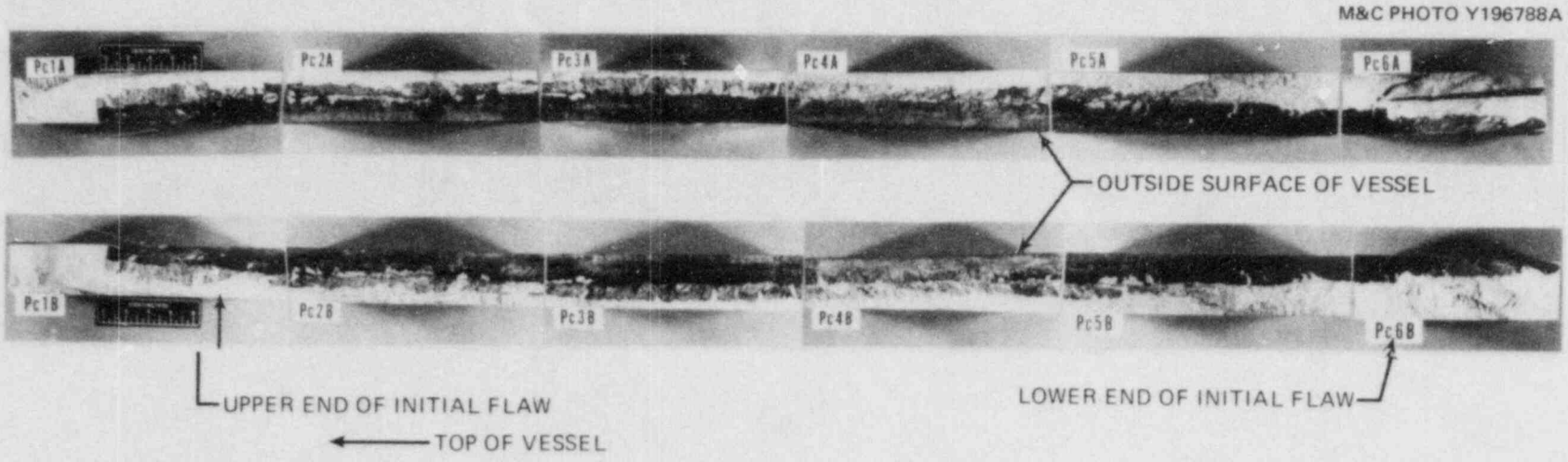

Fig. 10.8. Montage of fracture surface from PTSE-1. Only branch 1 surfaces are shown in pieces 6A and 6B. (See Fig. 10.3 for key to location.)

fracture surface are identified in Fig. 10.9. The original flaw, which was generated by hydrogen charging an electron-beam (EB) weld, is the smooth, dark-gray area on the sides of the specimens opposite the piece numbers. The original flaw is 1000 mm long and extends from Pc1 to Pc6. The average depth is 12 mm with some EB weld spikes extending up to 5 mm deeper into the material.

The first crack extension is the rough-textured, dark-gray area shown in the montage. It extends from about the center of Pc1 to the right edge of Pc6. The first crack extension branches in Pc6 with the primary crack (branch 1) extending to the right edge of Pc6. The axial projection of the first extension is about 1225 mm. The secondary crack (branch 2) extends 73 mm into Pc6A (not shown in Fig. 10.8) at an angle of about 59° from the primary crack and 34° from the plane of the original EB weld (Fig. 10.10). The first crack arrested at an average depth of 27 mm along most of its length, tapering off (after extending past the original flaw) to a depth of about 14 mm in Pc1 and about 10 mm in Pc6.

The second crack extension is the lighter gray, rough-textured region in the montage, which extends from the center of Pc1 to the center of Pc5. The depth of the second crack arrest is much more variable than that of the first arrest. The maximum crack depth of 41 mm occurs in sections Pc3 and Pc4.

The very light, shiny surfaces represent material broken apart at low temperatures after testing was complete. As can be seen in the montage, there are many unbroken ligaments in the second crack. Most of these extend into the crack from material beyond the arrest site, but

M&C PHOTO Y196781A

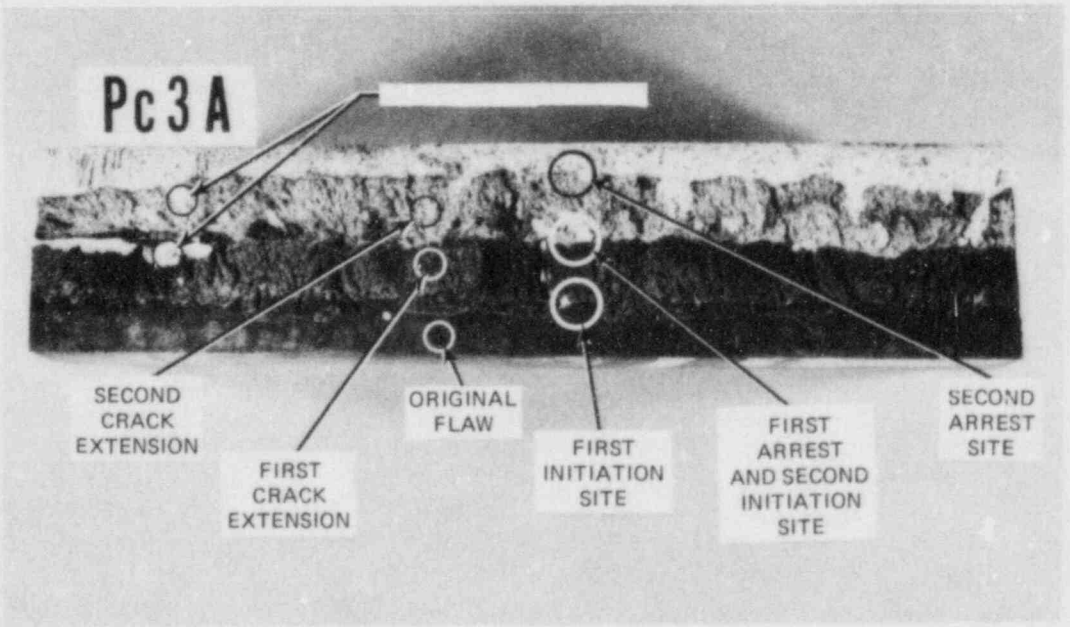

Fig. 10.9. Typical portion of fracture surface from PTSE-1 (surface A in segment 3).

M&C PHOTO Y196787A

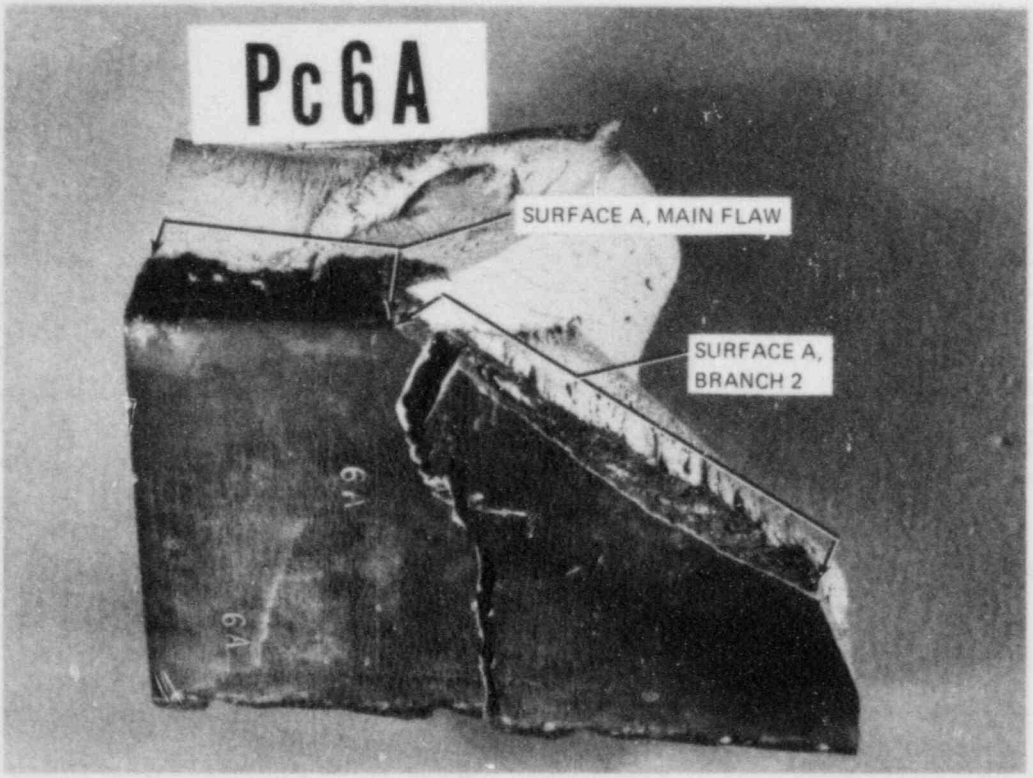

Fig. 10.10. Fracture surface showing propagation of first crack into Pc6A. Surface A of main flaw and of branch 2 is shown.

some are totally surrounded by cracked material. The first crack contains significantly fewer unbroken ligaments, most of which are totally surrounded by cracked material. There is a higher percentage of unbroken ligaments toward the ends of the first crack than at its center.

Detailed fractographic evaluations were performed for specimens taken from sections Pc2B, Pc3A, and Pc5A. The objectives of this work were to determine (1) the mode of failure for each crack, (2) if additional ductile fracture exists at the terminus of each crack, and (3) the nature of the unbroken ligaments.

Results indicate that the first crack initiated and ran in a cleavage mode to about half of its depth and then changed to mixed-mode failure (estimated to be about 90% cleavage and 10% ductile) until it arrested. A narrow band of ductile tearing was associated with the initiation of the first crack at some points along the crack length. There was no indication of increased ductile tearing in the area of the crack arrest. The second crack initiated and ran almost entirely in mixed mode, with slightly more ductile tearing than the first crack (estimated to be about 85% cleavage and 15% ductile). There was no indication of increased ductile tearing associated with the initiation or the arrest of the second crack. In some areas, a very narrow band (a few grains wide)

of nearly 100% cleavage was observed just after the second crack initiation. However, this was only observed in a few areas.

The existence of unbroken ligaments in the cracks did not seem to alter the fracture mode appreciably. Sometimes increased ductile tearing was observed at the sides of these ligaments, but not at the leading and trailing edges. The mode of crack propagation just past an unbroken ligament appeared to be the same as that preceding the ligament.

In summary, the crack arrests in this material do not appear to be associated with local increases in ductile tearing. However, slight changes in mode of crack propagation do occur. The most pronounced change is from cleavage to mixed mode halfway through (depthwise) the first crack extension. The temperature of the material at this transition is estimated to be about 125°C with an estimated K_I value of about 160 MPa•$\sqrt{m}$. This temperature is at the high end of the Charpy transition region and is just approaching the Charpy upper shelf for this material. Crack propagation in the second crack extension and in the second half of the first crack was at temperatures near or on the Charpy upper shelf for the material. The presence of mixed-mode crack propagation in this test is therefore thought to be associated with testing on or near the Charpy upper shelf. The increase in the proportion of ductile tearing in the second crack extension, compared with the first, is thought to result from the higher temperature.

10.3 PTSE-1 Posttest Fracture Analysis

R. H. Bryan D. A. Steinert

Two major tasks were undertaken to establish a basis for the final analyses of the PTSE-1 experiment: namely, to improve the utility of the OCA/USA computer program and to establish a qualified set of experimental data for input to fracture analyses. The experiment was planned so that actual transient temperatures throughout the vessel could be used for determining thermal stresses; thus, uncertainties inherent in heat transfer analysis of a real test assembly would be completely avoided.

The version of OCA/USA used in pretest and preliminary posttest analyses was designed to use temperatures either calculated on the basis of heat transfer parameters or experimentally measured temperatures. However, that version had inflexible output options and had an input structure that was not convenient for application to experimental investigations. The program has been extensively revised with provisions for plotting and tabulating results for arbitrarily specified times and locations. This feature alone reduces to a trivial level the manpower required to determine fracture analysis results that correspond precisely to experimentally observed events.

Pressures, strains, crack-mouth-opening displacements, and temperatures during each PTSE-1 transient were scanned and recorded at intervals of about 0.04 s by the primary data acquisition system. Thus, each of the three transients produced data records with about 2.5 million values. A series of data processing programs, which were written specifically for the pressurized-thermal-shock experiments, was used to evaluate the raw data and to generate data sets for further analysis.

With these programs, the performance of about 130 sensors has been evaluated, erroneous or anomalous data have been rejected, and calibrated data sets for input to OCA/USA or other use have been created. All 88 of the thermocouples that could potentially be used for OCA/USA input functioned normally throughout the transients. Data from five of these thermocouples were excluded on the basis of anomalous inconsistencies, which could have resulted from calibration errors or inaccurately specified locations.

Final fracture analyses are being performed with OCA/USA and calibrated data sets. In the final analyses, temperature-dependent values of Young's modulus E and the coefficient of thermal expansion α, both based upon values measured for PTSE-1 material, are being used. Values of the stress-intensity factor K_I at critical times in the transients are a few percent higher than the values previously reported,[1] principally as a result of using higher values of E and α.

10.4 Preliminary Fracture Analyses for the PTSE-2 Experiment

R. H. Bryan G. D. Whitman

Studies of pressurized-thermal-shock transients with a test vessel of low-upper-shelf (LUS) material were undertaken initially to determine whether new and useful information, beyond that expected from PTSE-1, on fracture behavior could be obtained with a vessel having low tearing resistance. Issues generally amenable to such transient experiments are: effects of sequences of warm-prestressing and anti-warm-prestressing episodes on crack initiation; behavior of cleavage fractures propagating into ductile regions; transient crack stabilization in ductile regions; and crack shape changes in bimetallic zones of clad vessels.

In the early stages of planning the pressurized-thermal-shock series, it was considered prudent to investigate these issues, whenever feasible, with the types of steels that are well characterized and best understood. Accordingly, the first experiment, PTSE-1, was conducted with SA508 Class 2 steel moderately degraded by a special temper. The use of LUS material in that experiment would have limited the latitude of attainable conditions and would have introduced ambiguities in the interpretation of the experiment by virtue of uncertainties in material properties. If LUS material had had no disadvantages relative to the SA508 Class 2 steel in PTSE-1, it would have presented no particular advantage in attaining the objectives of that test.

After it was realized that PTSE-1 had demonstrated warm prestressing and anti-warm prestressing, at least under a limited set of circumstances, and had succeeded in pushing a cleavage crack near to the ductile regime, the questions of necessity and feasibility of further tests were reexamined. The questions were:

1. Had warm-prestressing effects been explored adequately?
2. Could one expect to propagate a cleavage crack, without interruption, into the ductile regime with the facilities at hand?

3. Which type of material, SA508 or LUS, would be more suitable for another experiment?
4. What particular properties would be required for a feasible experiment?

PTSE-1 demonstrated, as expected, the strongly inhibiting effect of simple warm prestressing ($\dot{K}_I < 0$) on crack initiation. In at least one of the anti-warm-prestressing phases ($\dot{K}_I > 0$) of the PTSE-1A transient, K_I was much greater than K_{Ic} without crack initiation. This fact is a good indication that $\dot{K}_I$ being positive while $K_I \gg K_{Ic}$ is not a sufficient condition for crack initiation. In this instance, however, K_I during anti-warm prestressing was much smaller than its previously attained maximum value. This occurrence is shown in Fig. 10.11, which presents the K_I vs T trajectory of the PTSE-1A transient.

The warm-prestressing condition that needs to be studied further is one in which K_I increases during the anti-warm-prestressing phase to a level higher than that previously attained. This sequence is shown in

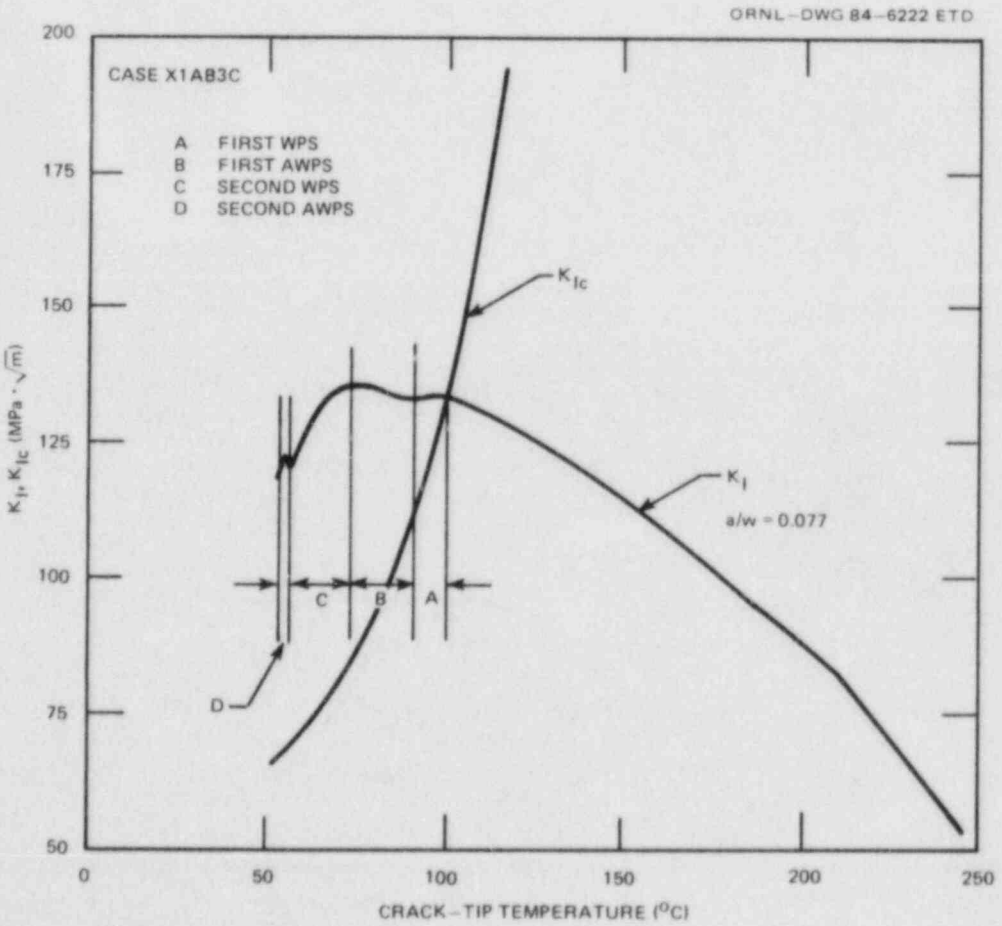

Fig. 10.11. Warm-prestressing (WPS) and anti-warm-prestressing (AWPS) stages of transient PTSE-1A.

Fig. 10.12. Small-scale experiments suggest that the prior maximum K_I level must be exceeded for the crack to propagate. Also, as discussed in Chap. 2, the change with time of the plastic zone at the crack tip is important. Consequently, during the phase when $\dot{K}_I > 0$, it is desirable to reach a state in which size of the plastic zone ahead of the crack increases beyond its prior maximum size. The PTSE-2 transient will be designed to study these factors.

Propagation of a cleavage crack into the ductile regime is feasible, with some risk of generating an unstable tear. Figure 10.13 is a plot of critical-crack-depth features of transients that illustrate the capability of the test facility to make a crack propagate into upper-shelf material. In these cases, the cleavage arrest loci coincide approximately with the purely ductile threshold temperature T_D contour from $t \approx 100$ s to $t \approx 200$ s. A crack arresting at this temperature would continue to grow at least in a ductile mode until it was deep and, consequently, in material well above T_D. The tearing would be terminated by depressurization, which is not explicitly included in the case presented in this figure.

The properties assumed for the cases shown in Fig. 10.13 were for material with low tearing resistance on the upper shelf, that is, LUS

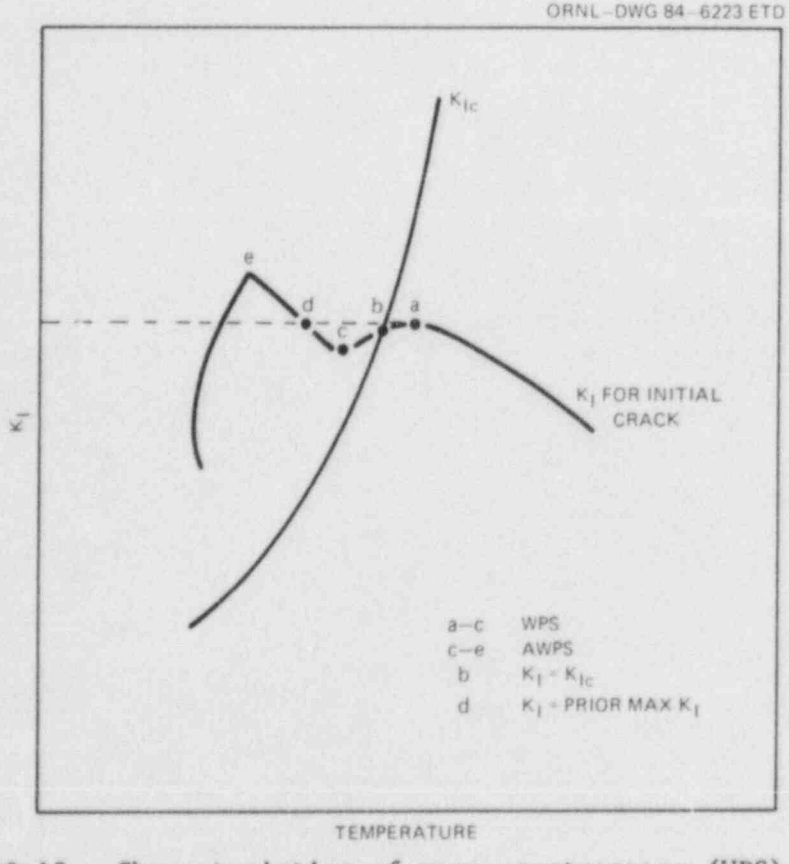

Fig. 10.12. Characteristics of warm-prestressing (WPS) and anti-warm-prestressing (AWPS) phases proposed for PTSE-2. According to one hypothesis, crack will propagate at point between c and e where plastic zone at crack tip becomes larger than largest prior plastic zone.

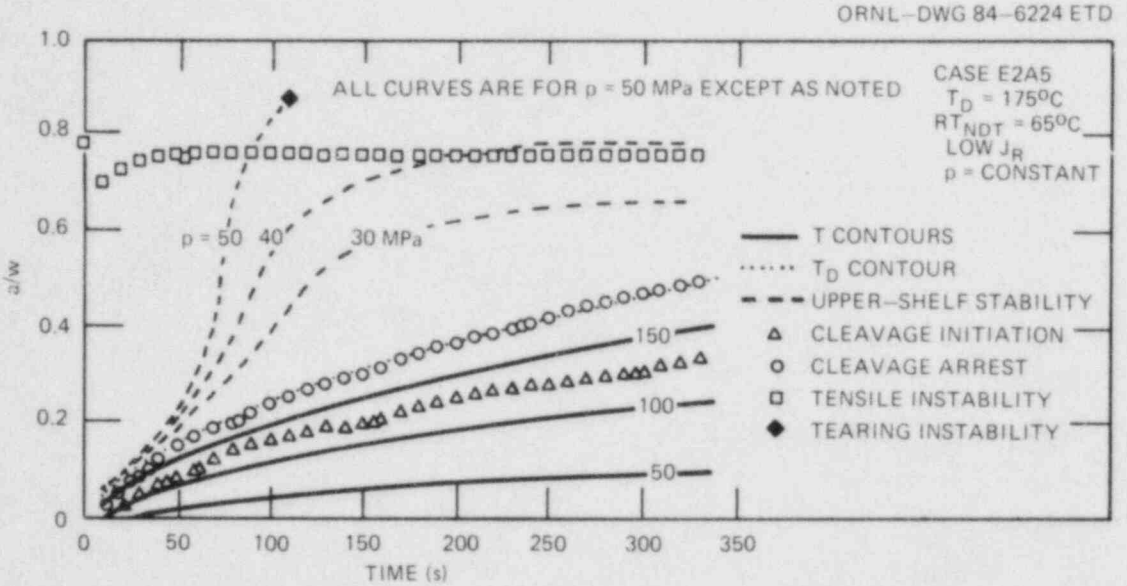

Fig. 10.13. Temperatures and critical crack depth loci (initiation, arrest, tearing stability, and tensile instability) for hypothetical PTSE-2 transients. Tearing stability loci show that arrested crack has high potential for metastable tearing, while proximity of arrest locus to ductile threshold temperature T_D contour indicates that crack would propagate in cleavage mixed mode nearly to T_D.

material similar to that in the V-8A test.[2] With normal upper-shelf toughness, as in PTSE-1, only a small amount of tearing is predicted. The PTSE-1 experiment showed this prediction of tearing to be conservative. Our conclusion is that an experiment with crack propagation into the upper shelf could be conducted with greater certainty and less risk of rupture if LUS material were used.

Material properties to be specified for the refabricated PTSE-2 vessel were investigated by further fracture analysis with the OCA/USA computer program. At this stage of planning, the acceptable values of RT_{NDT} had to be defined. The RT_{NDT} essentially determines the lower temperatures that must be achieved in the experiment. Cases were analyzed and evaluated for $40°C \leq RT_{NDT} \leq 65°C$. The results showed that the higher values of RT_{NDT} were clearly advantageous, because they allow deeper cleavage fracture penetration.

10.5 Preparation of Vessel for the PTSE-2 Experiment

R. H. Bryan G. C. Robinson
K. R. Thoms

Vessel V-8, which was used in the PTSE-1 experiment, will be repaired for use in PTSE-2. An insert of low-upper-shelf material will be welded into the existing cavity from which the PTSE-1 flaw was removed (see Fig. 10.14). Acceptable values for properties were selected for

ORNL–PHOTO 7214–84

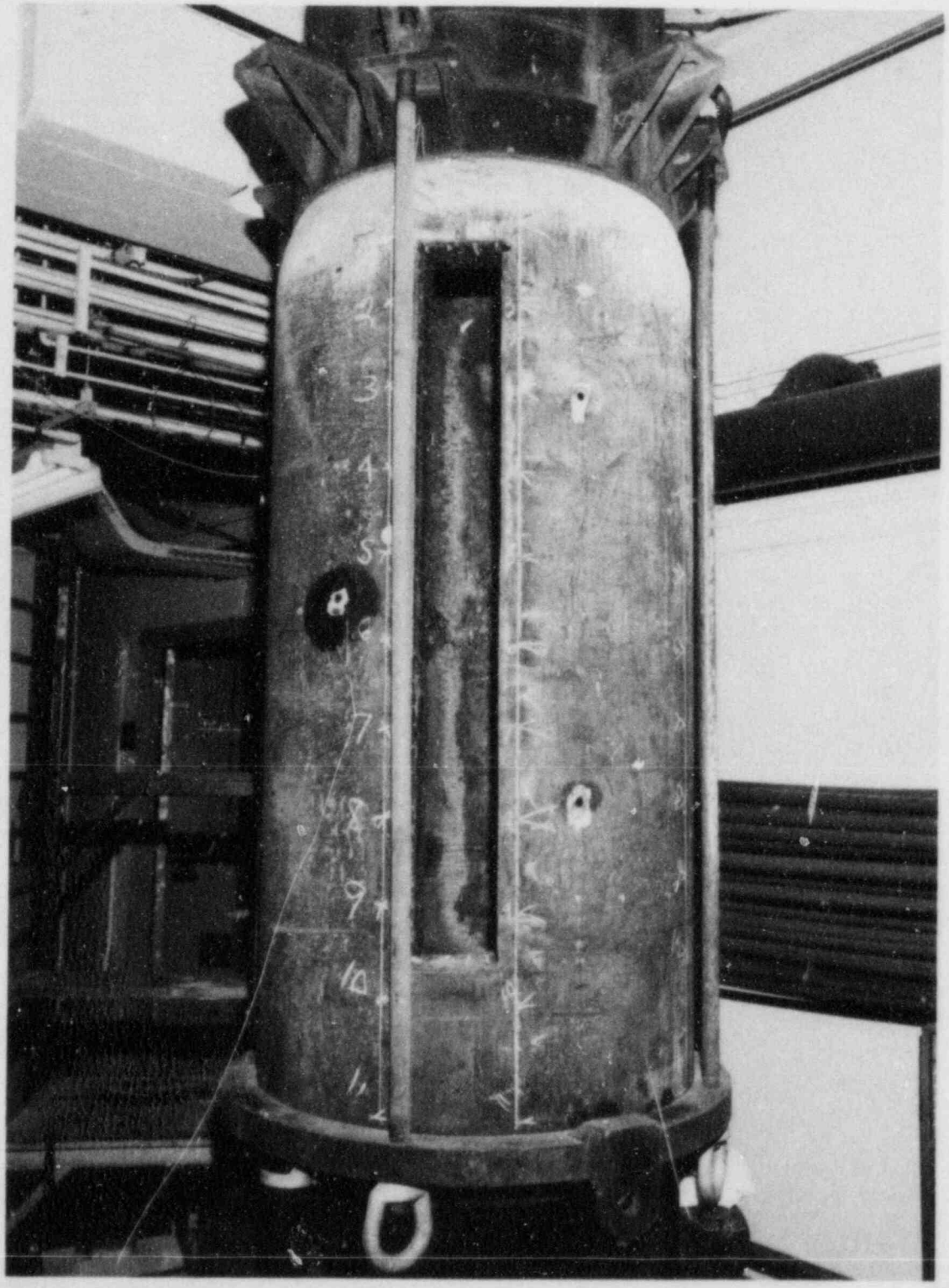

Fig. 10.14. Intermediate test vessel V-8 after removal of PTSE-1 flaw.

this insert as follows:

Yield strength, MPa	448 to 621
Charpy-V upper-shelf energy, J	54 to 68
Temperature at midpoint of Charpy-V energy transition, °C	52 to 91

Specifications for weld fabrication and vessel repair have been prepared. The quantity of weldment to be produced includes material from which test specimens will be made for determination of properties: Charpy, tensile, K_{Ic}, K_{Ia}, and J_R. Additional material will also be fabricated for six wide-plate crack-arrest specimens that will be tested by the National Bureau of Standards under HSST Task H 5.

Work on vessel instrumentation was initiated. The plan for data acquisition is generally the same as for PTSE-1. However, the thermocouple thimble has been redesigned to simplify fabrication and improve time response.

References

1. R. H. Bryan et al., "Results and Analyses of PTSE-1," *Heavy-Section Steel Technology Program Semiannual Prog. Rep. October 1983–March 1984*, NUREG/CR-3744, Vol. 1 (ORNL/TM-9154/V1), Martin Marietta Energy Systems, Inc., Oak Ridge Natl. Lab.

2. R. H. Bryan, "Posttest Study of V-8A," *Heavy-Section Steel Technology Program Quart. Prog. Rep. January–March 1983*, NUREG/CR-3334, Vol. 1 (ORNL/TM-8787/V1), Union Carbide Corp. Nuclear Div., Oak Ridge Natl. Lab.

CONVERSION FACTORS[a]

SI unit	English unit	Factor
mm	in.	0.0393701
cm	in.	0.393701
m	ft	3.28084
m/s	ft/s	3.28084
kN	lb_f	224.809
kPa	psi	0.145038
MPa	ksi	0.145038
$MPa \cdot \sqrt{m}$	$ksi \cdot \sqrt{in.}$	0.910048
J	ft·lb	0.737562
K	°F or °R	1.8
kJ/m^2	$in.\text{-}lb/in.^2$	5.71015
$W \cdot m^{-2} \cdot K^{-1}$	$Btu/h\text{-}ft^2\text{-}°F$	0.176110
kg	lb	2.20462
kg/m^3	$lb/in.^3$	3.61273×10^{-5}
mm/N	$in./lb_f$	0.175127
T(°F) = 1.8 T(°C) + 32		

[a]Multiply SI quantity by given factor to obtain English quantity.

NUREG/CR-3744
Volume 2
ORNL/TM-9154/V2
Dist. Category RF

Internal Distribution

1. D. G. Ball
2. B. R. Bass
3. R. G. Berggren
4. S. E. Bolt
5. R. H. Bryan
6. J. W. Bryson
7. R. D. Cheverton
8. J. M. Corum
9. W. R. Corwin
10. D. M. Eissenberg
11-12. D. S. Griffith
13. R. C. Gwaltney
14. S. K. Iskander
15. K. K. Klindt
16. A. P. Malinauskas
17. S. S. Manson
18. R. W. McCulloch
19. J. J. McGowan
20. J. G. Merkle
21-22. R. K. Nanstad
23. D. J. Naus
24-28. C. E. Pugh
29. G. C. Robinson
30. J. W. Roddy
31. G. M. Slaughter
32. J. E. Smith
33. R. W. Swindeman
34. K. R. Thoms
35. H. E. Trammell
36. C. D. West
37-40. G. D. Whitman
41. G. T. Yahr
42. ORNL Patent Office
43. Central Research Library
44. Document Reference Section
45-46. Laboratory Records Department
47. Laboratory Records (RC)

External Distribution

48. C. Z. Serpan, Division of Engineering Technology, Nuclear Regulatory Commission, Washington, DC 20555
49. M. Vagins, Division of Engineering Technology, Nuclear Regulatory Commission, Washington, DC 20555
50. Office of Assistant Manager for Energy Research and Development, DOE, ORO, Oak Ridge, TN 37831
51-52. Technical Information Center, DOE, Oak Ridge, TN 37831
53-327. Given distribution as shown in category RF (NTIS – 10)

NRC FORM 335 (2 84) NRCM 1102 3201 3202

U.S. NUCLEAR REGULATORY COMMISSION

BIBLIOGRAPHIC DATA SHEET

SEE INSTRUCTIONS ON THE REVERSE

1. REPORT NUMBER (Assigned by TIDC, add Vol. No., if any)
NUREG/CR-3744/V2
ORNL/TM-9154/V2

2. TITLE AND SUBTITLE
Heavy-Section Steel Technology Program Semiannual Progress Report for April-September 1984

3. LEAVE BLANK

4. DATE REPORT COMPLETED
MONTH: November
YEAR: 1984

5. AUTHOR(S)
C. E. Pugh

6. DATE REPORT ISSUED
MONTH: December
YEAR: 1984

7. PERFORMING ORGANIZATION NAME AND MAILING ADDRESS (Include Zip Code)
Oak Ridge National Laboratory
P.O. Box X
Oak Ridge, Tennessee 37831

8. PROJECT/TASK/WORK UNIT NUMBER

9. FIN OR GRANT NUMBER
B0119

10. SPONSORING ORGANIZATION NAME AND MAILING ADDRESS (Include Zip Code)
Division of Engineering Technology
Office of Nuclear Regulatory Research
U. S. Nuclear Regulatory Commission
Washington, DC 20555

11a. TYPE OF REPORT
Semiannual

b. PERIOD COVERED (Inclusive dates)
April-September 1984

12. SUPPLEMENTARY NOTES

13. ABSTRACT (200 words or less)

The Heavy-Section Steel Technology (HSST) Program is an engineering research activity conducted by the Oak Ridge National Laboratory for the Nuclear Regulatory Commission. The program comprises studies related to all areas of the technology of materials fabricated into thick-section primary-coolant containment systems of light-water-cooled nuclear power reactors. The investigation focuses on the behavior and structural integrity of steel pressure vessels containing cracklike flaws. Current work is organized into ten tasks: (1) program management, (2) fracture-methodology and analysis, (3) material characterization and properties, (4) environmentally assisted crack growth studies, (5) crack arrest technology, (6) irradiation effects studies, (7) cladding evaluations, (8) intermediate vessel tests and analysis, (9) thermal-shock technology, and (10) pressurized thermal-shock technology.

14. DOCUMENT ANALYSIS - a. KEYWORDS/DESCRIPTORS

Pressure vessels
Ferritic steels
Weldments
Irradiation
Cladding
Flaws
Thermal shock
Fracture mechanics
Crack arrest
Crack growth

b. IDENTIFIERS/OPEN-ENDED TERMS

15. AVAILABILITY STATEMENT
Unlimited

16. SECURITY CLASSIFICATION
(This page) Unclassified
(This report) Unclassified

17. NUMBER OF PAGES

18. PRICE

☆U.S. GOVERNMENT PRINTING OFFICE: 1984-544-045/4228